Design, Prototyping and Analysis of Axial-Flux Induction Motor for Line-Start Applications

by

Zhi Cao

Master of Electrical Engineering

A Thesis Submitted for the Degree of

Doctor of Philosophy

in

College of Science and Engineering

Flinders University, Australia

05 SEPTEMBER 2025

Supervisors:

Dr. Amin Mahmoud, College of Science and Engineering, Flinders University

A/Prof. Wen L. Soong, School of Electrical and Mechanical Engineering, The University of Adelaide

Dr. Solmaz Kahourzade, STEM, University of South Australia

Flinders
University

CONTENTS

ABSTRACT

Radial-flux induction motors (RFIMs) remain the predominant choice in industrial applications, largely owing to their robustness and structural simplicity. Nevertheless, their limited power density has driven increasing interest in axial-flux induction motors (AFIMs), which offer superior torque density and a more compact configuration. Despite these advantages, AFIMs remain underutilised in line-start applications due to practical challenges, such as higher manufacturing complexity, structural sensitivity, and the lack of standardised design and fabrication guidelines.

This thesis establishes a design and evaluation framework for line-start AFIMs. A geometry-driven electromagnetic design method is proposed, incorporating key constraints such as magnetic loading and current density at different radii, making the approach more aligned with the inherent characteristics of AFIMs. Additionally, material cost considerations are integrated to ensure design feasibility from both technical and economic perspectives. Multi-objective visualisation techniques are employed to reveal trade-offs and guide optimal design choices. The method is then applied to transform commercial RFIMs into AFIM counterparts for different pole numbers. A comprehensive sensitivity analysis is conducted to evaluate how variations in key geometric parameters, such as slot shape and slot number, affect the electromagnetic performance of both AFIMs and RFIMs, and to identify which parameters play a more critical role in each topology.

The work further investigates axial force, an issue that has attracted considerable attention in AFIMs. To address this, a static measurement technique is developed and validated both simulation and experimental results. This method enables accurate quantification of axial force without fully assembled thereby enabling accurate evaluation during early-stage prototyping. The outcomes provide valuable design reference for mechanical support structure, airgap management, and bearing selection in AFIM development. Various double-sided AFIM topologies are also analysed and compared to evaluate their impact on axial force mitigation and structural feasibility.

A stationary no-load testing methodology specifically developed for AFIM is proposed as an alternative to the conventional rotating no-load test. This approach enables an early-stage evaluation of motor performance without the need for rotor rotation or fully mechanical assembly. Moreover, the study introduces a classification of mechanical losses into voltage and airgap length dependent components. By employing combined strategy of stationary and

rotating no-load measurements, these components can be separated, thereby providing a more accurate assessment of electromagnetic characteristics of AFIMs at the preliminary evaluation stage.

Together, these contributions form a comprehensive investigation for the efficient design, prototyping, and evaluation of line-start AFIMs, supporting their practical deployment in industrial applications.

DECLARATION

I certify that this thesis:

1. does not incorporate without acknowledgment any material previously submitted for a degree or diploma in any university

2. and the research within will not be submitted for any other future degree or diploma without the permission of Flinders University; and

3. to the best of my knowledge and belief, does not contain any material previously published or written by another person except where due reference is made in the text; and

4. has been completed without the use of generative artificial intelligence tools.

Signed: Date: 05/09/2025

ACKNOWLEDGEMENTS

I am deeply grateful to Dr. Mahmoudi for kindly accepting me into the Electric Motor Group despite my lack of research experience at the time. What began as a simple assignment on electric motors unexpectedly sparked my curiosity for research, thanks to his encouragement and insightful feedback. In those early, uncertain stages, his patience and guidance were instrumental in helping me find direction and begin this journey.

I am truly thankful to A/Prof. Soong for his continuous mentorship and high standards. He consistently emphasised the importance of precision, clarity, and critical thinking in research. His rigorous review of my thesis—down to technical and linguistic details—greatly shaped my academic discipline. His deep knowledge and insightful suggestions inspired many of the directions taken in this thesis.

I also sincerely thank Dr. Kahourzade for her unwavering patience and support. She reviewed my work repeatedly, even when I made the same mistakes more than once. Her detailed feedback and encouragement helped me improve not only the quality of my research but also my attitude toward it, fostering a more careful and systematic approach.

I am deeply thankful to ROTOTECH Pty Ltd for their close collaboration and consistent support throughout the research process. Their contribution extended beyond technical discussions, including funding support and access to experimental resources, which were critical to the successful execution of this work. I also gratefully acknowledge the support of the Australian Government through the Research Training Program (RTP) Scholarship. Moreover, I also appreciate the support from Flinders University and The University of Adelaide. Special thanks to the workshop team at the University of Adelaide, especially Brad, whose manufacturing advice was crucial to the successful construction of the motor.

I also want to express my appreciation for all the help and encouragement received from my friends, Emad Roshandel, Yuan Yao, Qiang Gao, Rui Yuan, Xin Yuan, Linxi Chen, Mengtong Tang, Yang Fei, Daotong Zhang, Yidan Zhao and Wing Kong Ng. I will treasure the valuable moments and our friendships forever. I would also express my deep gratitude to my old friends back at China, Qi Gao, Yingrui Li, Chang Li and Changxu Dong, whose warm company, often through late-night video chats over drinks, helped me get through some of the most difficult times during my PhD journey.

Last but not least, I want to express my heartfelt love and thanks to my dad and mom. They have been my strongest source of support and motivation since I left my hometown 12 years ago. I could not have achieved what I have today without their endless encouragement, understanding, and unwavering belief in me. During moments of overwhelming pressure and confusion, they always reminded me to shake off the weight and get moving, to focus on what I could do, rather than worry about everything else. I love you both deeply, and this thesis is a tribute to you.

THESIS CONVENTIONS

The following conventions have been adopted in this thesis:

Typesetting

This document was compiled using Microsoft Word (Microsoft 365, Version 2404). MATLAB R2024b, ANSYS Electronic desktop 2023 R2, and Microsoft Excel (Microsoft 365, Version 2404) were used to produce schematic diagrams and other drawings.

Spelling

Australian English spelling conventions have been used, as defined in the Macquarie English Dictionary (A. Delbridge (Ed.), Macquarie Library, North Ryde, NSW, Australia, 2001).

Referencing

The IEEE style is used for referencing and citation in this thesis.

System of Units

The units comply with the international system of units recommended in an Australian Standard: AS ISO 1000-1998 (Standards Australia Committee ME/71, Quantities, Units and Conversions 1998).

PUBLICATIONS

[1]   **Z. Cao**, A. Mahmoudi, W. L. Soong and S. Kahourzade, "Design and Analysis of a Single-Sided 2.2kW Axial-Flux Induction Motor," *2024 IEEE Energy Conversion Congress and Exposition (ECCE)*, Phoenix, AZ, USA, 2024, pp. 4936-4943.

[2]   **Z. Cao**, A. Mahmoudi, S. Kahourzade, W. L. Soong and A. Mahmud, "Design and Analysis of Different Topologies of 4kW Double-Sided Axial-Flux Induction Motor," *2024 IEEE 34th Australasian Universities Power Engineering Conference (AUPEC)*, Sydney, Australia, 2024, pp. 1-5.

[3]   **Z. Cao**, A. Mahmoudi, S. Kahourzade and W. L. Soong, "A Study on Dual and Single Stator Axial-Flux Induction Machines," *2022 32nd Australasian Universities Power Engineering Conference (AUPEC)*, Adelaide, Australia, 2022, pp. 1-6.

[4]   **Z. Cao**, A. Mahmoudi, S. Kahourzade and W. L. Soong, "An Overview of Axial-Flux Induction Machine," *2021 31st Australasian Universities Power Engineering Conference (AUPEC)*, Perth, Australia, 2021, pp. 1-6.

[5]   **Z. Cao**, A. Mahmoudi, S. Kahourzade and W. L. Soong, "An Overview of Electric Motors for Electric Vehicles," *2021 31st Australasian Universities Power Engineering Conference (AUPEC)*, Perth, Australia, 2021.

[6]   **Z. Cao**, G. A. R. Cardenas, E. Roshandel, A. Mahmoudi, S. Kahourzade and W. L. Soong, "Comparative Study on Induction Machines: Three-Phase vs. Five-Phase Winding Configurations," *2021 31st Australasian Universities Power Engineering Conference (AUPEC)*, Perth, Australia, 2021.

[7]   **Z. Cao**, A. Yazdani, and A. Mahmoudi, "Intelligent robust pitch control of wind turbine using brain emotional learning," *IET Renewable Power Generation*, Jan. 2021.

[8]   **Z. Cao**, A. Mahmoudi, S. Kahourzade and W. Soong, "Surface Permanent Magnet Machines: A Comparative Study (4-pole vs. 40-pole motor)," *2020 IEEE International Conference on Power Electronics, Drives and Energy Systems (PEDES)*, Jaipur, India, 2020, pp. 1-6.

[9]   A. Mahmoudi, **Z. Cao**, S. Kahourzade and W. Soong, "PM-Free Axial-Flux Motors for Transport Electrification," *2024 IEEE International Magnetic Conference - Short papers (INTERMAG Short papers)*, Rio de Janeiro, Brazil, 2024, pp. 1-2.

[10]   W. L. Soong, E. Roshandel, **Z. Cao**, A. Mahmoudi and S. Kahourzade, "Axial Force Negative Stiffness in Axial-Flux Electric Machines," *2023 IEEE International Magnetic Conference - Short Papers (INTERMAG Short Papers)*, Sendai, Japan, 2023, pp. 1-2.

[11]   W. L. Soong, **Z. Cao**, E. Roshandel, A. Mahmoudi and S. Kahourzade, "Unbalanced Axial Forces in Axial-Flux Machines," *2022 32nd Australasian Universities Power Engineering Conference (AUPEC)*, Adelaide, Australia, 2022, pp. 1-6.

[12]   B. Li, A. Mahmoudi, S. Kahourzade, W. L. Soong and **Z. Cao**, "Thermal Prediction of Induction Machines Based on Finite Element and Analytical Methods," *2022 32nd Australasian Universities Power Engineering Conference (AUPEC)*, Adelaide, Australia, 2022, pp. 1-6.

[13]   T. T. To, E. Roshandel, A. Mahmoudi, **Z. Cao** and S. Kahourzade, "Optimization of IM Rotor Bars Inclination Angle using Analytical Model in Free FEA Software," *2021 IEEE Energy Conversion Congress and Exposition (ECCE)*, Vancouver, BC, Canada, 2021, pp. 4119-4126.

[14]   S. Kahourzade, A. Mahmoudi, E. Roshandel, and **Z. Cao**, "Optimal design of axial-flux induction motors based on an improved analytical model," *Energy*, vol. 237, p. 121552, 2021.

[15]   W. L. Soong, Emad Roshandel, **Z. Cao**, A. Mahmoudi, and Solmaz Kahourzade, "Axial Force Negative Stiffness in Axial‐Flux Electric Machines," IET Electric Power Applications, vol. 19, no. 1, Jan. 2025.

LIST OF FIGURES

XV

LIST OF TABLES

CHAPTER 1

INTRODUCTION

1.1　Background

Electric motors (EMs) are the most widely used energy conversion devices in renewable energy generation. Their ability to operate both as motors and generators makes them suitable for a wide range of applications. These include residential appliances, industrial manufacturing, commercial enterprises, and public transportation systems [1, 2]. In the industrial sector, EMs are extensively used to drive machinery and conveyor systems. Within the commercial sector, the power equipment such as refrigeration units and heating, ventilation, and air conditioning (HVAC) systems. In public transportations, EMs are increasingly adopted as a replacement for internal combustion engines (ICEs), offering a viable pathway toward net-zero emissions. Compared to ICEs, EMs exhibit significantly higher efficiency, thereby reducing operational costs and environmental impacts. In the residential domain, EMs are installed in a wide range of appliances, including washing machines, vacuum cleaners, and air conditioners [2, 3]. Importantly, EMs constitute the largest single end-use of electricity in the industrial sector, account for approximately 60% of total electricity consumption [2-4].

Radial-flux motors (RFMs) represent the most common configuration of EMs, characterised by a cylindrical rotor concentrically enclosed by the stator. In this arrangement, the magnetic flux crosses the airgap in the radial direction, i.e., perpendicular to the axis of rotation. In contrast, axial-flux motors (AFMs) adopt a disc-shaped topology in which the rotor and stator are positioned in parallel. This results in the magnetic flux traversing the airgap along the axial direction, parallel to the shaft. When a squirrel-cage rotor is employed in an axial-flux configuration, the motor is referred to as an axial-flux induction motor (AFIM), while its conventional radial counterpart is termed a radial-flux induction motor (RFIM), as illustrated in (Figure 1-1).

Some of the earliest recorded EMs were based on the axial-flux principle. Michael Faraday demonstrated a primitive disc-type motor in 1831, which can be regarded as one of

the first AFM [5]. Subsequently, in 1889, Nikola Tesla patented a motor design that also employed axial-flux operation. Despite these early developments, the development of the AFM almost ceased following the first patent of a RFM in 1937. Thereafter, progress in AFM technology slowed significantly, primarily due to the high-precision manufacturing requirements and the limited production capabilities available at the time [5, 6]. Interest in AFMs was renewed in the 1990s, driven by advancements in materials and manufacturing technologies. In particular, their inherent advantages in specific applications, such as in-wheel motor drives for electric vehicle (EV), have prompted renewed research into their design and performance [5, 6].

(a)   (b)
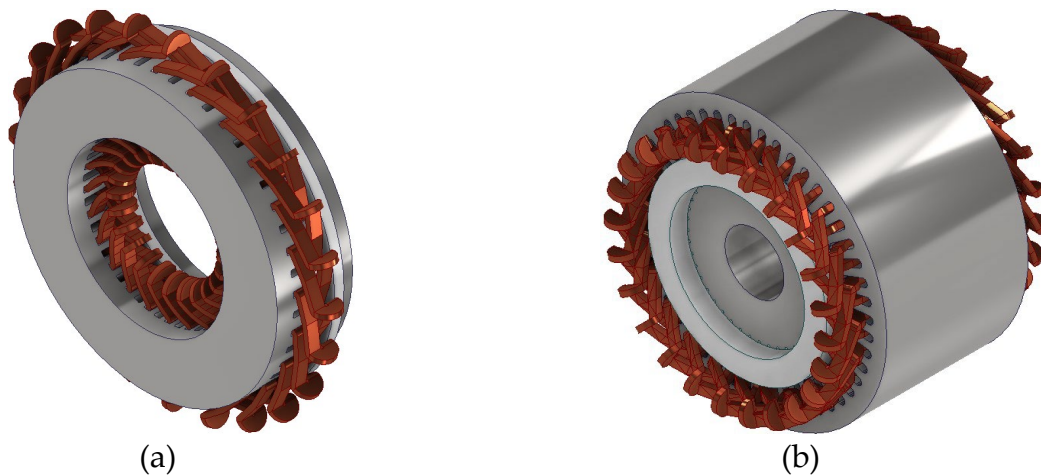
Figure 1-1 Axial (a) and radial (b) flux induction motors.

Table 1-1 Comparison of Line-Start and Inverter-Driven Motors Based on Operational and Cost Characteristics [6-9].

Feature	Line-Start Motor	Inverter-Driven Motor
Starting Method	Directly from AC mains	Controlled by variable-frequency drive (VFD)
Speed Control	Relatively fixed speed	Variable speed
Starting Torque	High ($\approx$ 200% of rated torque)	Adjustable
Efficiency	High @ fixed speed	High across range of speeds
Setup Cost	Low	High
Maintenance Cost	Low	High
Applications	Constant-speed applications	Variable-speed and precise control applications
Installation	Simple	More complex

Alternating current (AC) EMs can be divided into two categories, line-start and inverter-driven motors. A comparison of their key operational characteristics, cost implications, and application suitability is summarised in Table 1-1. Line-start motors are designed for near-constant speed operation and typically achieve their highest efficiency close to the rated load torque. These motors operate directly from the AC mains and are widely deployed in applications such as fans and pumps, where a fixed operating speed is acceptable. In

contrast, inverter-driven motors require a variable frequency drive (VFD) to control their speed and torque. Although this increases both system cost and complexity, it enables high efficiency over a broad range of operating conditions, making such systems well-suited to variable-speed applications.

Among line-start EMs, RFIMs have long been standard due to their robustness, cost-effectiveness and maintenance costs, making them ideal for extreme industrial environments and heavy-duty applications. However, growing demands for higher efficiency with more compact designs have prompted increased interest in alternative motor technologies.

One such alternative is the radial-flux line-start permanent magnet synchronous motor (RF-LSPM) [10, 11], which incorporates embedded permanent magnets to enhance efficiency, power factor, and torque density. The presence of magnets enables synchronous-speed operation and reduced energy consumption, particularly under variable load conditions. Despite these advantages, RF-LSPMs are associated with higher production costs and a risk of demagnetisation under extreme operating conditions [12-17].

Another promising alternative is the AFIM, which offers structural advantages such as improved magnetic material utilisation, more compact design, and superior thermal characteristics [14, 18-23]. These features offer the potential for higher torque density and reduced volume, particularly in applications where axial space is constrained. Despite these benefits, the adoption of AFIMs in line-start applications has lagged behind that of axial-flux permanent magnet motors (AFPMs), which have gained traction in variable-speed systems such as the YASA motor used in Mercedes-Benz EV [24]. The slower uptake of AFIMs can be attributed to the entrenched dominance of RFIMs and the challenges of manufacturing axial-flux topologies. However, recent advancements in fabrication techniques and materials are steadily lowering these barriers. Continued research and development may position AFIMs as viable alternatives to RFIMs in line-start applications where compactness, efficiency, and improved performance are of critical importance.

1.2 Research Problems and Motivations

Although AFIMs potentially offer electromagnetic and structural advantages, they have not been comprehensively investigated in prior research [7, 25]. Existing research has primarily focused on the modelling and design of AFPMs for variable-speed electric vehicle (EV) applications, with far fewer works dedicated to line-start AFIMs [19, 22, 26-29]. As discussed earlier, balancing cost and efficiency is important to the design of line-start motors.

Accordingly, one key research focus is to assess this trade-off in AFIMs in comparison with their RFIM counterparts. Achieving this requires a detailed examination of the AFIM design methodology, including its electromagnetic performance characteristics, to assess its viability as practical alternative for line-start applications.

EM design typically employs either analytical methods, such as magnetic and sizing equations, or numerical methods based on Maxwell's equations, such as the finite-element method (FEM). Each approach presents a trade-off between intuitive understanding and accuracy of analysis. While numerous well-established design techniques exist for RFIMs [30-33], the design methods for AFIMs have been discussed in comparatively fewer studies [19, 31-38].

Analytical sizing methods are known for their fast computational speed but rely heavily on empirical factors and assumptions such as linear magnetic materials, uniform airgap flux density, and the neglect of end effects. Consequently, their accuracy is lower than numerical methods. For non-conventional motor topologies, analytical approaches often lack generality and must be tailored on a case-by-case basis. This limitation is particularly evident in AFIMs, where one of the key design challenges lies in the lamination geometry. The stator and rotor lamination layers are characterised by a radial variation in cross-sectional geometry, such as tooth width, which leads to a non-uniform magnetic field distribution across the radius [5] (Figure 1-2(a)). In contrast, RFIMs maintain an identical cross-sectional geometry across all lamination layers along the stacking direction, resulting in a more uniform magnetic field distribution (Figure 1-2(b)).

(a)   (b)
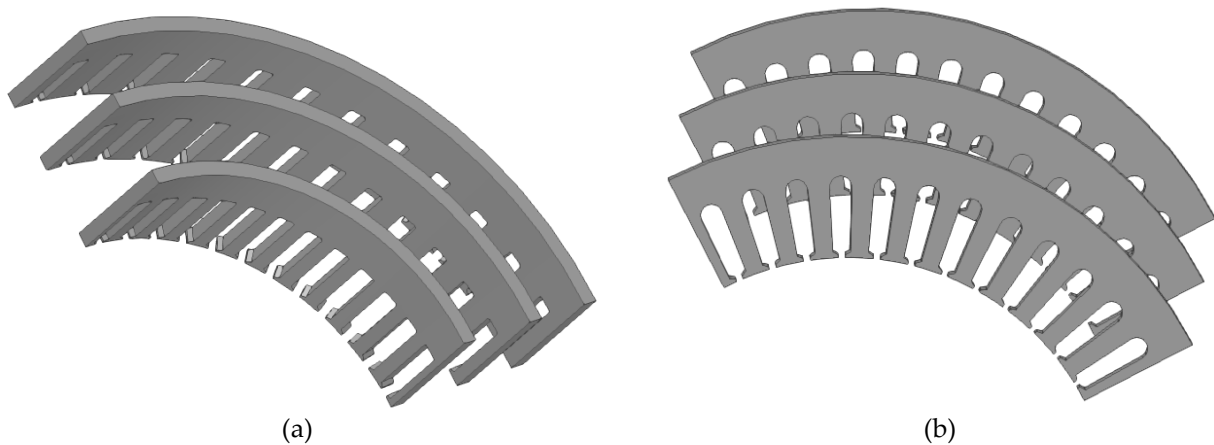
Figure 1-2 Axial-flux (a) and radial-flux (b) induction motors showing the stator lamination layers. The RFIM shows the same stator lamination cross-section at different stack length positions, however, the AFIM shows different lamination cross-section at different stack length positions.

To improve the generality and accuracy of AFIM sizing methods, it is essential to account for the radial variation in magnetic loading, such as the flux density in the tooth regions. Such an approach can reduce dependence on empirical factors and enhance prediction accuracy. The sizing approach proposed in [35] is employed average diameter magnetic and electric loading to establish an equivalent 2-D model for AFIM design, however this simplified method overlooks the inherent radial variation of these loadings. As highlighted in [39], such simplification can lead to significant inaccuracies in radially laminated AFIMs, as the magnetic field distribution across different radial layers is neglected. In particular, magnetic saturation in the rotor and stator teeth near the inner diameter cannot be reliably captured without 3-D FEM. However, the numerical methods for AFIM become even more time-consuming compared to the RFIM due to the increased 3D geometric complexity and the variation of magnetic fields with diameter. Therefore, it is necessary to explore a design procedure tailored to AFIMs that accounts for the variations in electric and magnetic loading, while achieving a balance between computational efficiency and accuracy.

EMs have a large attractive force between the rotor and stator which is proportional to the square of the airgap flux density (B_δ). In RFMs, under normal balanced operation, this produces a net zero force on the rotor due to structural symmetry (Figure 1-3(a)). However, in a single-sided AFIM, the parallel placement of the rotor and stator results in a large unbalanced force (Figure 1-3(b)). This force presents a particular challenge from both mechanical and electromagnetic perspectives, affecting structural design and the accuracy of performance estimation. Structurally, it requires reinforced mechanical components, such as shafts, bearings, and housings, capable of withstanding high axial loads.

(a)   (b)
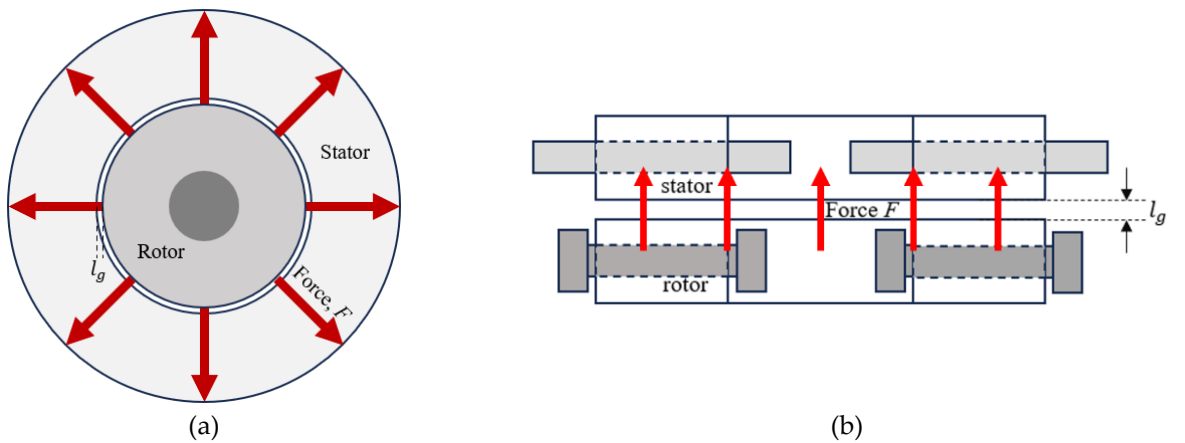
Figure 1-3 Attractive force distribution between the rotor and stator (a) RFIM (top view) and (b) AFIM (side view).

AFIMs typically feature a smaller airgap than AFPMs, which increases the risk of stator and rotor contact and makes accurate axial force prediction more critical. Despite its

importance, axial force has not been a major focus in previous research. While many studies have mentioned it as a challenge in AFPMs [40-44], methods for experimentally measuring or simulating axial force remain largely unexamined.

From the perspective of electromagnetic performance estimation, axial force contributes to increased mechanical friction losses, which can compromise the accuracy of efficiency estimation [45]. Although this thesis focuses on a 415V line-start AFIM and evaluates mechanical loss at a single voltage point to assess loading performance, no-load behaviour under varying supply voltages remains an important consideration, particularly for newly developed AFIMs. In such cases understanding the influence of voltage variation on axial force is essential for accurately predicting mechanical losses and achieving a more precise breakdown of total motor losses.

In addition, mitigating axial force is also a critical consideration in AFIM design. One potential approach is the adoption of double-sided AFIM configurations [22, 25, 46]. However, comparative studies among different double-sided AFIM topologies have not been conducted. As the effectiveness of axial force mitigation strongly depends on the rotor and stator arrangement, exploring the influence of various double-sided configurations on axial force cancellation is therefore essential.

Few studies have presented the mechanical design and construction aspects of AFM, particularly in relation to prototyping practices [47-49]. Existing works often omit essential considerations such as the references for bearing selection, shaft configuration design, and housing integration, leaving a gap in practical design guidelines for constructing structurally robust and adjustable AFM assemblies. The gap in design guidelines is especially critical for single-sided AFM, where the parallel rotor-stator arrangement permits an adjustable airgap. Such a feature enables performance tuning to meet specific torque and speed requirements but simultaneously introduces large axial forces that must be mechanically sustained. To address this, a dedicated mechanical design is proposed that supports adjustable airgap lengths while maintaining structural stability under axial loading conditions.

Experimental investigations on AFIMs have primarily aimed to validate the proposed design, FE simulation results, and analytical performance predictions [47-49]. The procedures commonly follow those established for RFIMs, including rotating and locked-rotor tests conducted at fixed airgap lengths. These tests necessitate a fully assembled motor.

In the no-load equivalent circuit of an induction motor, the rotor is electrically open circuit and functions to complete the magnetic flux path. This characteristic makes a

stationary no-load test theoretically feasible for RFIMs by using an unslotted rotor. However, implementing such a test still requires a supporting frame, shaft, and bearing to hold the motor components. In addition, varying the airgap length becomes impractical without having multiple rotors of different diameters.

The structural configuration of AFIMs, combined with the theoretical basis of the no-load test, motivates the development of a stationary no-load test procedure tailored specially for AFMs. Such an approach has not been previously reported in the literature, and its accuracy remains to be validated.

1.3   Research Objectives

1.3.1   Design of Axial-Flux Induction Motor

To develop a systematic electromagnetic design process for AFIMs based on electromagnetic loading principles, addressing limitations of existing methods that are largely derived from radial-flux machine designs and often overlook radial variations in loading specific to AFIMs. This includes selection of electric and magnetic loading parameters tailored to AFIMs, and the development of trade-off plots to visualise the impact of key parameters, such as slot geometry, pole number, flux density, material usage, torque, efficiency, and cost.

1.3.2   Comparative Study with RFIM

To perform a comprehensive comparison between the designed AFIM and its RFIM counterpart. This includes the evaluation of slot shape sensitivity, pole number impact, steady-state and dynamic performance differences, and cost-effectiveness. The comparison also includes experimental benchmarking using a prototyped machine.

1.3.3   Analyse and Mitigate Axial Forces in AFIMs

To investigate axial force behaviour in single-sided AFIMs through 3D finite-element analysis and experimental validation. Various double-sided configurations are proposed and assessed for their effectiveness in mitigating axial forces and achieving mechanical symmetry under practical operating conditions.

1.3.4   Prototype an AFIM

To construct a single-sided AFIM prototype based on the proposed electromagnetic design. The mechanical structure is designed to accommodate adjustable airgap control and withstand the high expected axial loads, while ensuring structural integrity and alignment.

1.3.5 Stationary No-Load Testing and Performance Evaluation

To propose a stationary no-load testing method for AFIMs using an unassembled rotor and stator. This includes validation of the method through FE simulations and experimental testing, allowing preliminary electromagnetic performance evaluation without requiring full motor assembly.

1.3.6 Exploring the Mechanisms of Mechanical Loss In AFIM

To analyse mechanical losses in AFIMs under no-load conditions using conventional rotating tests, investigating their dependence on airgap length and supply voltage. The loss data are incorporated into finite-element and equivalent circuit models to improve efficiency prediction.

1.4 Research Gaps

Although AFIM have shown promise as an alternative to conventional RFIM, several critical research gaps remain:

❖ **Electromagnetic Design:** Existing sizing and modelling methods are largely adapted from RFIMs and do not address the radial variations in electric and magnetic loading inherent to AFIMs.

❖ **Comparative Performance:** Comprehensive studies comparing AFIMs with equivalent RFIMs under line-start conditions are limited.

❖ **Axial Forces:** While axial force is recognised as a key challenge in AFIMs, systematic experimental and numerical investigations remain as gap.

❖ **Topology Trade-offs:** Double-sided AFIMs potentially offer improved torque and power density, but comparative studies of different topologies and their associated mechanical imbalances are lacking.

❖ **Manufacturing and Mechanical Design:** The manufacturing aspects of AFIMs are not well documented, and detailed discussion on mechanical design are limited.

❖ **Testing Methods:** Conventional motor tests require full mechanical assembly, but alternative low-cost methods, such as stationary testing, have not been explored for AFIMs.

1.5   Original Contributions

This thesis advances the field of AFIMs by addressing critical gaps in the design, analysis, and experimental testing. The work provides both theoretical and practical innovations, validated through simulations, experiments, and prototype development, the key contributions are categorised as follows.

1.5.1   Major Contributions to the Field

1.5.1.1 Development of electromagnetic design guidelines for AFIM

This work establishes a comprehensive methodology for converting conventional RFIM designs to optimised AFIM configurations. The proposed framework accounts for radius-dependent variations in magnetic flux density and current distribution, enabling precise geometric scaling while maintaining efficiency. Multi-objective Pareto frontiers are introduced to visualise trade-offs between efficiency, material cost, and power density, providing designers with a systematic tool to select optimal geometries for target applications. Case studies demonstrate that this method can effectively assist designers in selecting AFIM geometric configurations based on prioritised performance metrices.

1.5.1.2 Characterisation of axial force in single-sided AFIMs

The research presents an integrated experimental-computational approach to quantify and mitigate axial forces in AFIM. High-precision axial force measurement is performed using the civil engineering material testing equipment. The FE simulation method is also proposed and validated using experimental results. The validated model accurately predicts the axial force of the newly designed AFIM, around 5kN at nominal airgap, providing a reliable basis for bearing selection and mechanical structural design.

1.5.1.3 Advancing AFIM testing: introduction of a stationary no-load test method

The thesis introduces a novel stationary no-load test protocol for AFIM, allowing early assessment of electromagnetic performance without a full motor assembly. By validating it against conventional rotating no-load tests, the accuracy of the proposed method is

confirmed through both FE simulations and experimental measurements. This approach significantly reduces experimental complexity and cost, while enabling the electromagnetic losses and magnetising inductance evaluation under various airgap lengths. Furthermore, the method facilitates early equivalent circuit parameter extraction, supporting fast electromagnetic performance prediction before mechanical integration is finalised.

1.5.1.4 Unveiling mechanical loss mechanism in AFIM

Through a combination of theoretical analysis and experimental validation, this work investigates the influence of supply voltage and airgap variation on mechanical losses in AFIM. A mechanical loss separation method is developed that offers a more direct and assumption-free approach to mechanical loss quantification, thereby improving the accuracy of electromagnetic prediction under varying airgap lengths and supply voltage conditions.

1.5.2   Minor Contributions to the Field

1.5.2.1 Comparative study between AFIM and RFIM

A detailed comparison between AFIM and RFIM designs is conducted, highlighting the torque sensitivity of AFIMs to slot geometry and pole number. An optimal slot number ratio is identified to enhance starting and loading performance. Cost-efficiency trade-offs across pole variants are analysed to identify suitable RFIM-to-AFIM conversion cases.

1.5.2.2 Exploration of double-sided AFIM configurations

Several double-sided AFIM topologies are proposed and analysed, demonstrating improved axial force symmetry and higher power density. The study provides solutions for overcoming the limitations of single-sided AFIMs in high-power applications, where mechanical balancing is critical.

1.6   Scope of the Thesis

This thesis focuses on the design, modelling, and experimental investigation of axial-flux induction motors (AFIMs) for low-power, line-start applications. The study is limited to three-phase, squirrel-cage AFIMs operating at 415 V, 50 Hz, with rated powers of 2.2 kW and 4 kW. Both single-sided and double-sided motor topologies are considered.

The work concentrates on electromagnetic design, mechanical structure development, and experimental validation. The design methodology leverages analytical sizing and finite-element modelling, under electric and magnetic loading constraints. Geometric scaling and parametric studies are performed with reference to conventional radial-flux induction motors (RFIMs). Design inputs such as pole number, slot shape, and material usage are examined within this scope.

This thesis also encompasses mechanical aspects related to airgap adjustability and axial force considerations. Experimental activities are restricted to no-load, locked-rotor, and load tests under rated sinusoidal supply conditions. The thesis does not include thermal modelling, inverter-fed operation, high-speed dynamics, or advanced control strategies. The findings are primarily applicable to industrial line-start motors operating near rated load, where cost, robustness, and efficiency are critical

1.7   Thesis Outline

This thesis is divided into eight chapters as follows:

CHAPTER 1 introduces the background, research problems, objectives, contributions, and scope.

CHAPTER 2 reviews the literature on AFIMs, highlighting design challenges, axial force issues, and testing limitations.

CHAPTER 3 presents the theoretical foundation for AFIM design and FEA validation.

CHAPTER 4 outlines the AFIM design methodology and compares its performance with RFIMs under equivalent conditions.

CHAPTER 5 investigates axial force through simulation and experiment, including mitigation using double-sided configurations.

CHAPTER 6 details the construction of a 2.2 kW AFIM prototype with adjustable airgap.

CHAPTER 7 validates the design through load tests and introduces a stationary no-load testing method. Mechanical loss analysis is also conducted.

CHAPTER 8 summarises the key findings and proposes directions for future work.

CHAPTER 2

LITERATURE REVIEW

2.1   Electric Motor Types

Electric motors operate based on electromagnetic principles, where mechanical torque is produced by the interaction between the magnetic field (φ) and stator current (I). All motors consist of two main components: the stator, a stationary assembly containing windings, and the rotor, the rotating components.

Asynchronous motors, commonly known as induction motors, are classified according to their rotor construction. The squirrel-cage rotor, used in the majority of motors, consists of short-circuited conducting bars embedded in a laminated magnetic core, offering a simple, rugged, and cost-effective structure suitable for industrial and residential applications. Its advantages include low manufacturing cost and minimal maintenance requirements; however, it provides limited starting torque and does not support external speed control, making it less ideal for variable-speed applications [50]. The wound rotor employs three-phase windings similar to the stator, connected to external resistors through slip rings, allowing control of starting current and torque. This configuration enables adjustable starting performance and limited speed control by varying the external resistance during operation. However, it introduces additional complexity, increases manufacturing costs, and requires regular maintenance due to the presence of the slip rings and brushes. Wound-rotor motors are therefore typically used in applications demanding high starting torque, controlled acceleration, or limited variable-speed capability, such as cranes, elevators, and hoists [51].

Synchronous motors can be categorised based on their rotor construction. The permanent magnet rotor employs magnets that are either embedded within or mounted on the rotor surface, producing a strong magnetic field that contributes to higher efficiency and power density [52]. However, this design is less robust due to the potential risk of magnet demagnetisation under high operating temperatures or strong stator magnetic fields. The wound-field synchronous rotor can adopt either a salient pole or a round rotor

configuration. The salient pole rotor features protruding poles wound with field windings [53], and is typically used in low-speed, high-torque AC generators such as those found in hydroelectric power plants. In contrast, the non-salient pole rotor, is a smooth cylindrical rotor with distributed field windings [54], commonly employed in high-speed applications like steam turbine generators. In addition, the synchronous reluctance rotor operates based on the principle of magnetic reluctance between its direct and quadrature axes [53, 54]. Constructed from high-permeability magnetic materials, the synchronous reluctance rotor offers a simple and robust design, making it suitable for general-purpose such as pumps and fans.

Besides classifying asynchronous and synchronous motors by their different rotor topologies, they can also be categorised based on whether they are line-start or controlled by a variable frequency drive (VFD) [55]. Line-start electric motors are designed to start from and operate directly from the AC mains, they operate at relatively constant speed which is determined by the power supply frequency (50Hz or 60Hz) and their number of poles. Single-phase and three-phase induction motors (IMs) are commonly used for line-start applications, such as pumps and fans. In the industrial sector, IMs occupies around 80% market share due to their reliability, durability, low maintenance, cost-effective and longevity [4]. In seeking to improve the efficiency of line-start induction machines, techniques like improving the quality of laminations and using a copper rather aluminium rotor windings have been applied. In addition, line-start versions of permanent magnet synchronous machines are also commercially available.

Synchronous machines include permanent magnet synchronous motors (PMSM), brushless DC motors (BLDC) and synchronous reluctance motors (SynRM). Among these, PMSMs are the most favoured motors due to their higher efficiency, better power factor and precise speed control capability. Compared with IMs, PMSMs are more expensive due to the need for rare-earth permanent magnet materials and an inverter. Conversely, the key disadvantage of IMs is their lower efficiency which leads to higher electricity costs over long-time operation. On the other hand, the material cost of IMs is a subject to the wide fluctuations caused by policies and market disruptions, unlike the rare-earth materials used in PMSMs.

2.2   Market Share and Costs

According to the market share statistics, PMSMs accounted for around USD 45 billion of sales in 2022, rising to USD 48 billion in 2023 [4, 56]. In comparison, IMs represented

approximately USD 18 billion in 2022, increasing to around USD 20 billion in 2023 [4, 56]. With the rapid development of electric vehicles (EVs), the market share of PMSMs is expanding at an accelerated rate and is expected to continue growing. It is noted that IMs exhibit a higher growth rate, at 9.4% compared to 5.9% for PMSMs [56]. In industrial sectors, IMs retain a dominant position with approximately 80% of the market share, whereas PMSMs are predominantly deployed in EV and other variable-speed applications. A comparative study between a PMSM and an IM of 2.2kW power rating is summarised in Table 2-1. It is shown that, although the PMSM offers significantly higher efficiency, the requirement for rare-earth materials results in an approximately 68% increase in cost [57].

Table 2-1 Comparison of 2.2kW PMSM and IM electromagnetic performance and material cost [57].

	Torque Density *Nm/kg*	Efficiency %	Electromagnetic Material Cost $
IM	8.20	83.1	143
PMSM	9.70	91.3	242

Figure 2-1 Historical price trends of neodymium from 2010 to 2022 [58, 59].

PMSMs, particularly those employing neodymium-based rare-earth magnets, are heavily reliant on materials subject to large price volatility. As shown in Figure 2-1, the price of neodymium increased by over 300% between mid of 2020 and early 2022. Concerns about the availability of these rare-earth materials caused significant, though short-term, increases in the prices, with neodymium and dysprosium prices both escalating by about an order of magnitude. Subsequently, while the rare-earth prices showed a recent downward trend, they have not yet returned to their previous low level. It is generally recognised that motors with no rare-earth materials will lead to a significant reduction of material cost. However,

the trade-off between the material cost and motor efficiency should be carefully considered, otherwise, the increased costs due to sacrificing efficiency may offset or even exceed any cost savings from removing rare-earth materials [58].

2.3　Electric Motor Efficiency Standards
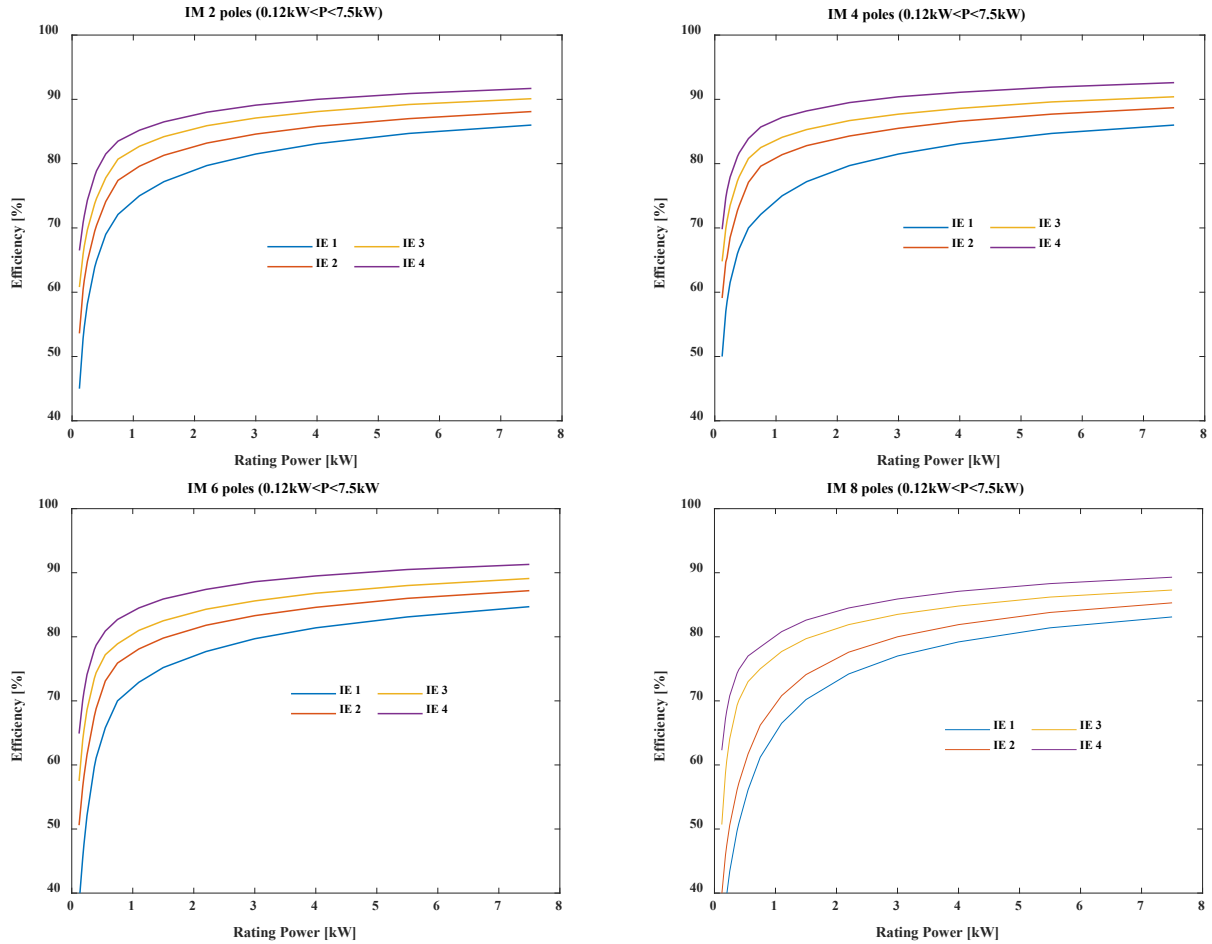
Figure 2-2 Efficiency levels defined by IEC60034-30 for 2, 4, 6, 8 poles, 50Hz induction motors [60-62].

The electric motor efficiency standards are limited to motors for single-speed applications. The US National Electrical Manufacturers Association (NEMA) standards [62] classify the motor efficiencies into four categories named standard efficiency, high efficiency, premium efficiency, and super premium efficiency for 50 and 60 Hz three-phase and single-phase motors [60-62]. Similarly, the International Electrotechnical Commission (IEC) offers another system for classifying single speed motor efficiency, known as IE1, IE2, IE3, and IE4 [62]. In 2014, the IEC 60034-2-1:2014 standard for electrical machines was published. This standard specifies methods for determining the losses and efficiency of all types of rotating electrical machines under specific testing conditions. Due to the

importance of energy efficiency in electric motors and the substantial potential economic and environment impacts, many countries are working on developing mandatory minimum energy performance standards to be implemented in the near future [63].

As indicated above the IEC 60034-30-1 standard classifies four minimum efficiency requirements (IE1-4) for 50Hz induction motors as shown in Figure 2-2 for 2, 4, 6 and 8 pole 50Hz induction machines in the output power range 0.12 to 7.5kW. The efficiency requirement increases from IE1 to IE 4 and also increases with increasing power rating and decreasing number of poles. In 2017, Europe decided that IE3 must be applied for line-start motors with rated power from 0.75kW up to 375kW. Similar regulations were earlier introduced in China and USA in 2016 and 2010, respectively. In summary, these policies and published efficiency standards are the driving force for extensive research and development of high efficiency electric motors. The design and materials for the motor can be considered as two important factors for enhancing the performance of electric motors [63].

As discussed in Chapter 1, the primary motivation behind the design of AFIMs is to improve power density while also maintaining high efficiency. Improvements in power density are expected to come from advancements in electromagnetic design methodologies, the adoption of innovative winding schemes, and the use of advanced materials with higher saturation limits and improved thermal capabilities. In addition, novel topologies such as axial-flux configurations inherently provide opportunities for higher torque per unit volume. A dedicated discussion on these trends provides a broader perspective, linking the motivation of this thesis to the evolving research landscape [63].

2.4 Introduction of Axial-Flux Induction Motor Topologies

2.4.1 Structure of Axial-Flux Induction Motor

Axial-flux (AF) electric motors operate based on the same electromagnetic principles to radial-flux (RF) electric motors but differ in their stator and rotor arrangements. The degree of freedom in designing the AF topologies are usually larger compared to the conventional RF electric motors. The AFIM features a variety of configurations, allowing it to be suitable for a wide range of applications with specific requirements, such as installation space, power density, etc. The topologies are typically categorised into two main configurations: North-North (NN) and North-South (NS) pole arrangements.

2.4.1.1 Single stator and single rotor (SSSR-AFIM)

The single-stator and single-rotor AFIM (SSSR-AFIM) represents the simplest topology (Figure 2-3). It is the favoured choice for low power applications [25]. From the magnetic field perspective, the flux flows in the axial and circumferential directions and the flux enters and leaves the stator and rotor at the same side. Due to the inherent characteristics of this structure, the large unbalanced axial force on the rotor is a significant concern [45, 64]. The presence of large unbalanced axial force is a challenge to the axial load-bearing capacity. If the stator and rotor are not accurately aligned, the resulting uneven distribution of axial forces can lead to unexpected vibrations or even rotor and stator contact [65].

(a)   (b)

(c)
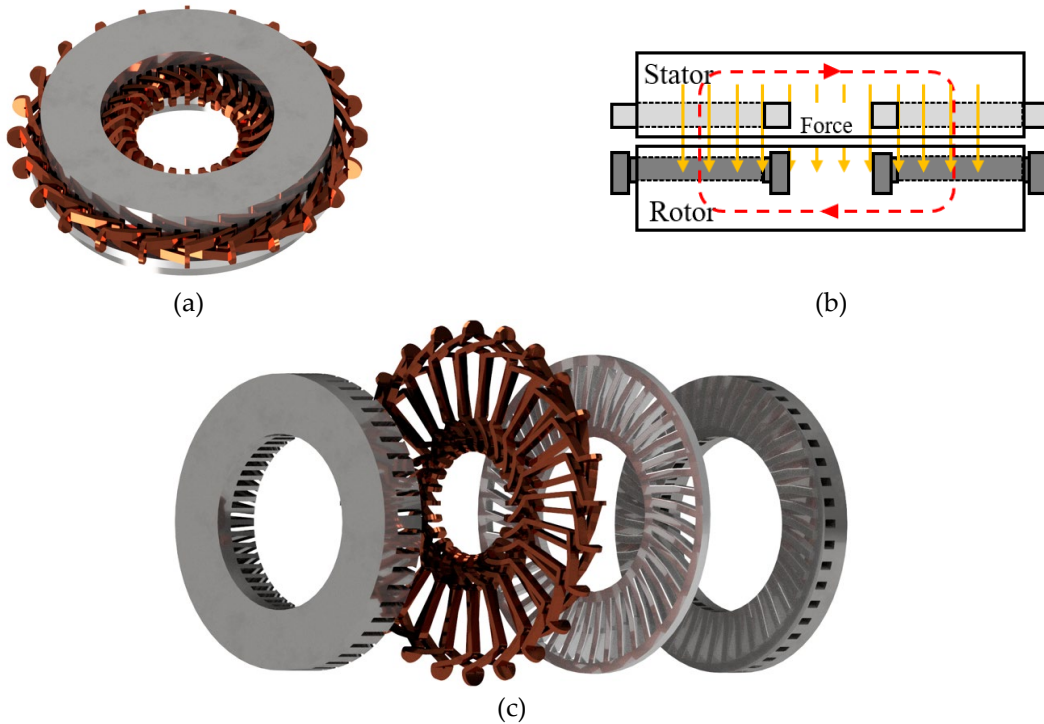
Figure 2-3 (a) single-sided AFIM, (b) flux path in single-sided AFIM, (c) single-sided AFIM components, from left to right: stator, winding, rotor bar, and rotor.

2.4.1.2 Double stator and single rotor (DSSR-AFIM)

(a)   (b)

(c)
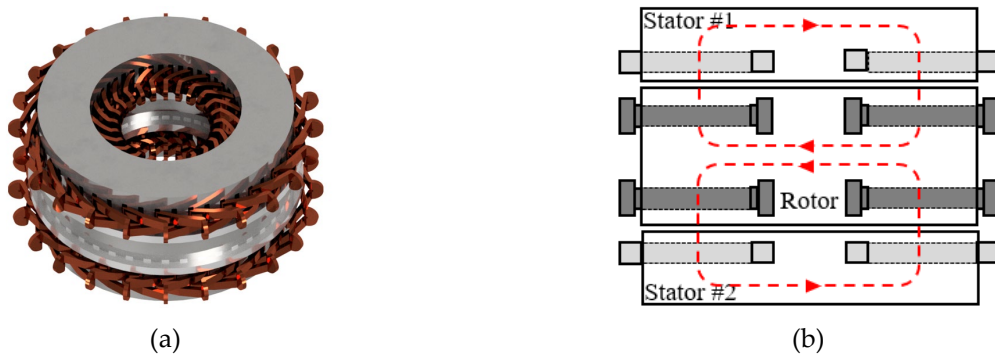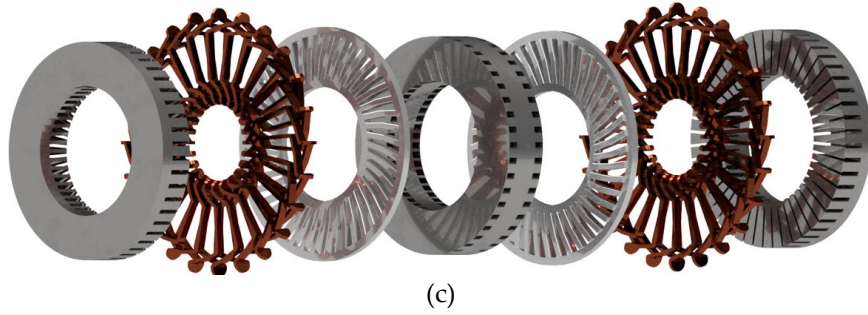
Figure 2-4 North-to-North topology of DSSR-AFIM, (c) from left to right: stator#1, winding#1, rotor bar#1, rotor, rotor bar#2, winding#2, and stator#2.

Given that the single-sided AFIM is formed by a disc-shaped rotor and stator, achieving a higher power rating requires an increase in diameter. However, continually increasing the diameter of a single-sided AFIM to meet higher power requirements presents significant constructional challenges. Additionally, because the moment of inertia is proportional to the square of the diameter, larger diameters result in slower acceleration and increased mechanical stress on the shaft and bearing. Such issues can undermine the structural integrity, performance of the machine and significantly increase cost of manufacturing. Taking advantage of the inherent structural flexibility of AFIM, the double-sided AFIM topology can effectively avoid these challenges, but this comes with a trade-off in terms of increased volume [5, 65].

(a)

(b)

(c)
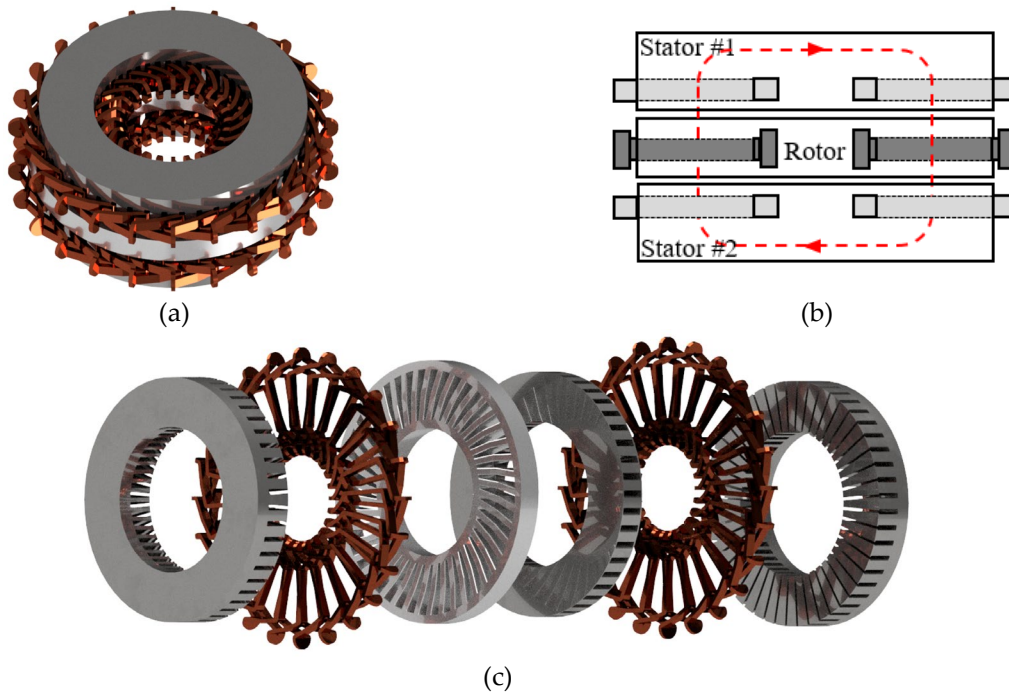
Figure 2-5 North-to-South topology of DSSR-AFIM. (c) from left to right: stator#1, winding#1, rotor bar, rotor, winding#2, and stator#2.

A double-sided axial-flux topology can be realised by positioning a single rotor between two outer stators, as illustrated in Figure 2-4 and Figure 2-5. Depending on the flux path between the stators, two principal categories of motor can be defined: the North-to-North (NN) topology and the North-to-South (NS) topology. Each exhibits distinct electromagnetic and mechanical characteristics which influence both the motor performance and the structural requirements. In the NN topology, two independent magnetic flux loops are established, resulting in both stators exhibiting the same magnetic polarity at a given circumferential position. This configuration is achieved by supplying the stator windings with currents of opposite direction and identical amplitude and frequency. Consequently, a symmetrical magnetic field distribution is produced across both stators [25, 65]. However, the requirement for two independent flux paths necessitates the inclusion of sufficient rotor back-iron to provide an effective magnetic circuit. As a result, the rotor weight cannot be reduced by eliminating the back-iron. In addition, any asymmetry in the two airgaps leads to unequal magnetic field strengths and results in different axial forces acting on the two sides of the rotor. Thus, a high level of assembly precision is essential to ensure balanced operation [5, 25]. An advantage of the NN topology is that a DSSR-AFIM can be constructed by combining two pre-optimised SSSR-AFIM units. This approach removes the need for further electromagnetic optimisation at the DSSR level and simplifies the development process [65].

In the NS topology, direct magnetic flux linkage occurs between the two stators, with opposite magnetic polarities. Both stators are supplied with currents of identical direction, amplitude, and frequency. This allows the elimination of the rotor back-iron and thereby increasing the achievable torque and power densities. The flux densities within the two airgaps are approximately equal, leading to balanced net axial forces on both sides of the rotor. Compared to the NN topology, the NS topology exhibits reduced sensitivity to airgap asymmetry and associated unbalanced forces. However, the reduction in rotor thickness, enabled by the absence of back-iron, must be carefully optimised to maintain mechanical strength while satisfying electromagnetic performance requirements [25].

2.4.1.3 Single stator and double rotor (SSDR-AFIM)
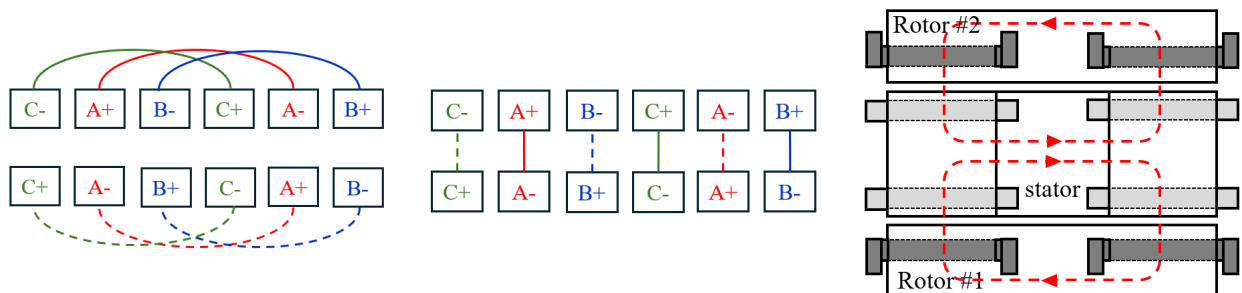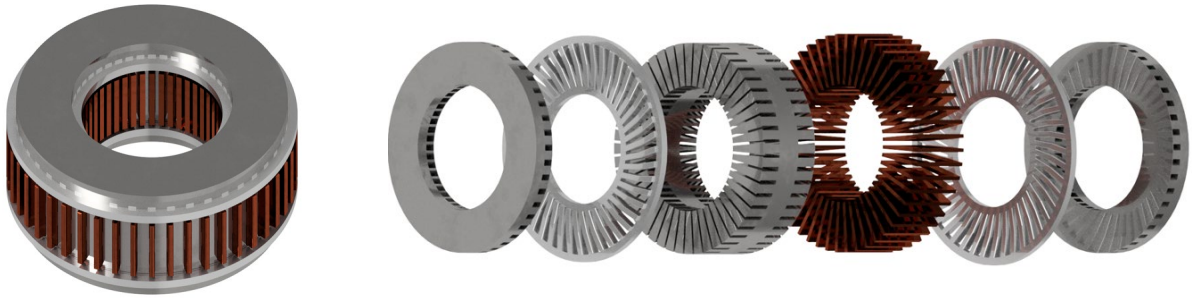
Figure 2-6 North-to-North topology of SSDR-AFIM. From left to right: rotor#1, rotor bar#1, stator, stator winding, rotor bar#2, and rotor#2.

The SSDR-AFIM can similarly be classified into two topologies based on the different magnetic flux loops: (1) the NN topology and (2) the NS topology. The NN topology can be achieved by two different winding configurations, including distributed and toroidal windings. The distributed winding includes two identical sets of distributed windings carrying the same amplitude of current with same frequency but in opposite directions. Alternatively, the single toroidal winding encircles the stator slots of both the top and bottom stators [37]. The toroidal winding for the NN topology is more complex as number of turns and diameter should be optimised to achieve the desired strength of the magnetic field. As there are two individual flux loops thus the stator back-iron thickness cannot be reduced. The NS topology for the DSSR-AFIM has similar features as the NS-SSDR-AFIM, the back-iron can be reduced but the optimisation of number of turns, diameters and the thickness of stator core needs to be done [39]. With regards to axial force, like the SSDR-AFIM, the NN topology is more sensitive to unequal airgaps as there are two independent flux paths, thus the flux will increase if the length of airgap decreases on the one sided and the rotor will be pulled towards that stator.
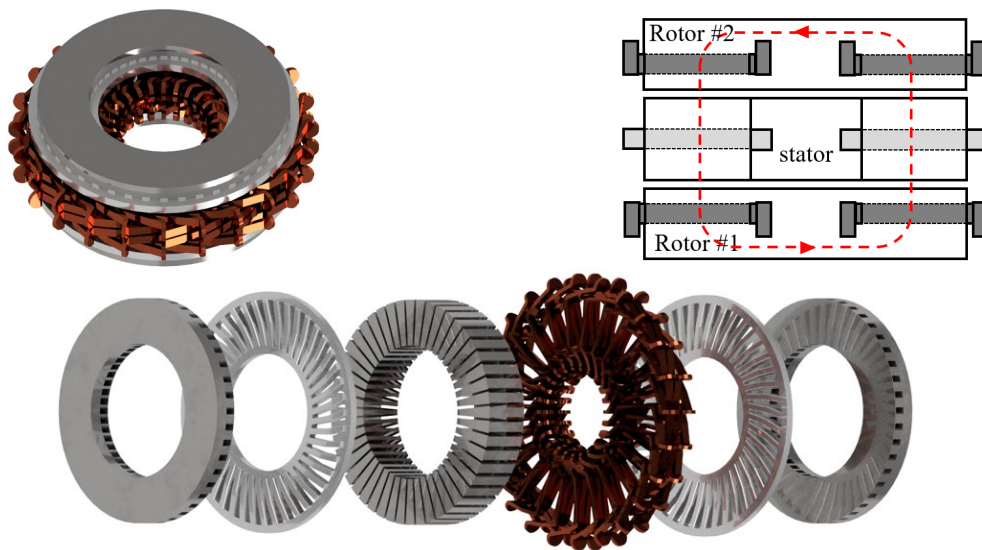
Figure 2-7 North-to-South topology of SSDR-AFIM. from left to right: rotor#1, rotor bar#1, stator, winding, rotor bar#2, and rotor#2.

2.4.1.4 Multi-Stage AFIM
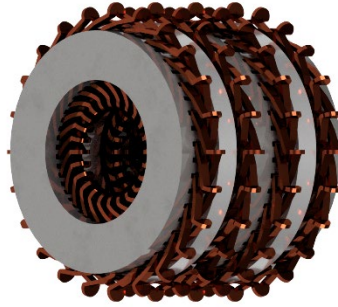
Figure 2-8 A example of a multi-stage AFIM (MSMR-AFIM).

A multi-stage AFIM can be constructed from the above-mentioned configurations with N stator and N+1 rotors or N rotors and N+1 stators. Multi-stage AFIMs allow opportunities to enhance the torque and torque density without increasing the outer diameter. Compared to the RFIM, the AFIM has more options for multi-stage construction due to its disc shape. Similarly, with the previously mentioned topologies, the multi-stage AFIM includes slotted or slotless, NN or NS topologies. The advantages and disadvantages of multi-stage AFIMs are similar to their basic structures [25].

2.5 Applications of Axial-Flux Motors

The special structure and electromagnetic features of axial-flux motors (AFMs) such as their planar and adjustable airgap, higher power density and compact construction make them suitable for various applications. Despite the advantages and potential application of line-start AFIMs, such as pumps, fans, etc, these motors are remain uncommon in both the market and practical use [66]. Compared with AFIMs, AFPM machines are more popular in the market and various applications, such as electric vehicles (EVs) [67], aerospace [68], renewable energy [69], industrial machinery, marine propulsion, etc [54, 55]. The axial-flux permanent magnet (AFPM) motors are gradually being integrated into EV wheels. The current EV can be classified into two types, namely "indirect-drive" and "direct-drive". Gears and a differential system are needed for the first type. The second solution, direct drive, does not need complex transmission systems, hence lowers the mechanical losses. The AFPM machine features including high power density and planar shape, making it suitable to be placed inside the wheel [70]. The AFPM machine can be constructed as double-

sided or single-sided. When assembling the AFPM machine, the high attractive forces leads to difficulties in aligning the stator and rotor and positioning the magnets on the rotor [71].

In the late 1970s, AFIMs experienced a brief development surge, though short term, driven by innovations in motor design for specific applications where the limited installation room was an important factor. In 1978, a design of an AFIM from Brimer was patented as a washing machine agitator. In the AFIM design, a single thin rotor was surrounded by two outer stators [72] In Brimer's AFIM, the entire rotor is constructed by aluminium, a non-ferromagnetic material with lower material strength. It also has the main drawback that the rotor may deform under high torque operation, making it unsuitable for high torque applications. To address this, other rotors for AFIMs were designed with ferromagnetic material and the flux-carrying capacity and strength of rotor were enhanced. In 1976, Senckel's design involved a laminated rotor with ferromagnetic bridges to enhance the strength of rotor and minimise the eddy currents in the rotor iron [72]. However, using ferromagnetic bridges produced another challenge, the large attractive force between rotor and stator under excitation which requires careful mechanical design. To enhance the efficiency of the AFIM, the squirrel-cage RFIM was firstly introduced to AFIM in 1966 by Morinigo [73]. Morinigo's AFIM design features similar components to DSSR-AFIM, including two facing stators with a rotor in the middle. The skewed rotor bars were made of copper with the outer and inner rings and rotor core was made of ferromagnetic material. Compared to the previous AFIM design patented by Senckel and Brimer, this design is more suitable for both motors and generators.

Besides the double-sided AFIMs, a single-sided AFIM was patented in 1997 by Gerling and Lürkens [74]. For the first time, the AFIM was implemented in a vacuum cleaner, where it was directly coupled to an impeller wheel with the same outer diameter [27]. Although the direct coupling of the rotor and impeller eliminated additional mechanical components, thereby reducing system complexity, this design was only implemented in a low-power application and was not extended to higher power ranges. Inspired by this design, further development involved shaping the rotor like a pump impeller and integrating it with a power electronic speed controller. This allows the entire pump axial length to be further reduced, enabling the removal of some conventional mechanical components altogether.

2.6 Design and Analysis of Axial-Flux Induction Motor

This sub-section aims to provide a comprehensive overview of past research on AFIM design and analysis, examining various methodologies, findings, and theoretical approaches that have advanced understanding in this field. The AFIM design can be categorised into two methods, including analytical methods and numerical methods. Analytical methods provide a quick design but tend to be less accurate, making them more suitable for the initial design stage. Finite Element Analysis (FEA) is mostly utilised in numerical methods. Although it offers accurate electromagnetic performance predictions and enables optimisation of factors such as the balance of material cost and efficiency, it requires significant computational resources and time. Therefore, a discussion of past research on the design of AFIMs is essential when proposing and choosing the appropriate method for AFIM design in this thesis.

2.6.1 Analytical Design and Analysis Methods

2.6.1.1 Analytical Sizing and Empirically Based Methods

The preliminary design often begins with sizing equations that relate the motor power to its volume. The research in [75] employs the analytical method for the proposed motor design. The relationship between the general size and the power density was established for further optimisation. By applying these equations, the design theoretical limitations can be easily estimated. For AF machines, the ratio of inner and outer diameter ($\lambda = D_{in}/D_{out}$) has a strong effect on the power density and less effect on the motor efficiency. The paper did not offer an exact optimal ratio for the AFIM design as the ratio is variable depending on multiple factors, such as the electrical loading, flux density and motor topology. While the paper successfully establishes the relationship between power density and the diameter ratio in axial flux machines, a critical factor seems to be ignored which is the difference in the rotor/stator lamination orientation between radial and axial motors. This is important because the electric and magnetic loading are the function of the motor radius. Failure to establish the theoretical limitations of electric and magnetic loading can lead to unexpected magnetic saturation and poor heat dissipation [75].

Mahmoudi et al [76] presented a detailed sizing approach for axial-flux permanent magnet motors (AFPM) inspired by Huang et al [75]. The presented design process consists of two steps, determination of the main dimensions of the target motor and optimising the geometry, such as slot width, by a GA iterative process. There are a number of empirical factors applied when confirming the main dimensions.

Boglietti et al [34] proposed a preliminary RFIM electromagnetic sizing based on a geometrical approach. Compared to the conventional design procedure, the electromagnetic equations are applied to the proposed method. An iterative process was

used specifically for the rotor geometry to achieve the desired torque value. However, the authors noted that several flux density parameters must be assumed and substituted into the equations to determine motor dimensions and meet the required specifications, a process that may introduce uncertainty. To address this concern, the authors argued that key design parameters, such as the maximum flux density and current density, can be reliably obtained from standard induction motor handbooks [34, 77].

Recognising the shared principles between AFIMs and RFIMs, Bitsi et al [35] proposed a preliminary electromagnetic sizing approach for a SSDR-AFIM which was inspired by Boglietti [34]. The proposed design procedure can be divided into two parts: (1) the electromagnetic sizing approach, including the height of back iron, and the height, and width of the teeth for both the rotor and stator; (2) an iterative process is applied to confirm the final dimensions with constraints of peak fundamental linear current density and rotor and stator tooth width, etc. The accuracy of the proposed design process was checked by observing the flux overlays in FEA. The study concluded that the proposed methodology can be readily adapted for single-sided AFIM designs as well.

2.6.1.2 Analytical Evaluation of AFIM Performance

More advanced analytical models divide the motor into magnetic subdomains to solve for flux distributions. Dianati et al. [38] introduced a five-region model using Fourier series and ampere's law to capture saturation effects, deriving inductance and rotor resistance via magnetic energy and rotor loss estimation.

Kahourzade et al. [19] presented a similar analytical model approach with greater optimization discussions and considerations. A 3kW single side AFIM was chosen as a study example, and five design variables from geometrical perspectives are considered, including number of turns per slot, outer diameter, ratio of inner to outer diameters, ratio of slot in slot pitch, stator tooth to yoke ratio and stator slot width to height. The objective functions are also given based on the design variables, maximum efficiency, product of maximum efficiency and power factor, minimum volume or mass, etc. The proposed subdomain technique for optimization design process provided an accuracy around 95% with a short simulation time of around 0.34s which is equal to 1/8 of one FEA step. The proposed approach is also suitable for application-based designs, such as traction, wind turbines and the application with multiple operating conditions. However, the geometrical approach was ignored such as the selection of the shapes of the rotor or stator slots, and especially for the starting capabilities, the rotor slot selection plays an important role.

Tapia et al. [78] also presented a similar analytical approach for AFIM which aims to be an alternative to FEA. Compared with the previous analytical model, a double-sided AFIM was considered and analysed through the solution of field equations. Similar to Dianati's model, the motor was also divided into subdomains, but the tooth-slot subdomain at this time was manipulated for simplification in the model via considering and equivalent homogeneous medium. The analytical results were validated against FEA and demonstrated excellent agreement, confirming the model's applicability for high-level performance prediction.

Dianati et al. [38] proposed an analytical model for designing and predicting the electromagnetic performance of AFIMs. The main difference compared to previous research is that the method for obtaining equivalent circuit parameters is based on five subdomains and boundaries conditions were defined from magnetic flux density and ampere's law. Fourier series analysis was applied to solve and define the vector potential equations in the subdomains. With the use of Ampere's law and no-load operation comparisons between saturated ampere-turns of the motor and unsaturated ones, the model importantly allows analysis of saturation effects in the AFIM. the AFIM's inductance and the rotor resistance (R_r) were obtained via calculating the magnetic energy and the rotor bar losses to complete the equivalent circuit. Validation was conducted by FEA and the observed errors are acceptable and hence proposed model delivers reasonable accuracy. Besides the electromagnetic performance prediction, an optimization algorithm was also proposed based on the analytical model. The optimized design can be delivered by applying constraints, such as thermal limits, efficiency targets and mechanical requirements.

2.6.1.3 Design Trade-Offs Analysis and Practical Constraints

An analytical design of a IE3 Efficiency class single-sided AFIM was proposed by Arabul et al. [26]. This paper discusses the design parameters of the single-sided AFIM. The rotating magnetic field was firstly solved by the integration of the assumed basic flux with respect to the radius (r) and pole form factor (α). For the geometrical approach, some simplifications and assumptions were firstly made, such as a constant airgap. By applying the same flux equations of the RFIM to the AFIM and ensuring that the magnetic properties are equal to the reference RFIM, hence the core volume of the single-sided AFIM estimated. However, the design process needs further estimations of the number of winding turns, shape of slots, size of slots and number of slots. In a further optimisation process, the paper focused on managing torque ripple and shows that skewing is an effective way to reduce the torque ripple but often reduces the efficiency. It concluded that the rotor bar skewing angle optimisation should consider not only stator slot number but also the number of the rotor

slots. Although the paper discusses the torque ripple effects on efficiency, it does not explore the potential trade-offs between the efficiency and rotor bar skewing angle, such as the winding configurations.

Mei et al [22] presented an analytical design for a six poles double-stator double-rotor (DSDR) AFIM intended for electric vehicles. The design focuses on reducing the back-iron in the motor, which leads to multiple potential advantages compared to the other topologies, including the reduction of axial forces, higher power density, and a more compact motor design. A double-sided motor equivalent electric circuit was proposed to predict the electromagnetic performance. The study also applied the Monte-Carlo random search algorithm to optimise the motor weight and efficiency by adjusting multiple variables, including rotor and stator slot dimensions, motor length, airgap length, and magnetic flux density limits. Although the proposed design method is fast and accurate, the choices of shape of rotor/stator slots, number of rotor/stator slots and winding configuration are critical to the AFIM design and were neglected by the proposed design method. With reduced back-iron rotor, a significant portion of the shaft load is then transferred to the aluminium bars, which have lower strength compared to electrical steel. This may lead to unexpected deformation or rotational failure. The proposed research is also constrained by focusing on only torque capability. For an EV motor, an efficiency map is essential to ensure effective operation across different speeds and loads [22].

Baranov et al. [79] developed a mathematical model of an AFIM with one stator and one rotor, focusing on maximising torque density. The model is based on the expression for electromagnetic torque as a function of the axial length and flux density in the airgap. This approach allows for estimating the main dimensions of the motor to achieve the higher torque. The model was then validated, demonstrating its effectiveness in designing AFIM with the specified volume and torque. However, proposed mathematical model risks overdesign, as power output also depends on the outer and inner diameters, which directly affect the motor active volume. Moreover, the validation lacks comprehensive comparison in terms of power-to-weight ratio, making it difficult to assess the practical compactness.

Boglietti et al [34] proposed a preliminary RFIM electromagnetic sizing based on a geometrical approach. Compared to the conventional design procedure, the electromagnetic equations are applied to the proposed method. An iterative process was used specifically for the rotor geometry to achieve the desired torque value. However, the authors noted that several flux density parameters must be assumed and substituted into the equations to determine motor dimensions and meet the required specifications, a process that may introduce uncertainty. To address this concern, the authors argued that

key design parameters, such as the maximum flux density and current density, can be reliably obtained from standard induction motor handbooks [34, 77].

2.6.2 Numerical Design and Analysis Methods

2.6.2.1 Role of 3-D FEA in AFIM Design

Due to the axial geometry, AFIMs require 3-D simulation to accurately capture electromagnetic behaviour. Unlike RFIMs with the uniform 2-D cross-sections, AFIM geometry varies with the radius. Thus, 2-D FEA may lead to misleading results. High-performance computing has made 3-D simulation more accessible, yet the time and resource demand remains a limitation [36, 78, 80].

2.6.2.2 Parametric Studies Using FEA

Nobahari et al. [81] proposed a study on the impact of skewing where a SSDR-AFIM was picked as an example due to its feature for eliminating the net attractive force between the rotor and stator with capabilities on achieving higher power density. The target for reducing the torque ripple was achieved, but as trade-off, the average output mechanical torque decreased and iron losses rapidly increased due to the saturation level of the iron. The authors introduced a new idea where the 1st rotor is not aligned with 2nd rotor and have rotational displacement without any skewing. The FEA results show the torque ripple is effectively reduced with avoidance of drawbacks from skewing. The loss characteristics show a similar level as the initial design. However, the authors ignored the starting performance of the motor which is one of the most important factors for line-start induction motors [81].

A sensitivity study on the number of rotor slots provided insights on the relationships between design parameters and electromagnetic performance, such as starting torque, torque ripple, rotor losses, and power factor [82]. The proposed study in [82] aims to analyse the effects of number of rotor slots on the electromagnetic performance, specifically focusing on torque, rotor losses, efficiency, and torque ripple. A 50kW, 6000rpm, four poles AFIM with a varying number of rotor slots, from 24 to 32, was investigated in this study. The results indicated that maximum torque was delivered with 24 or 25 rotor slots, while an odd number of rotor slots was associated with the significant increase in the torque ripple. With the increase in the number of rotor slots, the rotor losses are nearly inversely proportional to the number of rotor slots. The study only examines the rotor slot number within a specific range, which might limit the generalizability of the results as the combination of stator and rotor slot numbers is more critical.

In [83], the influence of airgap length on the performance of an AFIM was investigated. A 45kW AFIM with solid-rotor-core under different airgap lengths as discussed. It employed 2-D FEA simulations to investigate the effects of different airgap lengths on the rotor losses and efficiency. The paper concluded that increases in the airgap length result in higher copper losses and lower solid rotor core eddy current losses which correspond to the theoretical prediction. However, the study cases in this paper are insufficient to produce AFIM design guidelines for balancing the power factor and efficiency with varying airgap lengths. In addition, using 2D FEM for the AFIM analysis potentially limits the accuracy of the results due to the 3D effects.

2.7 Experimental Testing of Axial-Flux Induction Motors

```
Start → Measure cold resistance → Operate at rated condition for 30mins → Test and measure under load (6pts, 150% to 25%) → No-load test → End
```

1. **The procedure of the test of the electromagnetic performance at certain load and speed for the AFIM based on the IEEE standard.**

```
Start → Measure cold resistance → Operate at rated condition for 30mins → Test and measure under load (6pts, 150% to 25%) measure resistance before & after → No-load test → End
```
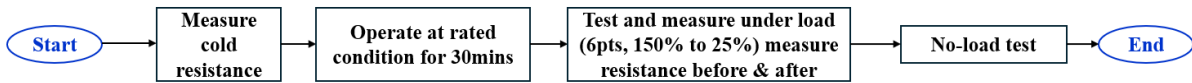
2. **The procedure of the test of the electromagnetic performance at certain load and speed for the AFIM based on the IEC standard.**

Figure 2-9 The experimental methods for the extraction of AFIM 's electromagnetic performance based on IEEE and IEC standards IEC60034 [84].

The experimental measurement of electromagnetic performance for AFIMs is conducted based on the IEEE or IEC standards. These published standards are applicable for single-speed operation at either a single load point or several load points. The flow chart of the measurement process based on published standards is shown in Figure 2-9. The IEEE 12 and IEC 60034-2-1 standards are limited to the performance measurement of the motor itself and unable to evaluate the performance of the inverter driven IM [60, 61]. This is however not an issue for this thesis which focuses on the line-start motors. Hence, the experimental methods outlined in these standards can be directly applied to the target motor.

The efficiency is one of the most important factors for evaluating the motor performance. Although the efficiencies at different loads are obtained by measuring the input and output power, splitting the losses in the motor can be useful, including identifying the conductive,

core, and mechanical losses. This is useful for diagnostics and ensuring compliance with standards [60-62]. In squirrel-cage induction motors, the ohmic losses are generated by the stator windings and rotor bars and end-windings. In order to split the rotor and stator ohmic losses, the standard IEC 60034-2-1 suggests that a locked rotor test be conducted with excitation of the winding at 25-50% of the motor's rated voltage, to prevent the overheating of the windings. The measured power, obtained using a power analyser during the test, consists of the stator winding and rotor winding losses from total power. However, the temperature rise leading to the increase of the stator and rotor resistances should be considered using a stator winding resistance temperature coefficient which is applied to update the resistance for the locked rotor test.

The core losses in an induction motor consists of hysteresis losses and eddy current losses. Hysteresis loss is a significant part of the core losses and depends on the magnetic properties of the core electric steel. The alternating magnetic field generated by the stator AC supply causes the magnetization and demagnetization of the iron core and the non-linear relationship between magnetic field strength (H) and magnetic flux density (B) creates the hysteresis loop [85]. The hysteresis loss is roughly proportional to the magnetic flux squared. The alternating magnetic flux produces eddy-current which flow in closed loops within the conductive core material. The eddy current loss is proportional to the square of the product of magnetic flux density and frequency and hence to square of the applied voltage. The overall core loss in the induction motor is generally dominated by the eddy current loss, resulting in the core loss being roughly proportional to V^2.

To estimate the core losses, the no-load active power of the induction motor is subtracted by the no-load winding loss, the result consists of the summation of the core and mechanical losses. Based on the no-load tests at different voltages, the active power (after subtracting the winding loss) can be plotted versus the square of voltage. The extrapolated intercept point with the y-axis (voltage equal to zero) represents an estimate of the mechanical loss.

2.8   Research Gap Discussion

As discussed, RFIMs are the main electric motor type used for many line-start industrial applications due to their various advantages, such as reliability, low cost, and well-established technology. With the ongoing evolution of electric motor efficiency standards [17], further optimisation of line-start RFIM efficiency and power density becomes increasingly challenging. The AFIM is a promising alternative to RFIMs and has gained growing attention due to its potential improvements in power density and efficiency.

However, the past research on AFIMs has not been as widely studied or as comprehensive as those of RFIMs. The other aspects of the AFIMs which have received limited attention in the literature are listed below:

- Despite the general sizing method, analytical modelling and numerical approaches having shown promising advancements, the design of AFIMs with respect to the constraints of the electric and magnetic loading, has not been extensively explored in current research. This is crucial for AFIM designs where it offers opportunities to optimise the cost/volume of AFIM while still meeting the desired efficiency and loading capability.

- Some of the past research studies, including several extensive studies on AFPMs, has focused primarily on design and manufacturing, with some even advancing to commercial deployment. A comprehensive comparative study between an AFIM and an equivalent RFIM has not been fully studied in the literature.

- Although most of the literature on AFIMs identifies that the axial attractive force as a significant concern, comprehensive studies on axial forces remain as research gap, such as experimental methods and numerical calculation methods. A detailed investigation of axial forces is helpful to guide development of improved manufacturing practices.

- The literature shows that double-sided AFIM designs offer superior torque density, power density, and mechanical balance compared to equivalent single-sided AFIM. In fact, variety of double-sided AFIM topologies offers different advantages and trade-offs and which can sometimes cause increased mechanical imbalances. Hence, a comparative study of different double-sided AFIM topologies is desirable.

- Although AFPMs have been commercialised and extensively studied, the manufacturing aspect of such motors are not fully described in the literature. In fact, the mechanical design and motor manufacturing yet to be fully discussed.

- Most of the experimental matters for electric motors have been studied widely and corresponding standards are available to guide these tests. Such tests can only be conducted after the motor has been assembled. However, given the unique of AFIM structure, the proposed stationary no-load test has never been studied before.

2.9   Chapter Conclusion

In this chapter, the existing literature on AFIM were reviewed, with the focus on AFIMs' structural configurations, applications, and design methods. The AFIM's advantages and disadvantages compared to the RFIM were discussed. The flexibilities and characteristics of

the topologies of AFIM were briefly described. The design and analysis of AFIMs were reviewed and summarised.

The chapter highlights several research gaps in the current AFIM research field, particularly the need for comprehensive comparative studies on electromagnetic performance between RFIMs and AFIMs. Additionally, the analysis of axial force in single-sided AFIMs requires further investigation to a robust mechanical design.

The literature has made significant contributions to the field of the design and analysis of AFIMs, particularly for various applications such as electric vehicles and renewable energy systems. However, there is a noticeable research gap regarding comprehensive design guidelines and geometrical parameter effects on the electromagnetic performance of AIFMs.

Although the potential of AFIMs is undeniable, ongoing research is needed to overcome the existing challenges, highlighted in Section 2.6. The comprehensive literature review presented in this chapter highlighted the possible future research field regarding AFIM design, geometrical parameter sensitivity studies, mechanical design and experimental test procedures.

CHAPTER 3

GEOMETRIC AND ELECTROMAGNETIC PRINCIPLES FOR AFIM DESIGN

This chapter presents the key geometric and electromagnetic considerations associated with the design of axial-flux induction machines (AFIMs). Due to their structural differences from conventional radial-flux induction machines (RFIMs), notably the axial orientation of the laminations (see Figure 1-1 and Figure 1-2), AFIMs exhibit increased sensitivity to parameters such as the inner-to-outer diameter ratio λ and the radial flux path distribution. Therefore, sizing methodologies developed for RFIMs are not directly applicable. To address this, analytical formulations specific to AFIM topologies are employed to identify practical limits for electric and magnetic loadings, considering structural constraints and dimensional dependencies. The main dimensions of each electrical machine are determined by the electrical machine output power equation, which in this chapter is applied to AFIMs under linear magnetic conditions.

3.1 Diameter Effects on Electric Loading
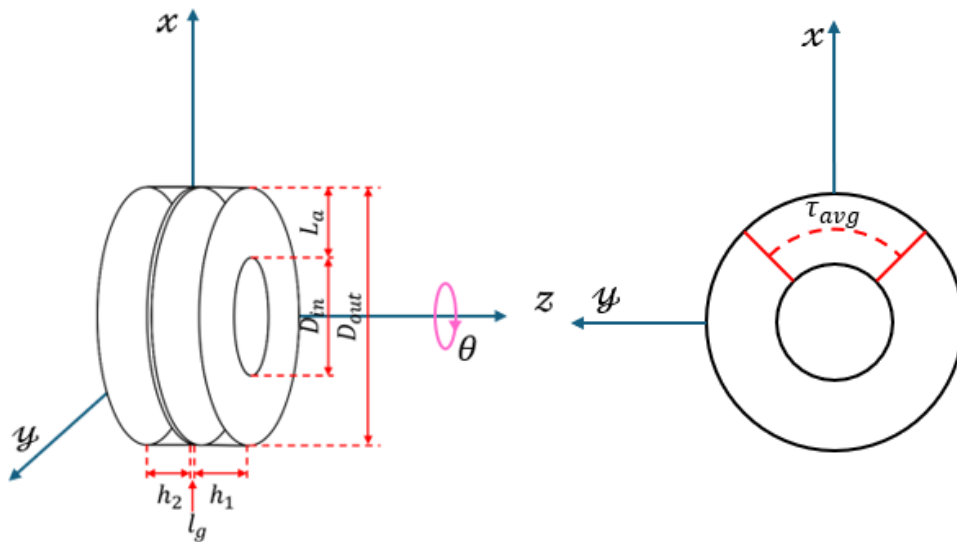
Figure 3-1 Simplified trimetric and top views of an AFIM with key dimensions and average pole pitch labelled.

where D_{out} and R_{out} are the stator/rotor outer diameter and radius, and D_{in} and R_{in} are the stator/rotor inner diameter and radius. The parameter τ is the circumferential distance between two adjacent magnetic poles (pole pitch) and the symbol τ_{avg} denotes the pole pitch at the average diameter.
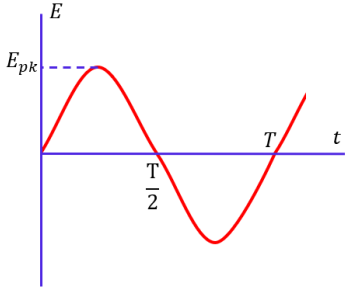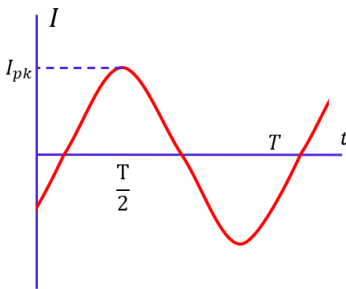
The geometric features of an AFIM are illustrated in Figure 3-1. Unlike the RFIM, where the stack length aligns with the rotational axis producing a uniform 2D radial cross-section (see Figure 1-2(b)), AFIMs employ radial "stacking" around θ axis (see Figure 3-1). This radial "stacking" necessitates defining an average diameter, D_{avg}, and an active stack length L_a, which are expressed by the relationships:

$$D_{avg} = \frac{D_{out} + D_{in}}{2} = R_{out} + R_{in} \tag{3.1}$$

$$L_a = \frac{D_{out} - D_{in}}{2} = R_{out} - R_{in} \tag{3.2}$$

Since the electric loading analysis and power calculations are sensitive to the excitation waveform, it is necessary to define the baseline waveform characteristics. Typical sinusoidal voltage and current waveforms are assumed to produce a uniform rotating magnetic field in the airgap, as illustrated in Table 3-1 [76].

Table 3-1 Typical sinusoidal waveform for an induction motor, with corresponding waveform factors [76].

Model	$e(t)$	$i(t)$	K_i	K_p
Sinusoidal			$\sqrt{2}$	$0.5 \cos \theta$

where the K_i and K_p denote the current waveform factor and power waveform factor. The current waveform factor ($K_i = \sqrt{2}$) represents the ratio of the peak current to its RMS value. The power waveform factor ($K_p = 0.5 \cos \theta$) expresses the ratio of real power to the product of peak voltage and peak current [76].

The radial variation of the cross-sectional geometry, such as the tooth width and airgap area, introduces complexity to the electromagnetic design of AFIMs. For initial sizing, the

cross section at the average diameter is often used to approximate the motor geometry as an equivalent 2D linear machine [34, 35]. However, this approach neglects the influence of the inner-to-outer diameter ratio on the electric loading, leading to suboptimal or possibly impractical designs. To improve the accuracy of AFIM design and modelling, it is necessary to analyse the variations of electric loading along the radial dimension. This impact can be investigated through the power-to-dimensions equations, which are derived in the following section.

The apparent power equation is the basis of the main dimension calculations of an AC motor as it directly influences the electromagnetic characteristics, which collectively define the motor's physical dimensions. These relationships are formalised through the following equations.

$$S_a = mE_{ph}I_{ph} \times 10^{-3} \text{ (kVA)} \tag{3.3}$$

The term m denotes the number of phases, and E_{ph} and I_{ph} refer to the phase induced electromotive force (EMF) and the phase current.

$$E_{ph} = 2K_B K_{dp} f N_{ph} \varphi_p \tag{3.4}$$

where K_B is the airgap flux waveform coefficient, which quantifies the shape factor of the flux distribution within the airgap. For a sinusoidal flux distribution, $K_B = \frac{\pi}{2\sqrt{2}} \approx 1.11$ [76, 86]. K_{dp} denotes the winding distribution factor, $K_{dp} = \frac{\sin(q\gamma/2)}{q\sin(\gamma/2)}$, where q and γ represent the number of slots per pole per phase and the slot pitch in electrical degrees. For instance, for a 48 slot, 8 pole, 3 phase motor designed with a distributed winding, the value of K_{dp} is 0.966. The magnetic flux per pole φ_p is obtained by integrating the airgap flux density over the pole area, as expressed in (3.5).

$$\varphi_p = \int_0^{\tau_{avg}} \int_0^{L_a} B_\delta(L, \tau) \, dL d\tau = B_\delta \tau_{avg} L_a \tag{3.5}$$

where B_δ is the average airgap flux density, the pole pitch at the average diameter τ_{avg} is given by (3.6) and the flux per pole (φ_p) can be expressed as (3.7).

$$\tau_{avg} = \alpha_\delta \frac{\pi D_{avg}}{2p} \tag{3.6}$$

$$\varphi_p = \frac{\pi}{8p} \alpha_\delta (D_{out}^2 - D_{in}^2) B_\delta \tag{3.7}$$

where the pole arc coefficient α_δ typically ranges from 0.7 to 0.9 to achieve optimal efficiency [87]. Substituting (3.7) into (3.4), the phase electromotive force E_{ph} can be expressed as:

$$E_{ph} = 2K_B K_{dp} \frac{pn}{60} N_{ph} \frac{\pi}{8p} \alpha_\delta (D_{out}^2 - D_{in}^2) B_\delta \tag{3.8}$$

The phase current I_{ph} can be related to the stator specific electric loading A_{avg} at the average diameter through the following expression:

$$I_{ph} = \frac{\pi D_{avg} A_{avg}}{m N_{ph}} = \frac{\pi (D_{out} + D_{in})}{2m N_{ph}} A_{avg} \tag{3.9}$$

where m denotes the number of phases, and N_{ph} denotes the number of turns per phase. Rearranging (3.9), the stator specific electric loading A_{avg} can be expressed as:

$$A_{avg} = \frac{m N_{ph} I_{ph}}{\pi D_{avg}} \, [\text{A/m}] \tag{3.10}$$

By substituting (3.8) and (3.9) into (3.3), the apparent power S_a [kVA] at the average diameter can be calculated as:

$$S_a = \frac{\pi^2}{60} \alpha_\delta K_B K_{dp} D_{avg}^2 L_a A_{avg} B_\delta n \times 10^{-3} \tag{3.11a}$$

Which can be rearranged to give:

$$D_{avg}^2 L_a = \frac{(D_{out} + D_{in})^2}{4} \frac{D_{out} - D_{in}}{2} \frac{60 S_a \times 10^3}{\pi^2 \alpha_\delta K_B K_{dp} n A_{avg} B_\delta} \tag{3.11b}$$

$$C = \frac{S_a}{D_{avg}^2 L_a} = \frac{\pi^2}{60} \alpha_\delta K_B K_{dp} B_\delta n A_{avg} \times 10^{-3} \tag{3.12}$$

$$T_{em} = \frac{S_a}{2\pi n/60} = \frac{60}{\pi^2} C (R_{avg} \pi D_{avg} L_a) \tag{3.13}$$

The electric motor constant (C), as defined in (3.12), represents the apparent power per unit volume (kVA·min/m³), and serves as a key parameter in evaluating the electromagnetic performance and physical dimensions. For instance, a relative higher motor constant is desirable in electric vehicle applications, as it enables a higher power density. Equation (3.13) provides a direct means to estimate the torque capacity of an AFIM based on the geometric and electromagnetic factors [88].

The real power output per unit volume (kW/m³) of the AFIM can be expressed as (3.14), where h represents the total thickness of the AFIM, given $h = h_1 + h_2$. The power density of the AFIM is directly proportional to the rotational speed (n), machine constant (C), average diameter (D_{avg}), and power factor (pf). On the other hand, it is inversely proportional to the total thickness of the motor h (see Figure 3-1). Equation (3.15) presents the inner-to-outer diameter ratio of the AFIM [76].

$$P_{out}/V = \frac{S_a \eta \cdot pf}{\frac{\pi}{4}(D_{out}^2 - D_{in}^2)\sum h} = \left(\frac{4\eta \cdot pf}{\pi}\right)\left(\frac{D_{avg}}{4h}\right)(Cn) \tag{3.14}$$

$$\lambda = D_{in}/D_{out} \tag{3.15}$$

The stator specific electric loading (A) is inversely proportional to the radius, making the inner to outer diameter λ a critical parameter in axial-flux motor design. This ratio directly influences both the torque/power density and efficiency. Studies [89-91] have demonstrated that the optimal torque/power density are achieved when λ lies within the range of 0.45 to 0.65. Furthermore, [92] explores how variations in λ impact overall efficiency. These investigations rely on iterative processes, often assuming a fixed outer diameter and a uniform average stator specific electric loading. Alternatively, to investigate the inner-to-outer diameter, (3.11(a)) can be rearranged into a function of diameter ratio and specific electric loading, enabling analytical identification of the ratio that maximise the power.

To analytically investigate the optimal diameter ratio λ and its effect, two assumptions are considered. The first assumes that the specific electric loading A_{avg} is applied to target motor. Under this assumption, the apparent power depends on both the inner and outer diameters, can be expressed as:

$$S_{a1} = f(D_{avg}, A_{avg}) = \frac{\pi^2}{60}\alpha_\delta K_B K_{dp}\frac{(D_{out}^2 - D_{in}^2)}{4}\frac{D_{out} + D_{in}}{2}A_{avg}B_\delta n \times 10^{-3} \tag{3.16a}$$

The second approach recognises that the slot packing density is highest near the inner radius as ratio of slot width to tooth width, is highest near the inner radius due to the smaller tooth width in this region, where the maximum specific electric loading A_{max} is assumed to occur. Under this assumption, the apparent power is expressed as:

$$S_{a2} = f(D_{in}, A_{max}) = \frac{\pi^2}{60}\alpha_\delta K_B K_{dp}\frac{(D_{out}^2 - D_{in}^2)}{4}D_{in}A_{max}B_\delta n \times 10^{-3} \tag{3.16b}$$

Based on these two formulations (3.16a and 3.16b), the maximum apparent power output can be determined by the optimised diameter ratio λ.

Case 1: Assuming A_{avg}, B_δ, and D_{out} are constant, the optimal diameter ratio (λ) can be determined by differentiating S_{a1} with respect to D_{in} to give $\lambda = 1/3$.

Case 2: Assuming A_{max}, B_δ, and D_{out} are constant, the optimal diameter ratio (λ) can be determined by differentiating S_{a2} with respect to D_{in} to give $\lambda = \sqrt{3}/3$.

The corresponding maximum apparent powers, $(S_{amax})_1$ and $(S_{amax})_2$, reflect different optimal diameter ratios under identical outer diameters. To enable a consistent comparison, both expressions are normalised using a constant average specific electric loading A_{avg}, as in (3.16a), highlighting the influence of λ on the apparent power.

$$(S_{amax})_2/(S_{amax})_1 \approx 0.887 \text{ or } (S_{amax})_1/(S_{amax})_2 \approx 1.127 \tag{3.17}$$

$$\frac{(S_{amax2}/V_{Fe})}{(S_{amax1}/V_{Fe})} = \frac{S_{a\_max2} \times (1 - \lambda_1^2)}{S_{a\_max1} \times (1 - \lambda_2^2)} = 1.18 \tag{3.18}$$

It is observed that, although Case 1 ($\lambda = 1/3$) provides a higher total apparent power output, Case 2 ($\lambda = \sqrt{3}/3$) achieves a significantly greater power density. The increased inner diameter in Case 2 minimises the core volume, thereby increasing power density. As shown in (3.18), despite an 11.3% reduction in total apparent power, the power density in Case 2 is approximately 18% higher than in Case 1.

(a)   (b)
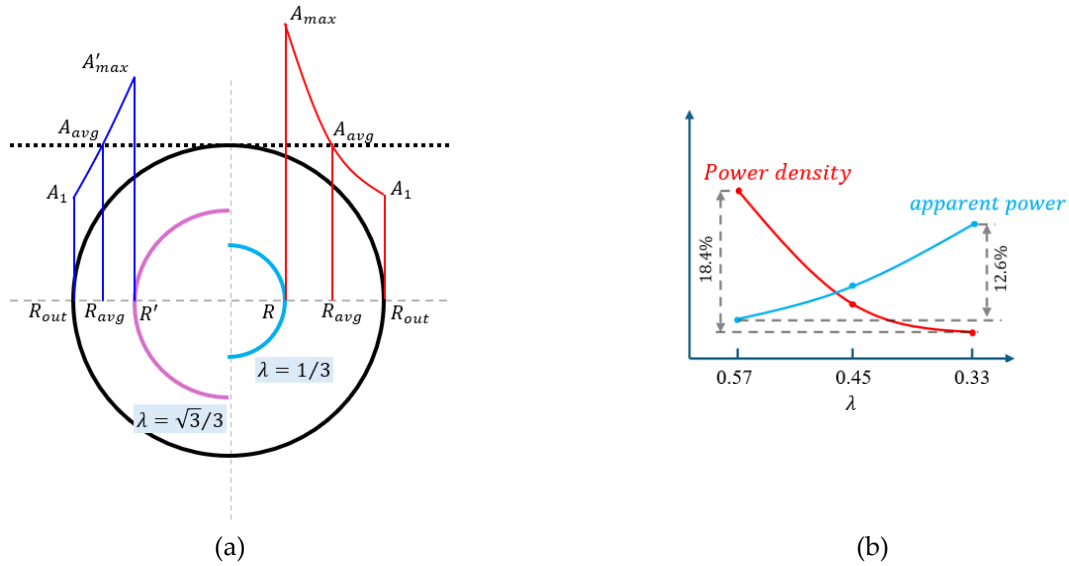
Figure 3-2 (a) Comparison of specific electric loadings for different inner-to-outer diameter ratios. (b) Variations of power density and apparent power under different diameter ratios.

Figure 3-2 shows the diameter ratio effects on specific electric loading, apparent power, and power density. It assumes the outer radius and the average stator specific electric

loading at the average radius are equal. Figure 3-2(a) illustrates the specific electric loading distribution at different radii, while Figure 3-2(b) highlights the trade-off between apparent power and apparent power produced by changes in the diameter ratio.

3.2   Characteristics of the AFIM Magnetic Circuit

The magnetic circuit structure of the AFIM shares similarities with the RFIM, consisting of five key elements: the airgap, rotor teeth, rotor back iron, stator teeth, and stator back iron. The magnetomotive force (MMF) equation, expressed as $\sum HL = \sum \mathcal{F}$, can be applied to all parts of the AFIM. Although the airgap length and slot widths remain constant across different radial layers, the AFIM stator and rotor tooth widths vary with the radial position. At the inner radius, the stator and rotor teeth are at their narrowest, and the teeth are widest at the outer radius. The flux density distribution within the airgap can be determined based on the same principles used for the RFIM. Specifically, the Carter's coefficient K_c is introduced to use the effective airgap length to account for the distortion of magnetic flux distribution caused by the slotting effect. For semi-closed slots (both stator and rotor slots) [88], the RFIM Carter's coefficient can be calculated as:

$$K_{c,s} = \frac{1}{1 - \gamma_1(l_g/w_{s,t})} \tag{3.19}$$

$$K_{c,r} = \frac{1}{1 - \gamma_2(l_g/w_{r,t})} \tag{3.20}$$

where γ_1 and γ_2 are expressed by (3.22) and (3.23), the $w_{r,t}$ and $w_{s,t}$ are the rotor and stator tooth width at the airgap, the $b_{s,o}$ and $b_{r,o}$ are the stator and rotor slot opening width.

In AFIMs, the Carter's coefficient $K_c(r)$ varies with the radius r due to the radial dependence of the stator and rotor tooth widths $w_{r,t}(r)$ and $w_{s,t}(r)$ at the airgap.

$$K_c = K_{c,s}K_{c,r} = K_c(r) = \frac{1}{\left(1 - \frac{\gamma_1 l_g}{w_{s,t}(r)}\right) \times \left(1 - \frac{\gamma_2 l_g}{w_{r,t}(r)}\right)} \tag{3.21}$$

$$\gamma_1 = \frac{b_{s,o}/l_g}{\alpha_1 + \alpha_2(b_{s,o}/l_g)} \tag{3.22}$$

$$\gamma_2 = \frac{b_{r,o}/l_g}{\alpha_1 + \alpha_2(b_{r,o}/l_g)} \qquad (3.23)$$

For semi-closed rotor and stator slots, α_1 and α_2 are assumed to be 4.4 and 0.75. For open slots, they are 5 and 1. In the case of fully-closed slots, K_c is assumed to be 1 [93]. The airgap flux density then can be expressed as follows:

$$B_\delta(r) = \mu_0 \frac{\mathcal{F}_m}{K_c(r)l_g} \qquad (3.24)$$

where $\mathcal{F}_m$ and μ_0 are the magnetomotive force and air permeability. Thus, due to the geometrical characteristics of AFIMs, the airgap flux density $B_\delta(r)$, produced by the stator MMF, varies significantly along the radial direction.
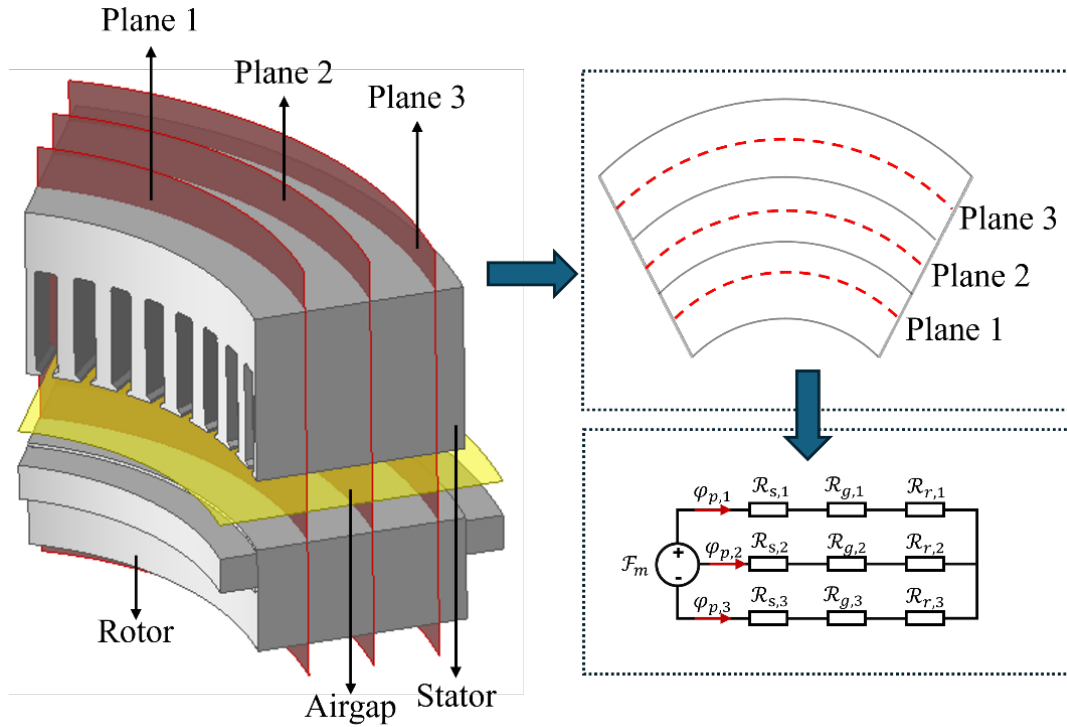
Figure 3-3 Radial segmentation and simplified magnetic equivalent circuit representation of an AFIM.

To more accurately model the non-uniform radial flux distribution in the AFIM, the stator and rotor can be divided into N concentric radial segments spanning the airgap region between the inner radius r_{in} and outer radius r_{out} (see Figure 3-3). Each radial segment is assumed to possess an approximately uniform magnetic field and is treated as an

independent magnetic path within a simplified equivalent magnetic circuit [94-97]. Two parallel magnetic circuit constraints are made when constructing this model.

Each radial ring element is subjected to an identical magnetomotive force (MMF), which can be expressed as:

$$\mathcal{F}_1 = \mathcal{F}_2 = \cdots = \mathcal{F}_m \tag{3.25}$$

The total magnetic flux per pole is obtained by summing the magnetic flux contributions from all radial ring elements, satisfying the principle of flux conservation:

$$\varphi_p = \varphi_{p,1} + \varphi_{p,2} + \cdots + \varphi_{p,N} = \sum_{k=1}^{N} \varphi_{p,N} \tag{3.26}$$
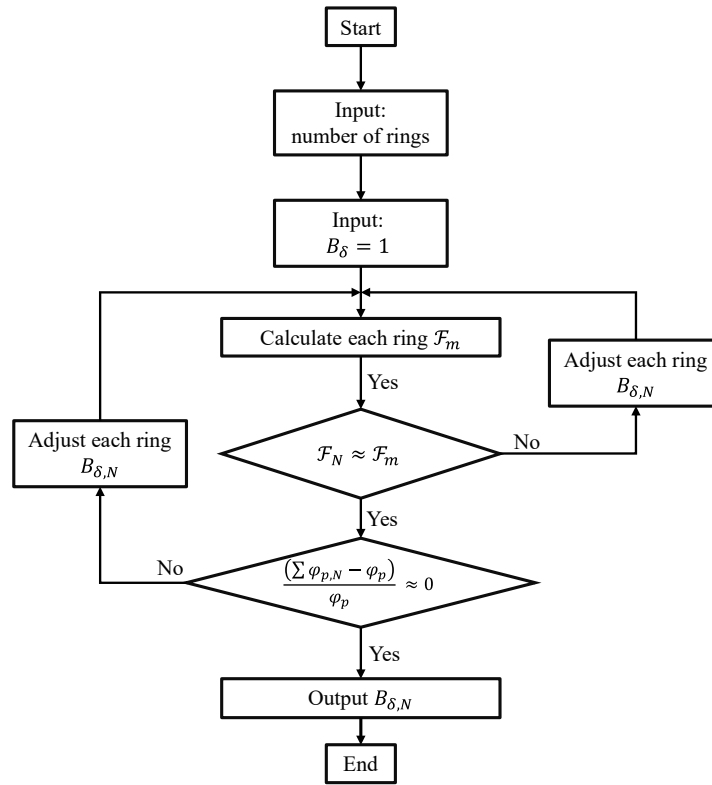
Figure 3-4 Segmented magnetic circuit iterative computation flowchart.

Figure 3-4 illustrates the flowchart of the segmented airgap flux density calculations. The radial variation of the airgap flux density $B_\delta(r)$ in the AFIM is determined through an iterative magnetic circuit approach. The airgap region is divided into N concentric radial elements, and the diameter ratio λ is fixed to preserve consistent geometrical proportions across the magnetic model. Each radial element is assumed to have a uniform magnetic field,

and constant airgap length l_g, as defined in (3.21). To initiate the procedure, the flux density $B_\delta(r)$ is firstly assumed to be uniform across all segments, and the corresponding initial target magnetomotive force $\mathcal{F}_N^0$ for each segment is calculated using (3.24). Under the constraint of a constant magnetomotive force $\mathcal{F}_m$ applied equally to all radial paths (3.25), the magnetic flux $\varphi_{p,N}$ in each segment is calculated by $K_c(r)$ and $B_\delta(r)$. The total magnetic flux per pole φ_p is then obtained by summing the contributions from all segments, in accordance with the flux conservation principle (3.26). If the calculated total flux deviates from the specified pole flux, the flux density $B_\delta(r)$ is scaled proportionally. Following this adjustment, the magnetic fluxes are re-evaluated. After each iteration, the conditions of equal magnetomotive force $\mathcal{F}_m$ and flux conservation are reviewed. The iterative process continues until the variation in $B_\delta(r)$ between iterations satisfies the constraints (3.25) and (3.26) [98].

Since the stator and rotor tooth widths $w_{s,t}(r)$ and $w_{r,t}(r)$ increase with radius in the AFIM, the ratios $l_g/w_{s,t}(r)$ and $l_g/w_{r,t}(r)$ decrease accordingly. As a result, the $K_c(r)$ gradually decreases with increasing radius. The relationship between $B_\delta(r)$ and $K_c(r)$ can be expressed as:

$$B_\delta(r) \propto \frac{1}{K_c(r)} \tag{3.27}$$

Although $B_\delta(r)$ increases with radius due to the inverse dependence on $K_c(r)$, the variation is limited. This is because the airgap length l_g is much smaller than the stator and rotor tooth width $w_{s,t}(r)$ and $w_{r,t}(r)$, leading to small changes in $K_c(r)$. As a result, the change in $B_\delta(r)$ in a radial direction is gradual.

Similar to the airgap flux density distribution, the rotor and stator tooth flux densities also vary with the radius as follows,

$$B_{r,t}(r) = B_\delta(r) \cdot \frac{A_g(r)}{A_{r,t}(r)} \tag{3.28}$$

$$B_{s,t}(r) = B_\delta(r) \cdot \frac{A_g(r)}{A_{s,t}(r)} \tag{3.29}$$

where $A_g(r)/A_{r,t}(r)$ and $A_g(r)/A_{s,t}(r)$ denote the spatial ratios of the airgap area to the rotor and stator tooth areas at the airgap, evaluated at radius r.

As the radius increases, the stator and rotor tooth body widths $w_{s,t}(r)$ and $w_{r,t}(r)$ increase significantly, while the slot body width $w_{r,s}$ and $w_{s,s}$, remain constant. This geometric expansion causes the magnetic flux to be distributed over a larger tooth cross-sectional area, leading to an increase in $B_{r,t}(r)$ and $B_{s,t}(r)$ along the radial direction.

The flux density in the back iron of the AFIM rotor and stator can also be estimated with a similar method.

$$B_{s,y}(r) = \frac{Q_{s,s,p}}{\pi h_{s,y}} B_\delta(r) w_{s,t}(r) \tag{3.30}$$

$$B_{r,y}(r) = \frac{Q_{r,s,p}}{\pi h_{r,y}} B_\delta(r) w_{r,t}(r) \tag{3.31}$$

where $Q_{r,s,p}$ and $Q_{s,s,p}$ are the number of rotor and stator slots per pole, respectively. $B_{s,y}(r)$ and $B_{r,y}(r)$ represent the flux densities in the stator and rotor yoke. It is observed that the flux density in the rotor and stator yoke increases with increasing radius when the airgap flux density is evenly distributed due to the increase in airgap area.

To further investigate the impact of the motor's geometric proportions on the magnetic flux distribution, the diameter ratio λ is varied while keeping the outer diameter constant. In this case, it is assumed that the $\mathcal{F}_m$ remains constant across all radial planes, the magnetic materials operate within their linear regions, and the airgap length remains unchanged. The stator and rotor tooth widths are considered to vary linearly with the radius. A larger diameter ratio, corresponding to a larger inner diameter, leads to a reduction of effective cross-sectional area at the airgap. Consequently, to maintain the same total magnetic flux and $\mathcal{F}_m$, the average airgap flux density increases. Furthermore, a larger diameter ratio λ leads to a smaller variation between the maximum and minimum flux densities along the radial direction.

3.3 Rotor and Stator Slot Geometrical Parameter Characteristics

In AFIMs, the rotor and stator slot configurations critically influence the magnetic coupling, flux distribution, and electromagnetic performance. The stator slot geometry primarily affects the flux linkage and leakage characteristics, whereas the rotor slot design governs the distribution of induced currents and directly impacts torque production at the

different speeds. Slot openings may be configured as open, semi-closed, or closed, each presenting distinct trade-offs. Open slots simplify manufacturing and enhance air circulation but typically result in higher leakage reactance, and magnetising current acoustic noise. Conversely, semi-closed and closed slots reduce leakage flux and reduce magnetising current, thereby improving magnetic coupling and overall efficiency. However, these benefits are offset by increased winding complexity and diminished thermal dissipation. Consequently, slot design must balance electromagnetic performance against manufacturability and thermal constraints [88, 93].

In RFIMs, these shapes are generally selected to ensure that the rotor and stator teeth have a constant width. This achieves a more uniform magnetic flux distribution, which helps reduce local magnetic saturation in the teeth. It also optimises the inductance profile, contributing to improved power factor and efficiency. Therefore, the parallel rotor and stator teeth configurations are chosen for the AFIM (see Figure 3-5).
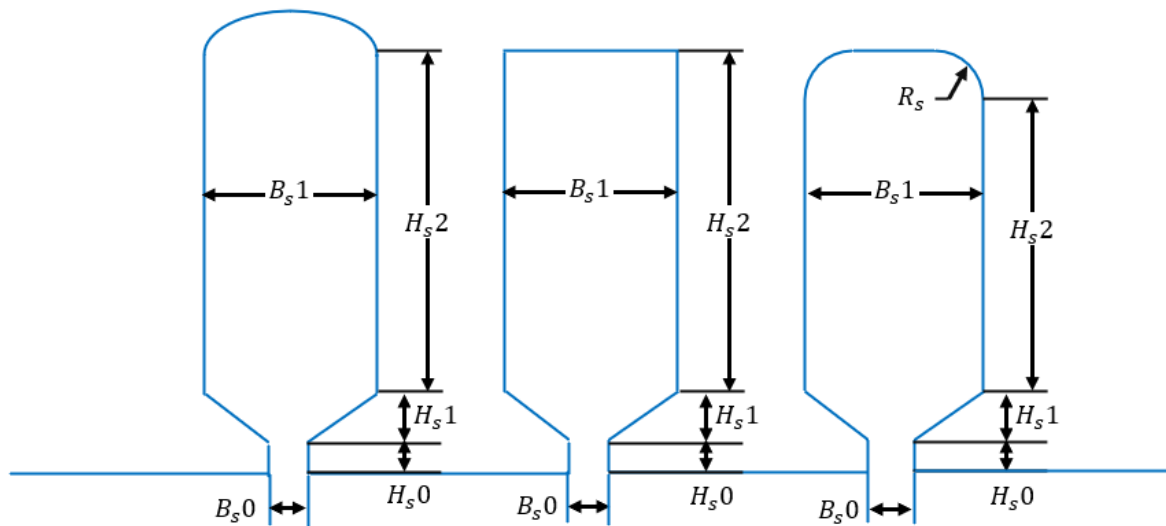
Figure 3-5 Shape of semi-closed parallel stator/rotor slots (left: circular top. Middle: flat top. Right: rounded top).
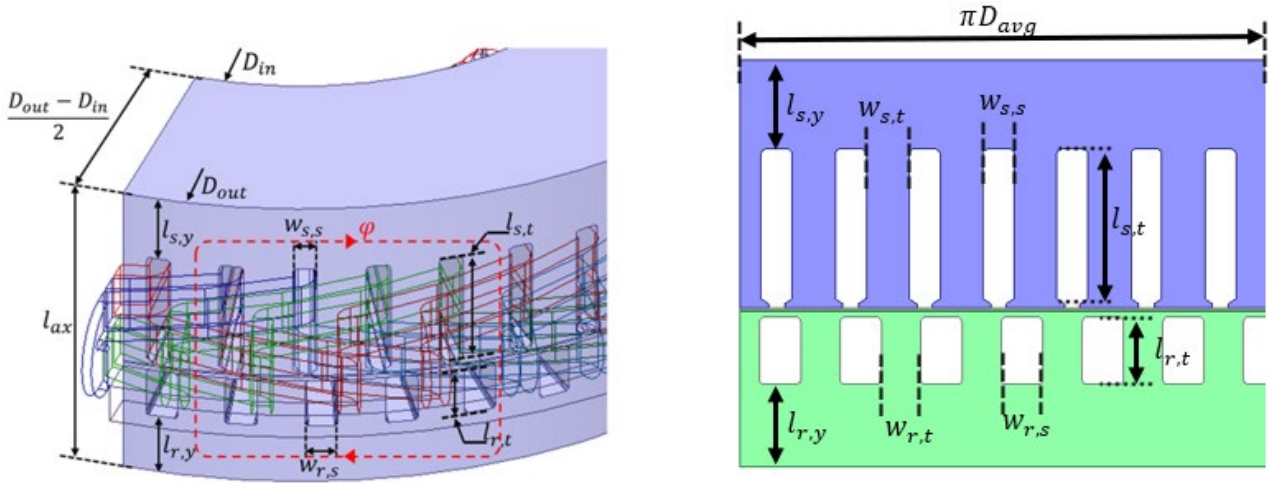
Figure 3-6 Geometrical representation of the AFIM core layout. Left: 3-D drawing of stator and rotor slot arrangement with key design parameters. Right: 2-D linear equivalent model, highlighting the tooth and slot dimensions for both the stator and rotor.

Figure 3-6 defines the motor dimensions used in both the 3-D model and 2-D equivalent linear machine model. The 2-D model represents the middle layer of the AFIM and is used to determine the rotor and stator geometric parameters. Equation (3.32) estimates the required thickness of the stator yoke ($l_{s,y}$) in an AFIM by equating the magnetic flux passing through the airgap to that which must be carried by the stator yoke without saturation.

$$l_{s,y} = \frac{\pi(D_{out} + D_{in})/2}{8p \cdot k_{Fe,s}} \frac{B_\delta}{B_{s,y}} \tag{3.32}$$

where $k_{Fe,s}$ is the stator-lamination stacking factor and $B_{s,y}$ is allowable stator yoke flux density. Equation (3.33) calculates the total area of the stator slots ($A_{s,s}$) based on the number of turns per phase and diameter of the conductors. The factor of 0.5 accounts for the assumed slot fill factor of 50%.

$$A_{s,s} = \frac{2m\pi N_{ph} \left(\frac{D_w}{2}\right)^2}{0.5 N_{s,s}} \tag{3.33}$$

where D_w is the winding diameter, $N_{s,s}$ is the number of stator slots and N_{ph} is the number of turns per phase. Equations (3.34) – (3.36) are then used to derive the detailed stator geometry. Equation (3.34) illustrates the stator tooth width $w_{s,t}$, obtained using the allowable magnetic flux density in stator tooth ($B_{s,t}$) and stacking factor ($k_{Fe,s}$). Equation

(3.35) finds the stator slot body width ($w_{s,s}$) by subtracting the tooth width from the total pitch. Finally, (3.36) estimates the stator slot depth ($l_{s,s}$) from the total slot area divided by the slot width.

$$w_{s,t} = \frac{\pi B_\delta D_{avg}}{N_{s,s} B_{s,t} k_{Fe,s}} \tag{3.34}$$

$$w_{s,s} = \frac{\pi D_{avg}}{N_{s,s}} - w_{s,t} \tag{3.35}$$

$$l_{s,s} = \frac{A_{s,s}}{w_{s,s}} \tag{3.36}$$

To obtain the geometric parameters at the rotor side, a similar method is applied. The length of the rotor (l_r) is the sum of the depth of the rotor slots ($l_{r,s}$) and the length of the rotor yoke ($l_{r,y}$). $B_{r,y}$ is the allowable flux density in the rotor yoke and $k_{Fe,r}$ is the rotor-lamination stacking factor. $\hat{\imath}_r, \hat{J}_r, K_{r,fill}$ are the rotor bar current amplitude, rotor bar current density and rotor-slot fill factor. $B_{r,t}$ is the maximum rotor teeth flux density and $N_{r,s}$ is the number of rotor slots. The following equations are given for the rotor side sizing approach.

$$l_{r,y} = \frac{\pi(D_{out} + D_{in})/2}{8p} \frac{B_g}{B_{r,y} k_{Fe,r}} \tag{3.37}$$

$$A_{r,s} = \frac{\hat{\imath}_r}{\hat{J}_r K_{r,fill}} \tag{3.38}$$

$$w_{r,t} = \frac{\pi B_g D_{avg}}{N_{r,s} B_{r,t} k_{Fe,r}} \tag{3.39}$$

$$w_{r,s} = \frac{\pi D_{avg}}{N_{r,s}} - w_{r,t} \tag{3.40}$$

$$l_{r,s} = \frac{A_{r,s}}{w_{r,s}} \tag{3.41}$$
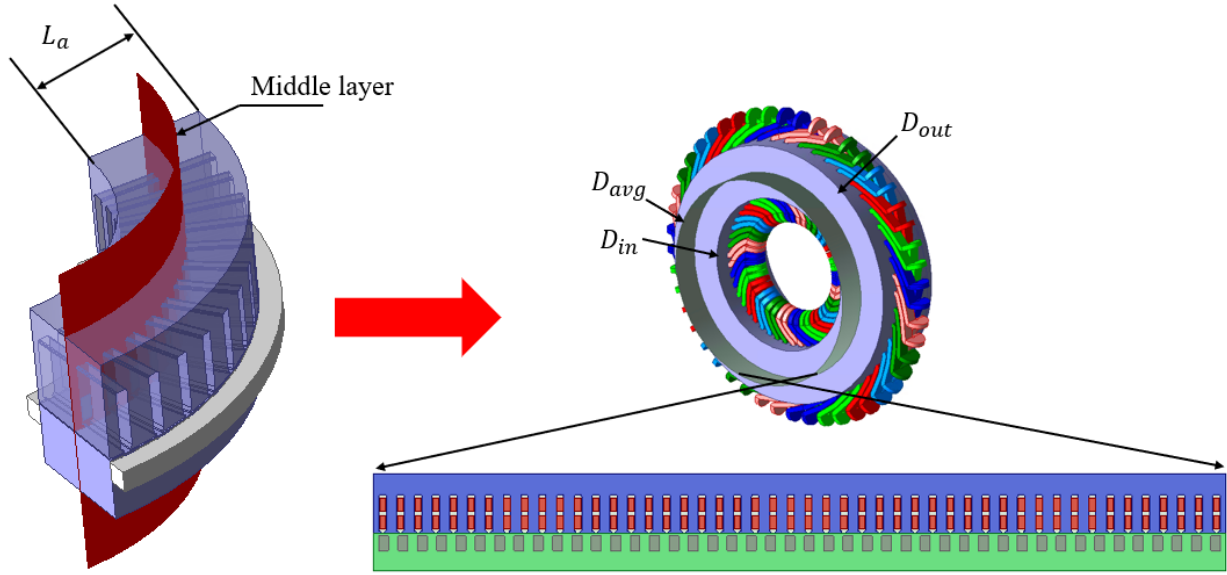
Figure 3-7 Transforming the 3-D geometry of an AFIM to a 2-D linear equivalent model.

Figure 3-7 illustrates the process of transforming the 3-D geometry of an AFIM into the corresponding 2-D linear equivalent model. 3-D FE simulations are typically complex and computationally intensive. Converting the model into an equivalent 2-D linear representation simplifies the process while preserving key geometric and electromagnetic characteristics. However, the 2-D model can only be used for the initial design of AFIMs, as the detailed magnetic behaviour cannot be accurately captured. In the equivalent linear 2-D model, the rotor moves in a linear direction instead of rotating. Hence, a force value is obtained in steady of the torque and the speed is expressed in metres per second (m/s) rather than revolutions per minute (RPM). The following equations can be used for the AFIM 2-D linear model.

$$D_{avg} = D_{in} + \frac{D_{out} - D_{in}}{2} \tag{3.42}$$

$$RPM = V_1 \times \frac{60}{2\pi r_{avg}} \tag{3.43}$$

$$\tau_m = F \cdot r_{avg} \tag{3.44}$$

where V_1 denotes the equivalent linear speed of the motor, r_{avg} is the average radius and F is the equivalent force corresponding to the torque τ_m.

This chapter has discussed the key geometrical parameters of the AFIM, including their definitions, design constraints, and influence on machine performance. These parameters

form the fundamental design space in which AFIMs are evaluated. Although the chapter primarily focused on parameter definitions and baseline considerations, it provides the necessary foundation for the subsequent analysis. In Chapter 4, these geometrical parameters are incorporated into a systematic FEA-based design study, where parameter sweeps and sensitivity analyses are performed. The results from these simulations establish the relationship between geometry, material cost, and performance, and serve as the basis for comparison with conventional RFIMs.

CHAPTER 4

SIMULATION-BASED DESIGN AND ANALYSIS OF AXIAL-FLUX INDUCTION MOTOR

4.1 Preliminary Sizing Approach: Converting Existing RFIM to AFIM

In the AFIM design process, applying the aforementioned analytical equations to estimate the main dimensions is vital, particularly when designing a novel machine type that has not yet been standardised. These theoretical formulations enable designers to quickly grasp the intrinsic relationships between the geometric parameters and the electromagnetic characteristics, thereby laying a solid foundation for subsequent optimisation, structural design, and simulation analysis. Besides, the design of AFIM can also benefit from the existing design experience, which combined with FE simulation software, enables detailed modelling and accurate verification of the motor's electromagnetic performance [73-77]. However, this combined approach is time consuming in the preliminary design stage. Therefore, to streamline the initial design process, this section focuses on transforming the existing RFIMs to their equivalent AFIMs with the newly defined magnetic and electric loading limits. This procedure is generic and can be applied to AFIMs with different number of poles.
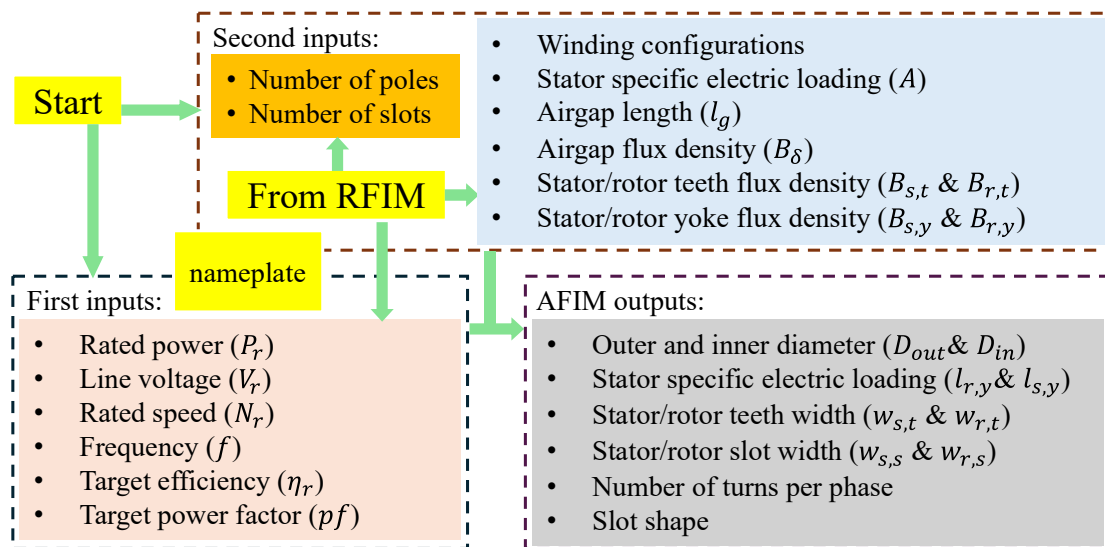
Figure 4-1 Flowchart for converting an existing RFIM to an AFIM.

Table 4-1 Key parameters of the benchmark commercial 2.2kW RFIM with four, six, and eight poles.

Commercial 2.2kW RFIM with four, six and eight poles				
		Four poles	**Six poles**	**Eight poles**
Stator outer diameter [mm]	$D_{s,out}$	165	165	211
Stator inner diameter [mm]	$D_{s,in}$	105	114.5	148
Rotor outer diameter [mm]	$D_{r,out}$	104.2	113.5	147
Rotor inner diameter [mm]	$D_{r,in}$	38	38	48
Axial length [mm]	L	105	130	180
Winding diameter [mm]	$D_{winding}$	0.8	1.4	1.024
No. of strands	-	1	1	1
No. of turns/phase	N_{ph}	564	528	704
Rated power [kW]	P_r	2.2	2.5	2.2
Rated speed [rpm]	n_r	1441	952	725
Rated torque [Nm]	T_r	15	22	30
Rated voltage [V]	V_r	415	415	415
Rated frequency [Hz]	f	50	50	50
No. of stator slots	N_{ss}	36	36	48
No. of rotor slots	N_{rs}	28	42	44
No. of phase	m	3	3	3
No. of poles	p	4	6	8
Airgap length [mm]	D_{airgap}	0.35	0.5	0.5
Winding material	-	Copper	Copper	Copper
Core material	-	50AW470	50AW470	50AW470
Rotor bar material	-	Aluminium	Aluminium	Aluminium

Table 4-2 Comparison between proposed AFIM predefined loading and permitted loading for RFIMs from literature [93].

	Parameters	**From RFIM literature**	**Predefined AFIM loading**
Specific electric loading [A/mm]	A_{avg}	28 - 45	20 - 40
Stator current density [A/mm²]	$\hat{J}_s$	$3-8$	$3-5$
Rotor current density [A/mm²]	$\hat{J}_r$	$3-6.5$	$3-4.5$
Airgap flux density [T]	B_g	$0.7-0.9$	$0.7-0.9$
Tooth flux density [T]	$B_{s,t}\ or\ B_{r,t}$	$1.4-2.1$	<1.6
Rotor yoke flux density [T]	$B_{r,y}$	1-1.9	<1.5
Stator yoke flux density [T]	$B_{s,y}$	1.4-2.7	<1.5

Figure 4-1 illustrates the design procedure for the 2.2kW AFIM. The process commences with defining the design specifications, including the power rating, number of poles, frequency, and voltage. The outer diameter of the AFIM is determined by the electrical output power equation, while the inner diameter is derived from sensitivity studies on the optimal inner-to-outer diameter ratio. Preliminary estimates of the tooth widths and yoke lengths are further refined by referencing flux density values obtained from the corresponding components of the RFIM. These values are then adjusted based on the flux distribution within the AFIM, which subsequently allows for a redefinition of the

permissible flux density levels suitable for the AFIM design. Table 4-1 tabulates the key parameters of the commercial line-start RFIMs which were used as design references for the new AFIM designs. Table 4-2 illustrates the differences between the proposed AFIM predefined loadings and permitted loadings for RFIMs from the literature.

4.1.1 Simulation-Based Analysis of Inner-to-Outer Diameter Ratio Effects on AFIM Performance

As discussed in **CHAPTER 3**, the conventional electric motor general sizing approach is not well-suited for AFIM design. This limitation arises from the assumption of uniform magnetic and electric loading distributions, an oversimplification that neglects the radial variation of these parameters inherent in axial-flux motors. The resultant higher flux density and current density can cause saturation and possible overheating near the inner diameter. Although an initial inner-to-outer diameter ratio of 0.577, which theoretically offers the highest power density, was implemented in the 3-D ANSYS FEM model (see Section 3.1 and [90-92, 99]), it posed practical challenges, as it provided insufficient space to place the inner end-windings. In addition, past research appears to have a limited understanding of how the diameter ratio ($\lambda = D_{in}/D_{out}$) affects the performance of the AFIM, such as efficiency and material cost. This is important because the diameter ratio can impact not only the electromagnetic performance but also the cost-effectiveness.

D_{in}

D_{out}

(a)　　　　　　　　　　　　　　　　　　　(b)
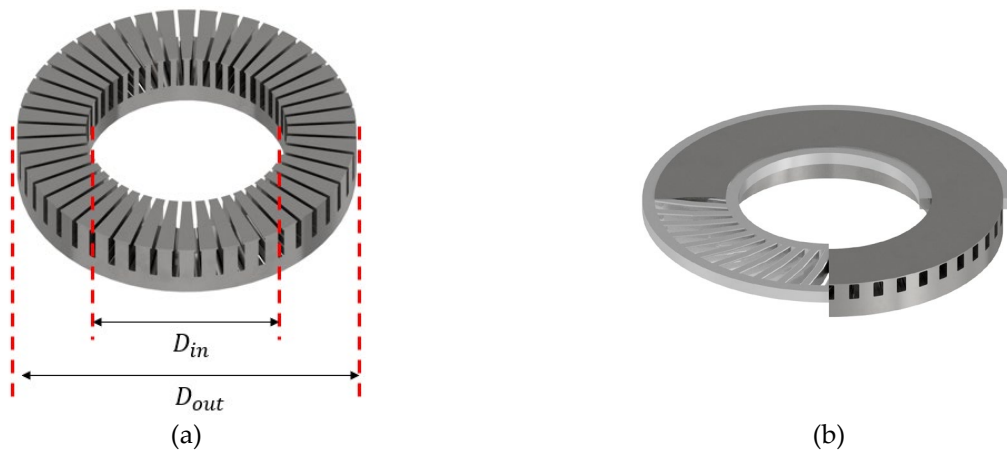
Figure 4-2 (a) 3-D view of designed stator (b) 3-D view of rotor with bars showing skewing.

The following section examines the inner-to-outer diameter ratio effect on various performance factors, such as torque, efficiency, stator electric loading, current density, flux density, and material cost, using 3-D FE simulations. The machine output power is kept constant. The influence of this ratio on each performance metric serves as a reference for the motor prototype design and offers guidance for AFIM designers to prioritise either material

cost or efficiency, depending on specific application requirements. The properties and geometry of the designed eight-pole 2.2kW AFIM are tabulated in Table 4-3. The proposed unwound stator and rotor with bars are given in Figure 4-2 along with the specified inner and outer diameters.

Table 4-3 The geometry and properties of the designed eight-pole 2.2kW AFIM.

Outer diameter [mm]	D_{out}	275
Inner diameter [mm]	D_{in}	163
Axial length [mm]	L	78
Wire diameter [mm]	D_{wire}	0.861
No. of strands	-	2
No. of turns/phase	N_{ph}	896
Rated power [kW]	P_r	2.2
Rated speed [rpm]	n_r	725
Rated torque [Nm]	τ_r	30
Rated voltage [V]	V_r	415
Rated frequency [Hz]	f	50
No. of stator slots	N_{ss}	48
No. of rotor slots	N_{rs}	44
No. of phase	m	3
No. of poles	p	8
Airgap length [mm]	D_{airgap}	0.5
Winding material	-	Copper
Core material	-	M19_24G
Rotor bar material	-	Aluminium
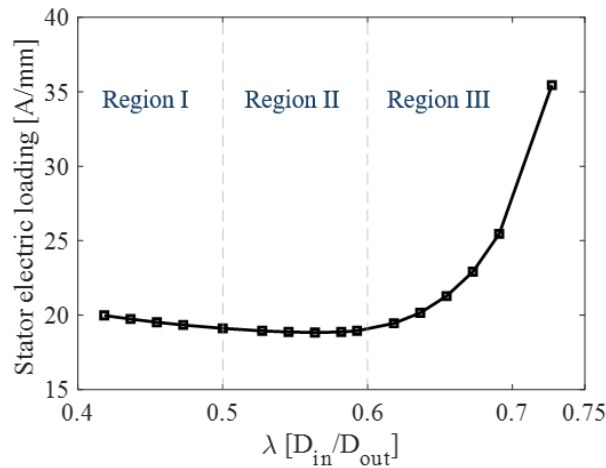
Figure 4-3 Stator specific electric loading as a function of diameter ratio.

In the eight-pole 2.2kW AFIM design, the considered diameter ratio must be greater than 0.4, as a smaller value would result in excessively narrow stator and rotor teeth or even cause adjacent slots to intersect near the inner diameter. Figure 4-3 shows the average stator specific electric loading versus the diameter ratio. In region III, where the diameter ratio is

larger than 0.6, the average stator specific electric loading increases with the diameter ratio, which is the opposite behaviour observed in the equivalent RFIM. Conversely, in region I and region II (for diameter ratios below 0.6), the electric loading increases with decreasing diameter ratio diameter ratio. This is because the smaller inner diameter leads to larger stator specific loadings at the inner diameter, thereby increasing the average value.
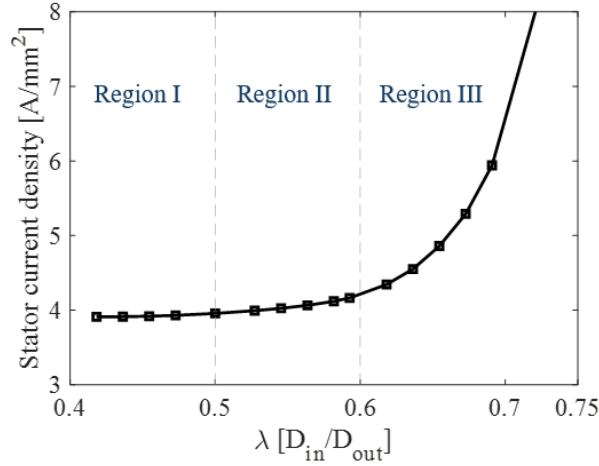
Figure 4-4 Stator current density as a function of diameter ratio.

Figure 4-4 illustrates the variation of stator current density with respect to the inner-to-outer diameter ratio (λ). As λ increases, the average airgap area decreases. To maintain the same output power under reduced interaction area, a higher electric loading is required, leading to an increase in stator current density, especially near the inner radius. In contrast, lower diameter ratios provide a broader radial span for winding placement, which can reduce current concentration and lower thermal stress. However, excessively low diameter ratios (small inner diameter) result in impractically narrow stator or rotor teeth, compromising mechanical integrity, increasing material usage, and negatively affecting electromagnetic performance. When λ exceeds approximately 0.65 (region III), the reduction in airgap area becomes rapid, sharply increasing required electric loading. This causes the stator current density to rise at an accelerating, nearly exponential rate. By comparison, Regions I and II correspond to moderate λ values where the airgap area changes more gradually, leading to a relatively constant current density with only a small rate of increase.

Figure 4-5 shows the flux density magnitudes at different diameter ratios. The results are based on the 2.2kW AFIM with a fixed outer diameter and a constant supply voltage. In the figure, the $B_{s,t}$ and $B_{r,t}$ represent stator and rotor tooth flux densities, $B_{s,y}$ and $B_{r,y}$ are stator and rotor yoke flux densities. It is observed that the trends are similar as mentioned in section 3.2. The inner diameter is varies to evaluate its influence on magnetic loading

within the motor. As the diameter ratio increases, both the flux densities in the yoke and teeth regions of the stator and rotor are increased. This trend is primarily due to the reduced airgap area caused by a larger inner diameter, which leads to an increase in flux density to maintain the same power rating. Thus while a higher diameter ratio may produce a lighter motor design, it also raises the risk of magnetic saturation, particularly in the stator and rotor yoke. Compared to the yoke regions, the width and height of the teeth are typically constrained by the slot number and pitch and therefore do not significantly decrease as the inner diameter changes. As a result, the flux density in the tooth regions increases relatively gradually. In contrast, the changes of inner diameter significantly influence the area of the yoke region, thereby causing a steeper increase in flux density.
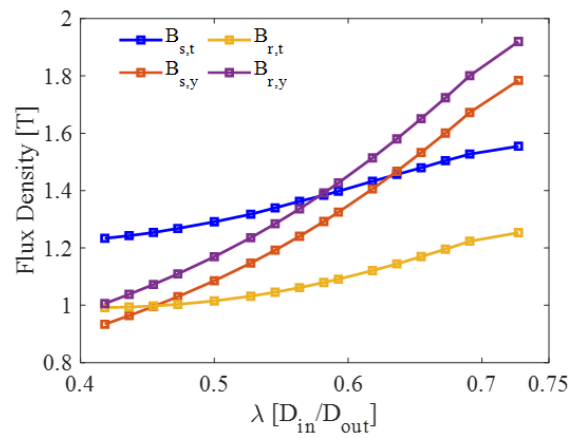
Figure 4-5 Flux densities as a function of inner-to-outer diameter ratio in different components, stator and rotor teeth and yoke.

Consequently, the inner-to-outer diameter ratio is preliminarily set in the range of 0.5 to 0.65, based on the preceding analysis of stator current density, specific electric loading, and magnetic loading, ensuring that the machine operates within the unsaturated region of the core material. To finalise this selection, further investigations are required from other perspectives, such as efficiency, torque output, and material cost.
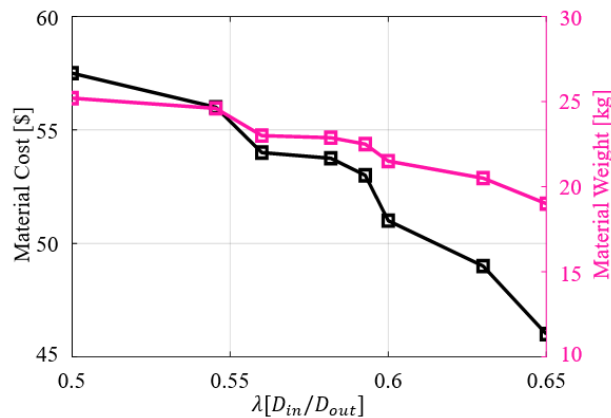
Figure 4-6 Variation of material cost and weight with respect to the diameter ratio.
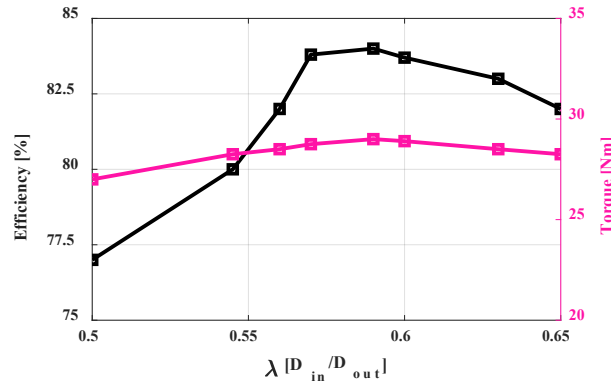
Figure 4-7 Variation of efficiency and torque with respect to the diameter ratio.

Figure 4-6 and Figure 4-7 show the material cost, weight, torque, and efficiency at different diameter ratios. Diameter ratios below 0.577 and above 0.6 give lower output torque at same speed, while those near 0.6 exhibit higher efficiency with relatively lower material cost.
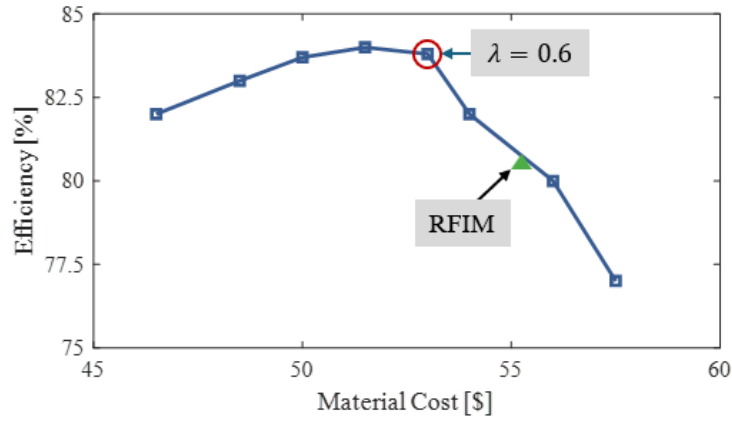
Figure 4-8 Variation of full-load efficiency with material cost, highlighting the commercial RFIM full-load efficiency with the corresponding material cost.

Figure 4-8 shows the relationship between the AFIM full-load efficiency and material cost for varying diameter ratios, highlighting two key points. The efficiency was calculated as the ratio of output mechanical power to the total input power, including copper losses in both stator and rotor windings, iron losses in the stator and rotor cores. The relatively low efficiency observed at certain diameter ratios is primarily attributed to increased copper losses from higher current densities or elevated core losses under high magnetic loading. The peak efficiency at diameter ratio of 0.6 results from a balanced trade-off between copper and iron losses, where the airgap area, magnetic loading, and winding utilisation are optimised.

The figure also compares the commercial RFIM radius with the optimal AFIM design at a diameter ratio of 0.6. The RFIM baseline design (green triangle) achieves an efficiency of

around 80% at a material cost slightly above $55. In contrast, the AFIM design with a diameter ratio of 0.6 (red circle) reaches a higher efficiency of approximately 83.5% while reducing the material cost to around $52. Consequently, a diameter ratio of 0.6 is selected for the 2.2 kW eight-pole AFIM design.

4.1.2 Simulation-Based Analysis of Shape of Rotor and Stator Slot Effects on AFIM Performance

(a)   (b)   (c)   (d)
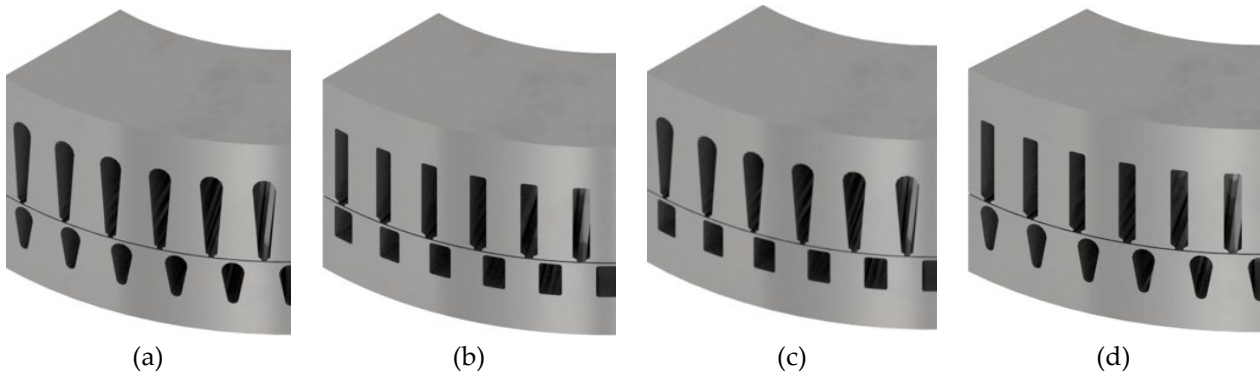
Figure 4-9 The four combinations of teardrop and rectangular slot shapes considered for the stator and rotor.

The previous sections have demonstrated the preliminary sizing approach and the simulation-based choice of the optimal diameter ratio, using the predefined magnetic and electric loading parameters from the benchmark equivalent commercial RFIM. Although a similar stator and rotor slot geometry (teardrop shape) was initially adopted for the newly developed AFIM, is RFIM tooth profile proved unsuitable due to the radius-dependent variation in the tooth width and the differing lamination orientations inherent to the AFIM design. The following section demonstrates a comparative analysis of four stator and rotor slot combinations (see Figure 4-9), each with identical slot areas, evaluated through 3D FE simulations for the 2.2kW eight-pole AFIM. The two key parameters considered for the line-start machine are starting torque and the rated efficiency.
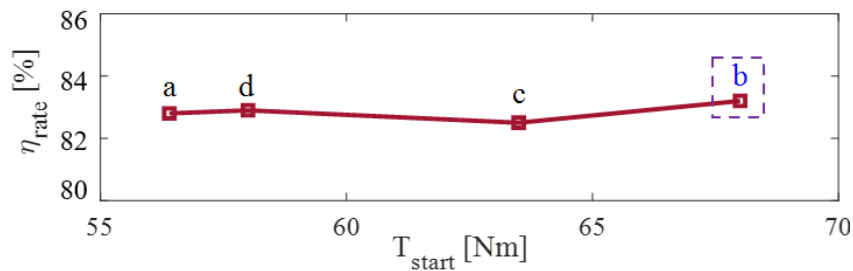
Figure 4-10 Rated efficiency of the AFIM versus starting torque for the four cases.

The rated efficiency (η_{rate}) for AFIM cases (a)-(d) versus starting torque is given in Figure 4-10. The rated efficiency values across the four cases are similar, which is because their identical slot areas and similar magnetic and electric loading conditions. The similar design parameters produce comparable copper losses, which is the largest portion of the total losses. Moreover, the overall magnetic interaction between the rotor and stator remains largely unaffected although the different slot shapes introduce local variations in the flux path. On the other hand, the slot shape has a larger impact on the starting torque (T_{start}). The rectangular slots (Case (b)) provide more uniform flux paths and better coupling, resulting in a starting torque approximately 21% higher than that of the teardrop slot configuration (Case (a)).
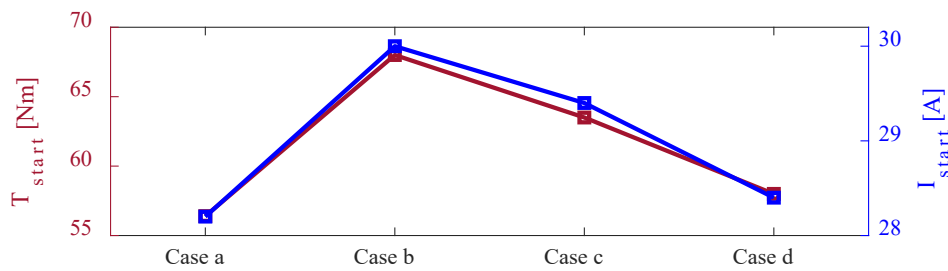
Figure 4-11 Effects of stator and rotor slot shape combinations on the starting torque and current of the AFIM.

Figure 4-11 compares the effect of slot shape on the starting performance of the AFIM by comparing the starting current (I_{start}) across the four cases. Case (b) exhibits the highest starting current, indicating a higher excitation demand during startup. It shows around 6% higher starting current compared to Case (a). Moreover, with the teardrop shaped slot such as in case (a), (c) and (d), the slot geometry features a non-uniform slot width. This can lead to narrower tooth widths between adjacent slots near the inner diameter, resulting in structural weakness and increased manufacturing complexity. Consequently, to achieve a constant reluctance and a more uniform flux distribution and higher starting torque, Case (b) with rectangular stator and rotor slots was selected as the final design.

4.1.3 Stator Winding Configurations for Designed Eight-Pole AFIM

The stator winding configuration selection for the designed AFIM is important as it directly affect the magnetic field strength and distribution, thereby affecting the generated torque. There are two main winding configurations, concentrated and distributed windings. Each configuration offers distinct advantages and drawbacks. Concentrated windings typically lead to simpler manufacturing, lower copper losses, and provide more available space near the inner diameter due to the shorter end-windings. However, as each coil spans

fewer teeth, they tend to produce higher torque ripple as a result of the non-uniform and localised flux distribution. Moreover, it also leads to increased harmonic distortion due to the resulting non-sinusoidal magnetomotive force (MMF). On the other hand, distributed windings achieve smoother torque and a more sinusoidal magnetic flux distributions, thus enhancing overall machine efficiency. Although distributed winding configurations give higher copper losses from longer end windings which poses a risk of insufficient space for end-winding placement near the inner diameter, the substantial improvement in torque ripple reduction and magnetic flux quality make them generally the best choice for AFIMs.

The distribution factor (k_d) and pitch factor (k_p) are critical parameters in selecting winding configurations because they directly affect the induced EMF ($E = 4.44 \cdot f \cdot N \cdot \Phi \cdot k_d \cdot k_w$), efficiency, and harmonic content and they can be expressed by the following equations,
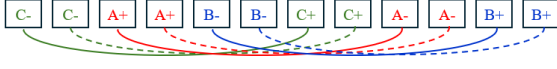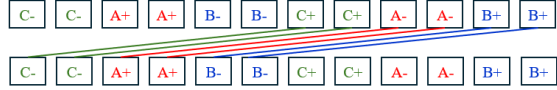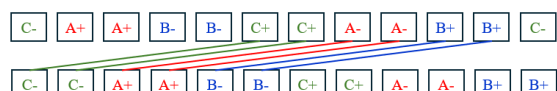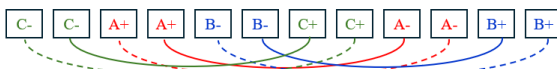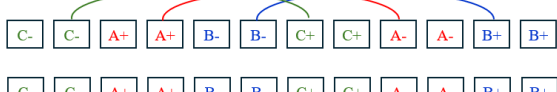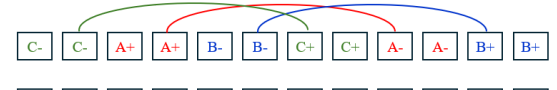
$$k_d = \frac{\sin(q \cdot \alpha/2)}{q \cdot \sin(\alpha/2)} \qquad (3.42)$$

$$k_p = \cos\left(\frac{\pi \cdot y}{\tau}\right) \qquad (3.43)$$

where q and α are the number of slots per pole per phase and the electrical angle between adjacent slots. The terms y and τ denote the coil span and pole pitch.

Table 4-4 illustrates seven proposed winding configuration options, cases 1-3 are categorised as distributed lap windings and cases 4-7 are distributed concentric windings. Note that the same number of turns per slot, 56 turns per slot, are used in all the winding configurations. Case 1 and Case 2 provide the maximum winding factor and thereby the highest induced EMF. However, the longer end-windings pose a challenge when placing them near the inner diameter. Case 3 short-pitched lap windings to reduce harmonic content, though at the cost of a lower winding factor of 0.836. Among them, Case 6 and Case 7 offer the lowest winding resistance with an acceptable winding factor of 0.933, making them suitable for high-efficiency designs. Each winding configuration has its own advantages and limitations, but these factors alone are insufficient to determine which one should be implemented in the prototype. Therefore, FE simulations were conducted for each winding type to evaluate and compare key performance factors, including power factor, starting torque, efficiency, and transient response under full load.

Table 4-4 Winding configuration options and comparisons of design and performance factors.

Case		Description
Case 1		Single-layer, lap winding, full pitch Slot span: 6, $R_s = 2.84\Omega$ $k_p = 1, k_d = 0.966, k_w = 0.966$
Case 2		Double-layer, lap winding, full pitch Slot span: 6, $R_s = 2.59\Omega$ $k_p = 1, k_d = 0.966, k_w = 0.966$
Case 3		Double-layer, lap winding, short pitch, offset layers Slot span: 5, $R_s = 2.35\Omega$ $k_p = 0.866, k_d = 0.966, k_w = 0.836$
Case 4		Single-layer, concentric winding, full pitch Slot span: 5/7, $R_s = 2.85\Omega$ $k_p = 0.966, k_d = 0.966, k_w = 0.933$
Case 5		Single-layer, concentric winding, short pitch Slot span: 5, $R_s = 2.60\Omega$ $k_p = 0.966, k_d = 0.966, k_w = 0.933$
Case 6		Double-layer, concentric winding, short pitch Slot span: 5, $R_s = 2.35\Omega$ $k_p = 0.966, k_d = 0.966, k_w = 0.933$
Case 7		Double-layer, concentric winding, short pitch, offset layers Slot span: 5, $R_s = 2.35\Omega$ $k_p = 0.966, k_d = 0.966, k_w = 0.933$

The starting torque is plotted in Figure 4-12(a), and it is observed that Case (3), (6) and (7) deliver higher starting torque and are thus picked for further investigation. Figure 4-12(b) presents that Case (6) delivers higher power factor and is only slightly lower in efficiency. However, Figure 4-12(c) shows that case 6 has a longer settling time from transient to steady state, about 200ms. Both cases (3) and (7) show similar settling times, and the zoomed-in torque curve shows that case (7) delivers a slight lower torque ripple at full-load operation. Hence case (7) was finally selected for the designed AFIM.

(a)

(b)

(c)
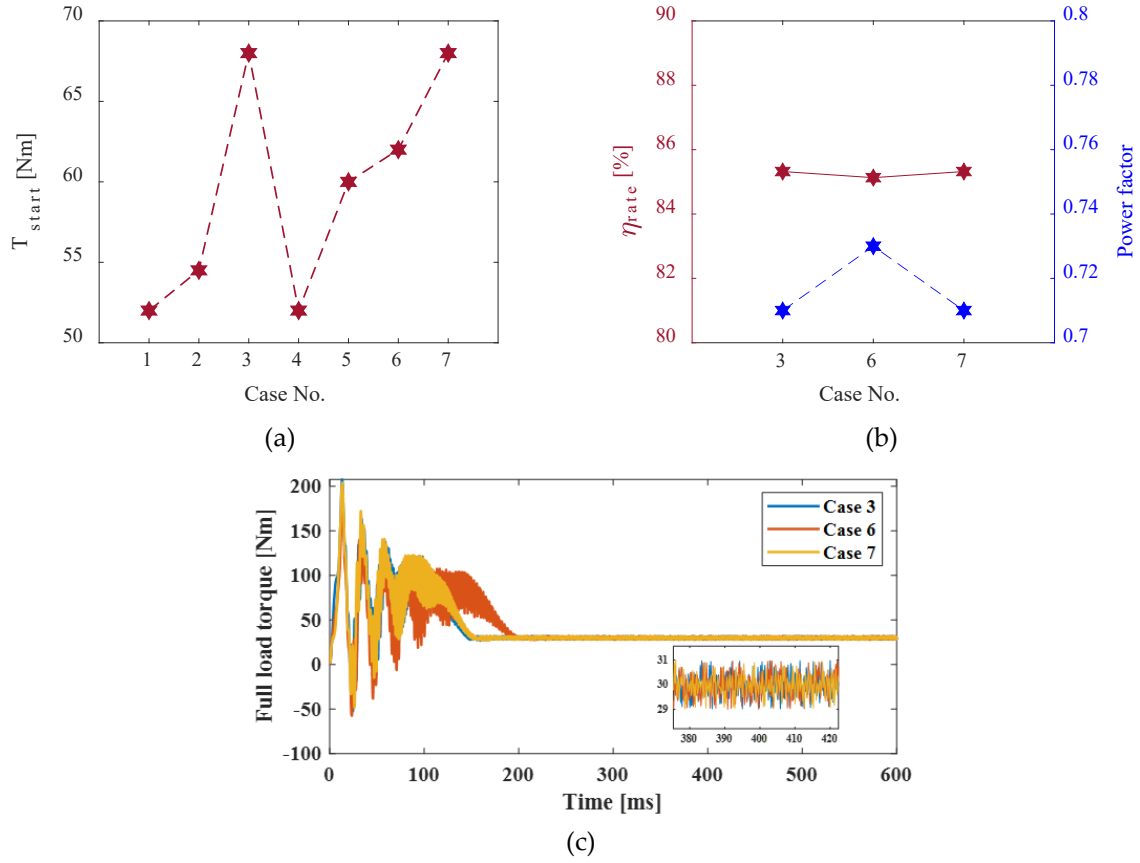
Figure 4-12 FE calculated (a) starting torque, (b) rated efficiency and power factor and, (c) transient response for different winding configurations.

4.1.4 Pareto Front Look-up for Preliminary Sizing

In this subsection, the AFIM designs are developed four-pole and six-pole configurations by using the same sizing methods and sensitivity studies. As a result, a preliminary sizing approach look-up map is introduced to illustrate the relationship between multiple factors, such as material cost, diameter ratio, efficiency, current density and flux density. This approach aims to identify the trade-offs and allow AFIM designers to select the optimal general size quickly based on varying priorities. The properties and dimensions of the designed four, six, and eight poles AFIMs are listed in Table 4-5.

Figure 4-13 illustrates the efficiency versus material cost for alternative 2.2kW AFIM designs with four, six, and eight poles. The designs are generated through geometric parametric variations, including stator and rotor yoke lengths ($l_{s,y}$, $l_{r,y}$), and outer and inner diameters (D_{in} , D_{out}). These variations directly affect both the material cost and electromagnetic performance, such as efficiency, linear current density, and flux density. Some high-cost designs do not offer proportionally higher efficiency. These curves suggest that the considered geometric parameters lead to a convergence toward around 81-82%

efficiency. Other influential factors such as the winding configuration and slot size are not included in this analysis and may further affect the overall design performance. At a similar efficiency level, it is observed that higher material cost does not significantly improve efficiency, as increasing $l_{s,y}$ or $l_{r,y}$ beyond the required flux path capacity only adds to the mass and cost without increasing efficiency.

Table 4–5 Summary of the designed four, six, and eight poles AFIM dimensions and properties.

Design Specifications				
Rated power [kW]	P_r	2.2		
No. of poles	p	4	6	8
Rated speed [rpm]	n_r	1441	952	726
No. of stator slots	N_{ss}	36	36	48
No. of rotor slots	N_{rs}	28	42	44
Inner diameter [mm]	D_{in}	143	150	163
Outer diameter [mm]	D_{out}	235	260	275
Diameter ratio		0.61	0.58	0.60
Stack length [mm]	L_s	76	70	69
Rated torque [Nm]	τ_r	15	22	30
No. of turns/slot	N_{ts}	47	44	44
Rated voltage [V]	V_r	415		
Rated frequency [Hz]	f	50		
No. of phases	m	3		
Wire diameter [mm]	D_{wire}	0.813		
Airgap length [mm]	D_{airgap}	0.465		
Winding material	-	Copper		
Core material	-	M19_24G		
Rotor bar material	-	Aluminium		
Degree of Freedom				
Rotor and stator yoke ratio	$l_{r,y}:l_{s,y}$	0.85 – 1.3		
Inner and outer diameter ratio	$D_{in}:D_{out}$	0.55 – 0.65		

(a) Four-pole   (b) Six-pole   (c) Eight-pole
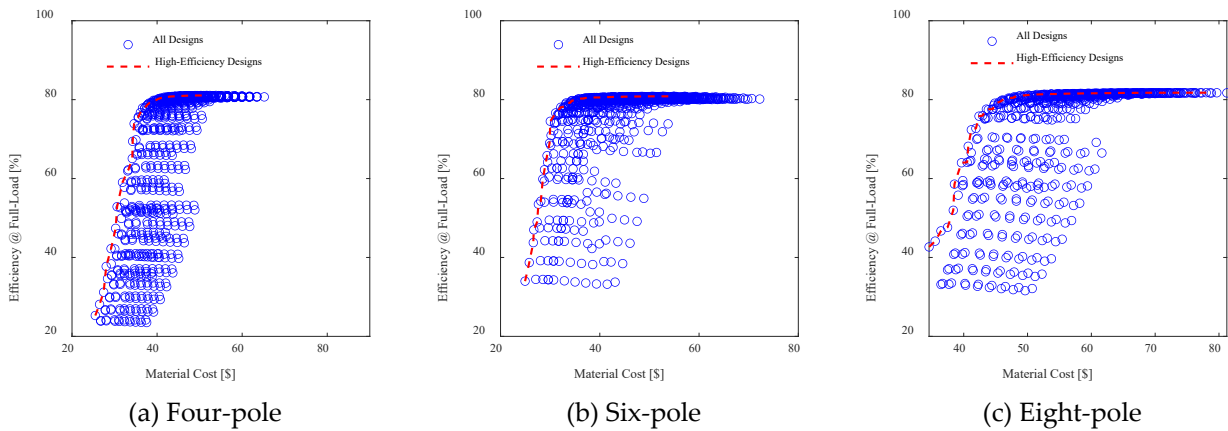
Figure 4–13 Efficiency versus material cost for 2.2kW AFIM designs with different pole numbers. Each plot shows all evaluated designs (blue symbols) and highlights the high-efficiency candidates (red lines).

(a) Four-pole   (b) Six-pole   (c) Eight-pole
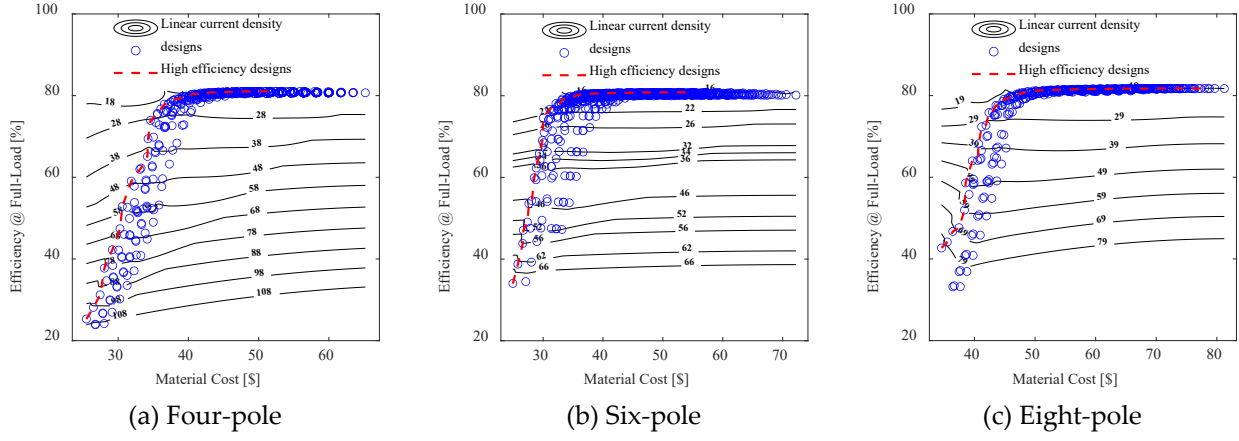
Figure 4-14 Efficiency versus material cost for various designs showing contours of linear current density in A/mm, with the ratio of rotor yoke length to stator yoke length ($l_{s,y}$: $l_{r,y}$) constrained within the range of 0.85 to 1.3.

The efficiency-cost trade-off under different pole numbers (four, six and eight poles) is illustrated in Figure 4-14, which includes contours of linear current density, and the red dashed curve highlights the high-efficiency solutions for a given cost. It is important to note that Figure 4-14 presents only the refined design subset, where overdesigned solutions, those exhibiting excessive material usage without proportional efficiency improvement, have been deliberately excluded. These results are obtained by varying the rotor-to-stator yoke length ratio ($l_{s,y}$: $l_{r,y}$) within the range of 0.85 to 1.30, while constraining the electromagnetic loading within the predefined limits presented in Table 4-2.

(a) Four-pole   (b) Six-pole   (c) Eight-pole
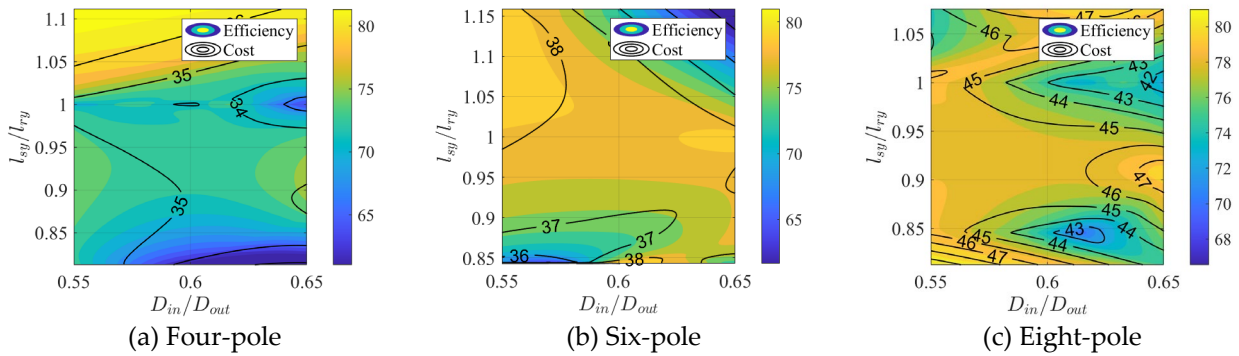
Figure 4-15 Superimposed efficiency and material cost contours versus the ratio of stator to rotor yoke and the diameter ratio of 2.2kW AFIM designs with different pole numbers, with the stator specific electric loading is constrained between 20 and 40 A/mm.

Figure 4-15 presents example design colour maps for the four, six, and eight pole AFIMs. It is noted that the look-up colour map restricts the inner-to-outer diameter ratios between 0.55 and 0.65, and specific electric loadings between 20 and 40 A/mm. These constraints highlight feasible regions of practical designs that exhibit efficient cost-performance trade-

offs. By utilising these colour maps, designers can better understand how varying parameters affect the electric loading and material cost.

4.2 FE Simulation Based Comparative Studies on RFIM and AFIM

Beyond establishing the design principles and methodologies of AFIMs, a comprehensive assessment requires systematic evaluation of their topological distinctions from RFIMs across three critical aspects: electromagnetic field behaviour, geometric sensitivity, and material economy. This section conducts a benchmark analysis of line-start AFIM and RFIM configurations to reveal characteristic advantages through quantified performance contrasts. While RFIM maintain industrial prevalence, their design optimisation ceiling is fundamentally constrained by inflexible structure and lower power density. These limits motivate the consideration of AFIMs as a power-density-enhanced alternative, necessitating systematic benchmarking through geometric equivalence transformations of commercial RFIM baselines. The comparative framework evaluates multiple performance metrics including the effects of rotor slot number, rotor/stator slot shapes, the dynamic responses, electromagnetic performance, and material cost.

4.2.1 Sensitivity of Electromagnetic Performance to Slot Shapes in AFIM and RFIM

Building upon the parametric definition of the AFIM geometries through the predefined electromagnetic loading parameters in Section 3.1, which established the influence of rotor and stator slot shapes on the AFIM performance, a comprehensive sensitivity analysis comparing the slot shape effects in AFIMs and RFIMs is presented below.

Figure 4-9 illustrates four sets of rotor and stator slot shape combinations. It is noted that the rotor slots for both the AFIM and RFIM case (a) and (d) are designed with an inverse-tear-drop shape and both case (b) and (c) have rectangular rotor slots. The area of the stator and rotor slots are kept as constant. FEA is employed to predict the performance characteristics of the benchmark RFIMs and the designed AFIMs. As mentioned, AFIMs require 3-D FEA to obtain accurate results due to the differences in the core lamination orientation. In contrasts, RFIMs can often achieve reasonable accuracy using 2-D FEA. Figure 4-16 presents the rotor and stator slot shape effects on the torque and current versus speed performance. Figure 4-17 compares the starting torque and current of different combinations. The rectangular and tear-drop stator/rotor slots provide parallel stator/rotor

teeth for the AFIM and RFIM designs, respectively. When applying different rotor/stator slot shapes to the AFIM and RFIM, the τ_{start} and I_{start} show inverse trends. From a starting current perspective, the largest differences are labelled, and the differences are 5.3% and 6.3% for the AFIM and RFIM respectively. On the other hand, the biggest differences are 12% and 7.0% for the AFIM and RFIM, respectively. It is concluded that the rotor and stator slot shape combination have a stronger effect on τ_{start} than I_{start}. Moreover, compared to the RFIM, the AFIM is more sensitive to the shape of stator and rotor slots from a starting torque perspective. Both the AFIM and RFIM with parallel rotor and stator teeth provide higher τ_{start} and I_{start}.

(a)   (b)
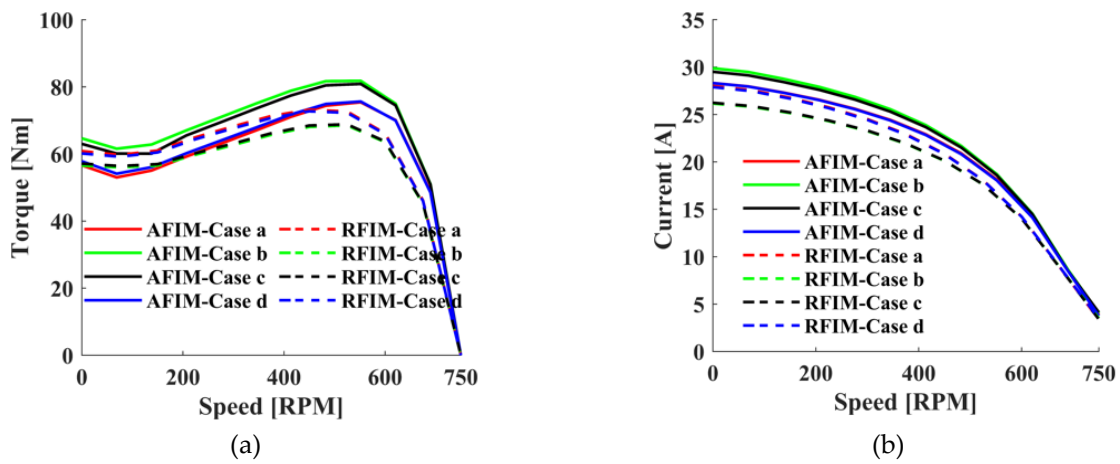
Figure 4-16 Eight-pole AFIM and RFIM performance predictions as a function of speed under different rotor/stator slot configuration cases. (a) torque vs. speed, (b) current vs. speed.

(a)   (b)
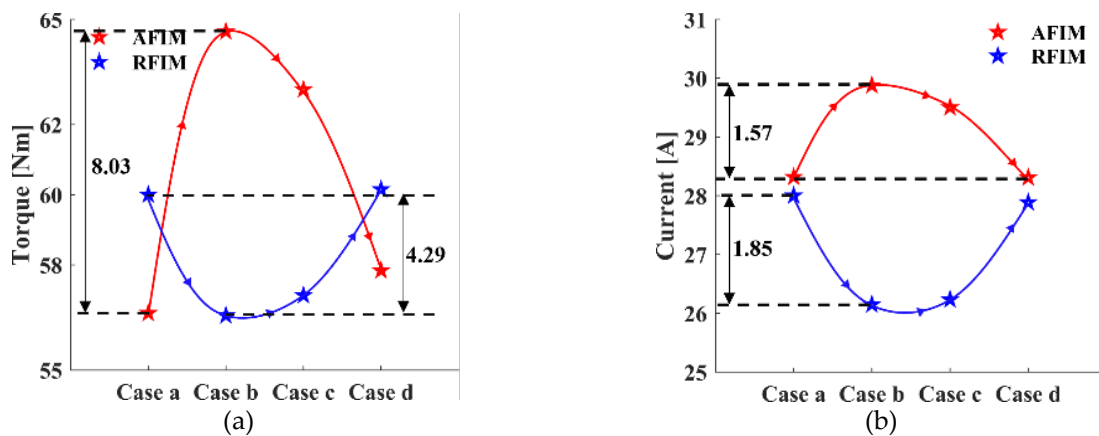
Figure 4-17 Effects of stator and rotor slot shape configurations on starting torque and current of the eight-pole AFIM and RFIM.
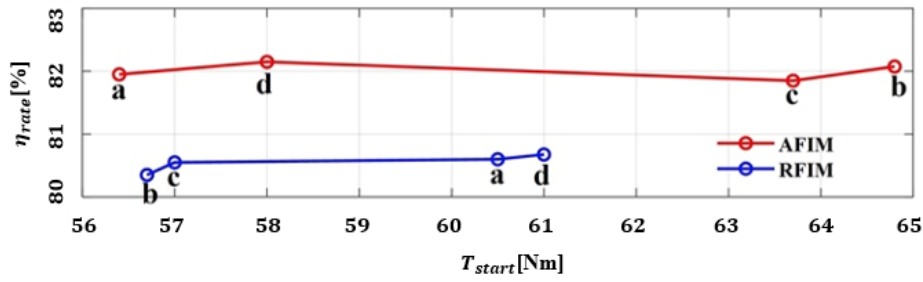
Figure 4-18 Rated efficiency versus starting torque, location of the four cases of both the AFIM and the RFIM.

The rated efficiency (η_{rate}) for both AFIM and RFIM cases (a)-(d) versus starting torque is given in Figure 4-18. From cases (a)-(d), in terms of τ_{start}, the AFIM shows higher sensitivity to the stator/rotor slot shape compared with the baseline RFIM. On the other hand, the η_{rate} for both AFIM and RFIM show only small changes. Moreover, the higher efficiency of the AFIM can be attributed to its shorter magnetic flux path and reduced leakage flux, which together reduce both copper and core losses compared with its equivalent RFIM.
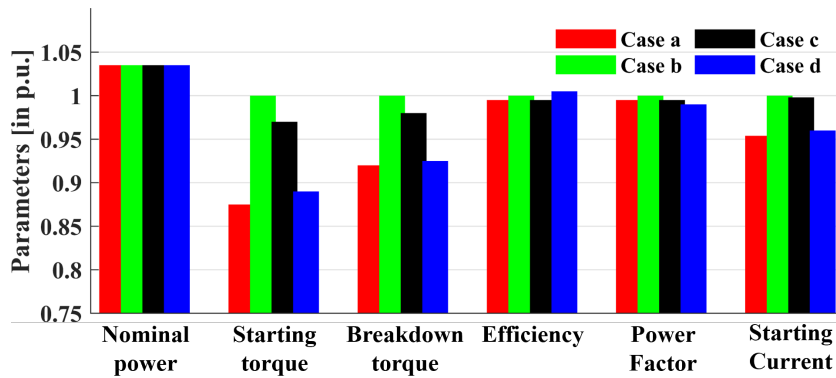
Figure 4-19 Electromagnetic performance for the AFIM with different cases with case b as the baseline.

Figure 4-19 shows the effects of slot shape on the four AFIM cases. The power factor and efficiency given here is under full-load operation and all values are per-unitised. The base value for nominal power is set at 2.0kW, and all other performance metrics are normalised with respect to case (b), which has rectangular rotor and stator slots. The full-load performance results indicate that the power, efficiency and power factor exhibit similar levels across the different cases. The rectangular rotor and stator slot configuration is selected for further analysis in later sections due to its better starting torque capabilities.

4.2.2 Sensitivity of Electromagnetic Performance to Number of Rotor Slots in AFIM and RFIM

The shape of the stator and rotor slots has now been confirmed. Next, the optimal choice for the number of rotor slots is studied. The effect of this on the electromagnetic torque production, torque ripple, rotor losses and efficiency are investigated. A lower number of rotor slots produces higher losses and lower airgap torque variation. So, the trade-off between electromagnetic noise and efficiency depends on the design purpose.
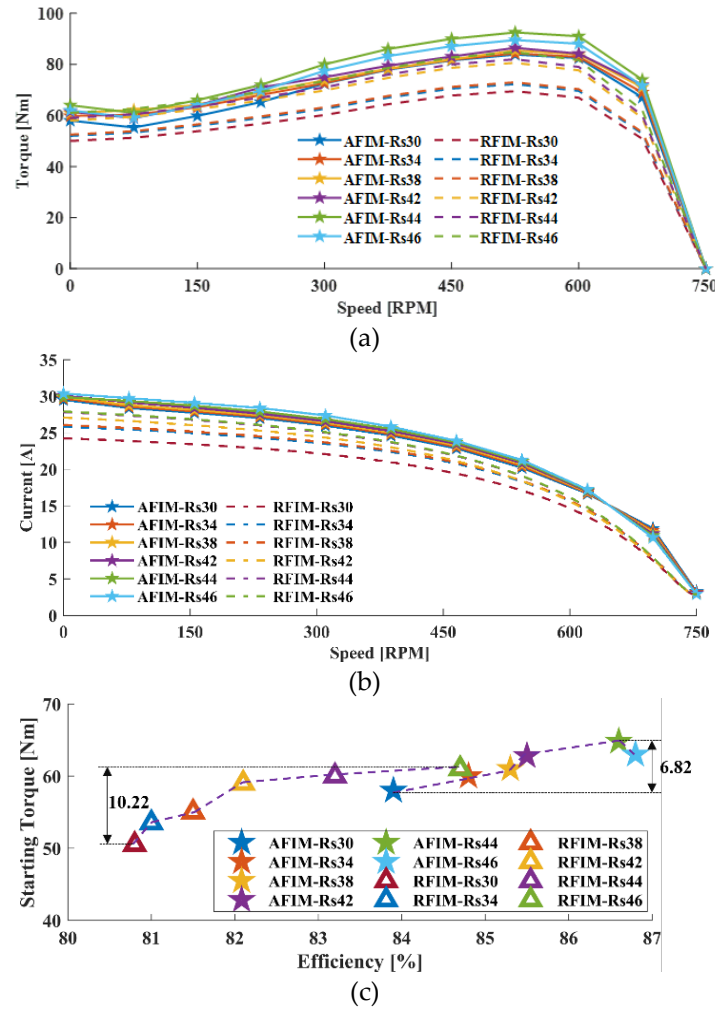
Figure 4-20 Effect of different numbers of rotor slots for the eight-pole AFIM and RFIM as a function of speed. (a) Torque versus speed. (b) Current versus speed. (c) Starting torque versus full load efficiency.

The effect of the rotor slot number on the eight-pole RFIM and AFIM was studied. The number of stator slots is kept as 48 with the rotor slot number varying from 30 to 46. With the changes in the rotor slot number, the rotor slot width is changed to keep the total slot area and hence the rotor resistance as a constant. The effect of rotor slot number on the stator current and electromagnetic torque versus speed of the machine for the AFIM and RFIM are presented in Figure 4-20s (a) and (b), respectively. The number of rotor slots has a more significant effect on the current and torque in the RFIM compared to the AFIM. Figure 4-20(c) shows the trade-off between the starting torque τ_{start} versus the rated efficiency η_{rate} for

the six AFIM and six RFIM designs. The η_{rate} for both motor types increase with the ratio of the number of rotor and stator slots ($N_{r,s}/N_{s,s}$) and the AFIM has a higher η_{rate} than RFIM for the same ratio of N_{rs}/N_{ss}. In terms of τ_{start}, the rotor slot number has a stronger effect on the RFIM than the AFIM.
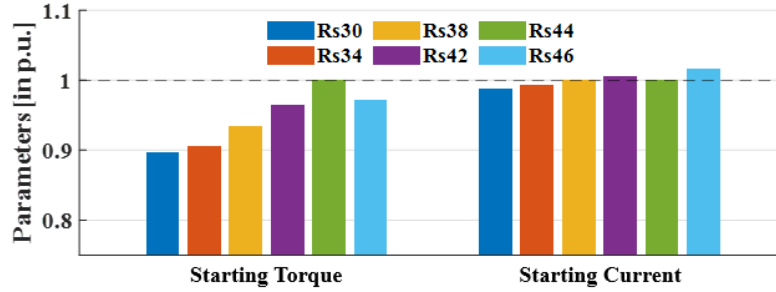
Figure 4-21 Eight-pole AFIM starting torque current in p.u. with different numbers of rotor slots.

Figure 4-21 presents the relationship between the starting torque τ_{start} and starting current I_{start}, for different numbers of rotor slots for the eight-pole AFIM. A critical observation from the data is the sensitivity of τ_{start} to variations in the rotor slot number, this contrasts with the relatively modest response of I_{start} to the same parameter. This is because the I_{start} is primarily governed by the supply voltage and the equivalent impedance of the stator circuit and so is less affected by the interaction of the slot harmonics. As the commercial eight-pole RFIM with 44 rotor slots specifications indicates, the τ_{start} is around two times of the rated torque and its design effectively balances the trade-off between leakage reactance and rotor resistance. Moreover, this configuration exhibits the third highest I_{start}, showing the compromise between the starting torque and the current limitation imposed by the electromagnetic design constraints.
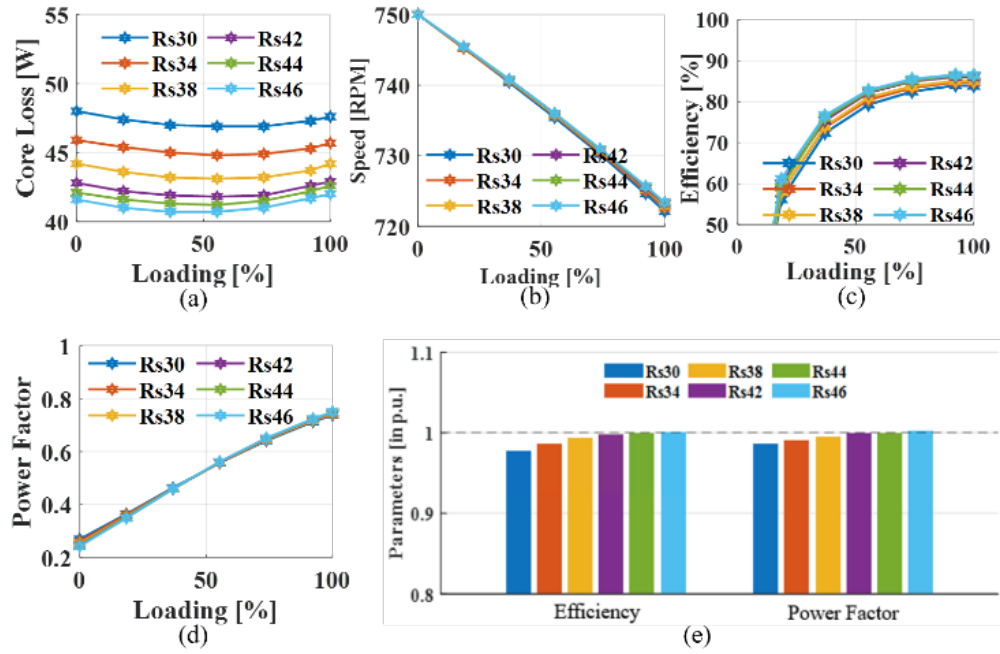
Figure 4-22 Comparison of the AFIM performance with different numbers of rotor slots as a function of load: (a) core loss, (b) speed, (c) efficiency, (d) power factor, (e) efficiency and power factor at full load in per unit.

Figure 4-22 evaluates the loading performance of the AFIM across varying rotor slot numbers, showing the differences in core loss, rated speed, and efficiency. The inverse relationship between core loss and rotor slot count stems from the redistribution of magnetic flux density across a greater number of slots (see Figure 4-22(a)). Figure 4-22(b) indicates a minimal influence of the rotor slot number on the rated speed. The efficiency in Figure 4-22(c) marginally increases with higher number of rotor slots. The power factor (Figure 4-22(d)) remains unaffected by the rotor slot number, due to its dependence on the stator-side impedance and the magnetizing characteristic. At full load, the normalised perfomracne indices (Figure 4-22(e)) shows that the AFIM with 44 rotor slots offers a balanced compromise between efficiency and power factor. Given these reasons, alongside prior observations regarding the starting behaviour shown in Figure 4-21, the 44 rotor slots configuration was selected for further study.

4.2.3 Steady-State Electromagnetic Performance Comparisons and Analysis

The steady-state electromagnetic performance of electric motors is a critical factor in determining its efficiency, torque, and operational behaviour. It is typically evaluated through FEA simulation or experimental testing. This section presents a comparative

analysis of the steady-state performance parameters of AFIMs and RFIMs via FEA simulations. The key parameters consist of torque, current, efficiency, and power factor.

(a)   (b)
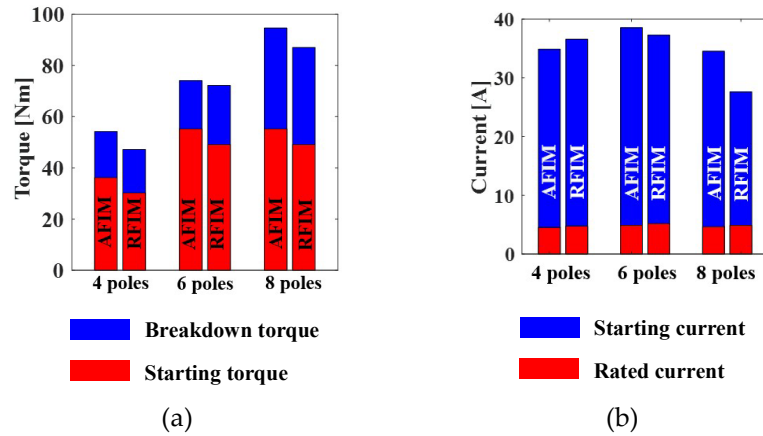
Figure 4-23 Comparison of electromagnetic performance for AFIMs and RFIMs with different number of poles. (a) Torque characteristics: starting torque (red) and breakdown torque (blue). (b) Current characteristics: rated current (red) and starting current (blue).

Figure 4-23 compares the steady-state electromagnetic performance of AFIMs and RFIMs for different number of poles. The AFIMs consistently produce higher starting torque than the RFIMs across all pole numbers, with both motor types presenting an increase in starting torque as the pole number rises (See Figure 4-23(a)). Both RFIMs and AFIMs have comparable rated currents, the four-pole RFIM has a high starting torque while the six and eight pole AFIMs show higher starting current (see Figure 4-23(b)). This behaviour arises from the interdependence between pole number, torque demand, and flux distribution. At a fixed power rating, increasing the pole number reduces the synchronous, which in turn necessitates a higher torque output Figure 4-24 shows the torque-speed and current-speed characteristics of the AFIMs and RFIMs for different number of poles. These figures collectively show the AFIM's potential as a high-performance alternative to conventional RFIMs in applications demanding compactness. However, these findings must be contextualised within the inherent limitations of simulation-based studies, which abstract away critical real-world mechanical and manufacturing uncertainties, such as stator-rotor alignment challenges for such a large diameter disc-shape motor, surface finish and manufacturing variability, structural integrity uncertainties and unquantified mechanical losses.
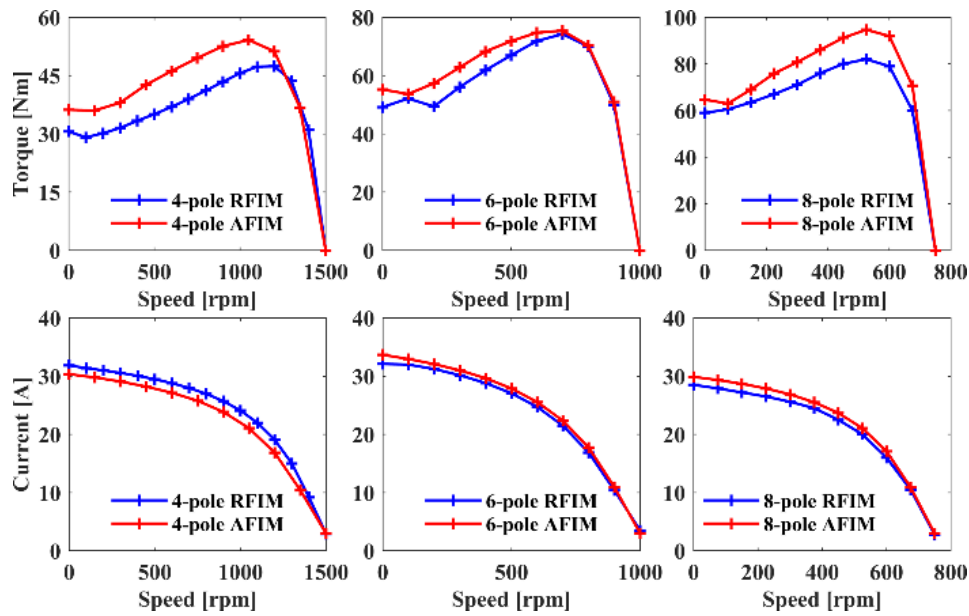
Figure 4-24 Comparison of torque and current versus speed for AFIMs and RFIMs with different number of poles.

It is noted that both RFIMs and AFIMs have no mechanical losses considered at this stage. Table 4-6 presents a comparison of rated power factor and efficiency from FEA at 50%, 75%, and 100% of loading. The efficiency differences between the four and six pole AFIM and RFIM designs are small, but the eight-pole AFIM design shows slightly higher full-load efficiency, particularly at full load.

Table 4-6 Summary of efficiency and power-factor for the studied motors.

Output	Type	Poles	Efficiency			Power Factor		
kW		#	50% load	75% load	100% load	50% load	75% load	100% load
2.2	AFIM	4	81.8	82.1	81.6	0.59	0.71	0.78
	RFIM		81.4	82.3	81.1	0.61	0.72	0.81
	AFIM	6	82.3	82.7	82.6	0.61	0.70	0.79
	RFIM		82.5	82.4	82.4	0.57	0.71	0.80
	AFIM	8	82.7	83.1	83.4	0.59	0.69	0.81
	RFIM		82.4	82.3	82.1	0.61	0.72	0.82

Figure 4-25 compares the efficiency of the designed AFIMs with the commercial RFIMs for the different number of poles (4-pole, 6-pole, and 8-pole) against the international efficiency standards (IE1-IE4) [60-62]. It highlights that the designed AFIMs achieve higher efficiency levels than the RFIMs, especially, the 8-pole AFIM shows significant improvements in efficiency compared to its RFIM baseline (moving from IE2 to IE3).
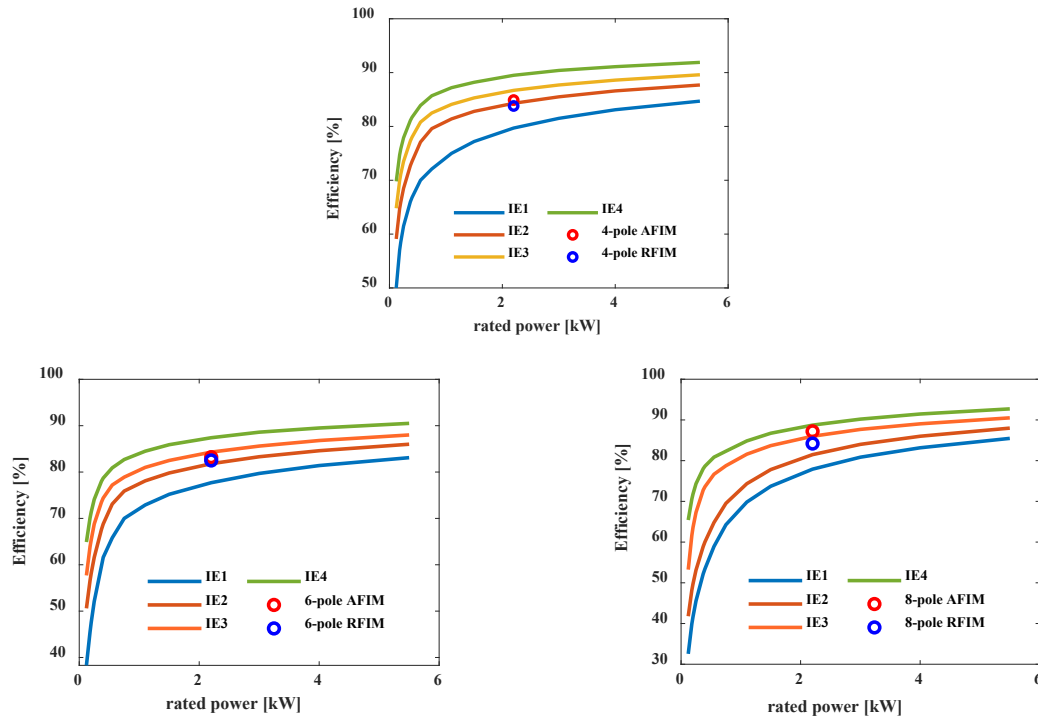
Figure 4-25 Designed AFIMs and commercial RFIMs compared with efficiency standards (IEC60034-30).
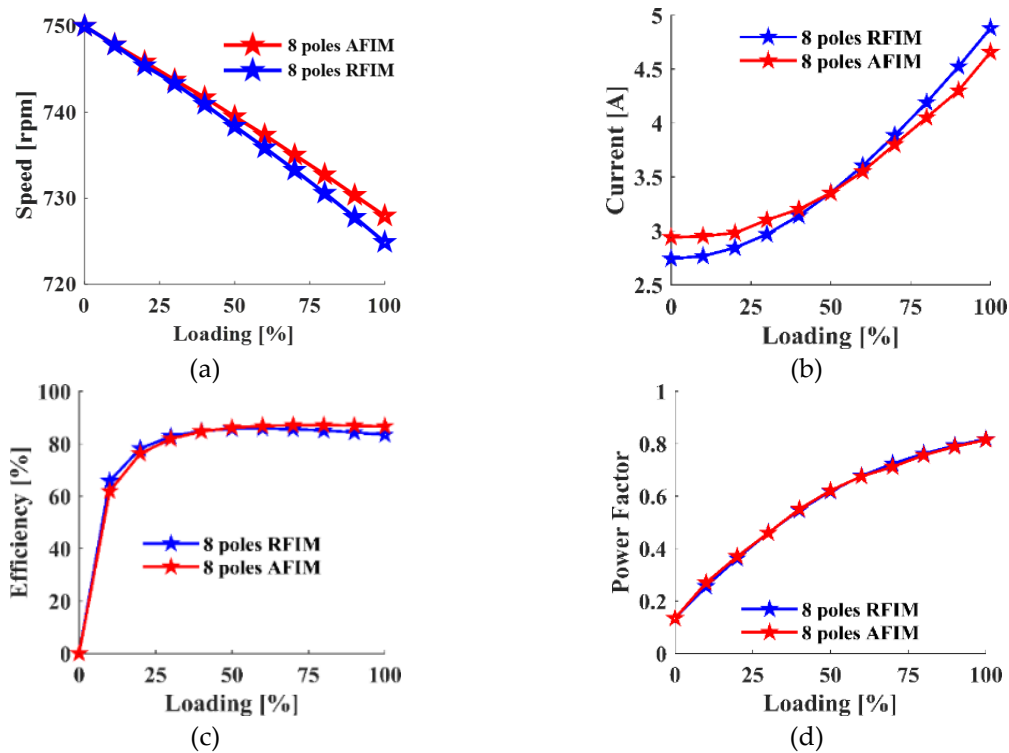
Figure 4-26 Comparison of the predicted eight-pole AFIM and RFIM performance parameters under varying loading conditions. (a) speed, (b) current, (c) efficiency, (d) power factor.

(a)   (b)
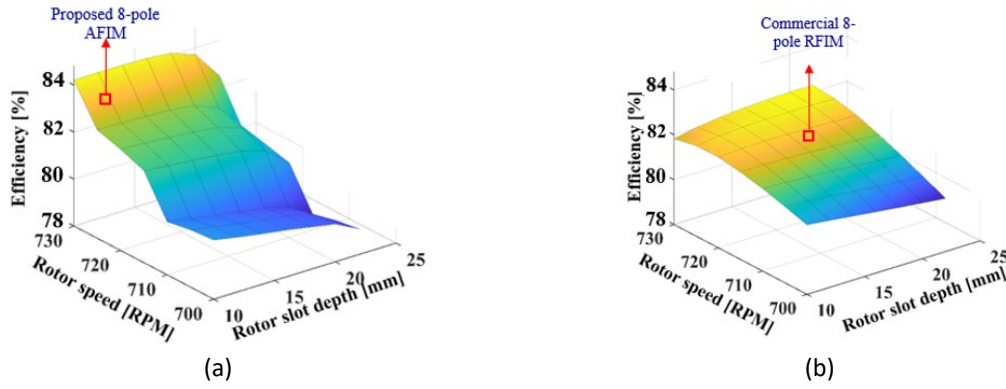
Figure 4-27 Effects of rotor slot depth on the efficiency and rated speed.
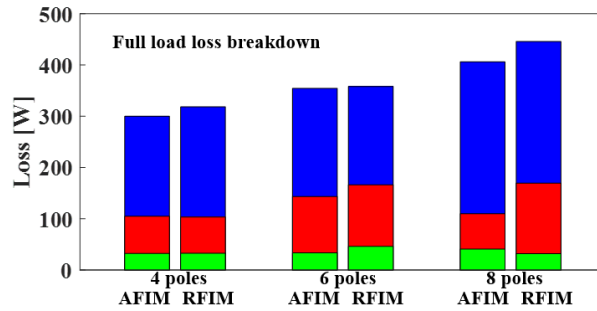
Figure 4-28 Full-load loss breakdown for four, six, and eight-pole AFIM and RFIM designs. Stator winding loss (blue), rotor bar loss (red) and core loss (green).

Figure 4-26 shows the eight-pole AFIM and RFIM machine speed, current, efficiency and power-factor under different loading conditions. The RFIM has a slightly higher full-load slip (3.6%) compared to the AFIM (2.9%). The AFIM has a slightly higher no-load current but a lower full-load current. The AFIM has higher efficiency above about 40% load and both machines reach their maximum efficiency around 75% load.

Figure 4-27 explores the effect of rotor slot depth and compares the efficiency performance of the eight-pole RFIM with its AFIM version across varying rotor speeds and rotor slot depths. Both motors present a decrease in efficiency while increasing the rotor slot depth. In addition, the efficiency of the AFIM is more sensitive to the rotor slot depth.

In Figure 4-28, the major loss components under full load operation are given including stator winding loss (P_{cu}), rotor bar loss (P_{bar}) and core loss (P_{core}). The stator winding loss is the largest portion followed by the rotor bar loss. At higher numbers of poles, the AFIM designs have lower rotor copper loss which produces a lower total loss compared to the corresponding RFIM design.

4.2.4 Comparison of Dynamic Response Between AFIM and RFIM
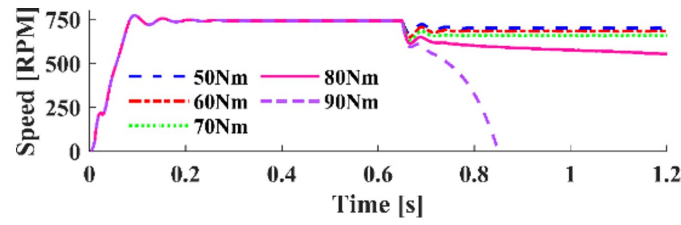
(a) Eight-pole RFIM with step loadings.
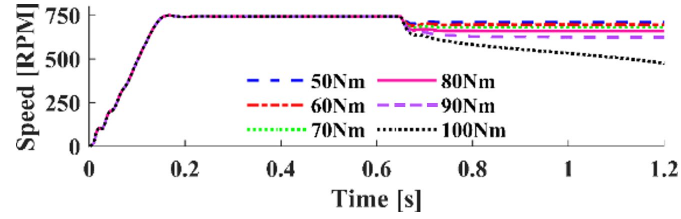
(b) Eight-pole AFIM with step loadings.
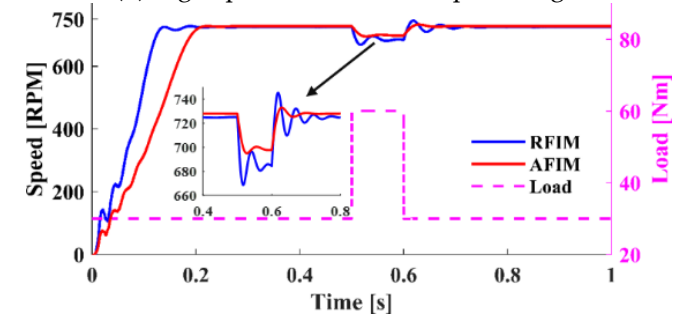
(c) Eight-pole AFIM and RFIM response to pulse loadings.
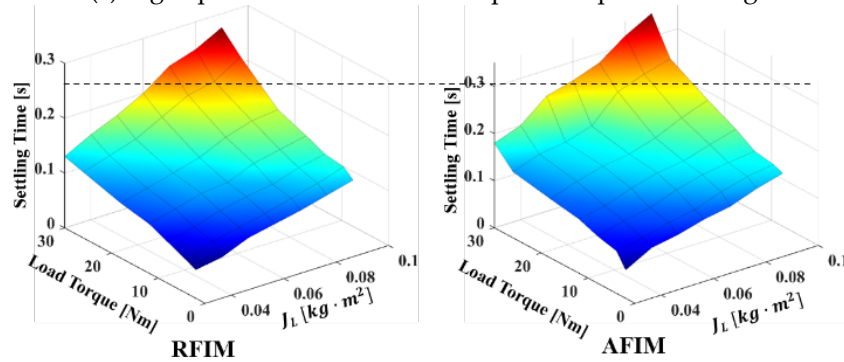
(d) Eight-pole AFIM and RFIM settling time with different loadings and load inertias.

Figure 4-29 Eight-pole AFIM and RFIM dynamic response to different loads.

Figure 4-29(a) and (b) depict the speed response of the RFIM and AFIM whilst being subject to different step loads from 50Nm to 100Nm in 10Nm steps. The RFIM can stably operate up to 70Nm while the AFIM can operate up to 90Nm. The analysis of the speed response under a rapid change in loading is shown in Figure 4-29(c). A pulse load is added at 0.5s to 0.6s where the load increases to 60Nm. It is observed that the RFIM has larger amplitude speed transients compared to the AFIM (see zoomed-in plot). The surface plot shows that both load inertia and load torque affect the settling time. Since the AFIM has larger inertia, the AFIM takes longer to approach the steady state (see. Figure 4-29 (d)).

Figure 4-29(d) illustrates the rise and settling times of the two motor topologies during no-load and full-load conditions. The rise time is defined as the time taken to increase from

10% of the final value to 90% of the final value, where the final value is the steady state speed. The settling time is the time taken to reach within a 2% tolerance of the final value. It is observed that, RFIMs significantly outperformed the AFIMs due to the in lower rotating inertia compared to the RFIMs.

4.2.5 Comparison of Material Weight/Cost Between AFIMs and RFIMs

The eight-pole AFIM has a power density of around 92W/kg which is higher than the equivalent RFIM (about 81W/kg). The weight of the electromagnetic materials used to estimate the cost of the AFIM and RFIM designs (see Figure 4-30). The weights are per-unitised versus the six-pole AFIM total material weight. With the increase of the number of poles, the material weight for both the AFIM and RFIM designs are increased. The stator and rotor core material weight are the largest portion followed by the stator winding weight while the rotor bars contribute the smallest share. The stator winding weight for the AFIM is always lower than the corresponding RFIM. The AFIM designs have reduced total weight and material cost for higher pole numbers.

(a)

(b)
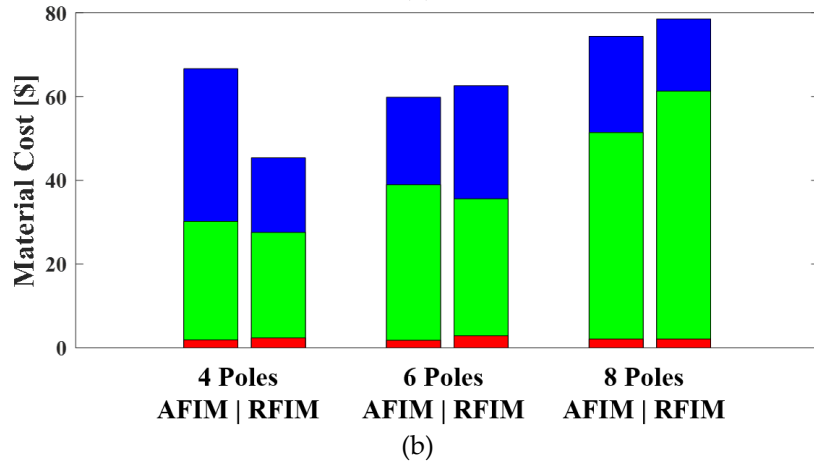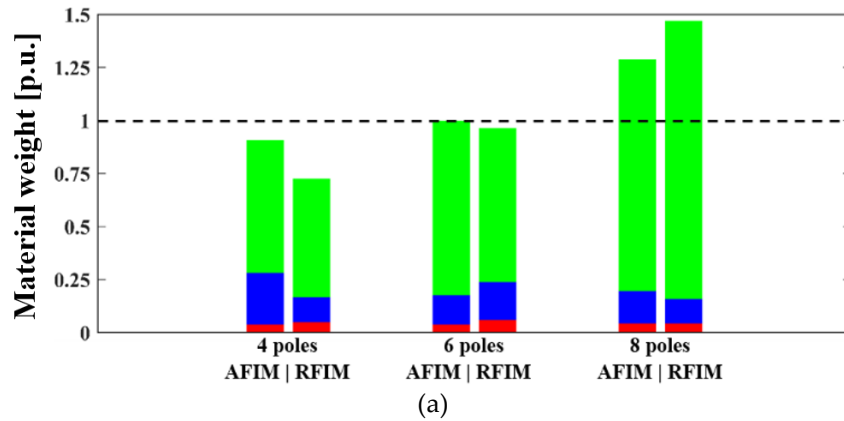
Figure 4-30 (a) Material weight and (b) material cost ($USD) for the RFIMs and AFIMs with different number of poles (Green=Iron core, Blue=copper winding, Red=aluminium bar).
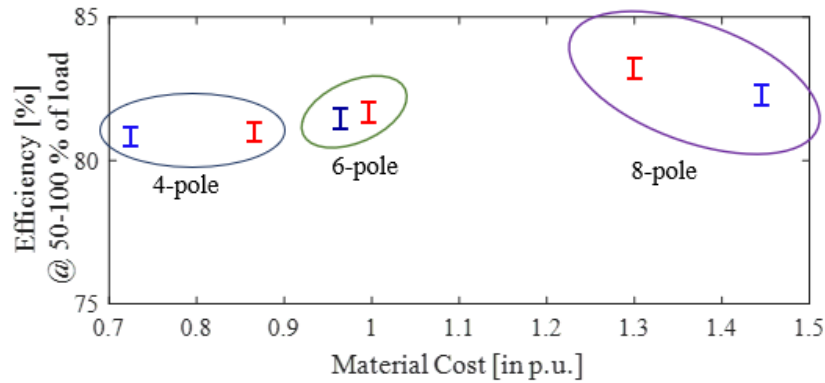
Figure 4-31 Efficiency at 50-100% of load versus material cost, showing the locations of the AFIM (red) and RFIM (blue) designs.

Figure 4-31 illustrates the variation of efficiency and the material cost for the AFIM and RFIM designs. The following cost figures were used: iron core 2.56 USD/kg, aluminium bar 3.1 USD/kg, 7.5 USD/kg. It is shown that the four-pole AFIM has higher efficiency than the RFIM, but the material cost increases over 20%. The six-pole AFIM and RFIM have similar material cost and efficiency. The greatest improvement in cost and efficiency is seen for the eight-pole AFIM design. Therefore, AFIMs with higher number of poles can significantly outperform their equivalent RFIMs in terms of material cost and efficiency.

In this section, a comprehensive comparative study on four-pole, six-pole and eight-pole line-start AFIMs and RFIMs provided guidelines and recommendations on converting RFIMs to AFIMs. The sizing equations and design values from the RFIMs were applied for the AFIM geometry design. A sensitivity study on the number of rotor slots showed that the AFIM design is less sensitive to this parameter compared to the RFIM. The dynamic responses showed that the AFIM has longer settling time (due to higher rotor inertia) but higher torque capability than the RFIM. The electromagnetic performance and material cost comparisons show that at higher pole numbers, AFIMs can provide higher power density and higher efficiency. The eight-pole AFIM showed a 10% material cost decrease and a 2% increase in efficiency.

CHAPTER 5

SIMULATION AND EXPERIMENTAL ANALYSIS OF AXIAL FORCE IN SINGLE-SIDED AFIMS

One of the key challenges in the design and construction of the single-sided axial-flux induction motors (AFIMs) is the axial force acting between the stator and rotor. This force increases steeply as the airgap decreases, exhibiting characteristics of negative stiffness (see Figure 5-1). Our first 300W single-sided AFIM prototype failed due to high unbalanced axial forces between the rotor and stator. To address this issue, it is essential to understand the nature of axial force and establish a clear relationship between the airgap length and the resulting force. This chapter presents both experimental and simulation-based investigations to quantify and analyse the axial force behaviour.
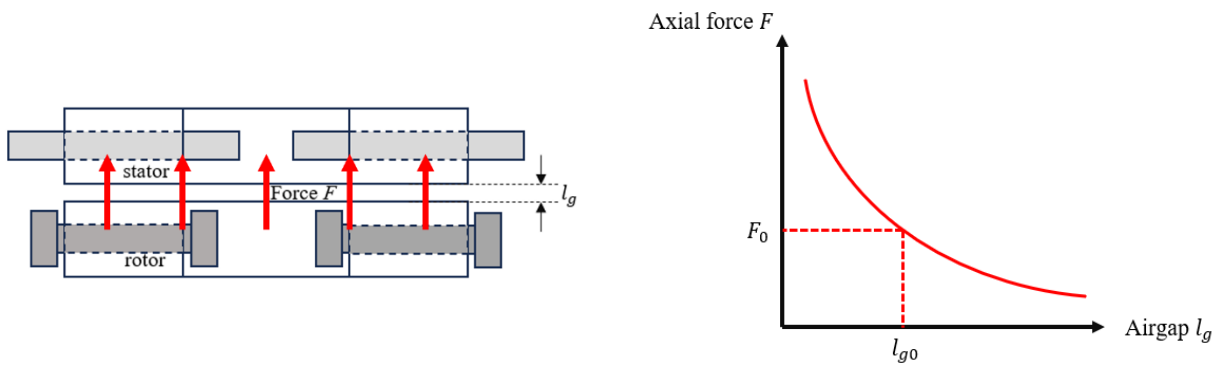
Figure 5-1 Axial force in AFIM (left) and force versus the airgap length curve (right) [45, 64].

Compared to the single-sided AFIMs, the negative stiffness of an AFPM is generally lower due to their inherently larger effective airgap length. However, the strong magnetic attraction from the permanent magnets poses significant challenges during assembly. Unlike AFIMs, AFPMs often require special equipment to prevent rotor-stator contact and ensure safe installation [43-45, 64]. While the discussion so far has primarily explained the variations in the axial force with respect to the airgap length, it is also important to consider the effect of the excitation method, whether current or voltage driven. The current-driven excitation refers to an inverter-fed system, where the current is controlled by a power electronic converter allowing for the precise control over motor operation. Voltage-driven refers to the line-start operation, where the motor is directly connected to the AC mains

power supply without control. These two methods have different the axial force behaviour with variations of the airgap length.
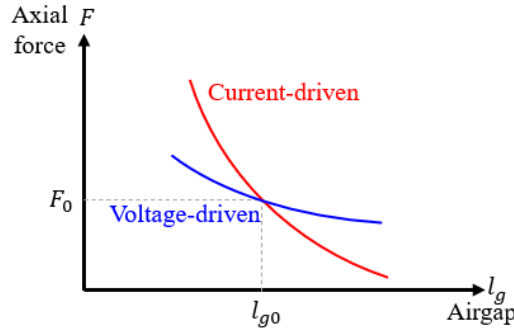
Figure 5-2 A conceptual comparison of axial force variations in voltage driven and current driven AFIM under different airgaps.
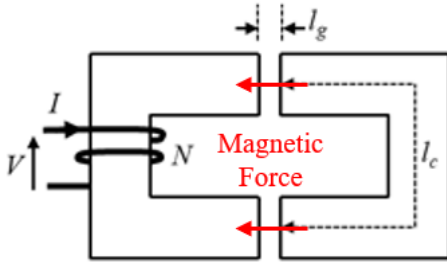
	Ideal behaviour with decreasing airgap length	
	Current driven	Voltage driven
Reluctance	Decrease	Decrease
Flux	Increase	$\approx$ Constant
Current	Constant	Decrease
Force	Increase	$\approx$ Constant

(a)   (b)

Figure 5-3 (a) Electrically excited motor C-core configuration [45, 64]. (b) C-core pull-in behaviour under DC (current-driven) and AC (voltage-driven) excitation.

In the current-driven operation, the excitation current remains constant, regardless of airgap length variations. As the airgap length increases, the reluctance ($\mathcal{R}$) of the magnetic circuit rises leading a drop in the inductance (L) and consequently a reduction in the flux linkage and the axial force. In contrast, under the voltage-driven operation when the airgap increases, the AFIM naturally draws more magnetizing current (I_m) to compensate for the rising magnetic reluctance and to maintain the magnetic coupling between the stator and rotor. However, this compensation is not perfect, as it is limited by the core saturation, copper losses and increased leakage flux. As a result, the flux density still tends to decrease, leading to a reduction in the axial force but with a smaller negative axial stiffness than for current-driven operation (see Figure 5-2).

Figure 5-3 presents a magnetic circuit with a coil wound around a section of a core. The C-core can be used as a simplified model for analysing the relationship between axial force and airgap length in the AFIM under voltage or current excitation. The stored magnetic energy in airgap $W(l_g)$ is used to derive the magnetic force (F) as follows,

$$W(l_g) = \frac{1}{2} \frac{[B_\delta(l_g)]^2}{\mu_0} V \tag{5.1a}$$

$$B_\delta(l_g) = \frac{\mu_0 N_{ph} I_{ph}}{l_g} \tag{5.1b}$$

$$V = \pi(R_{out}^2 - R_{in}^2) l_g \tag{5.1c}$$

the symbol μ_0 is the permeability of free space. The term $B_\delta(l_g)$ denotes the airgap flux density as a function of the length of airgap. The term V is the airgap volume. N_{ph} and I_{ph} represent the number of turns per phase and phase current. In terms of the AFIM, R_{out} and R_{in} are the outer and inner radii.

The magnetic energy stored in the airgap as a function of airgap length is given by the following equations and the axial force can be obtained by differentiating the magnetic energy $W(l_g)$ with respect to the airgap length l_g.

$$W(l_g) = \frac{1}{2} \frac{\mu_0 N_{ph}^2 I^2}{l_g} \pi(R_{out}^2 - R_{in}^2) l_g \tag{5.2a}$$

$$F(l_g) = -\frac{d}{dl_g} \left[\frac{1}{2} \frac{\mu_0 N_{ph}^2 I^2}{l_g} \pi(R_{out}^2 - R_{in}^2) l_g \right] \tag{5.2b}$$

$$F(l_g) = \frac{1}{2} \frac{\mu_0 N_{ph}^2 I^2}{l_g^2} \pi(R_{out}^2 - R_{in}^2) = \frac{1}{2} \frac{[B_\delta(l_g)]^2}{\mu_0} \pi(R_{out}^2 - R_{in}^2) \alpha_s \alpha_r \tag{5.2c}$$

the stator tooth ratio α_s is the ratio of the total area of the stator teeth at the airgap to the airgap area. In this work, the rotor tooth ratio α_r is unity due to the closed rotor slots [45, 64, 86].

Since the axial force $F(l_g)$ is a function of the airgap flux density squared, it can be estimated using the simplified no-load equivalent circuit of the IM for further analysis. The airgap flux density B_δ is linked to the induced back-EMF E, which is determined by the terminal voltage V through a voltage divider consisting of the stator leakage inductance L_{sl} and the magnetising inductance L_m [45, 64].

$$E = V \frac{j\omega_e L_m}{j\omega_e(L_{sl} + L_m)} = V \frac{1}{(L_{sl}/L_m) + 1} \tag{5.3}$$

where ω_e is the electrical angular frequency. Based on (5.3), the ratio of the airgap flux density with the airgap l_g to the nominal airgap flux density $B_{\delta 0}$ corresponding to a nominal airgap l_{g0} can be derived as follows,

$$\frac{E(l_g)}{E(l_{g0})} = \frac{B(l_g)}{B(l_{g0})} = V\frac{(L_{sl}/L_{mg0}) + 1}{(L_{sl}/L_m(l_g)) + 1} \tag{5.4}$$

Equation (5.4) expresses the dependency of the airgap flux density on the airgap length, under the assumption of linear magnetic conditions, where the stator leakage inductance L_{sl} remains a constant and is not influenced by the change of the airgap. Here, the magnetising inductance is evaluated at the different airgap lengths and is denoted as the $L_m(l_g)$ and L_{mg0}, respectively. The latter term is the magnetising inductance at nominal airgap (0.5mm).

5.1   Simulation Basis for Axial Force Measurement

The development of the magnetic force measurement allows researchers to guide the mechanical design and bearing selection of AFMs. The axial force between the rotor and stator in the FEA package used, ANSYS Maxwell can be defined by the following equations.

$$F_{z-axis} = \oiint f_{z-axis}dA \tag{5.5a}$$

$$F_{z-axis} = \oiiint f_{z-axis}dV \tag{5.5b}$$

$$F_{z-axis} = \frac{1}{2\mu_0}\oiint B_{z-axis}{}^2 dA \tag{5.5c}$$

where F_{z-axis} denotes the total axial force, f_{z-axis} is the axial force density, B_{z-axis} is the normal component of the flux density along the axial direction, and μ_0 is the permeability of free space.

The ANSYS Maxwell has two embedded functions: the volume force density and surface force density. Therefore, the airgap force can be determined by integrating the force density over the surface or volume ((5.5a) and (5.5b)). In addition, it is also possible to directly use the force definition (5.5c) and directly compute the axial force using the flux density.
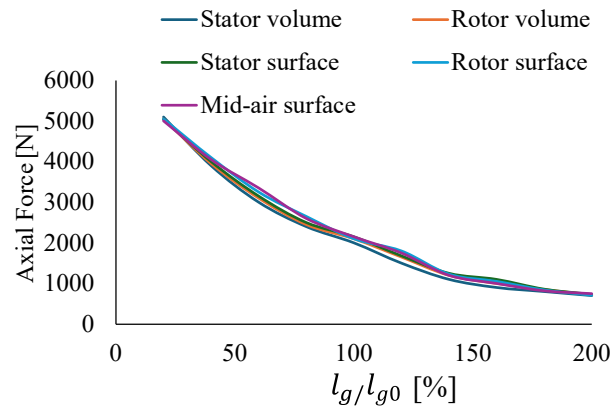
Figure 5-4 The calculated axial force versus airgap using different methods in ANSYS.
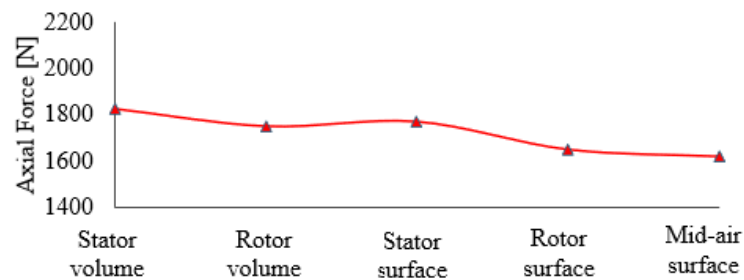
Figure 5-5 The calculated axial force at nominal airgap length at different locations in the model.

Table 5-1 Design specifications of the 300W axial-flux induction motor used for axial force analysis.

Design Parameters		
Dimensions [mm]		
Outer diameter	D_{out}	151.5
Inner diameter	D_{in}	85
Stack length: stator/rotor	L_s/L_r	48/25
Slot depth: stator/rotor	$L_{s,s}/L_{r,s}$	36/12
Airgap length	l_g	0.5
Rating		
Rated voltage [V]	V_r	415
Rated current [A]	I_r	4
Rated power [W]	R	372
Rated speed [RPM]	n_r	730
Rated torque [Nm]	τ_r	5
Winding		
Number of poles	p	8
Number of slots: stator/rotor	N_{ss}/N_{rs}	24/18
Conductor material: stator/rotor	-	Copper/Aluminium
Number of turns per phase	-	816

Figure 5-4 shows the 3-D simulated results of the AFIM axial force under the no-load steady-state conditions, showing the effect of varying airgap lengths, ranging from 0.05mm

to 1mm at the rated line voltage of 415V. The axial forces are extracted from multiple regions within the motor, including the stator and rotor volumes, stator and rotor surfaces, and the mid-airgap surface. Minor discrepancies between regions are attributed to numerical approximations or mesh settings. Figure 5-5 shows the nominal airgap axial force obtained from the different locations. Overall, the axial forces across the different regions are consistent and considered acceptable for the further analysis. The results in the rest of this chapter are obtained using the mid-air surface. In addition, if the calculated axial force values are used for the bearing selection or mechanical design, the maximum value should be taken.
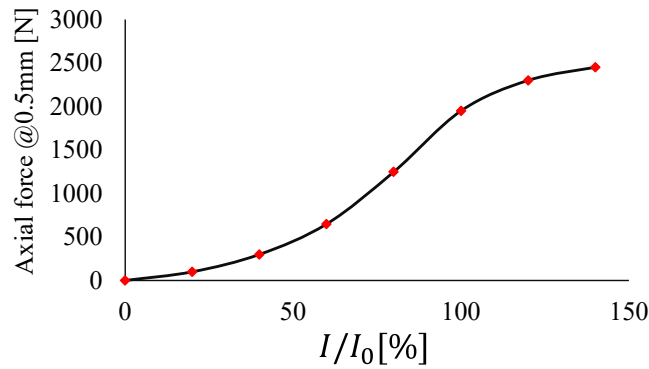
Figure 5-6 Current-driven AFIM: average axial force obtained from five components versus current for nominal airgap length.

Figure 5-6 shows the AFIM axial force versus current results at the nominal airgap length of 0.5mm. It is observed that the axial force is initially proportional to the current squared ($F \propto I^2$) and this relationship continues until magnetic saturation occurs, at which point the force becomes flat ($> I_{rate}$).
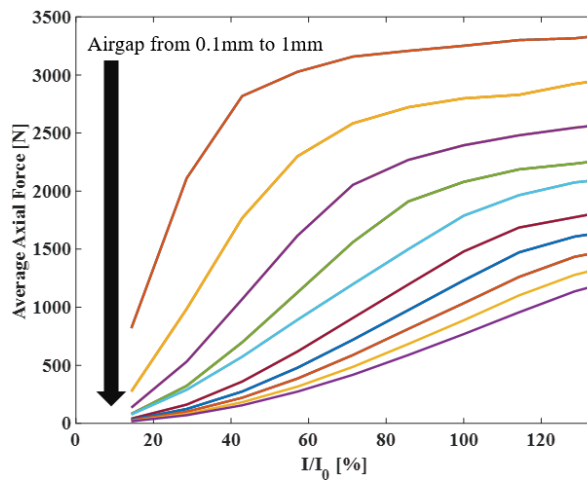
Figure 5-7 Current-driven AFIM: axial force versus current for different airgap lengths.

The peak of the no-load current of the target 300W AFIM (see Table 5-1) with 0.5mm is 3.20A. The variation of the force versus current with airgap length as parameter was obtained from the FEA is plotted in the Figure 5-7. This figure shows the high level of saturation with smaller airgaps. The rate of the variation of the axial force by the current increase reduces with the increase of the airgap length. This is mainly because of the increase of the reluctance and the flux density drop in the airgap.
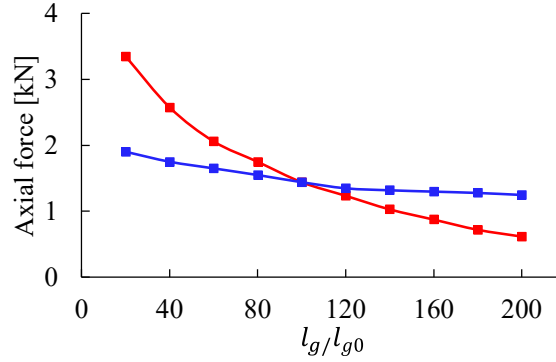
Figure 5-8 Axial force versus airgap ratio: 3-D FEA results under current (4A, red curve) and voltage (415V, blue curve) driven cases.

Figure 5-8 shows the axial force variations under the different airgap ratios for the voltage and current driven cases. For the current-driven case (red curve), the axial force decreases significantly as the airgap ratio increases. This indicates that under the current-driven case, the axial force is highly sensitive to airgap changes and thus has higher negative stiffness. In contrast, in the voltage-driven case (blue curve), the axial force remains relatively stable across varying airgap ratios, showing a slight decline, and hence has smaller negative stiffness. Both cases validate the previously discussed electromagnetic theory and shows a comparison of axial force variations in voltage-driven and current-driven AFIM under different airgaps.

Moreover, the common types of bearings such as ball and roller bearings, have limitations in withstanding high axial loads. As a result, an angular contact ball bearing is preferred. The 70 series single-row angular contact ball bearings, available with different contact angles, are designed for varying rotating speeds and high axial loads. For instance, bearing series 7000 with a 15° contact angle can support dynamic loads of 5.1kN and static loads of 2.6kN. To choose the best option, the diameter of the bearing should be carefully determined based on the shaft size and noting that larger bearing generally have large mechanical losses.

5.2   AFIM Axial Force Experiments and Results

As shown in the last section, the axial force varies with the changes in the airgap length. However, in 3-D FEA, the axial force is calculated using the flux density, which is challenging to replicate in experiments. While direct measurement of flux density is possible, such as using the hall effect sensors, search coils, and magneto-optical sensors, applying these instruments during testing not only increases the cost but, more importantly, presents a significant challenge for small airgaps. Consequently, developing a low-cost, straightforward, and practical approach is essential for measuring the axial force in the AFIMs.
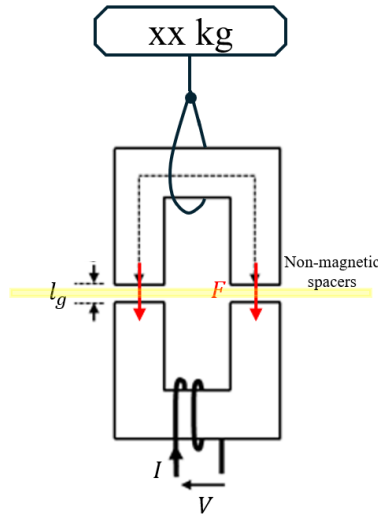
Figure 5-9 A simplified schematic diagram of a force measurement setup.

Figure 5-9 shows an example setup used for measuring the axial force for the C-core, a similar setup is applied to the target AFIM. The wound C-core is fixed in position during the test. Non-magnetic spacers of known thickness are placed on top of it. The unwound C-core is lowered on to the stator until it contacts the spacer. Then, the unwound C-core is then raised to apply an upward force to separate it from the wound C-core. The weight (force) for separation with the unwound C-core weight offset is recorded for each spacer thickness. The experimental axial force tests were carried out using the 300W AFIM.
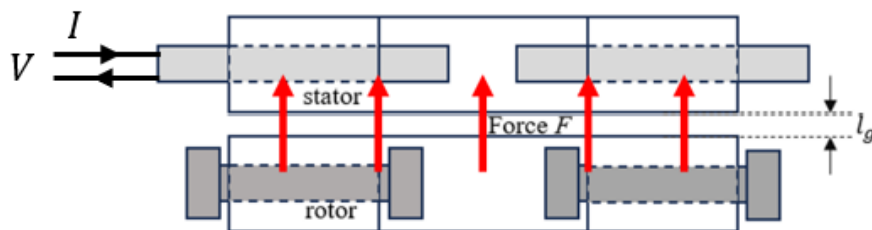
Figure 5-10 Experimental axial force of axial-flux induction motor testing conceptual drawing.

The testing concept is illustrated in Figure 5-10 where the axial force between the rotor and stator is measured as a function of airgaps. To achieve the no-load AC rotating condition of the AFIM in a static test, phase A is supplied with a DC current which is equal to the peak of the no-load current of the AFIM. The negative half of the peak no-load current is injected to phase B and C of the motor. This current distribution among the windings is achieved when two phases are connected in parallel with each other, and the remaining phase is connected series with the others (see Figure 5-11). It is noted that the injected current simulates the $d-axis$ flux (magnetizing flux), which is equivalent to applying rated AC voltage to the winding.
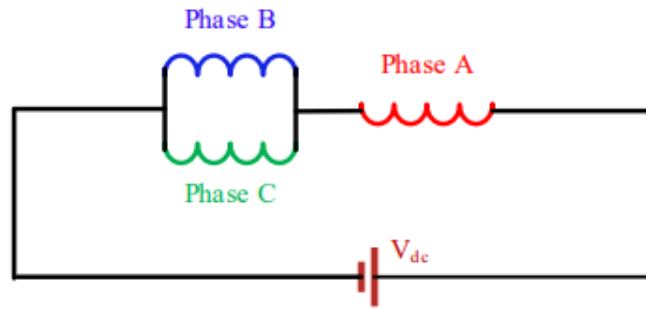
Figure 5-11 The DC supply arrangement to emulate the AC no-load conditions of the AFIM.

| (a) | (b) |

Figure 5-12 The 300W AFIM used for the axial force measurement. (a) stator, (b) rotor with shaft.
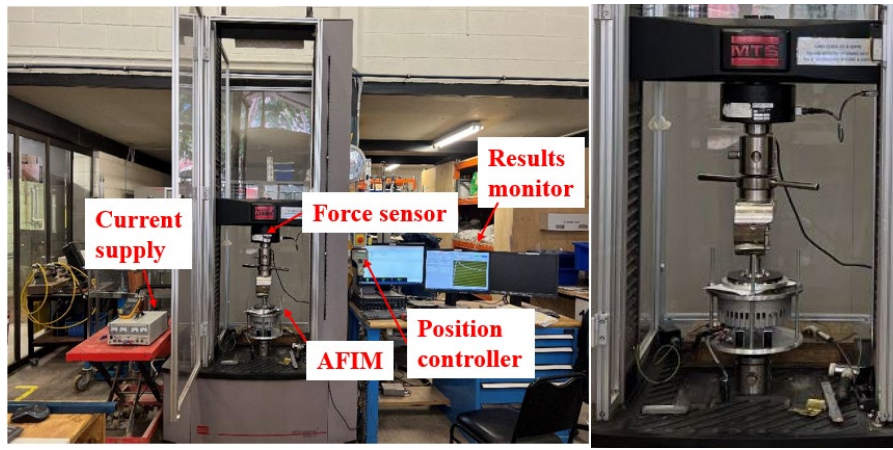
Figure 5-13 Experimental axial force measurement setup: using civil engineering material properties testing rig.

In the axial force experiment, a precision-controlled civil engineering material testing system (MTS) was used (see Figure 5-13) and the test AFIM is shown in Figure 5-12. The force sensor, rated at 300kN, was significantly larger than the maximum measured force ($\approx$ 5kN), which could affect the accuracy of the results. Therefore, accurately zeroing the force sensor and ensuring the repeatability of measurements was essential. To minimise the potential resulting errors, multiple axial force measurements for each airgap length were taken.
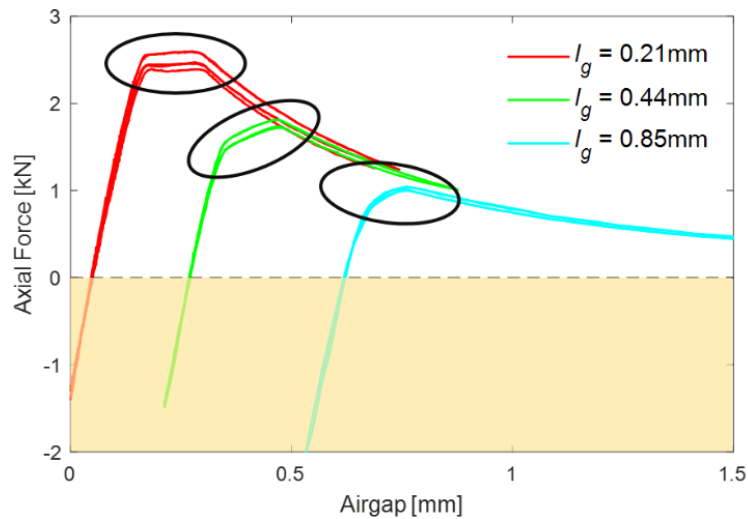
Figure 5-14 Measured axial force versus airgap trajectories for three different airgaps.

Figure 5-14 shows the measured axial force versus displacement curves for three different spacer-thicknesses. The shadowed part below zero shows the initial pressure applied downward on the stator and spacer and hence it is negative. To accurately measure the axial force, it is essential to find the peak force where the rotor just separates from the spacer and stator. The right side of curve shows the measured force with gradually increasing airgap, where the force is the magnetic attractive force between the stator and

rotor. Moreover, at lower airgaps of 0.21mm and 0.44mm, it is observed that the upper curve corresponds to when the airgap is increasing while the lower curve is when the airgap is decreasing. It is possible that the installation causes slight non-uniformity in the airgap between the rotor and stator. In addition, there may be a hysteresis effect in the magnetic material, which means the magnetisation response lags the changes in the magnetic field strength when decreasing or increasing the airgap. At a higher airgap of 0.85mm, the hysteresis effect is much less, and the weaker overall force reduces the impact of the non-uniform airgap separation.
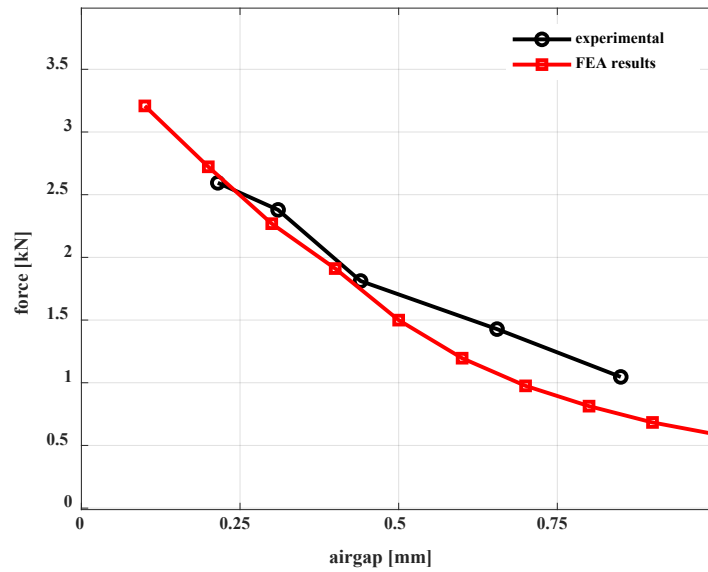
Figure 5-15 The axial force variations versus airgap of the AFIM when injecting 3.2A current to the stator windings.
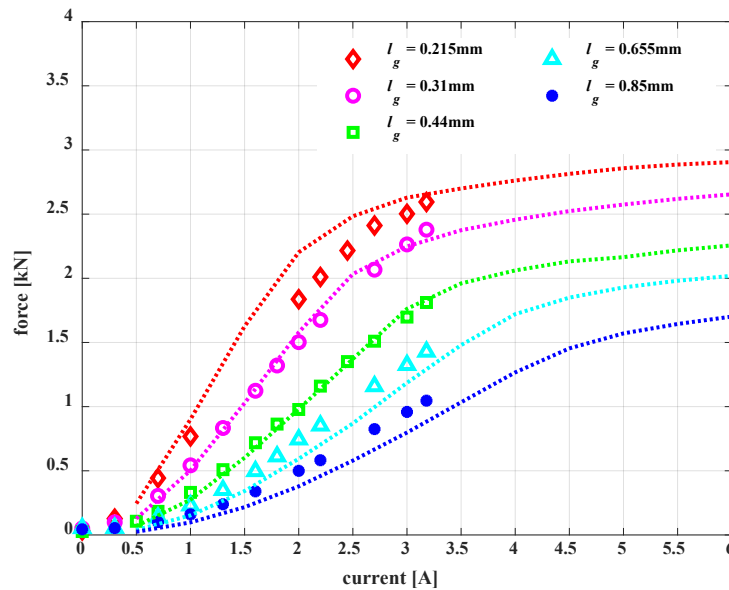
Figure 5-16 Axial force versus current for different airgaps (symbols: experimental results, lines: 3-D FEA simulations).

85

Figure 5-15 presents the axial force comparisons between the experiment and FEA simulations. It is observed that the experimental AFIM results show a similar trend to the 3-D FEA simulation results with a maximum error of 20% at the higher airgap length. According to this figure, the slope of the line, known as the negative stiffness, is larger until about a 0.7mm airgap and then it reduces significantly after this point.

Figure 5-16 shows the AFIM axial force versus current results for five different airgap lengths. To ensure the safety of machine, the injected current must not exceed the rated current for extended times, therefore, only a few high current points were used. The FEA simulation results are similar to the experimental results when applying a spacer thickness close to the nominal airgap ($l_g = 0.44mm$). As predicted in the magnetic circuit theory, the axial force is approximately proportional to the square of the injected current until the magnetic saturation occurs. The results in Figure 5-16 show a reasonable correspondence with each other.

5.3 Simulation Basis of AFIM Tilting Torque Calculation

In addition to the axial force analysis, the AFIM also produce tilting torque when a non-uniform airgap length eccentricity occurs. It is shown in Figure 5-17 which defines the tilting eccentricity as the ratio of the largest change in airgap (Δg) to the nominal airgap ($\epsilon = \Delta g / g_0$). Hence, values of tilting eccentricity of 0 and 1 represent a uniform airgap length and the rotor just touching the stator at one side

To calculate the tilting torque τ_{tilt}, the rotor surface is split into left and right regions about the tilting axis. The torque on either half is evaluated using the flux density distribution, and any imbalance in these torques produces the net tilting torque. The equations below are derived from the Maxwell stress tensor, where $B(r,\theta)$ is the rotor surface magnetic flux density as a function of the radial position r and angular position θ, μ_0 is the permeability of free space, and $r\sin(\theta)$ is the projection of the lever arm onto the tilting axis. The integration is carried out over the radial span from the centre of the rotor to its outer diameter R_{out}, and angularly over 0 to π, which corresponds to one half of the rotor surface.

$$\tau_{left} \ or \ \tau_{right} = \int_0^{R_{out}} \int_0^{\pi} \frac{B(r,\theta)^2}{2\mu_0} \cdot r\sin(\theta) \, d\theta \, dr \tag{5.5}$$

$$\tau_{tilt} = \tau_{left} - \tau_{right} \tag{5.6}$$
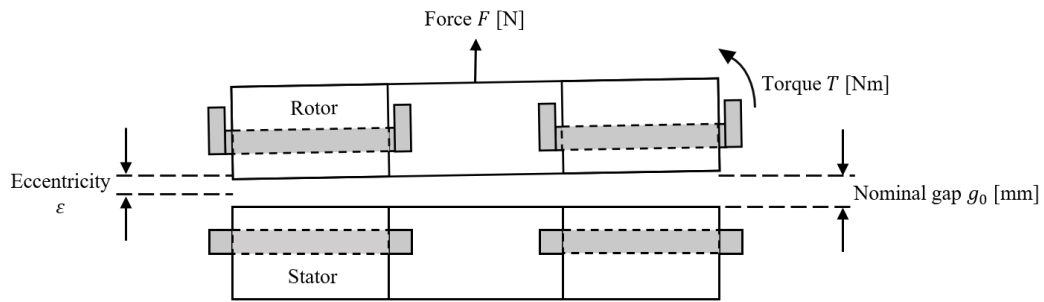
Figure 5-17 A conceptual drawing of tilting torque and eccentricity definition.
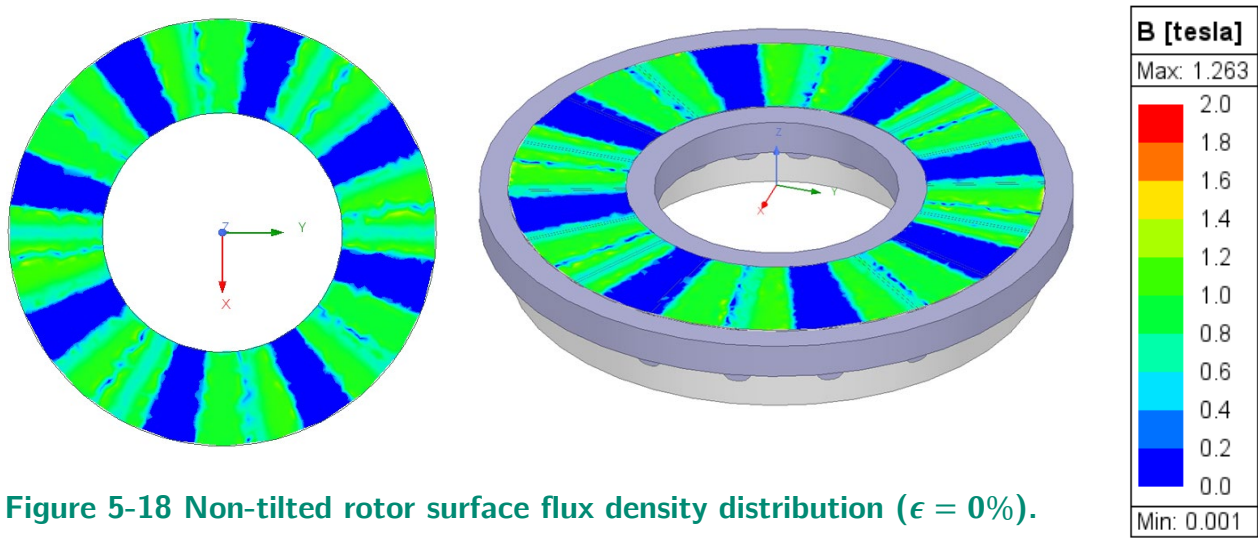
Figure 5-18 Non-tilted rotor surface flux density distribution ($\epsilon = 0\%$).
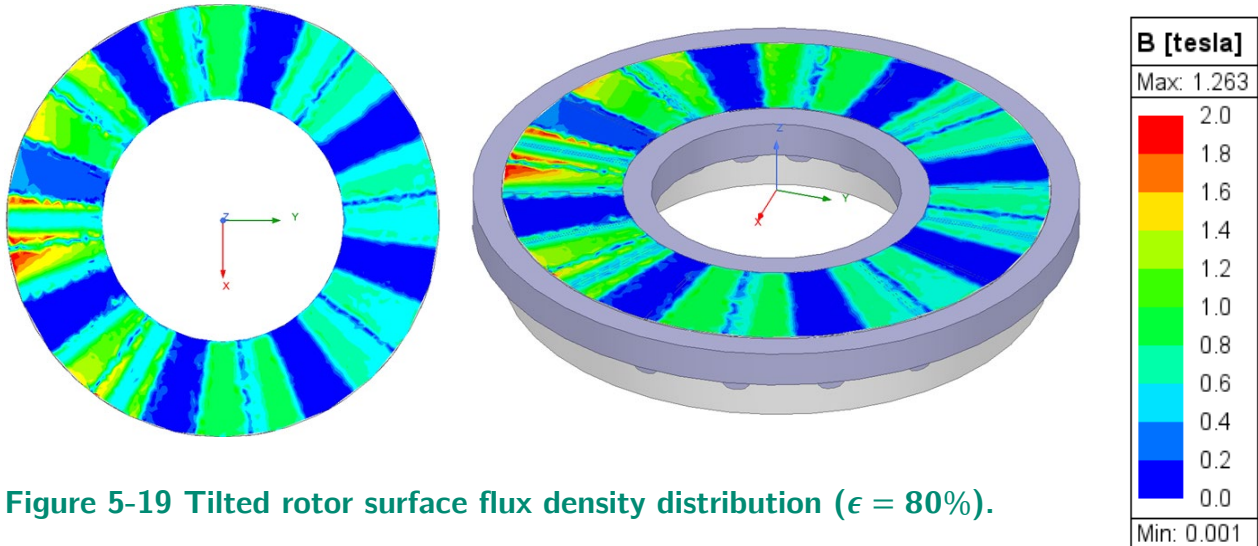
Figure 5-19 Tilted rotor surface flux density distribution ($\epsilon = 80\%$).
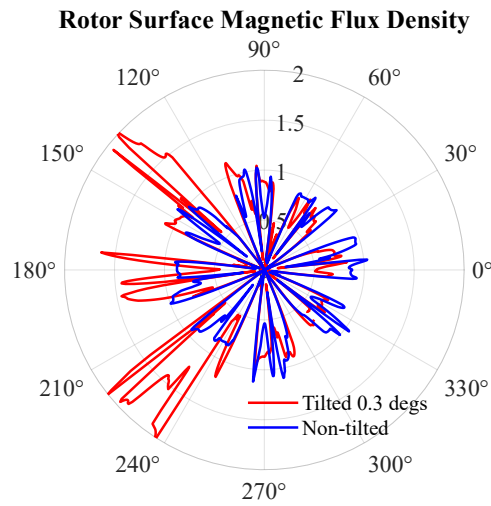
Figure 5-20 Polar plot of rotor surface magnetic flux density magnitude under non-tilted and 0.3° ($\epsilon = 80\%$) tilted conditions.

To evaluate the tilting torque, a three-step approach was conducted based on FEA. First, the same procedure used for axial force evaluation is repeated, where a current excitation is applied to the stator. Specifically, Phase A carries 3.2A, Phase B and Phase C each carries -1.6A. Under this excitation, the magnetic flux density on the rotor surface is obtained using FEA. Second, the rotor is then tilted clockwise by 0.3° ($\epsilon = 80\%$) around the x-axis to introduce asymmetry. As a result, the airgap varied from 0.1mm on the left edge to 0.9mm on the right edge, causing an imbalance in the flux density distribution. The FEA calculated tilting torques are found from the flux density magnitude contour plots shown in Figure 5-18 and Figure 5-19 for the non-tilted and tilted configurations. The polar plot is given to visualise the rotor surface magnetic flux density for the non-tilted and tilted rotor (Figure 5-20). The non-tilted rotor shows a uniform magnetic field, while the rotor tilted to the left-hand side shows a higher flux density on the left and lower flux density on the right. The tilting torque is found by integrating the product of the axial pressure from the magnetic flux density and the distance from the vertical axis.
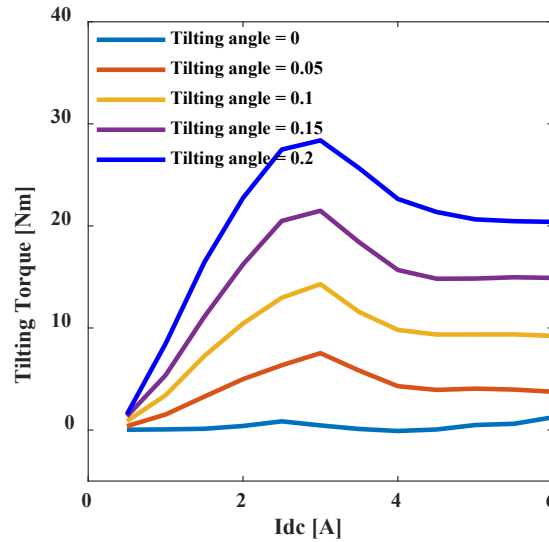
Figure 5-21 Tilting torque versus current for different tilting angles in degrees.
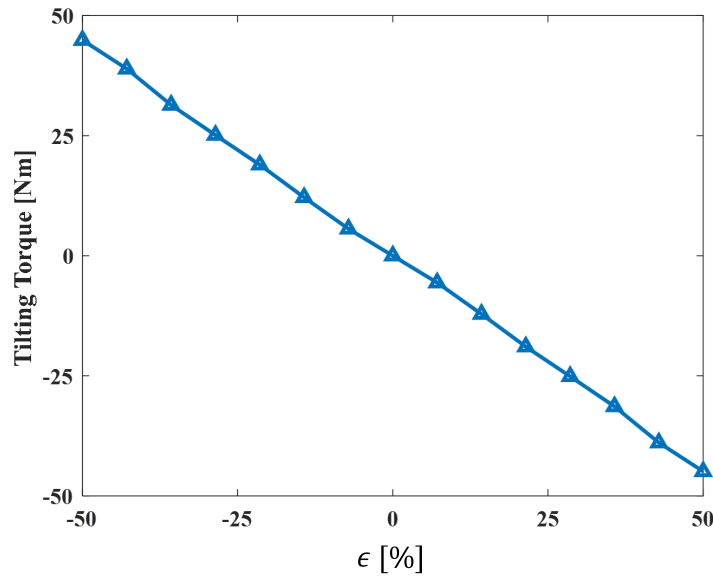
Figure 5-22 3-D FE simulation results for the AFIM rotor tilting analysis for I_{dc} = 3.2A.

Figure 5-21 shows the variation of tilting torque with respect to the injected current for different tilting angles. As the tilting angle increases, the tilting torque becomes more sensitive to the changes of applied current. This is because a larger tilting angle leads to a greater airgap asymmetry, particularly a significantly reduced airgap on the one edge of the rotor, which enhances the uneven flux density distribution. For all cases in Figure 5-21, the tilting torque increases with current up to a certain point, after which it starts reducing. This non-linear behaviour is caused by magnetic saturation in the core, especially at higher tilting angles, where the localised magnetic flux density becomes high enough to limit further tilting torque increase despite increasing current. As a result, although the tilting torque

exhibits an approximately proportional relationship with both the tilting angle and the excitation current under the low-current conditions, this proportionality becomes less significant at higher current levels due to the magnetic saturation. The tilting torque results are given in Figure 5-22 for the current-driven AFIM (see Table 5-1). It is observed that the tilting torque is nearly linearly proportional to the tilting eccentricity and has a negative sign.

In this section, an investigation was performed on the variation of axial force with airgap and also a tilting torque analysis with tilting eccentricity. An experimental test procedure for measuring the variation of the axial force with airgap for the current-driven AFIM is demonstrated and used to validate the FE predictions. Double-sided AFIMs are proposed to be a potential way to produce a zero net airgap axial force. In practice, ensuring a perfectly parallel rotor and stator for AFIMs is not an easy job, therefore, slight rotor or stator tilting effects were also investigated in this section. From the 3-D FE predictions, the maximum tilting torque is around 50Nm for the machine considered.

5.4 Design and Analysis of Double-sided AFIMs

(a) SSSR-AFIM   (b) DSSR-AFIM
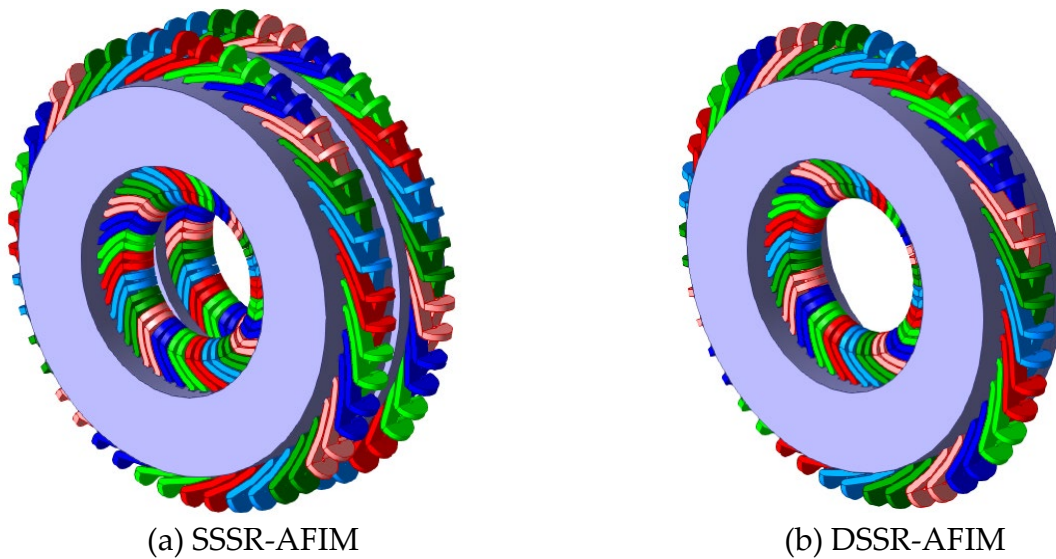
Figure 5-23 3-D views of (a) single-stator single-rotor AFIM, (b) double-stator single-rotor AFIM.

The single-stator single-rotor AFIM (SSSR-AFIM) has one rotor, one stator, and one set of windings. This is treated as the simplest type of AFIM and is a common candidate for low power rating applications. The flux flows in the axial and circumferential directions and the flux enters and leaves the stator and rotor at the same side. The double-sided single-

rotor AFIM (DSSR-AFIM) consists of a single rotor in the middle of two stator cores (see Figure 5-23(b))

(a)   (b)
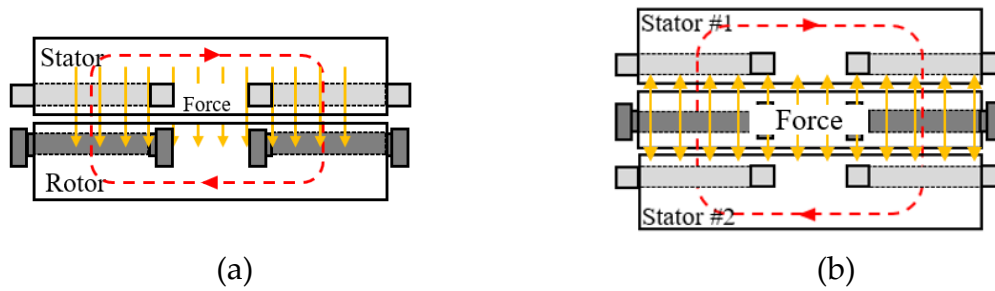
Figure 5-24 Alternative geometries for AFIM: (a) single-sided and (b) double-sided configurations with different flux paths.

Figure 5-24 reflects the flux path differences in the two AFIMs. Compared with the SSSR-AFIM, the flux paths can be designed in two types. In this "NS" configuration, the flux path travels across both airgaps (Figure 5-24(b)) and hence this configuration is less sensitive to unequal airgaps and the rotor back iron can be reduced. The single-stator double-rotor AFIM (SSDR-AFIM) also provides features like the DSSR-AFIM such as eliminating the attractive force and reducing the back iron in the stator part. However, it has the disadvantages that the largest heat generating component, the stator, is located between the two rotors and thus the cooling effectiveness is reduced. Also from a manufacturing perspective, in dual airgap AFIMs, the rotating parts should be mechanically connected and hence prototyping a SSDR-AFIM has more difficulties than DSSR-AFIMs.

In this section, a 2.2kW eight-pole DSSR-AFIM with two sets of three-phase distributed windings is proposed (see Figure 5-23(b)) for replacing its equivalent SSSR-AFIM (see Figure 5-23(a)) while keeping a similar weight. The proposed study plan in Figure 5-25 indicates that there are two main steps in the design process: 1) general sizing approach for a 1.1kW eight-pole SSSR-AFIM. 2) Combining two SSSR-AFIMs and the reduction of the rotor back iron to produce the DSSR-AFIM design. The NS flux path in Figure 5-24(b) is chosen in the proposed motor for reducing the use of the rotor back iron and reducing the negative stiffness. A comparative study on the DSSR and SSSR AFIMs is proposed to present the differences in electromagnetic performance.
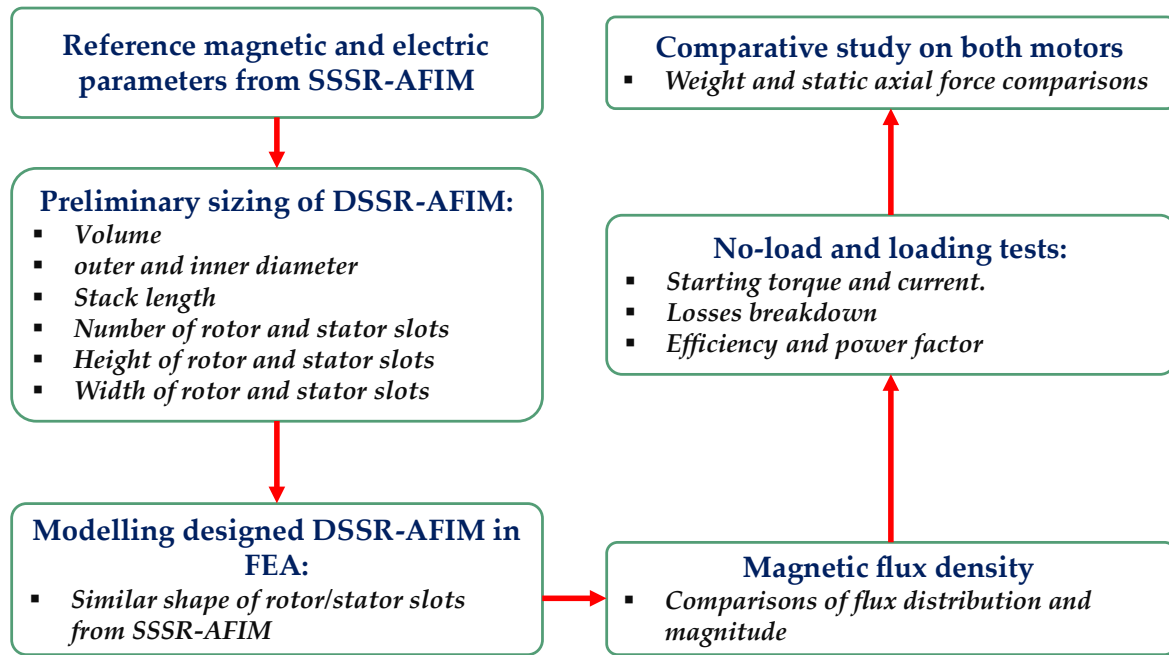
Figure 5-25 The flowchart of the proposed comparative study on SSSR-AFIM and DSSR-AFIM.

5.4.1 Dimensions of 2.2kW DSSR-AFIM

The general sizing equations discussed in **CHAPTER 4** are applied to approximately estimate the size of the proposed motor. The obtained geometry size consists of the volume of the motor, the rotor/stator slot/tooth width and length and the length of the stator yoke. It is noted that the proposed DSSR-AFIM has no flux path in the rotor back iron and hence the calculation of the length of the rotor yoke can be eliminated. Figure 5-26 indicates the geometry dimensions, magnetic flux path distributions and magnetic flux path distributions and magnetic and electric variables from the initial 2.2kW SSSR-AFIM design. As the proposed DSSR-AFIM is the combination of two SSSR-AFIMs with a reduction in the rotor back iron, the single-sided AFIM sizing approach can be applied first.
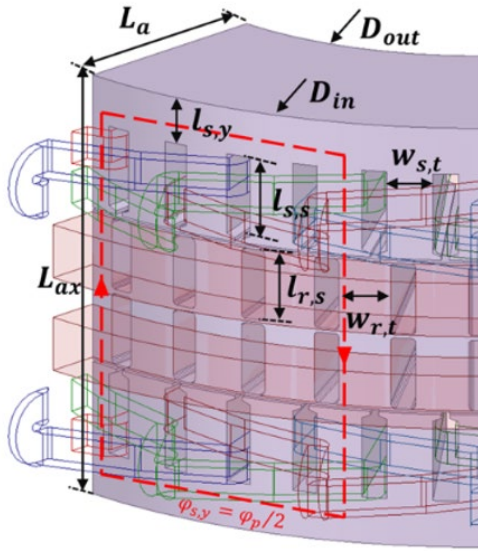
Known parameters from SSSR-AFIM	
A_{avg} [A/m]	22,433
B_g [T]	0.7161
$B_{s,t}$ [T]	1.3903
$B_{s,y}$ [T]	1.1237
$B_{r,t}$ [T]	1.2357
No. stator slots	48
No. rotor slots	44
$\hat{\imath}_r$ [A]	164.75
$\hat{\jmath}_r$ [A/m²]	2.8998

Figure 5-26 The design dimensions and essential magnetic and electric loading parameters.

$$V_a = V_{a1} = \frac{\sqrt{6}}{3} V_r \sin(\omega t)$$
$$V_b = V_{b1} = \frac{\sqrt{6}}{3} V_r \sin(\omega t - \frac{2\pi}{3})$$
$$V_c = V_{c1} = \frac{\sqrt{6}}{3} V_r \sin(\omega t - \frac{4\pi}{3})$$

$$(5.6)$$
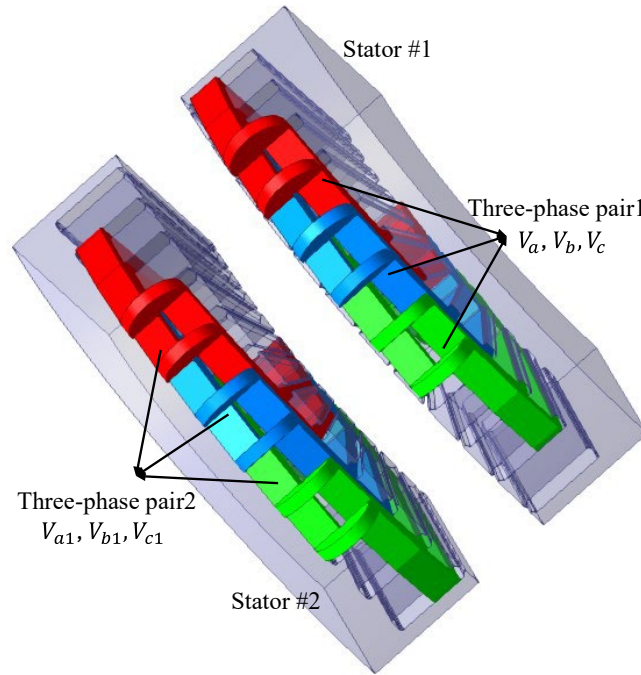
Figure 5-27 Winding configuration of the DSSR-AFIM.

Table 5-2 Design variables for the 2.2kW, 8 pole SSSR-AFIM and DSSR-AFIM.

		SSSR-AFIM	DSSR-AFIM
Rated power [kW]	P_r	2.2	
No. of poles	p	8	
No. of stator slots	N_{ss}	48	
No. of rotor slots	N_{rs}	44	
Rated voltage [V]	V_r	415	
Rated frequency [Hz]	f	50	
Winding material	-	Copper	
Iron core material	-	M19_24G	
Rotor bar material	-	Aluminium	
Rated speed [rpm]	n_r	726	727
Inner diameter [mm]	D_{in}	163	142
Outer diameter [mm]	D_{out}	275	235
Stack length [mm]	L_s	69	95
Rated torque [Nm]	τ_r	30	30
Airgap length [mm]	l_g	0.465	0.465
Weight [kg]	-	22.5	22.2

It is noted that the width of the rotor and stator teeth depends on the radius of the 2-D layer which is chosen for the flux density calculations. In this section, the average diameter layer (D_{avg}) is used for the sizing approach. Table 5-2 lists the identical and modified design dimensions and specifications of both eight-pole double and single-sided AFIMs. In order to create a fair test to accurately determine the performance parameter differences of both AFIMs, a similar total weight was used (see Table 5-2). Figure 5-27 shows the winding configuration of the DSSR-AFIM. Balanced voltage sources in parallel are used for the two sets of windings as given in equation (5.6) where ω and t are electrical angular frequency and time.

5.4.1.1 FE simulation results and discussion

(a)   (b)
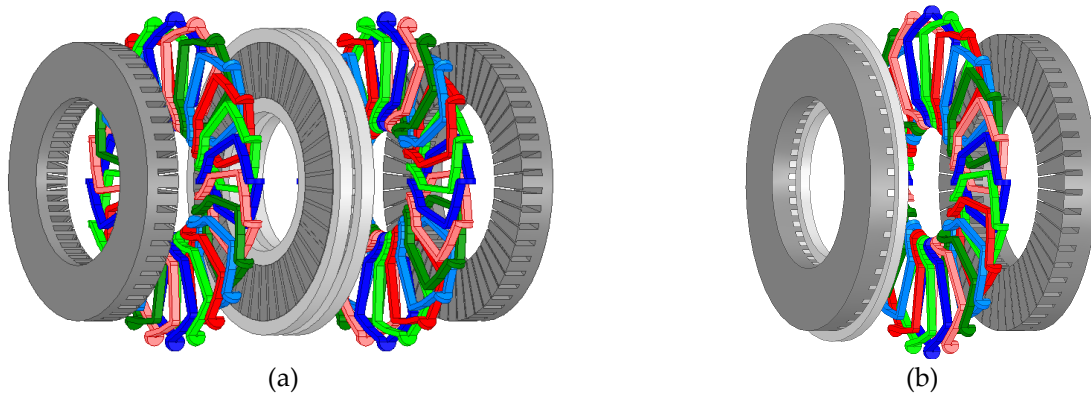
Figure 5-28 The exploded 3-D views for DSSR-AFIM (a) and SSSR-AFIM (b).

In this section, the performance predictions of both the DSSR-AFIM and SSSR-AFIM are carried out. For the conventional RFIM, 2-D FEA simulations produce high accuracy results

as the effect of end-windings is the only neglected parameter. However, simulating AFIMs in 2-D FEA provides a lower accuracy and hence only 3-D simulation results are given in this section.

The exploded views for both motors are given in Figure 5-28. Compared with the SSSR-AFIM, the DSSR-AFIM is less disc shaped as it has a larger stack length and a smaller outer diameter. Figure 5-29 shows the component weight breakdown. It is noted that all weight values are per unitised where the SSSR-AFIM total material weight is considered as the base value. The DSSR-AFIM has lower rotor with bar weight as a reduced rotor back iron is required. Figure 5-30 reports the magnetic flux density distribution of both motors. This allows a visual confirmation of the saturation level of the core material.
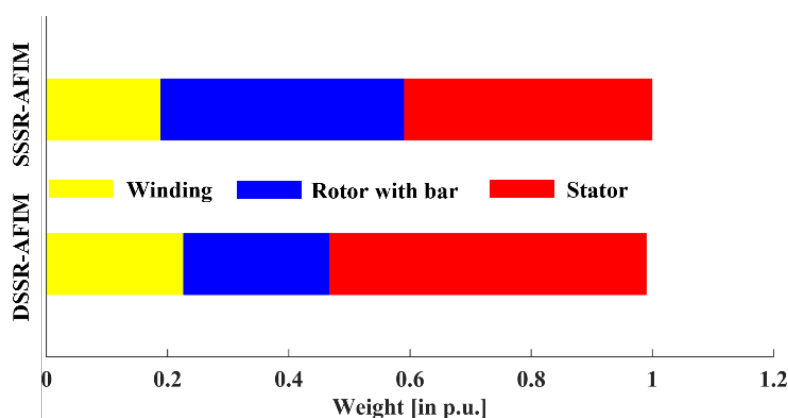
Figure 5-29 Weight breakdown comparisons between DSSR and SSSR AFIMs.
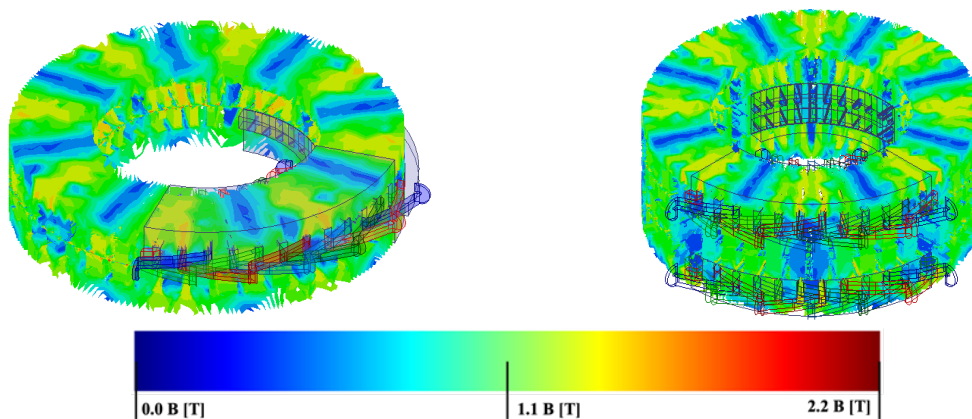
Figure 5-30 No-load magnetic flux density distribution.

(a) SSSR-AFIM   (b) DSSR-AFIM
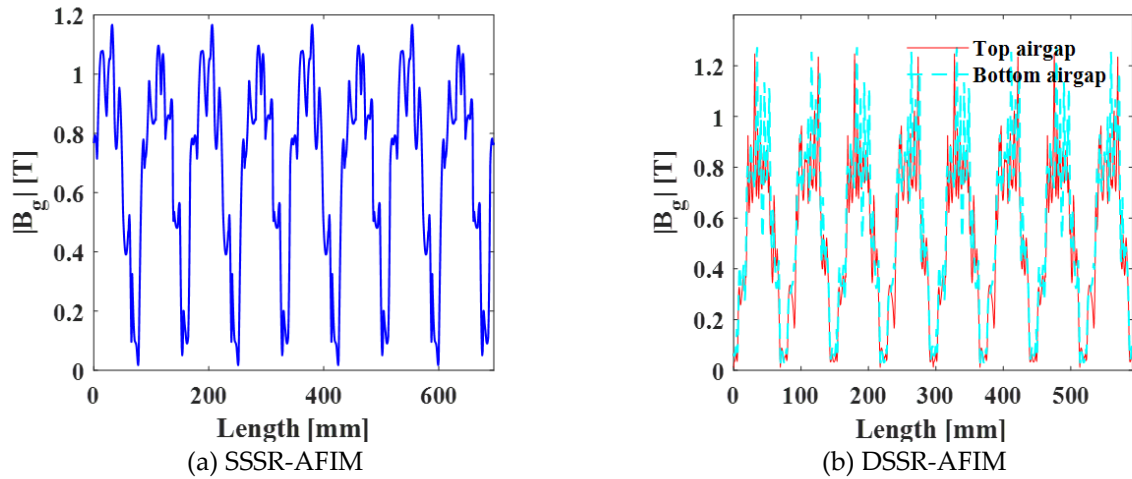
Figure 5-31 Middle layer absolute airgap flux density for both motors under the no-load condition.

Both motors have similar flux density distributions, and the maximum flux density occurs around the rotor/stator teeth. Figure 5-31 determines the middle layer absolute airgap flux density for both motors. The average airgap flux density for the SSSR-AFIM and the DSSR-AFIM are around 0.65T and 0.69T. Ideally, the amplitude of flux density in both airgaps are expected to be equal. The top and bottom airgap flux density of the designed DSSR-AFIM in Figure 5-31(b) reflects this correlation and expectation.
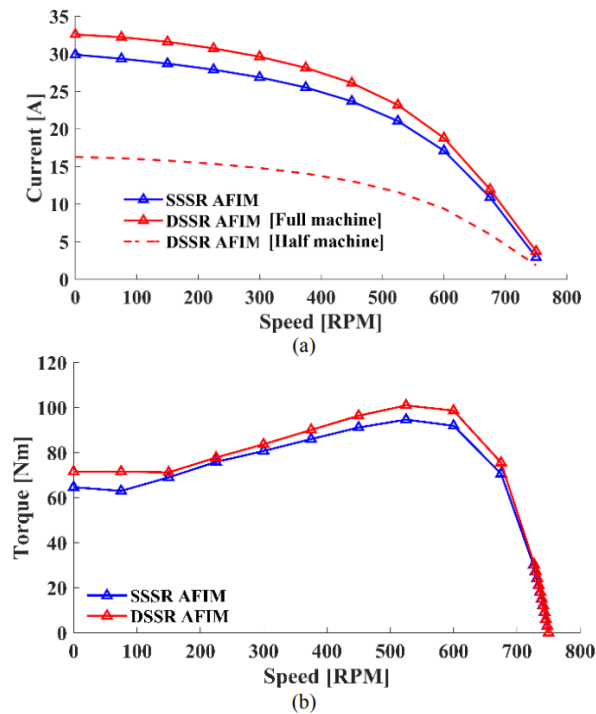
Figure 5-32 Performance prediction of the motors as a function of speed. (a) phase current versus speed. (b) torque versus speed.

The stator phase current and electromagnetic torque against speed are presented in Figure 5-32(a) and (b), respectively. These curves show the current and torque versus speed characteristics of the benchmark SSSR-AFIM and the proposed DSSR-AFIM. In Figure 5-32(a), the blocked rotor current for the half-DSSR-AFIM and SSSR-AFIM are at 16.3A and 29.9A, respectively. The current amplitude for the DSSR-AFIM is expected to be around half of the SSSR-AFIM as the two stator windings are in parallel. Figure 5-32(b) shows the torque as function of speed. It is observed that the DSSR-AFIM delivers a higher starting torque about 7Nm and higher breakdown torque (about 6Nm) compared with the SSSR-AFIM (See Table 5-3).

Table 5-3 Summary of performance parameters for DSSR-AFIM and SSSR-AFIM.

Output	Type	Poles	Efficiency [%]			Power Factor				Torque [Nm]		
kW		#	50% Load	75% Load	100% Load	50% Load	75% Load	100% Load	100% Load	Locked Rotor	Pull Up	Pull Out
2.2	SSSR-AFIM	8	81.7	82.1	82.6	0.59	0.69	0.81	30.0	64.6	59.0	94.6
2.2	DSSR-AFIM	8	81.3	81.5	81.9	0.51	0.62	0.74	30.0	71.6	70.5	100.9

(a)   (b)
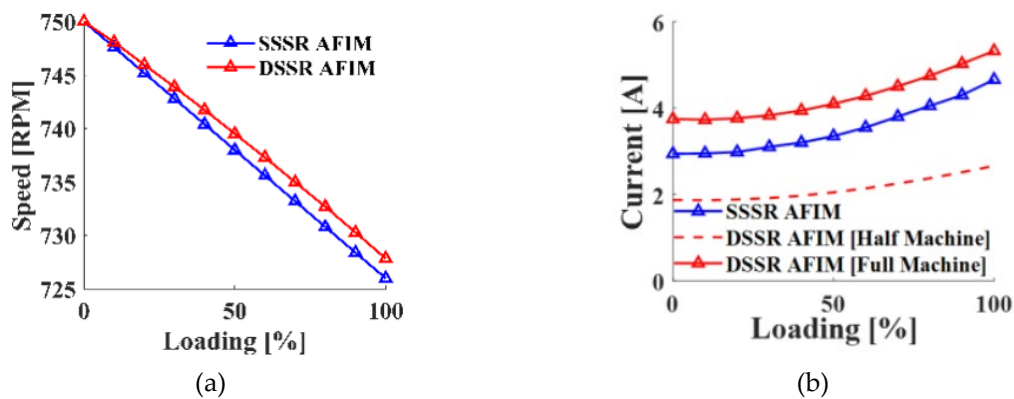
Figure 5-33 Comparison of the predicted rotating speed and current amplitude as a function of loading.
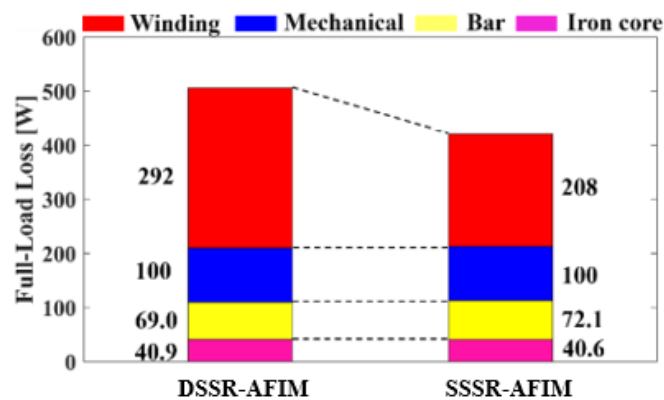
Figure 5-34 Component loss breakdown under full-load operation.

Figure 5-33(a) shows the speed versus load characteristics for both the SSSR-AFIM and DSSR-AFIM. At the full load condition, the rated speed for the motors are very similar. Figure 5-33(b) presents the stator phase current amplitude versus load. It shows that at all loads the DSSR-AFIM has a lower current compared to the SSSR-AFIM, and at rated load the DSSR-AFIM requires 2A less current than the SSSR-AFIM. Table 5-3 tabulates the key performance parameters at 50%, 75% and 100% of full load and Figure 5-34 summarise the loss breakdown at the full load operation point. It is observed that the power factor is higher in the SSSR-AFIM than the DSSR-AFIM. At 100% load the power factor is 0.78 and 0.74 for the SSSR-AFIM and DSSR-AFIM respectively. Compared with the SSSR-AFIM, the DSSR-AFIM delivers lower efficiency at all loads which is caused by the higher winding losses, as shown in Figure 5-34.

(a)   (b)
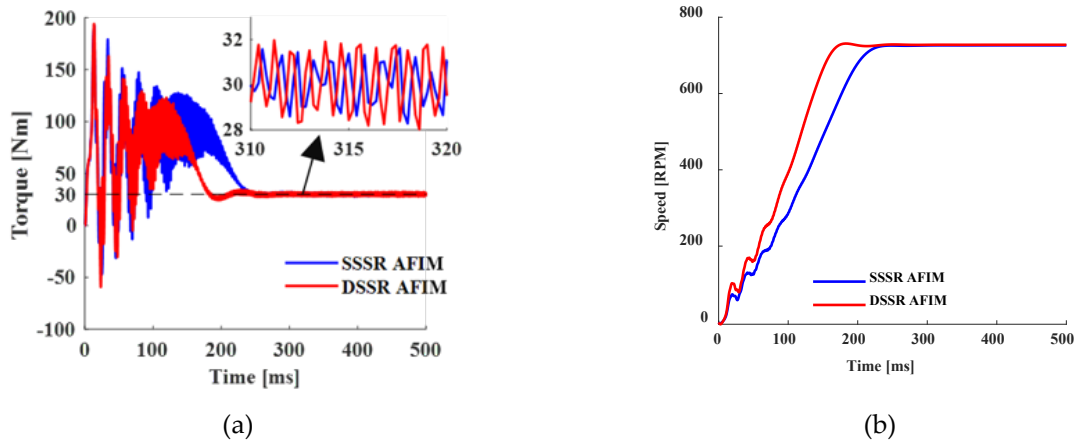
Figure 5-35 Torque and speed dynamic response against simulation time.

Figure 5-35 shows the dynamic response of the motors under full-load operation. Compared with the torque and speed response of the SSSR-AFIM, the DSSR-AFIM takes a shorter time to reach steady state due to the lower rotor mass and radius and thus lower inertia. However, a zoom-in view in Figure 5-35(a) shows that the DSSR-AFIM has slightly higher torque ripple comparing to the SSSR-AFIM. The maximum torque ripple of the SSSR-AFIM and the DSSR-AFIM are measured at 2Nm and 1.5Nm. As mentioned earlier in this chapter, the double-sided AFIM offers a potential solution for achieving zero net attraction force, particularly when a single rotor with reduced back iron (DSSR-AFIM), with one flux loop crossing both airgaps. In the following section, the axial forces in the SSSR-AFIM and DSSR-AFIM are compared and discussed.

Figure 5-36 presents the attraction force density distribution observed in the SSSR-AFIM, where the axial force density pressure is approximately 300kN/m². To manage this large axial force, several mechanical design features can be implemented, such as using angular

contact ball bearings, which are capable of withstanding high axial loads. In addition, making the stator and rotor housing design more rigid can help prevent unwanted displacement, thereby enhancing the overall structural reliability and robustness. Figure 5-37 illustrates the attraction force density distribution for the DSSR-AFIM, the average axial force density is also measured at 300kN/m², similar to the SSSR-AFIM, as shown in Figure 5-36. Notably, the DSSR-AFIM is designed and simulated with equal airgap lengths on both sides.

Figure 5-38 (a) and (b) provide visualisation of the force distribution for the designed DSSR-AFIM, revealing that while the force density amplitude is similar to that of the SSSR-AFIM, the forces in each airgap act in opposite directions. Consequently, the net force, defined as the difference between the forces in each airgap, ideally cancels out. However, maintaining equal airgap lengths on both sides during manufacturing and assembly is challenging. Nevertheless, the through flux path case (see Figure 2-7 and Figure 5-23(b)) in the designed DSSR-AFIM makes it less sensitive to unequal lengths on the two sides compared to the separate flux path case (See Figure 2-6).

Quarter trimetric view SSSR-AFIM   Quarter +y axis view SSSR-AFIM
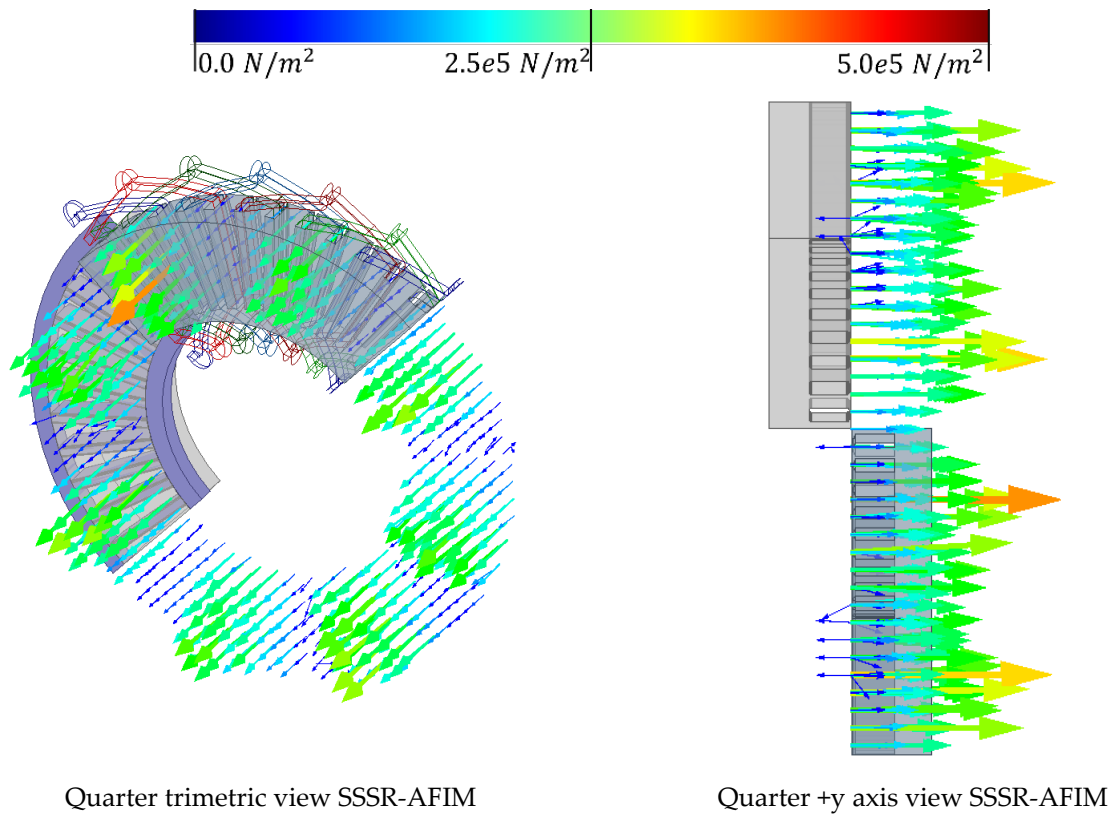
Figure 5-36 The attraction force density distribution for the SSSR-AFIM.

Quarter trimetric view DSSR-AFIM   Quarter +y axis view DSSR-AFIM
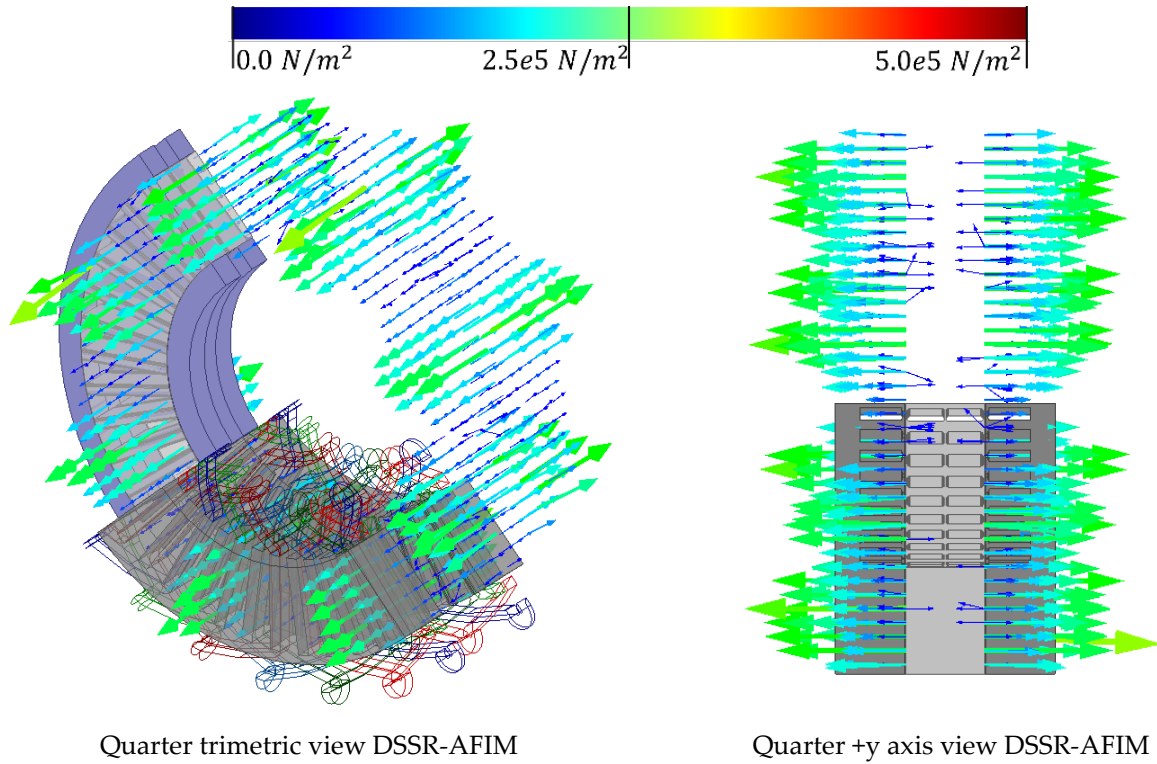
Figure 5-37 The attraction force density distribution for DSSR-AFIM.

The pressure distribution for both motors is given in Figure 5-38. Figure 5-38(a) and (b) illustrates the pressure distribution overlays and polar plots of the SSSR-AFIM and DSSR-AFIM around the motor circumference. The pressure distribution and polar plots for both motors are similar as they have similar airgap flux densities. However, it is noted that the SSSR-AFIM has unbalanced forces while the DSSR-AFIM forces cancel each other.

(a)   (b)
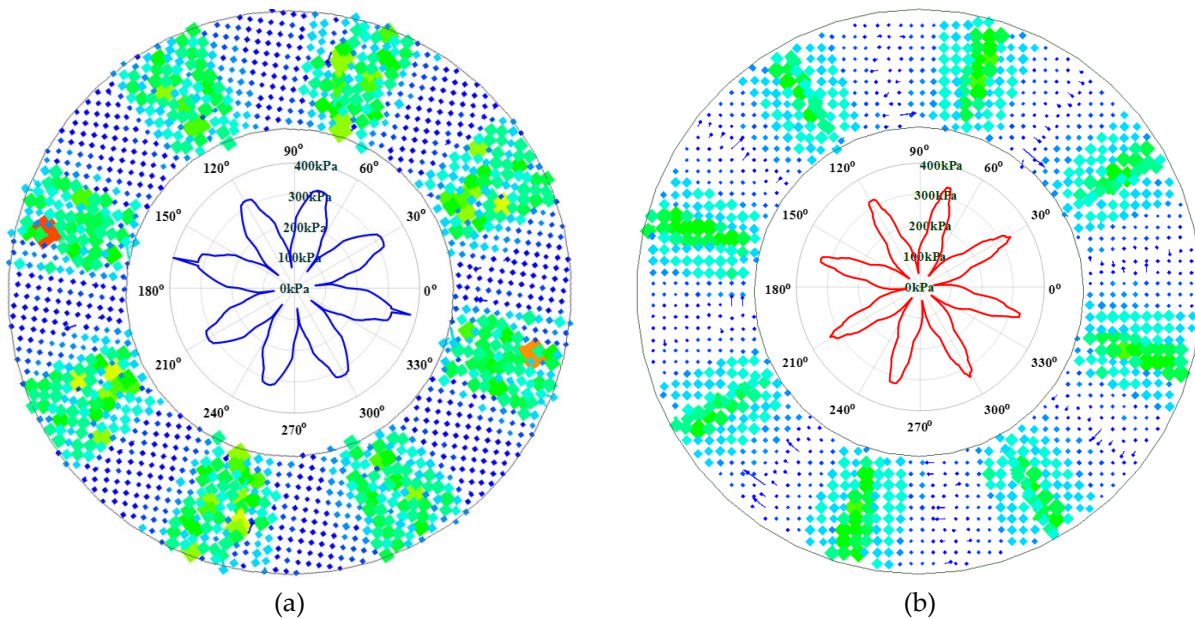
Figure 5-38 Pressure distribution on (a) SSSR-AFIM and (b) DSSR-AFIM.

In this section, a comparison between a 2.2kW DSSR-AFIM and a SSSR-AFIM with similar material weight has been proposed and analysed. Also, the design process for combining two sets of 1.1kW SSSR-AFIM with reduced rotor back iron to form the 2.2kW DSSR-AFIM has been described. 3D FEA was used for the simulation results. The transient and steady state performance has been compared, including response time, starting torque, blocked rotor current, loading performance as well as force analysis. The simulation results confirm that for a similar weight, the DSSR-AFIM delivers a faster response due to its lower rotor inertia. Compared with the SSSR-AFIM, the DSSR-AFIM has a smaller diameter, which reduces the risk of eccentricity. However, the DSSR-AFIM exhibits higher winding loss, leading to lower overall efficiency. From an attraction force perspective, the DSSR-AFIM has reduced axial force and thus lower mechanical losses.

5.4.2 Topologies of 4kW DSSR-AFIM

As mentioned in **CHAPTER 2**, the structural flexibility of AFIM allows for multiple configurations, including single-sided and double-sided AFIMs. In this section, an investigation on different double-sided AFIMs is carried out.

(a)   (b)   (c)   (d)
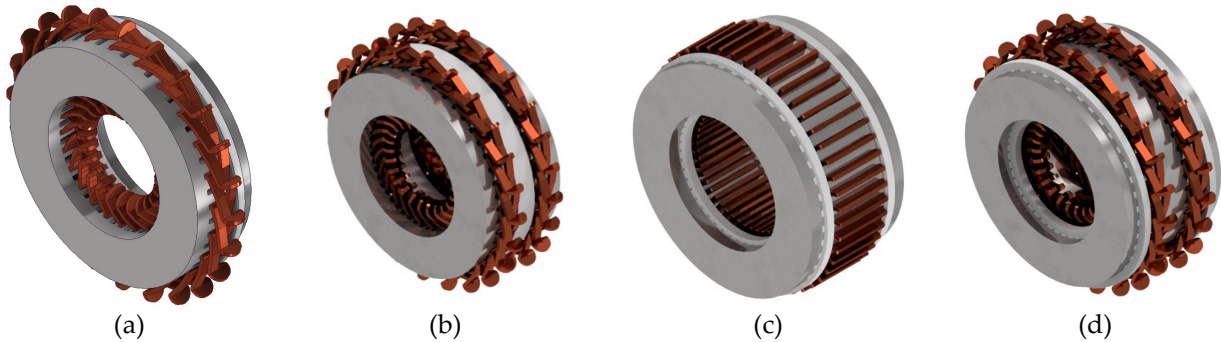
Figure 5-39 Designed single-sided and double-sided AFIMs, Case (a) single-sided AFIM with distributed windings, Case (b) NS topology single-rotor double-sided outer distributed wound stators, Case (c) NN topology surrounding single toroidal wound stator with two outer rotors, Case (d) NN topology single distributed-wound stator with two outer rotors.

Figure 5-39 shows alternative proposed designs for the AFIM, including single-sided and a double-sided AFIMs. Figure 5-39(a) presents the reference single-sided 2.2kW eight-pole AFIM with double-layer distributed winding. Figure 5-39(b) illustrates the proposed single rotor with double distributed wound outer stators. In this design, the magnetic flux

passes from one stator, through the rotor, to the other stator (see Figure 2-4). The two sets of distributed windings each carry the same amplitude of current in the same direction, thereby achieving the NS topology. Figure 5-39(c) shows the single toroidal-wound stator with two outer rotors. The toroidal windings encircle the middle stator core (see Figure 2-5). The magnetic flux generated by the toroidal winding is shown in Figure 2-4. In this design, the stator back iron thickness is up to two times the thickness in a single-sided AFIM. Figure 5-39(d) shows a single stator with two distributed windings with two outer rotors. The magnetic flux path in this configuration is similar to the configuration shown in Figure 5-39(c). Figure 5-39(b) and Figure 2-4 and Figure 2-5 presents the other two topologies of the double-sided AFIM, surrounding the rotor with two outer stators. The NN and NS topologies are still available by changing the relative current directions in the two stators. The toroidal winding is no longer suitable for these two topologies because the toroidal winding complicates the assembly and manufacturing process, and the middle rotor results in longer end-windings, leading to higher resistance. The reference eight-pole 2.2kW single-sided AFIM electric and magnetic loading parameters, dimensions and specifications are tabulated in Table 5-2.

5.4.2.1 FE simulation results and discussion

Table 5-4 Comparison of the main dimensions, volume, and weight for different of AFIM cases.

	Case (a)	Case (b)	Case (c)	Case (d)
D_{out} [mm]	275			
D_{in} [mm]	163			
L_{ax} [mm]	78.5	131	157	
V [litre]	2.26	3.77	4.52	
Weight [kg]	24.40	42.80	48.90	48.20
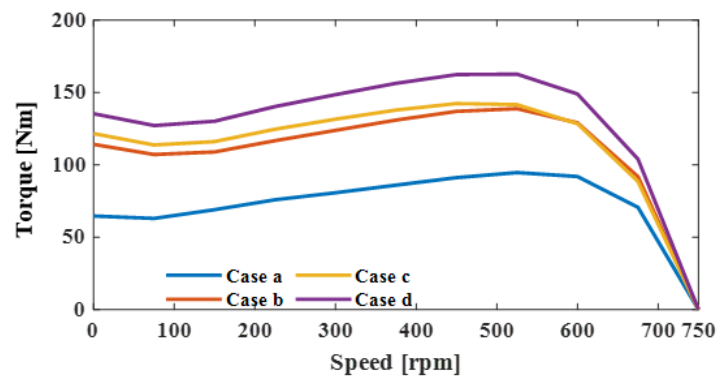
Figure 5-40 3-D FEA simulation predicted torque versus speed.
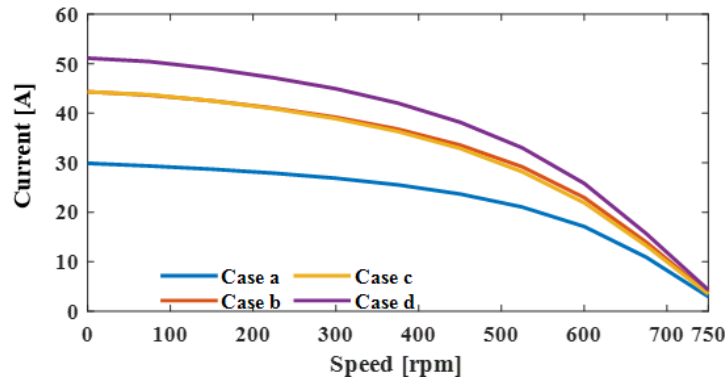
Figure 5-41 3-D FEA predicted current versus speed.

Figure 5-40 and Figure 5-41 present the 3D FEA simulation results of the designed AFIMs, illustrating the relationship between the current and torque as a function of speed. For the designed double-sided AFIMs, the single distributed-wound stator with two outer rotors (Case d) offers the highest starting torque, about 135Nm, making it suitable for applications where high initial load is critical. In Figure 5-41, Case (d) exhibits the highest starting current, which aligns with its highest starting torque. The topology, surrounding a single toroidal-wound stator with two outer rotors (Case (c)), shows a slightly lower starting torque than Case (d) which is also reflected in Figure 5-40. The single-rotor double-sided outer distributed wound stators give the lowest starting torque and current among these three double-sided AFIMs.

Table 5-5 Comparison of electromagnetic performance for the single sided AFIM and the three double-sided AFIM.

	Case (a)	Case (b)	Case (c)	Case (d)
P_{rate} [kW]	2.2	4		
n_s [rpm]	750			
n_{rate} [rpm]	726	714	721	718
τ_{rate} [Nm]	30	53		
τ_{start}[Nm]	60	114.2	121.6	135.3
I_{start}[A]	30	44.2	44.3	51.1
$I_{no-load}$[A]	2.80	3.50	4.80	4.30
η [%]	83.80	83.70	83.30	83.60
Torque density [Nm/kg]	1.23	1.24	1.08	1.09
Power density [W/litre]	973.45	1061.00	884.96	884.96

Table 5-4 compares the general dimensions and weight of the different AFIM topologies. In all cases, the outer and inner diameters are equal. The motor volume is calculated as the sum of the electric steel volumes, excluding the stator end-winding and rotor end-rings. Cases (c) and (d) have the same electric steel volume, with the differences in the material weight attributed to the stator end-winding copper. Case (b) is the lightest among the

double-sided cases, with the weight around 1.6 times that of the benchmark single-sided case, shown in Case (a).

(a)

(b)

(c)
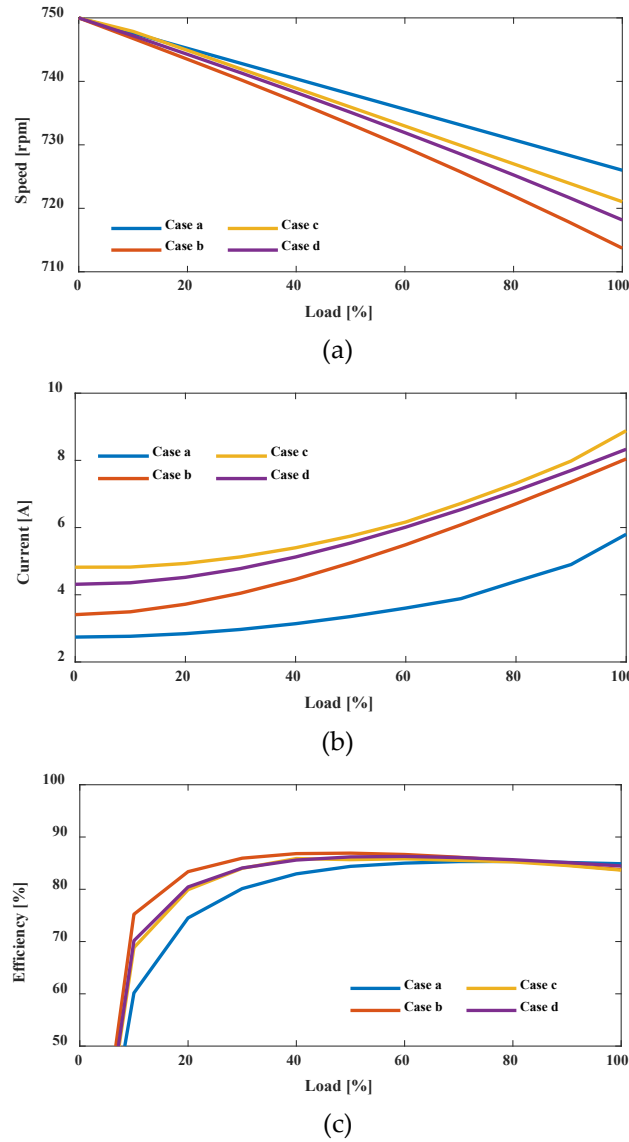
Figure 5-42 3-D FEA simulation results of 2.2kW reference single-sided AFIM and 4kW double-sided AFIMs, across various loadings, (a) speed vs. load, (b) current vs. load, (c) efficiency vs. load.

Figure 5-42 shows the electromagnetic performance versus load for the designed AFIMs. It is important to note that the single-sided AFIM with distributed windings is a 2.2kW single-sided AFIM and the others are 4kW double-sided AFIMs. Comparing the double-sided AFIMs, case c, the toroidal wound single stator, offers the highest rated speed. Case b, the single-rotor double-sided outer distributed wound stators, which features single rotor with reduced back-iron, has a significant drop in the speed. However, in Table 5-6, this case offers higher power density due to the significant drop in the volume compared to case c and case d, the single distributed-wound stator with two outer rotors.

Figure 5-42(b) illustrates the current versus load characteristics. It is observed that case c with the toroidal winding has highest current at all loads. In addition, as reflected in Table 5-6, case c, surrounding the single toroidal wound stator with two outer rotors, offers slightly lower torque density than case d, the single distributed wound stator with two outer rotors. Figure 5-42(c) presents the efficiency under various loadings. At the light loading region, case b, the NS topology single rotor double-sided outer distributed wound stators, exhibits the highest efficiency. Both the NN topologies with the single distributed and toroidal wound stator (case c and case d) share the same motor topology but with different winding configurations. They exhibit very similar overall efficiency values, but case d demonstrates slightly higher efficiency, particularly under full-load conditions. This is also reflected in Figure 5-42, where the NN topology with a single toroidal-wound stator (case c) exhibits slightly higher losses due to the increased winding losses.

Figure 5-43 shows the loss breakdown for the designed AFIMs. It is observed that both the NS topology single-rotor double-sided outer distributed-wound stators (case b) and the NN topology surrounding the single toroidal-wound stator with two outer rotors (case c) have similar losses contributions from the stator winding, rotor bar, and the iron core. The NN topology case c has larger winding losses, particularly at higher loading conditions.

At the lighter loading region, case b exhibits the highest efficiency. Both case c and case d share the same motor topology but with different winding configurations. They exhibit close overall efficiency values, and case d demonstrates slightly higher efficiency, particularly under full load conditions. This is also reflected in Figure 5-43, where case c exhibits slightly higher losses due to the increased winding losses. Figure 5-43 shows the loss breakdown for the designed AFIMs. It is observed that both case b and case c have similar loss contributions by the stator winding, rotor bars, and the iron core. Case c with the toroidal wound stator has larger winding losses, particularly at higher loading conditions.

Table 5-5 presents a performance comparison between the four cases. The motor torque density is an important parameter while designing the motor as it allows for the design of more compact machines with higher torque output. The reduction in volume allows for greater adaptability in situations where space and weight constraints are important. For the double-sided AFIMs, case b, which features a single rotor with two outer stators, offers the highest torque and power density. The toroidal-wound double-sided AFIM, case c, does not have better electromagnetic performance than case d. However, from a construction perspective, the more compact end-windings of case c allows smaller inner-to-outer diameter ratios.
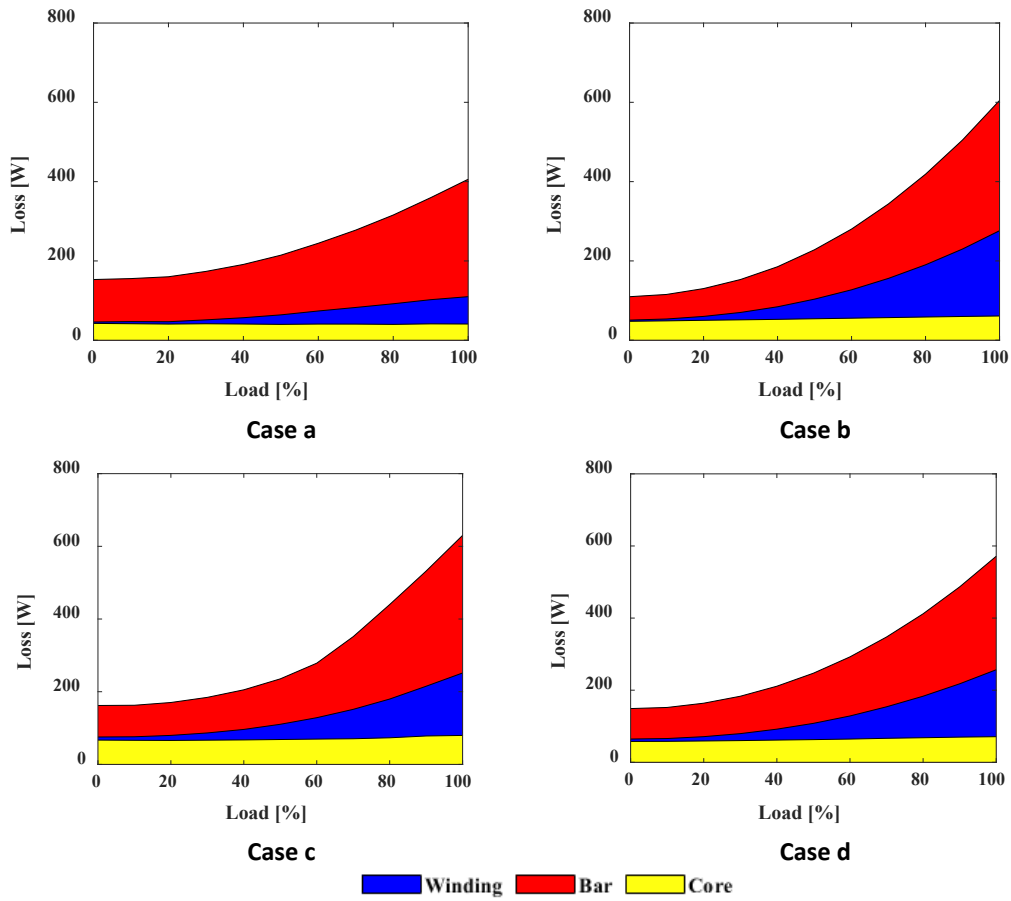
Figure 5-43 Loss breakdown of 2.2kW single-sided AFIM and 4kW double-sided AFIMs across various loadings.

This section discussed the different topologies of 4kW double-sided AFIMs. The design process on combining two 2.2kW single-sided AFIMs to form the double-sided 4kW AFIMs has been described. The comparative studies regarding no-load and loading electromagnetic performance on the different topologies have been discussed. The simulation results show that all the cases have their own benefits regarding the torque density, efficiency and starting performance. Case b offers higher torque and power density and the highest full-load efficiency among the double-sided AFIM designs. From a construction and assembly perspective, case b, surrounding a single rotor with two outer stators, is the best topology. In contrast, both case c and case d present multiple challenges in maintaining a consistent airgap length on both sides and mechanically linking the two outer rotors. Any discrepancy in these parameters could result in unbalanced axial attractive forces, which affects the bearing selections.

CHAPTER 6

<div align="right">

CONSTRUCTION OF
2.2kW EIGHT POLE AFIM

</div>

6.1 Introduction

The compact design, resulting in high-power density, has made the axial-flux motor become an attractive option. The fabrication of the laminated stator and rotor of axial-flux motor are more complex and expensive than the radial-flux motor, primarily due to the variations in tooth width. Currently, most available commercialised axial-flux motors are axial-flux permanent magnet synchronous motors (AFPMSM). Since the price of rare-earth magnet materials has escalated by an order of magnitude, it is worthwhile to investigate axial-flux motors without permanent magnets, with the axial-flux induction motor (AFIM) presenting a viable alternative for further discussion. Additionally, the AFPMSM shows challenges during the assembly process, due to the inherent strong magnetic field generated by the magnets. The previous literature has mainly been confined to the analytical and simulation analysis [53, 65] of AFIMs for various applications, while comprehensive construction guidelines or the detailed design process discussion have not been discussed in the literature. This section introduces the construction and mechanical design for the proposed 2.2kW eight poles AFIM.

The radial-flux induction motor shows a uniform 2-D cross-section and is normally constructed by tacking identical laminations. These laminations are produced by using a die to punch the desired lamination shape.

The die design is crucial in the stamping process and should be carefully designed to handle the required tolerances and complex geometries of the stator/rotor slot shapes. The presence of raised edges in the punched laminations, known as burrs, during the stamping process should undergo post-processing as unwanted contact between adjacent layers can result in undesired airgaps between the laminated layers and stacking length. Moreover, the burrs can allow eddy currents to flow, leading to increased core losses, and hence, diminished electromagnetic performance. Laser cutting is another traditional machining process with high flexibility and precision. However, the potential drawbacks should be

carefully considered, as thermal stress on the layers can affect the magnetic properties. Chemical milling which is another sheet machining process. Unlike the previous two methods, the chemical milling process effectively eliminates the cutting-edge and thermal stress. However, the uniformity of each layer and smoothness may not be guaranteed. In addition, the process is normally too slow and expensive for commercial production.

In this section, the prototype of a 2.2kW eight pole AFIM is introduced. Table 6-1 shows the general size and the proposed materials.

Table 6-1 Dimensions size of 2.2kW eight pole AFIM.

2.2kW eight pole AFIM		
No. of stator slots	N_{ss}	48
No. of rotor slots	N_{rs}	44
No. of phase	m	3
No. of poles pairs	p	4
Airgap length [mm]	D_{airgap}	0.5
Outer diameter [mm]	D_{out}	275
Inner diameter [mm]	D_{in}	163
Axial length [mm]	L	78
Winding diameter	$D_{winding}$	1.219
Winding material	-	Copper
Core material	-	50AW470
Rotor bar material	-	Aluminium

6.2 Stator and Rotor Fabrication

The axial-flux motor stator/rotor lamination process needs special stamping equipment, a rolling stamping machine. The manufacturing process for the axial-flux stator consists of several steps. Firstly, the silicon steel lamination material is cut into a long strip of the designed thickness, which is the sum of the stator/rotor yoke and slot depth. A specialised punching tool is then designed to accurately stamp this steel strip with desired slot shape. As the width of the stator/rotor teeth changes with the radius, the interval between punching adjacent teeth needs to be accurately calculated based on the thickness of layer and radius. Such that when the strip is wound, the desired slot structure is produced. Following this, spot welding is performed on the starting and ending points of the steel strips to fix them in place, ensuring that the laminated stator/rotor core remains structurally stable. The stator/rotor laminated core is further secured by either bonding or laser welding on the back surface to improve its rigidity.
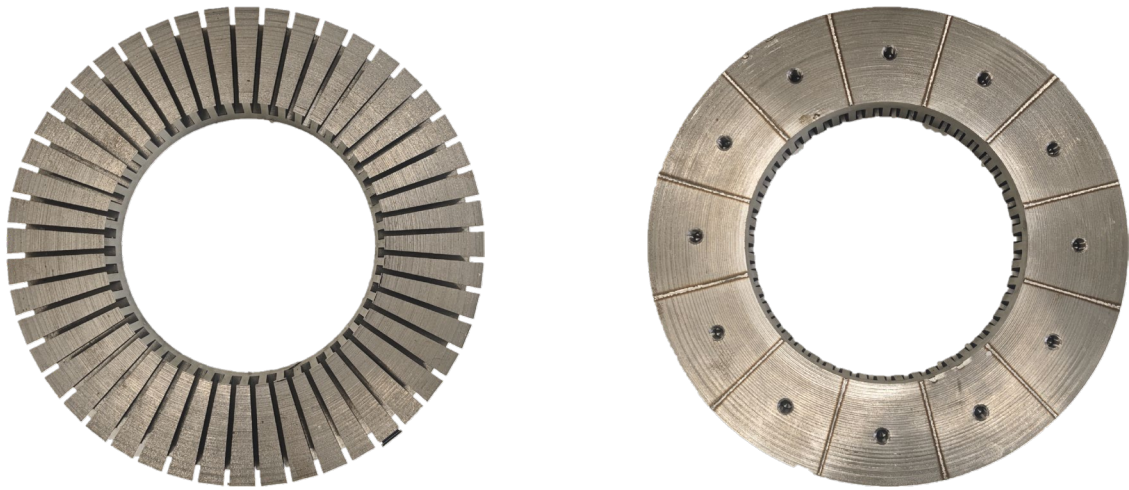
Figure 6-1 Unwound laminated stator, front and back views. The rear view shows radial laser welds and mounting holes.

Figure 6-2 Laminated rotor with aluminium bars front and back views.

The axial flux stator and rotor were constructed by a Chinese company based on the proposed 2.2kW 8-pole design. They also diecast the rotor. The construction process took approximately one months and twenty days for the shipping to Australia. Figure 6-1 shows the laminated stator before winding.

Section 4.1.3 discussed the different winding configurations and case 7 was selected based on its superior electromagnetic performance and manufacturability. Following this decision, the stator is sent to a local electric motor company, Gawler Motor Rewinders, for the winding process. To improve winding flexibility and the ease of insertion of it into the stator slots, each conductor is formed using two parallel strands of copper wire. The overall effective conductor diameter is 1.219 mm, with each individual strand having a diameter of approximately 0.862 mm, as calculated based on the equivalent cross-sectional area. Using two strands of smaller diameter wire facilitates better handling during manual coil insertion

while maintaining the required electrical and thermal characteristics. After coil placement, the stator undergoes vacuum pressure impregnation (VPI) using epoxy resin to enhance insulation strength, improve thermal conductivity, and ensure winding fixation. The impregnated stator is then cured under controlled temperature to solidify the resin. Since the motor adopts a Y-connection scheme, there are only three external leads. A quick resistance check is then conducted using a multimeter, yielding a phase-to-neutral resistance of approximately 2.7ohms. The phase balances was also confirmed, with all three windings showing consistent values. This result was further validated using a power analyser and variac, showing good agreement with the FEA model discussed in Section 4.1.3.

Aluminium die casting is a well-established manufacturing technique for producing squirrel-cage induction rotors. In this project, five prototype rotors were manufactured by the Chinese supplier using aluminium die casting at approximately 640 °C, above the melting point of aluminium. An aluminium alloy containing around 0.16% lead, 12% silicon, and other trace elements was selected to improve flowability and ensure uniform filling of the rotor slots during casting. To reduce torque ripple, the rotor slots are skewed by 7° and designed as closed slots. The skew effectively reduces torque ripple by distributing slot harmonics, while the closed-slot design helps suppress high frequency magnetic variations and simplify the die casting process. In addition, the rotor slots are positioned 1mm below the rotor surface to provide extra machining allowance for surface finishing. This ensures that, after casting and grinding, the rotor surface remains smooth and uniform without compromising the slot geometry (see Figure 6-2 and Figure 6-4).

Following surface finishing, a concentricity check was performed to verify the alignment of the rotor's geometric centre with its rotational axis. This step ensures the rotor runs with minimised vibration and mechanical imbalance during testing.
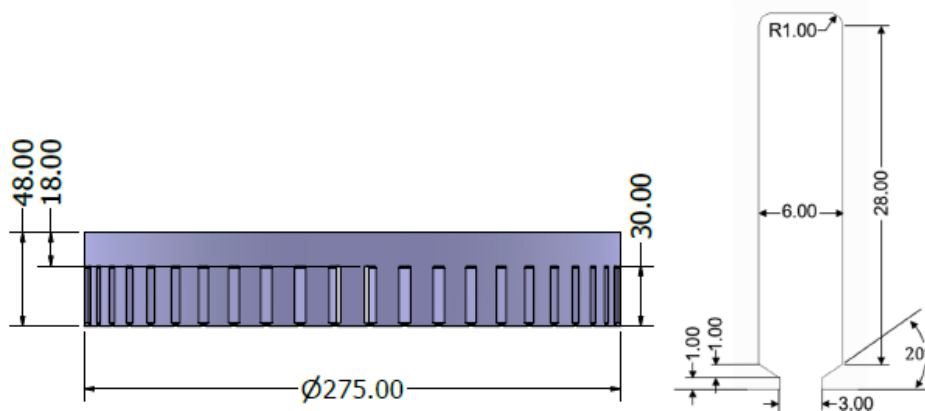
Figure 6-3 Dimensions of proposed AFIM stator and stator slot dimensions.
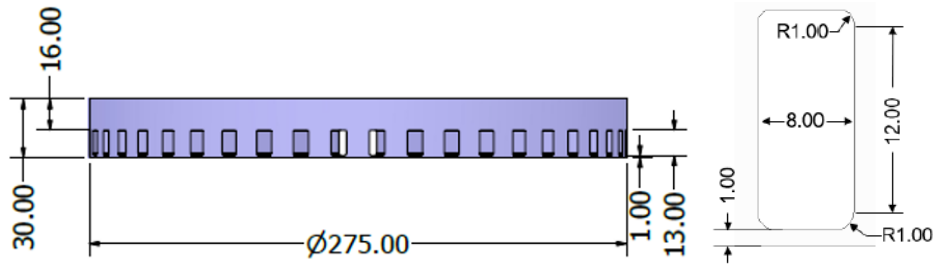
Figure 6-4 Dimensions of proposed AFIM rotor and rotor slot dimensions.

6.3   Housing and Shaft Fabrication
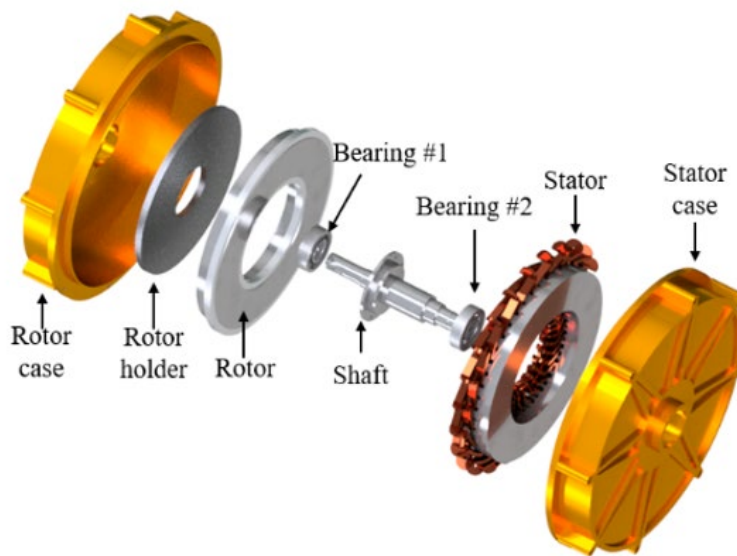
Figure 6-5 Exploded view of the proposed AFIM assembly showing key components, including the rotor case, rotor holder, bearings (#1 and #2), shaft, stator and stator case.

Figure 6-5 illustrates the proposed motor's structure. Unlike conventional radial-flux machines, this axial-flux motor features a significantly larger stator and rotor outer diameter of 275mm, which necessitates a modified shaft design. A fully integrated one-piece shaft with a large-diameter rotor back plate would result in excessive material wastage and inefficient manufacturing. To address this, the design adopts a modular approach which in the central shaft is rigidly connected to the rotor back plate via a bolted flange interface (M10×15mm), as shown in Figure 6-6. This configuration not only improves manufacturing efficiency and material utilization but also allows easier assembly and potential rotor replacement.

Table 6-2 Housing and assembly specifications

2.2kW eight pole AFIM housing and assembly specifications	
Housing wall thickness [mm]	10
Housing outer diameter [mm]	390
Stator end-winding clearance [mm]	30
Total housing axial length [mm]	150
Bench mounting hole	M16 ×1.5 ×20
Frame assembly hole	M10 ×1.5 ×15

(a)   (b)

Figure 6-6 Shaft and rotor holder, (a) 3-D drawing proposed shaft and rotor holder, (b) picture of fabricated shaft and rotor holder.

Figure 6-7 Picture of fabricated motor housing.

The motor housing is fabricated as a single-piece structure via lathe turning, providing high concentricity and mechanical rigidity. Given that the housing is designed for laboratory use, environmental sealing against dust or moisture is not considered. The housing features an approximate wall thickness of 10mm and an outer diameter of 390mm, allowing sufficient clearance for the stator outer end-winding, which is measured at 30mm. As shown in Figure 6-5, the stator is mounted directly to the inner face of the housing via bolts. The threaded hole depth on the stator side is 5 mm, and M10 × 1.5 button-head hex socket screws are used to ensure secure fastening (see Figure 6-7 and Figure 6-8). After

complete assembly, the housing has an axial thickness of approximately 150mm, and the shaft protrudes 195 mm from the mounting surface, ensuring compatibility with the test rig and the coupling fixtures (see Table 6-2).

Figure 6-8 Rotor and wound stator in the housing.

Table 6-3 Key specifications of the SKF 7305 BECBP and SKF 6305 bearings [100].

Parameter	Value	
Model	SKF 6305	
Inner diameter [mm]	25	
Outer diameter [mm]	62	
Width [mm]	17	
Basic dynamic load rating (C) [kN]	23.4	
Basic static load rating (C_0) [kN]	11.6	
Fatigue load limit (Pu) [kN]	0.49	
Limiting Speed	16,000	
Reference Speed	24,000	
Weight [kg]	0.218	
Parameter	Value	
Model	SKF 7305 BECBP	
Inner diameter [mm]	25	
Outer diameter [mm]	62	
Width [mm]	17	
Contact angle (α) [deg]	40	
Basic dynamic load rating (C) [kN]	26.5	
Basic static load rating (C_0) [kN]	15.3	
Fatigue load limit (Pu) [kN]	0.655	
Limiting Speed	15,000	
Reference Speed	24,000	
Weight [kg]	0.233	

Compared to the conventional RFIM, the single-sided AFIM inherently experiences significantly higher axial forces due to its topology. To accommodate this, a 10mm thick rotor holder is incorporated, and suitable bearings (see Figure 6-6) must be selected to withstand the axial load. The axial force calculation method described in **CHAPTER 5** is employed to determine the expected forces. Under the minimum airgap length of 0.1mm, the peak axial forces calculated during steady-state operation are 5.5kN under voltage

driven and 7.7kN under current-driven operation. During the start up transients, where the motor encounters peak flux build-up and maximum slip, the axial forces are observed have transients of up to 20kN. This value is approximately five times the steady-state level and underscores the necessity of proper structural and bearing design in the AFIM.

The design uses two bearings to accommodate the radial and axial loads arising during motor operation. However, to optimise for cost-effectiveness and axial force results, only bearing #1 (see Figure 6-5) is designed to carry axial force. An SKF 7305 BECBP bearing is selected for this role, offering thrust static and dynamic load ratings of 15 kN and 27 kN, respectively. Bearing #2, an SKF 6305, is selected for its radial load-handling capability, with static and dynamic ratings of 12 kN and 23 kN (see Table 6-3).

6.4 Airgap Length Adjuster

Although the designed 2.2kW AFIM design has a nominal airgap of 0.5 mm, achieving such a narrow gap in a large diameter single-sided axial-flux structure presents considerable mechanical challenges. Fixing the rotor at this airgap can lead to failure during rotation due to manufacturing tolerances or axial displacement under load. In fact, a previous 300 W AFIM prototype with a fixed 0.5 mm airgap failed to rotate due to excessive magnetic attraction forces and insufficient structural clearance. To mitigate such risks and enhance the experimental flexibility, the current design adopts an axially-adjustable rotor-side bearing seat.

As shown in Figure 6-9 and Figure 6-10, the bearing seat integrates two functional components: a bearing positioner for precise axial adjustment, and a locking ring to secure the adjusted position. The 3-D design and fabricated parts are shown in Figure 6-9(a)-(b) and Figure 6-10(a)-(b), respectively. The entire airgap adjustment mechanism was custom manufactured at the Mechanical Engineering Workshop of the University of Adelaide.

To reduce the airgap, the adjustment process begins by twisting the outer ring (bearing locker) to the unlocked position. Once unlocked, the inner ring (bearing positioner) is rotated clockwise, moving bearing #1 (see Figure 6-5) closer to the stator, thereby decreasing the airgap. To increase the airgap, the bearing positioner is rotated anticlockwise, shifting the rotor-side bearing seat away from the stator.

(a)   (b)
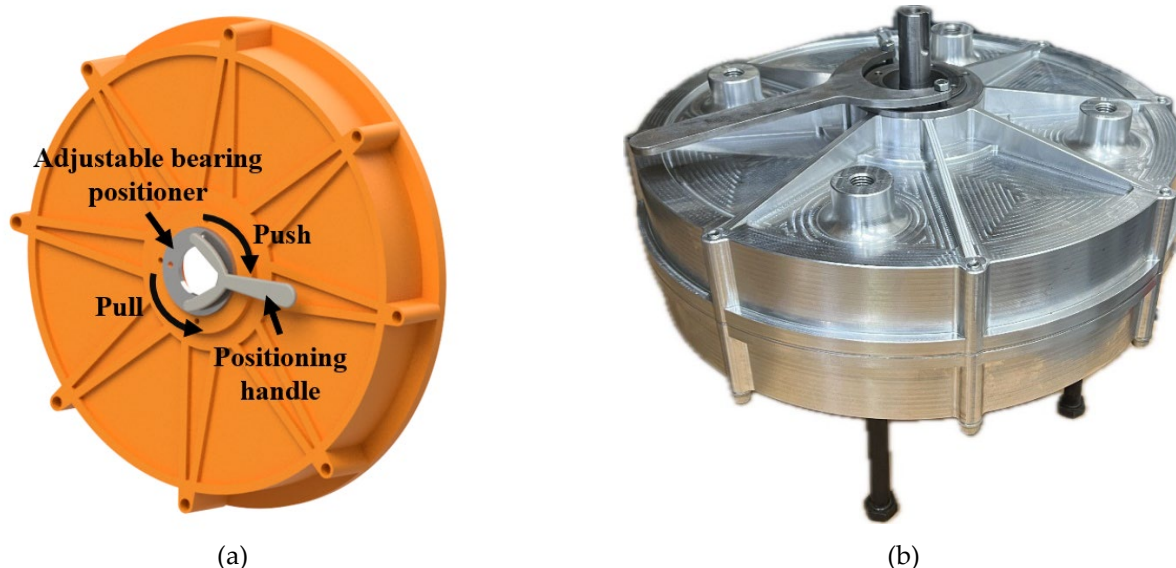
Figure 6-9 Airgap adjuster: (a) 3-D drawing, (b) picture of fabricated airgap adjuster.

(a)   (b)

Figure 6-10 Airgap locker: (a) 3-D drawing, (b) picture of fabricated airgap locker.

The bearing positioner incorporates a precision screw mechanism with a thread pitch of 2 mm, meaning a full 360° rotation results in a 2 mm axial movement. This design enables precise control over the airgap length; for example, a 90° turn yields a 0.5 mm adjustment. To assist with manual adjustment, the eight evenly-spaced structural ribs on its surface can be used, each representing a 45° increment. These ribs serve as reference points, allowing the operator to estimate the rotation angle and, correspondingly, the airgap change with reasonable accuracy. This adjustability is essential not only for characterizing the motor's sensitivity to airgap variation, but also for systematically investigating axial force effects under controlled displacement steps.

Moreover, for enhanced precision, an angular indicator or graduated scale can be integrated into the bearing positioner assembly. This enables direct reading of the rotation

angle, allowing fine control over the axial position without relying solely on visual estimation. Such a feature is particularly useful in experiments requiring repeatable and quantifiable airgap settings. The adjustability is thus essential not only for characterizing the motor's sensitivity to airgap variation, but also for investigating axial force effects under controlled conditions.

CHAPTER 7

EXPERIMENTAL DISCUSSION ON 2.2KW EIGHT POLE AFIM

A proposed 2.2kW, 8 pole, 415V AFIM was prototyped (see Figure 7-1) and then tested in the electric motor laboratory of the University of Adelaide. The specifications of the AFIM are tabulated in Table 6-1. This chapter presents the results from multiple experimental tests to evaluate the electromagnetic performance of the newly prototyped AFIM, including rotating and stationary no-load, locked rotor and load tests.
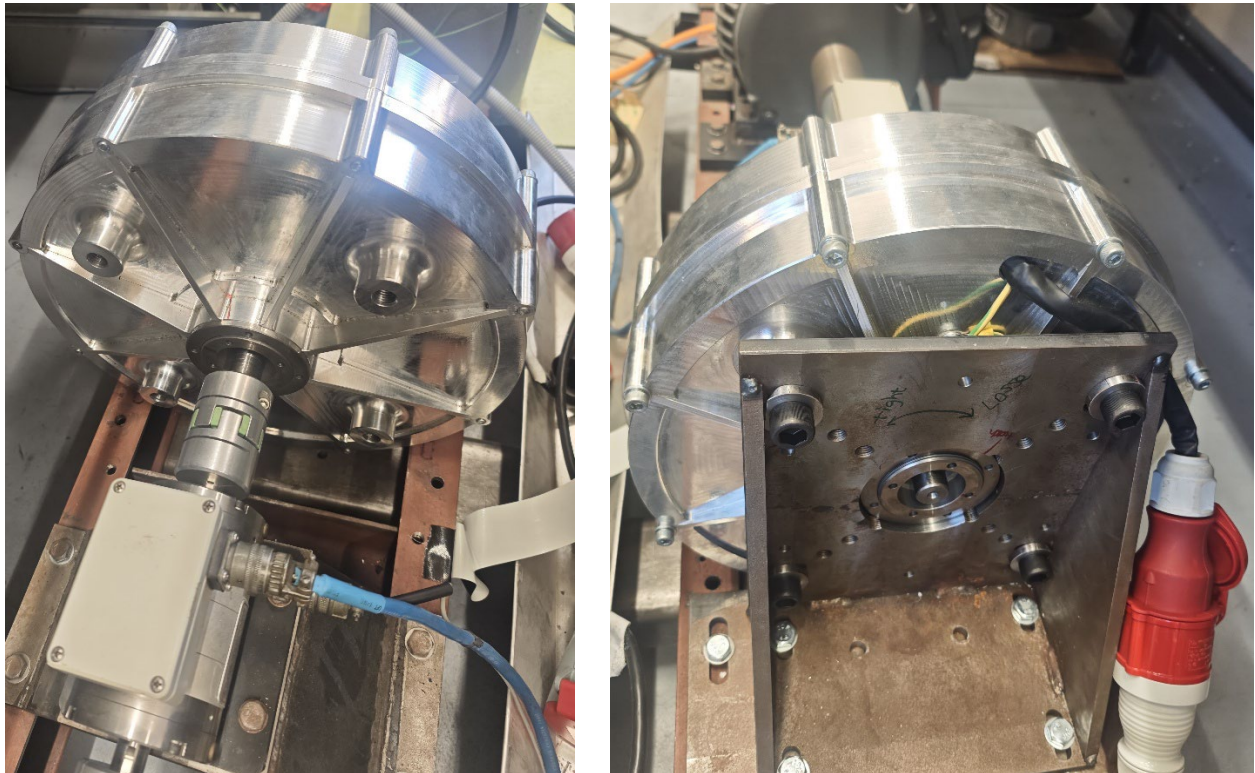
Figure 7-1 Prototype AFIM on the dynamometer.

Table 7-1 Studied 2.2 kW line-start AFIM electrical characteristics and geometry.

Electrical parameters			
Rated line voltage [V]	415	Rated power [W]	2200
Frequency [Hz]	50	Number of poles	8
Geometry and dimensions			
Stator/rotor outer diameter [mm]	275	Stator/rotor inner diameter [mm]	163
Number of stator slots	48	Number of rotor slots	44
Stator slot height [mm]	30	Rotor slot height [mm]	13
Airgap length [mm]	0-2	Frame axial length [mm]	150
Mounting height [mm]	195	Frame diameter [mm]	400

7.1 No-Load Test

Both the AFIMs and RFIMs share the same electromagnetic principles when performing the no-load test. However, for the AFIM, is unique structure allows other testing methods, such as the proposed stationary no-load test with different airgaps. The purpose of the no-load test is to extract the core loss resistance (R_c), magnetizing reactance (X_m), as well as the mechanical losses (P_M). In this test, balanced three-phase voltages are applied to the stator winding at the rated frequency (f_N) with no load applied to the motor shaft. In this test, the slip of the induction machine is very low and is close to zero. It should be noted that the injected terminal voltage is normally varied from (1.1-1.2) V_{rated} to $0.3\,V_{rated}$ while the rotor speed shows no significant reduction [101].
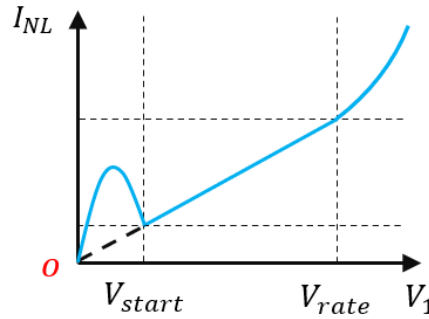
Figure 7-2 A typical current-voltage curve of the IM under no-load operation.

Figure 7-2 shows the typical variation of the measured no-load current with the applied voltage in AFIMs. The black dashed line shows the ideal current results which are typically obtained from FEA simulation, theoretical calculations, and dynamometer-driven no-load test where ethe machine operates at near synchronous speed. During the IM no-load testing, an initial current peak is often observed at low voltages. It arises due to mechanical friction, which acts as a small load torque and prevents the motor from rotating until a certain threshold voltage is passed. As a result, the IM initially operates in the locked rotor condition. Once the applied voltage exceeds this threshold voltage, the motor overcomes the frictional resistance and accelerates to close to synchronous speed. In this region, the no-load current transitions into a near linear relationship with voltage, as the magnetizing current becomes approximately proportional to the applied voltage and the magnetic core operates below saturation. At voltage approaching the rated level, a nonlinear increase in current is typically observed, indicating the magnetic core saturation.

It arises due to the mechanical friction, which acts as a small load and prevents the motor from reaching the synchronous speed. Once the applied voltage exceeds this peak point, the

motor overcomes the frictional resistance and accelerates toward near-synchronous speed. In this region, the no-load current shows a linear relationship with the voltage, as the magnetizing current becomes approximately proportional to the applied voltage and the magnetic core operates below saturation. At voltages exceeding the rated level, a nonlinear increase in current is observed, indicating that the magnetic core saturation.
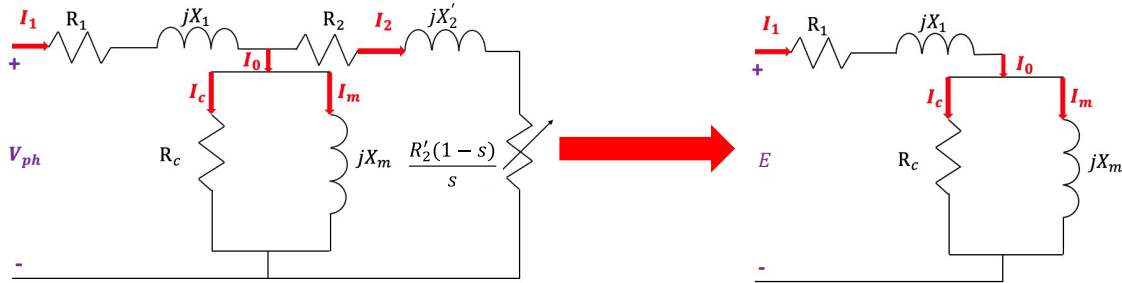
Figure 7-3 Equivalent circuit for induction machine under no-load test.

Figure 7-3 presents the equivalent circuit under the no-load test (right side). It is noted that the resistances and inductances in the no-load condition consists of the magnetizing and stator leakage reactance, and the stator winding and core resistance. Therefore, an extra DC test is required for measurement of the stator winding resistance and the locked rotor test is used to find X_1. The no-load power equation is as follows.

$$P_{NL} = P_{Fe} + P_M + 3I_{NL}^2 R_1 \qquad (7.1)$$

The core losses are proportional to the square of the terminal voltage and the mechanical losses are assumed to be only a function of the rotating speed of motor and not the terminal voltage (only for RFIM) and can be expressed as

$$f(V_1^2) = P_{Fe} \qquad (7.2)$$

In the no-load test, the slip is around zero ($s = 0$), the rotor side is open-circuit and thus the core resistance can be extracted using the following equations:

$$\tilde{E} = \tilde{V}_{ph} - \tilde{I}_{NL}(R_1 + jX_1) \qquad (7.3)$$

$$R_c = \frac{3E^2}{P_{Fe}} \qquad (7.4)$$

The magnetizing reactance under no-load conditions is given below,

$$\tilde{I}_c = \frac{\tilde{E}}{R_c} \qquad (7.5)$$

$$\tilde{I}_m = \tilde{I}_{NL} - \tilde{I}_c \tag{7.6}$$

$$X_m = \frac{E}{I_m} \text{ or } X_m = \frac{3E^2}{Q} \tag{7.7}$$

7.2 Locked-Rotor Test

The main purpose of the locked or blocked rotor test is to determine the stator leakage reactance X_1 referred rotor resistance R'_2 and rotor leakage reactance X'_2. During the test, a reduced voltage is applied while the rotor is held stationary, resulting in a slip $s = 1$. Under this condition, the magnetizing branch draws negligible current due to the low voltage, allowing it to be neglected.
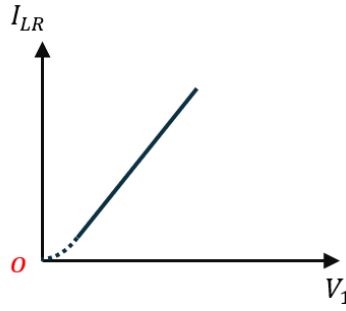
Figure 7-4 A typical current-voltage curve under IM blocked rotor operation.

Figure 7-4 presents the current versus voltage curve under the locked-rotor test. Conceptually, the current is expected to be directly proportional to the terminal voltage ($V_1 \propto I_{LR}$). However, experimental results often do not perfectly reflect this relationship (dashed line in Figure 7-4). At low voltages, the current exhibit a quadratic dependence on the voltage instead of a linear one. This nonlinearity arises due to magnetic saturation in the bridge region. At low excitation levels, the magnetic reluctance of the thin bridge is relatively low until it saturates. The equivalent circuit for the IM is given in Figure 7-5, for locked-rotor condition.
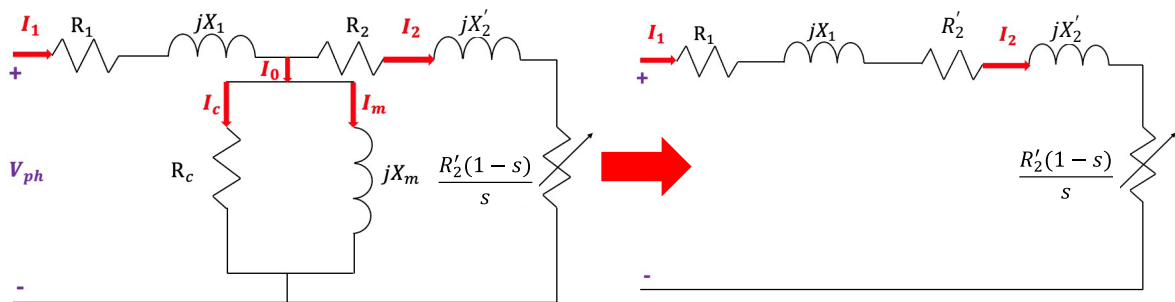
Figure 7-5 Equivalent circuit for IM under the blocked-rotor test.

The rotor resistance R_2' and locked-rotor impedance can be obtained via the equations below and knowing the value of the stator resistance R_1 from a DC test.

$$P_{BR} = 3I_{BR}^2(R_1 + R_2') \tag{7.8}$$

$$\frac{V_{BR}}{I_{BR}} = Z_{BR} = \sqrt{(R_1 + R_2')^2 + (X_1 + X_2')^2} \tag{7.9}$$

Therefore, the sum of the reactance is:

$$X_{BR} = X_1 + X_2' = \sqrt{(Z_{BR})^2 - (R_1 + R_2')^2} \tag{7.10}$$

It should be noted that the actual split of the rotor and stator reactance is unknown, but empirical equations can be used to roughly calculate the split. The squirrel-cage induction machine can be divided into the four classes listed in Table 7-1 [93].

Table 7-2 Different Classes for Various Induction Machines.

Class A	$X_1 = X_2'$. Normally starting torque with high starting current, low operating slip.
Class B	$X_1 = 0.4X_{BR}$, $X_2' = 0.6X_{BR}$. Normally starting torque with low starting current, low operating slip.
Class C	$X_1 = 0.3X_{BR}$, $X_2' = 0.7X_{BR}$. High starting torque with low starting current, high operating slip.
Class D	$X_1 = X_2'$. High staring torque with high starting current, high operating slip.

7.3   Loss Breakdown Conceptual Discussion
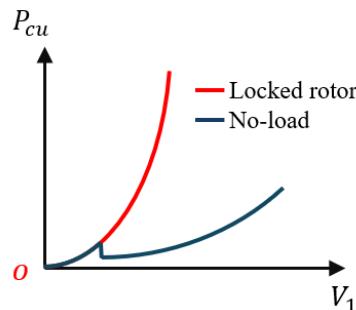
Figure 7-6 Expected trends of copper loss under the IM no-load and locked rotor tests.

The loss components can be separated through the no-load and locked rotor tests. Figure 7-6 compares the copper losses (P_{cu}) as a function of the supply voltages under the locked-

rotor and no-load operations. When the rotor is locked, no back EMF is induced resulting in a high current flow through the stator windings. At low voltages, the copper loss in the no-load test shows a similar trend to the locked-rotor test, as the motor needs sufficient torque to overcome the starting friction. A higher voltages, as the rotor rotates at or near the synchronous speed (see Figure 7-7), a larger back EMF is generated. Hence the current is smaller, and the copper losses become lower.
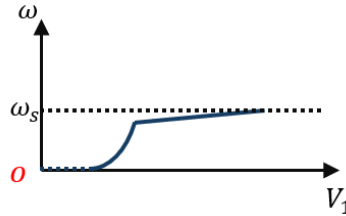
Figure 7-7 Expected trends of speed as a function of supply voltage.
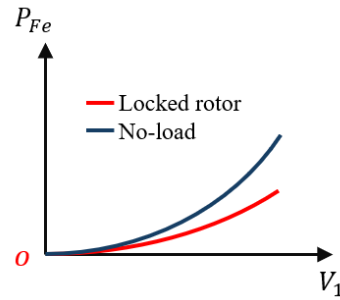
Figure 7-8 Expected trends of core losses under the no-load and locked-rotor tests with supply voltage.

Figure 7-8 presents the expected trends of core losses under the no-load and locked-rotor tests. The eddy-current loss (P_{eddy}) and hysteresis loss (P_{hyst}) are the two main loss components and they vary roughly quadratically with the supply voltage (see Equation (7.11)).

$$P_{Fe} = P_{eddy} + P_{hyst} = k_e B^2 f^2 + k_h B^2 f \tag{7.11}$$

where k_e and k_h are the eddy current and hysteresis loss coefficients, respectively, and f and B represent the frequency and the peak flux density.

The magnetic flux density in the core is proportional to the supply voltage ($B \propto \frac{V_1}{f}$). In the no-load test, the rotor rotating speed is very close to synchronous speed and the back EMF is roughly equal to the terminal voltages. In the locked-rotor test, the rotor is stationary, and the back EMF is zero. The most of supply voltage appears across the winding resistance

and leakage reactance (see Figure 7-8) resulting in a much lower flux density in the core (see Table 7-3).

Table 7-3 Comparison of the core loss related the parameters under the no-load and locked rotor tests.

	B(T)	F_r(Hz)	P_{Fe}
No-load	Higher	0	Higher
Locked rotor	Lower	50	Lower

The above loss breakdown theory is well suited to both the RFIMs and AFIMs. However, the presence of the large axial forces in the AFIMs makes it more challenging to separate the core and mechanical losses under no-load testing.
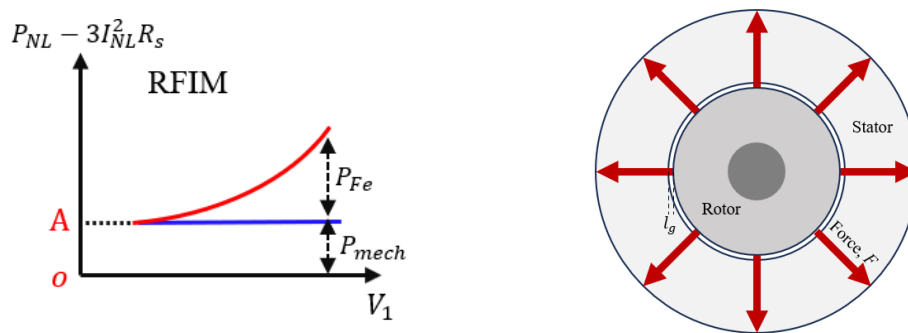
Figure 7-9 The expected trends of core loss and mechanical loss with supply voltage in the RFIM.
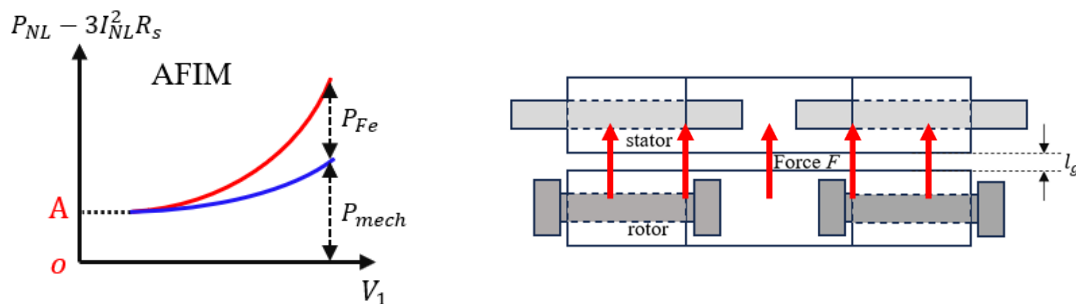
Figure 7-10 The expected trends of core loss and mechanical loss with supply voltage in a single-sided AFIM.

Figure 7-9 and Figure 7-10 present the sum of the no-load core loss and mechanical loss under different applied voltages. Extrapolating the red curve to the point (A), where the terminal voltage is zero, is a commonly used method for estimating the mechanical loss for RFIMs but this is not suitable for AFIMs. This can be explained by the force distribution

within the motor (see right side of Figure 7-9 and Figure 7-10). In the RFIM, the mechanical loss (bearings) is only affected by the rotational speed, whereas in AFIMs, this is affected by both the rotational speed and by the axial force. The axial force in AFIMs results in greater bearing losses. As a result, a new theoretically predicted loss curve is developed specifically for AFIMs. In AFIMs, the mechanical loss is no longer constant and likely increases approximately quadratically with the applied voltage.

In RFIMs, the mechanical loss is influenced by rotating speed. In contrast, in AFIMs, the mechanical loss is affected not only by the rotating speed but also by the axial force. The axial force in AFIMs imposes significant load on the bearing system, leading to a greater rolling resistance. As a result, a new theoretically predicted loss curve is given for the AFIMs. Its mechanical loss is no longer constant and increases approximately quadratically with the applied voltage.
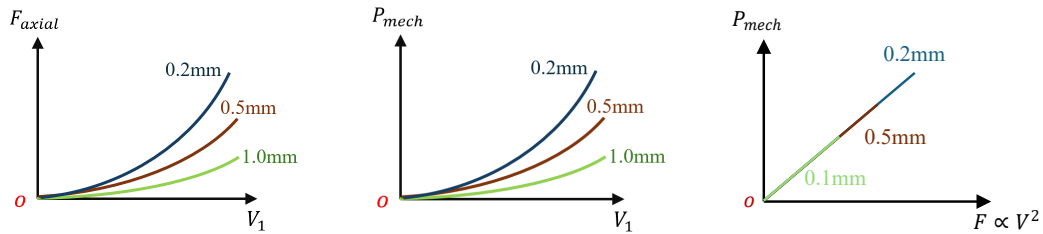
Figure 7-11 Expected effect of airgap length effects on the mechanical loss and axial force variations with supply voltage.

Figure 7-11 presents the expected experimental results that the axial force is proportional to the square of voltage and that the mechanical loss is proportional to force. These curves demonstrate that the airgap length significantly affect these parameters. With this understanding, the AFIM performance can be accurately predicted, and the design can be optimised by adjusting the airgap length.

7.4 Stationary No-Load Tests for AFIM with Different Airgaps

In the no-load testing of RFIMs, the rotor rotates freely while no mechanical load is applied. This enables the measurement of the total no-load power, comprising the stator copper loss, core losses in the stator and rotor, as well as mechanical losses. The mechanical losses are typically assumed to be constant across the range of voltage tested and can be

estimated by extrapolating the no-load power versus squared voltage curve to zero voltage, where the core loss is negligible.

However, for the single-sided AFIMs, the situations become significantly more complex. The presence of a large voltage-dependent axial force, especially under the small airgaps, introduces additional mechanical losses arising from the increased bearing friction (see Figure 7-10 and Figure 7-11). These losses are nonlinear with respect to the supply voltage and complicate the separation of core and winding losses.

To address this issue, this section introduces a new stationary no-load test method tailored for the single-sided AFIM. In this approach, the back of the rotor or an uncast rotor is placed on the wound stator, separated by the non-magnetic spacers of the known thickness. The rotor iron completes the magnetic path, allowing "no-load" excitation of the stator under controlled airgap conditions. Stationary testing has been used in the past for the measurement and comparison of stator core losses under various conditions [102]. However, it has not previously been adopted, as in this study, as a substitute for the conventional rotating no-load test in induction machines.
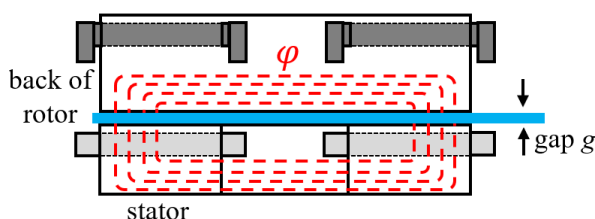
Figure 7-12 The flux path in the stationary no-load test using the back of a cast rotor.

Table 7-4 Comparison of conventional and stationary no-load tests for AFIMs.

Aspect	Conventional no-load test	Stationary no-load test
Rotor rotation	Required	Not required
Test complexity	Requires full assembly	Structurally simple
Rotor current	Small	Zero
Mechanical loss	Voltage dependent	Eliminated
Influence of axial force	Significant	None
Measurable losses	Core, winding, mechanical	Core, winding
Applicable to small airgaps	Poor	Good
Accuracy of loss separation	Limited	High
Voltage current characteristic	Affected by mechanical loss	Clearly observable

As shown in the Figure 7-12, the stator is energised by a three-phase voltage, and the generated magnetic flux circulates the stator yoke and teeth, through the airgap, and into the rotor yoke. Under these conditions, the AFIM can be represented by a simplified equivalent circuit consisting solely of the magnetising branch: stator resistance, magnetising

reactance, and core loss resistance. The elimination of the rotor copper loss and mechanical loss allows for a more accurate characterisation of the voltage-current and core losses. When combined with the conventional no-load test results, it will be shown that this method enables the estimation of the voltage- and airgap-dependent mechanical losses through a comparative analysis. Table 7-4 presents the differences between the conventional and stationary no-load tests.

| Case A: back of cast rotor | Case B: back of uncast rotor | Case C: front of uncast rotor |
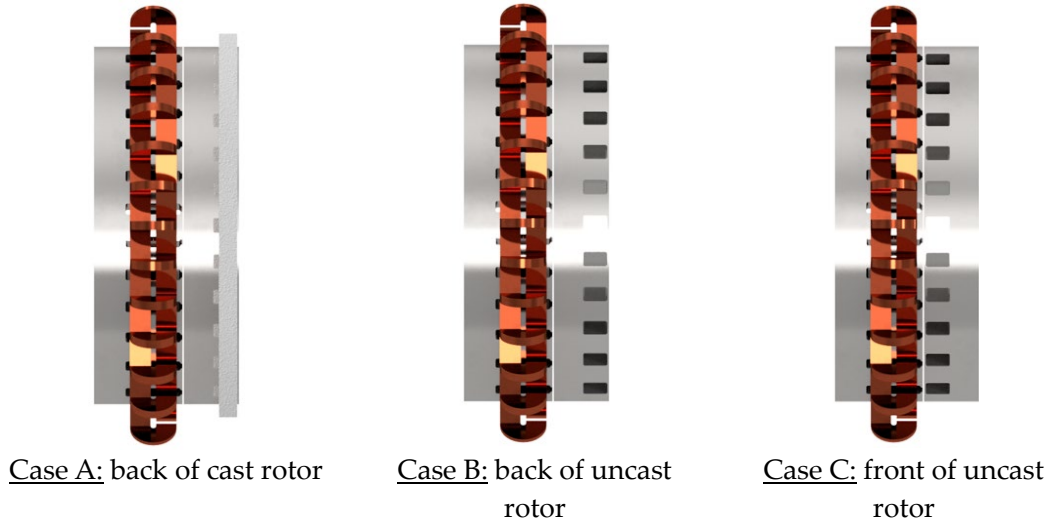
Figure 7-13 AFIM stationary no-load test schematics.

Figure 7-13 presents the three alternative AFIM stationary no-load test arrangements using (1) the back of the cast rotor, (2) the back of the uncast rotor, and (4) the front of the uncast rotor. These cases provide flexibility for performing the test before or after rotor casting. In cases A and B, the back side of the rotor is placed on the air gap. These configurations provide a relatively short magnetic flux return path to the stator. Case C, where the front side of the uncast rotor faces the stator, represents the configuration that most replicate the magnetic path conditions of a conventional rotating no-load test.

(a) Case A   (b) Rotational Case
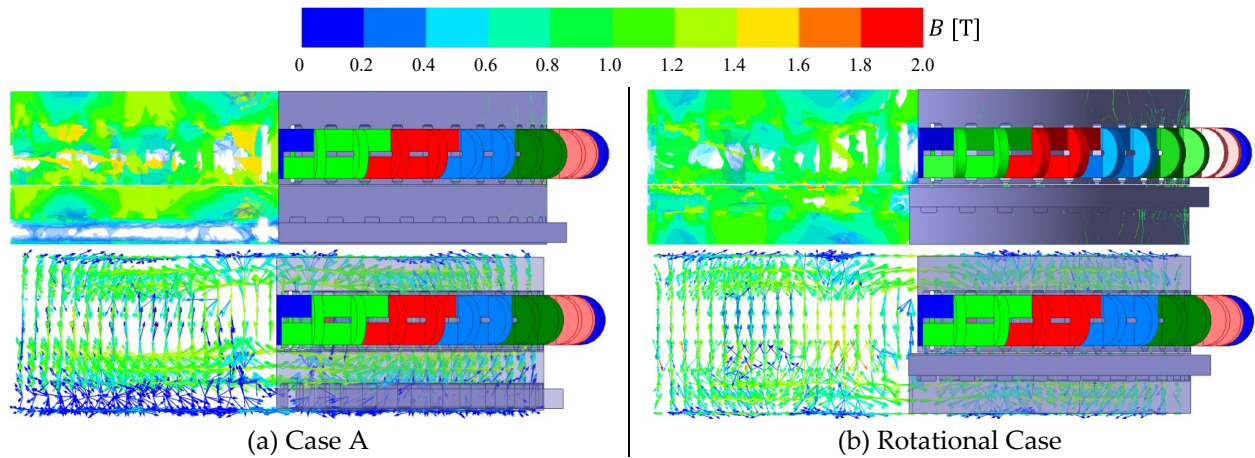
Figure 7-14 Magnetic flux density (B) field comparisons between (a) Case A and (b) Rotational Case.
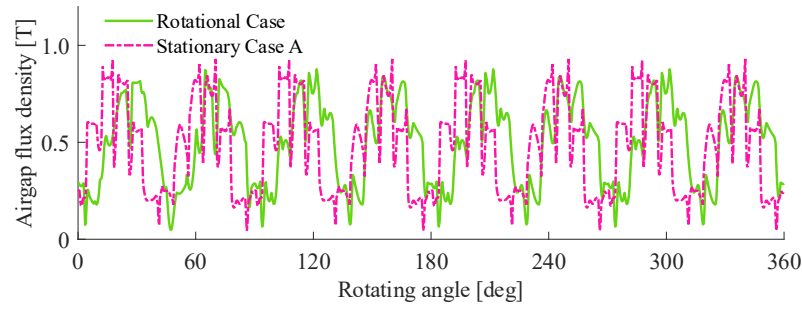
Figure 7-15 FEA airgap flux density comparison between rotational case and stationary case A.

Figure 7-14 compares the airgap magnetic flux density distribution for the stationary (Case A) and the rotational cases, both of which exhibit a similar range (0-2T). In Case A, the flux density field exhibits shorter flux paths and more concentrated flux density vectors, suggesting a shorter effective magnetic path length. In contrast, the rotational case demonstrates elongated and spatially uniform flux vectors, indicative of a longer magnetic flux path due to the slotting effect.

Figure 7-15 indicates the differences between the rotational case and the stationary case A. In case A, the airgap flux density consists of a 50Hz fundamental component and additional harmonics, which collectively produce the sharp peaks observed in the figure. In contrast, during synchronous rotation under no-load conditions, the flux density becomes fundamentally dominated (50 Hz) as the rotor rotates in synchronism with the stator field, effectively at zero relative frequency, resulting in the smoother profile observed.
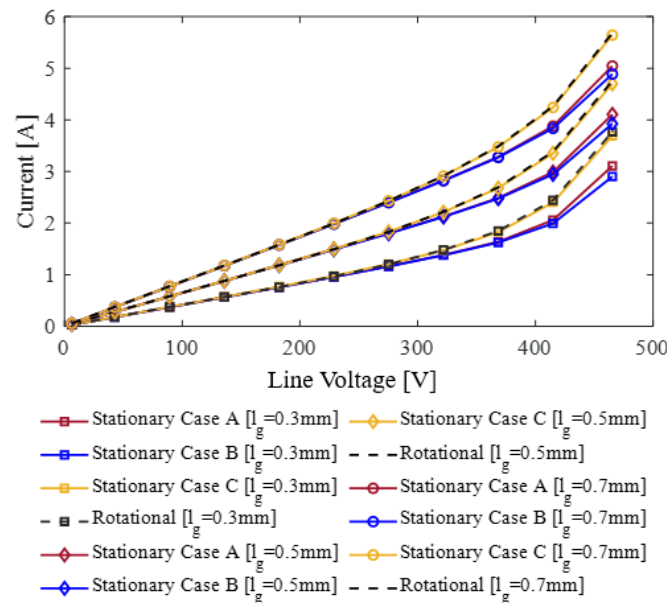
Figure 7-16 3-D FEA stationary no-load current versus voltage at different airgap lengths for back of cast rotor test, back of uncast rotor test, and front of uncast rotor test.

To verify the feasibility of the stationary no-load test method, the AFIM stationary no-load test is first done through 3-D FEA simulations for the different configurations (see Figure 7-13). Figure 7-16 illustrates the stationary no-load test voltage and current characteristics. All four cases have similar voltage and current curves in the unsaturated region. In case A and case B, the back of the rotor with and without bars are placed on the wound stator, case A has a slightly higher current than case B at higher voltages (larger than rated voltage of 415V), likely due to the presence of the aluminium rotor bars. These two configurations show comparable results. Case C, the front of the rotor with no bars, and the rotational case yield similar results. However, case C and the rotational case have a steeper rise in the current at higher voltages. In the lower voltage no-load tests, the magnetic core operates below saturation, and the flux path length presents minimal effects on the current. At higher voltage, the configurations with longer flux paths (case A and case B) give higher magnetic reluctance resulting in higher magnetizing current. As a result, the stationary no-load test method is acceptable for assessing the V-I characteristics.
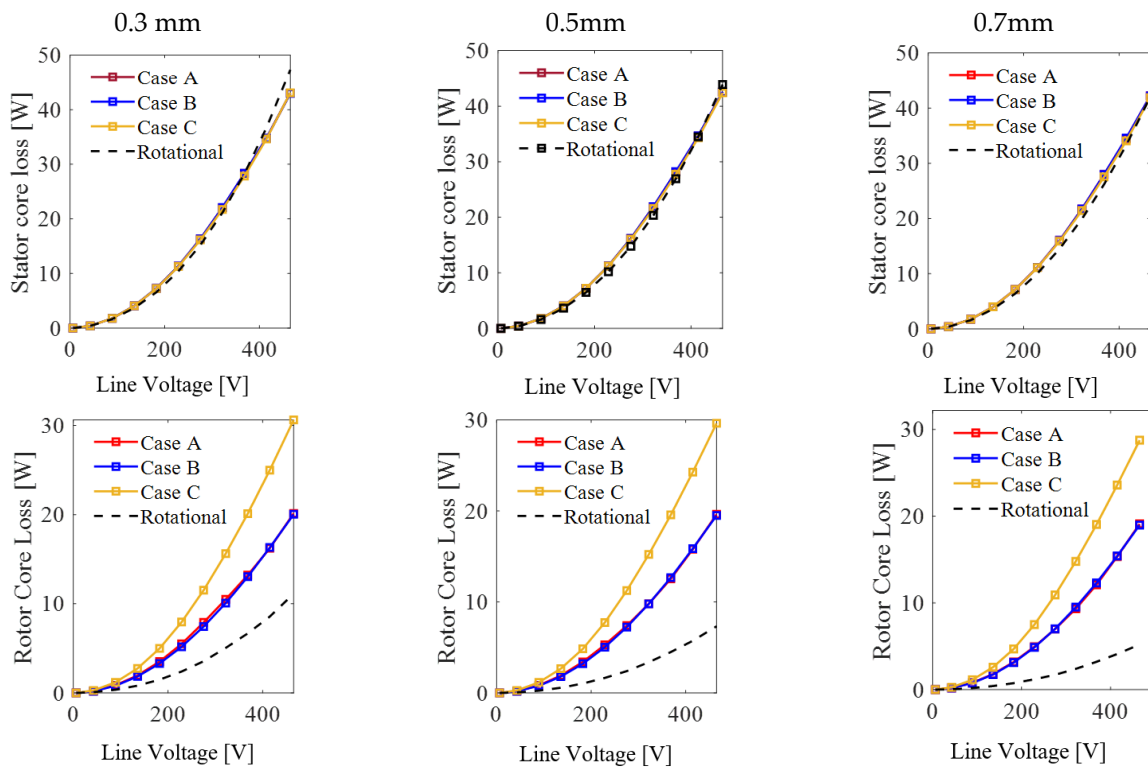
Figure 7-17 Core losses from 3-D FEA stationary and rotational tests.

The 3-D FEA no-load simulation results allow for separating the stator and rotor core losses (see top of Figure 7-17). As the stator core loss is primarily affected by the terminal voltage and frequency, hence all the cases give similar results. the lower figures of Figure 7-17 compare the core losses of the AFIM under the stationary and rotational no-load tests for different airgap lengths and structural configurations (Case A-C). It is observed that the

rotor core loss in all stationary cases is significantly higher than that in the rotational case across the full voltage range. In the stationary tests, the rotor remains static while being exposed to the full relative frequency (50Hz) alternating magnetic field generated by the stator. As a result, this leads to substantial hysteresis and eddy current losses. In contrast, under rotational conditions, the rotor operates near synchronous speed, and the relative frequency between the rotor and stator magnetic field is reduced to around zero. Consequently, the rotor experiences a much lower frequency, resulting in significantly reduced core losses.
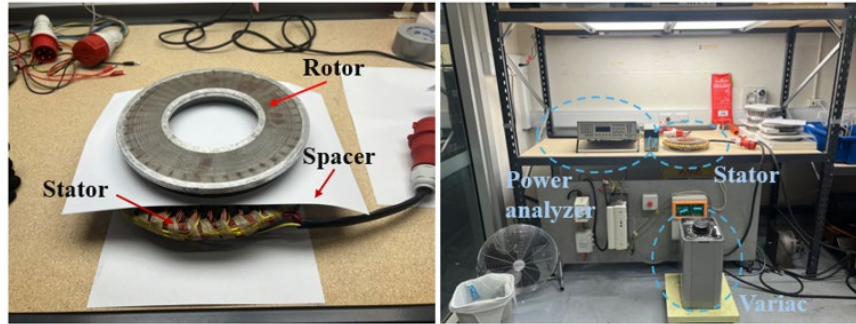
Figure 7-18 AFIM stationary no-load experimental set-up (left: stationary test, right: testing rig).

Among all the stationary cases, case C exhibits the highest rotor core loss, due to the presence of rotor slots, the flux has the longest rotor path length (through the rotor teeth and yoke). Therefore, the rotor core loss obtained from the rotational test is considered to best represent the fundamental rotor core loss. However, the comparison of the calculated and measured iron loss in the stationary test provides a convenient means for checking the accuracy of the modelled iron loss without the need to separate mechanical losses.

As only a cast rotor is available in the lab, only case A could be tested. To achieve the different airgap lengths, non-magnetic spacers with known thickness ($\approx 0.1mm$ per piece) are placed between the stator and the rotor. The phase-to-phase resistance is initially checked and was measured at 5.4ohms, hence the phase -to-neutral resistance of 2.7ohms. Figure 7-19 shows the current and corresponding power loss measured under the stator-only condition, where up to 20% of the rated voltage is incrementally applied. As observed, the phase current exhibits a nearly linear relationship with voltage, which aligns with the expectations for this configuration. Such stator-only testing can also be used to estimate the iron loss characteristics of the stator core material under varying excitation conditions. By repeating the measurement across different voltage levels or frequencies, one can extract the dependency of core loss on flux density and frequency. This makes the method suitable for validation of core loss models [102].
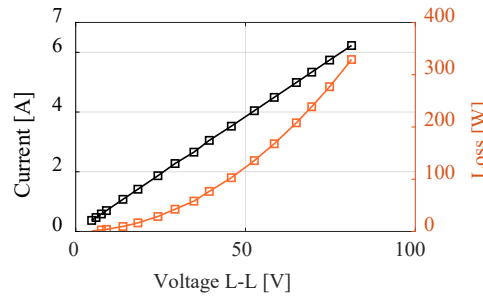
Figure 7-19 Stator-only testing, with 20% of rated voltage applied.
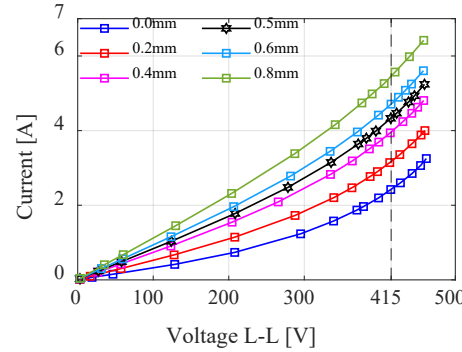
Figure 7-20 Stationary experimental testing showing current versus voltage at different airgaps.

Figure 7-20 presents the measured voltage-current curves for six different airgap lengths. It is observed that at same excited voltage and frequency, the current increases with airgap length. This is because the longer airgap length increases the reluctance of the magnetic circuit and reduces both the magnetizing inductance (L_m) and magnetizing reactance (X_m). The test results also proved the prototyped AFIM is not highly saturated as the curve is nearly linear, particularly for currents below the rated voltage of 415V. It is also essential to monitor any increases in winding resistance (R_s) due to heating. The winding resistance was initially measured at 2.7ohms, which then increased to 2.85ohms after 30 minutes of testing. To accurately separate the winding loss (see Figure 7-19), it is necessary to allow for cooling after each set of testing.
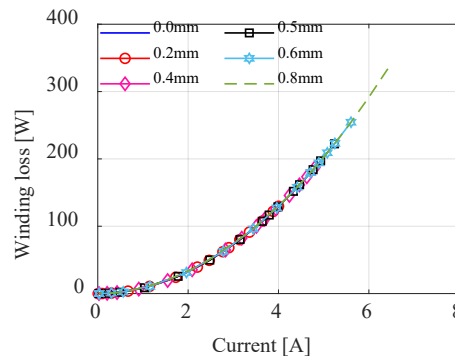
Figure 7-21 Separated loss from experimental stationary no-load test for winding losses.
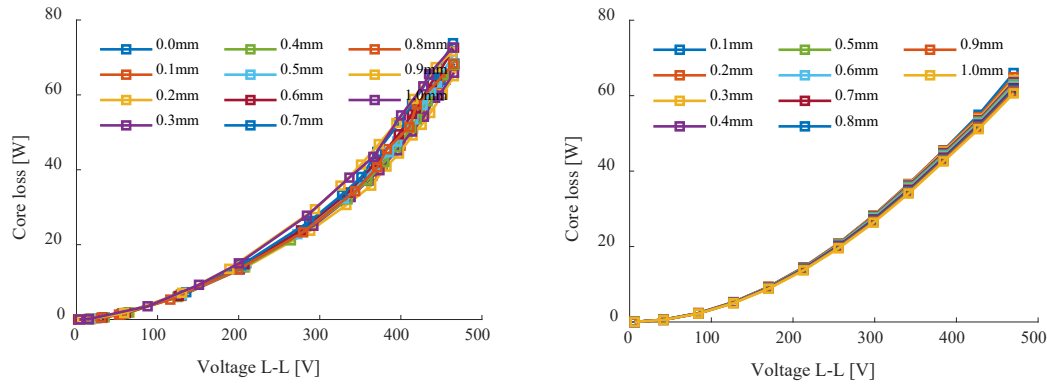
Figure 7-22 Core loss comparison between the experimental and 3-D FEA stationary no-load tests.

Figure 7-22 shows the results of the experiment and FEA stationary no-load tests, which demonstrate the core loss versus terminal voltage for different airgap lengths. The test aims to validate that the core in the lab and FEA model present similar properties. For the lab tests, the total power can be captured from the power analyser and hence the core loss is extracted from the differences between the input power and the winding loss. It is important to note that the changes in the stator resistance due to the temperature fluctuations are not accounted. The core loss from the lab shows variations between 64W to 73W. The core loss from FEA shows variations between 60W to 68W. Consequently, the stationary no-load FEA and experiment results show a reasonable match. This also confirms that the FEA model is suitable for further validation and comparison with the experimental results.

(a)

(b)
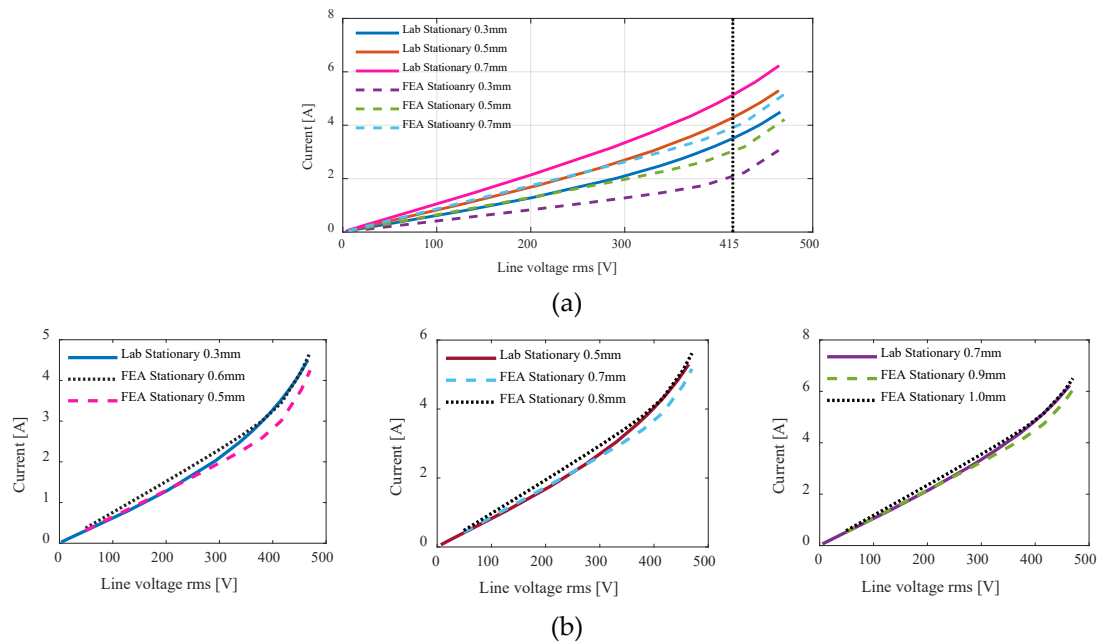
Figure 7-23 Stationary no-load test for both the lab and FEA, (a) non-corrected lab versus FEA stationary results, (b) corrected lab versus FEA stationary results with offset of 0.2mm or 0.3mm.

The equivalent circuit parameters from the proposed AFIM stationary FEA no-load and the locked rotor simulations were used to predict the AFIM performance and the results compared with the full FEA results (see Figure 7-24). There is a good correspondence at the key points, such as at the starting, and from no-load to rated load, however in the middle speed region, there are some significant differences. Thus, the proposed AFIM stationary test method has the capabilities to initially predict the electromagnetic performance with the relatively simple tests on the manufactured and unassembled AFIMs.

Figure 7-23 illustrates the FEA and lab stationary no-load current versus voltage at different airgaps of 0.3mm, 0.5mm, and 0.7mm. Notably, the airgap length can be easily and precisely set at the predefined value in the FEA modelling. However, achieving the exact airgap length in the lab is difficult due to the surface irregularities, which produce an airgap length "offset" value. This offset value can be experimentally determined by comparing the FEA and lab results and was found to be about 0.2mm (see Figure 7-23(b)). It illustrates the lab test results show good correspondence with the FEA simulation results with this offset value for the different airgap values. Figure 7-24 and Table 7-5 show the simplified equivalent circuit parameters from the lab and FEA stationary tests, excluding the core loss resistance (R_c). As previously discussed in Figure 7-17, the stationary condition leads to an overestimation of the rotor core loss, which undermines the accuracy of R_c obtained from the no-load test. Therefore, the R_c is not reported here to avoid the misleading interpretation.

Table 7-5 Equivalent circuit parameters for different methods.

	R_1 [Ω]	R_2' [Ω]	X_m [Ω]	X_1 [Ω]	X_2' [Ω]
FEA EC	2.7	2.52	50.72	3.85	3.85
Lab stationary EC	2.7	2.14	67.72	4.21	4.21
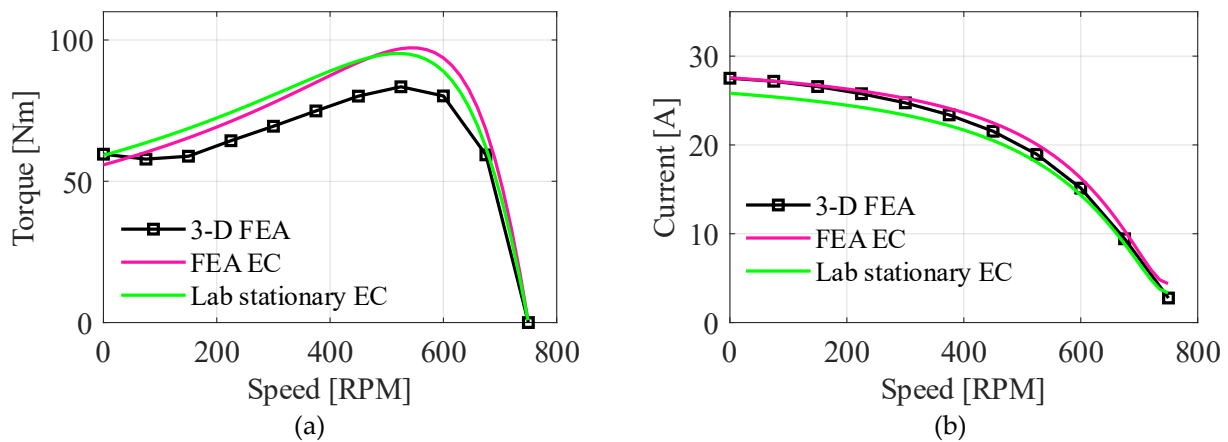
Figure 7-24 Corrected stationary FEA EC, rotating FEA, and FEA EC (a) torque and (b) current characteristics using an offset gap value of 0.2mm.

7.5   Rotating Tests for AFIM with Different Airgaps

As 3-D FEA has now confirmed the validity of the proposed stationary no-load test using both stationary and rotating tests, only experimental comparisons between the stationary and rotating tests are presented in the following sections. As mentioned in Section 6.4, the bearing positioner has a thread pitch of 2mm per 360° rotation, which allows the airgap to be adjusted by controlling the rotation angle of the positioner. The "zero" airgap position, where the rotor just contacts the stator was found to occur at an angle of 18°. This angle serves as the baseline reference for the estimated airgap values during the test.

It is also important to note that the designed airgap adjustor uses the motor housing as a reference, where eight evenly-spaced structural ribs around the circumference provide an approximate 45° increments for estimation (see Figure 7-26(a)). Based on this thread pitch, each 45° rotation corresponds to an airgap change of 0.25 mm. However, due to the absence of a precise angular index, the actual rotation angle during adjustment was difficult to determine. This limitation was consistently observed during experimental procedures, where repeatable and fine airgap adjustments proved challenging. Therefore, the airgap values reported in the following sections and sometimes a range (eg. 0.5-0.625mm) rather than exact values, in order to more accurately represent the real conditions faced during the testing.

Although the reported airgap values are approximate, further insight into the actual airgap value can be obtained by comparing the experimental and FEA results. As demonstrated in the stationary no-load test, such comparisons are useful for identifying the airgap offset value from the true electromagnetic gap. In the following section, no offset calibration was performed during the initial testing phases, neither under rotating no-load nor loading conditions.

The results presented in the following sections show the above airgap estimate and do not incorporate any offset, though this estimated later. This approach ensures that the original test conditions are represented and that the impact of mechanical and assembly tolerances remains visible. To highlight the influence of airgap offset, additional figures are provided in which the performance curves are reprocessed with an estimated correction applied. A example is given in Figure 7-46, where a consistent discrepancy of approximately 0.3 mm between experimental and FEA results suggests this is the likely airgap offset, caused by mechanical tolerances in the assembled prototype.

7.5.1 Rotating No-load Tests for AFIM with Different Airgaps
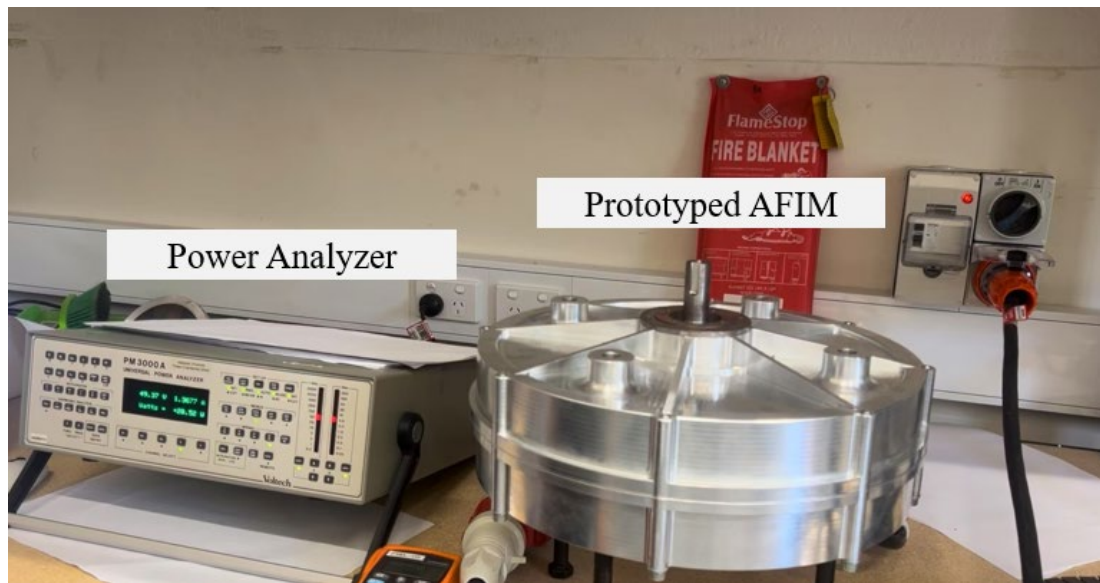
Figure 7-25 Prototype AFIM rotating no-load test setup.

(a)	(b)
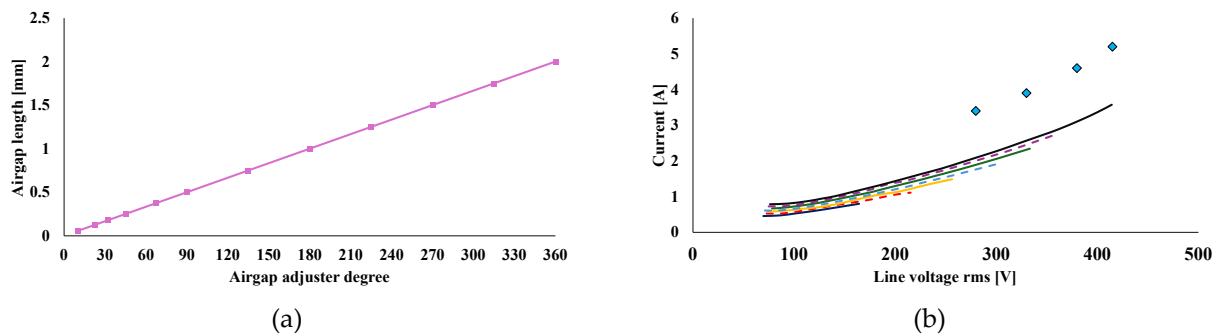
Figure 7-26 (a) Airgap adjuster rotation angle versus corresponding expected airgap length, (b) Measured no-load current versus line voltage at smaller airgap settings.

Table 7-6 Airgap adjuster rotation angle versus airgap and the corresponding maximum operating voltage.

Adjuster degree [deg]	Airgap change [mm]	Max volts [V]
≈18	≈0.00	-
≈22	≈0.12	164.3
≈40	≈0.20	215.5
≈55	≈0.30	256.4
≈65	≈0.37	300.5
≈75	≈0.42	333.4
≈80	≈0.45	358.7
≈90	≈0.50	414.4

Figure 7-25 presents the setup used for the no-load rotating test of the prototyped AFIM. Figure 7-26(b) shows the voltage and current profiles at lower airgap length settings. The light blue symbols indicate results obtained prior to rotor surface smoothing, reflecting the minimum tolerable airgap of the unsmoothed prototype. It is also observed that the assembled AFIM fails to exhibit complete I-V characteristics at small airgaps above certain voltage levels (see Figure 7-26(b)), accompanied by abnormal acoustic noise indicative of rotor-stator contact. This is likely caused by the axial force, resulting in reduction of the airgap and hence rotor-stator contact.

Table 7-6 presents the relationship between the adjustment rotation angle, the resulting feed distance, and the corresponding maximum operating voltage at which the motor can safely function without rotor-stator contact. As the adjuster rotates from approximately 22 degrees to 90 degrees, the expected airgap length increases from about 0.13mm to 0.5mm, allowing higher operating voltages from 164V to 414V. The plotted curve on the right illustrates this trend, showing a nonlinear relationship between voltage and displacement. This behaviour reflects the increasing axial force and mechanical displacement risk at smaller airgaps, thereby the prototype AFIM with rated voltage is unable to safely operate at the expected 0.5mm airgap. As the airgap increases, the risk of rotor-stator contact is reduced. Experimental observations confirm that at larger airgap settings, the motor can be gradually run up to the rated voltage without any physical contact between the rotor and stator.

Figure 7-27 compares the no-load current-voltage characteristics obtained under stationary conditions with those measured during rotation, both with and without the dynamometer connection, across a range of airgaps. It is observed that when the airgap adjuster reaches around 90 degrees to 112.5 degrees, corresponding to an airgap length of 0.5mm to 0.62mm, the motor can complete the full current-voltage profile without rotor-stator contact. The figures show a close agreement between the stationary no-load testing method. This consistency demonstrates that the stationary configuration, by simplifying experimental procedures, serves as a practical alternative for characterising the magnetising current behaviour in the AFIM.
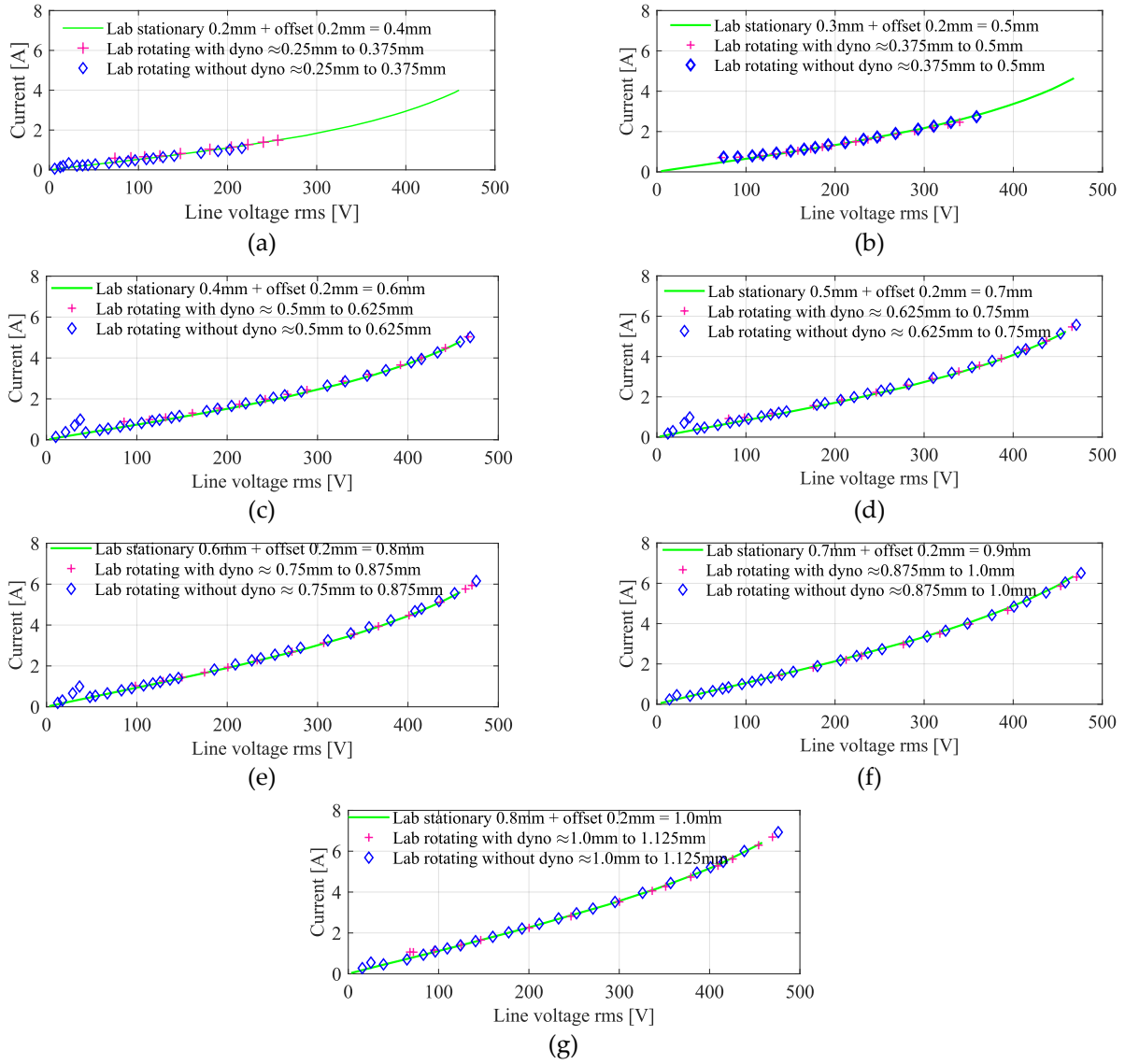
Figure 7-27 No-load experimental current versus line voltage at various airgaps under three conditions: stationary (green line), rotating with dynamometer connection (pink crosses), and rotating without dynamometer connection (blue diamonds).

The magnetizing reactance X_m is an important parameter for characterising the magnetic behaviour and saturation effects in induction motors, particularly in the axial-flux configurations where airgap sensitivity is high. A comparison of the value of X_m of the AFIMs obtained from stationary and rotating no-load tests under various airgap lengths is shown in Figure 7-28. The results demonstrate a consistent trend wherein X_m initially rises with increasing current, reflecting the nonlinear permeability response at low excitation levels. A comparative analysis of the stationary and rotating profiles indicates a close agreement, especially within the mid-to-large airgap regimes (0.8 mm to 1.0 mm). This correlation substantiates the stationary no-load testing method as a reliable and repeatable technique for estimating the magnetizing reactance of AFIMs. The method proves particularly valuable in scenarios where rotational testing is constrained by mechanical

imbalance, high axial force, or safety concerns, such as in early-stage prototyping. These findings also highlight the unique challenges faced in AFIM design, where the axial airgap must be tightly controlled to balance electromagnetic performance against mechanical feasibility. The stationary testing process developed herein offers a practical and effective method for design verification without the need for complex test setups or precision aligned rotating fixtures.
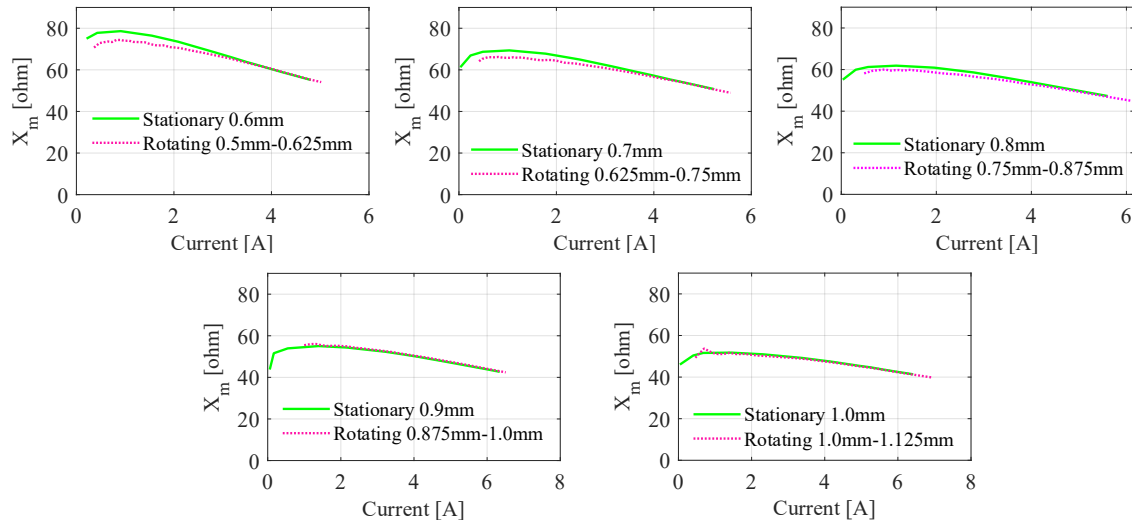
Figure 7-28 Measured variation of magnetizing reactance with no-load current for the prototype AFIM under both stationary and rotating conditions at 50Hz, across a range of airgap lengths.

Table 7-7 No-load and locked rotor equivalent circuit parameters collected from lab stationary and rotating tests.

	R_1 [Ω]	R_2' [Ω]	X_m [Ω]	X_1 [Ω]	X_2' [Ω]
Stationary 0.6mm	2.7	2.14	60.76	4.21	4.21
Rotating 0.5-0.625mm	2.7	2.42	60.11	4.15	4.15
Stationary 0.7mm	2.7	2.14	55.39	4.32	4.32
Rotating 0.625-0.75mm	2.7	2.52	54.99	4.27	4.27
Stationary 0.8mm	2.7	2.13	50.98	4.24	4.24
Rotating 0.75-0.875mm	2.7	2.38	50.07	4.19	4.19
Stationary 0.9mm	2.7	2.20	48.51	4.34	4.34
Rotating 0.875-1.0mm	2.7	2.47	47.15	4.18	4.18
Stationary 1.0mm	2.7	2.17	44.37	4.23	4.23
Rotating 1.0-1.125mm	2.7	2.23	43.87	4.20	4.20
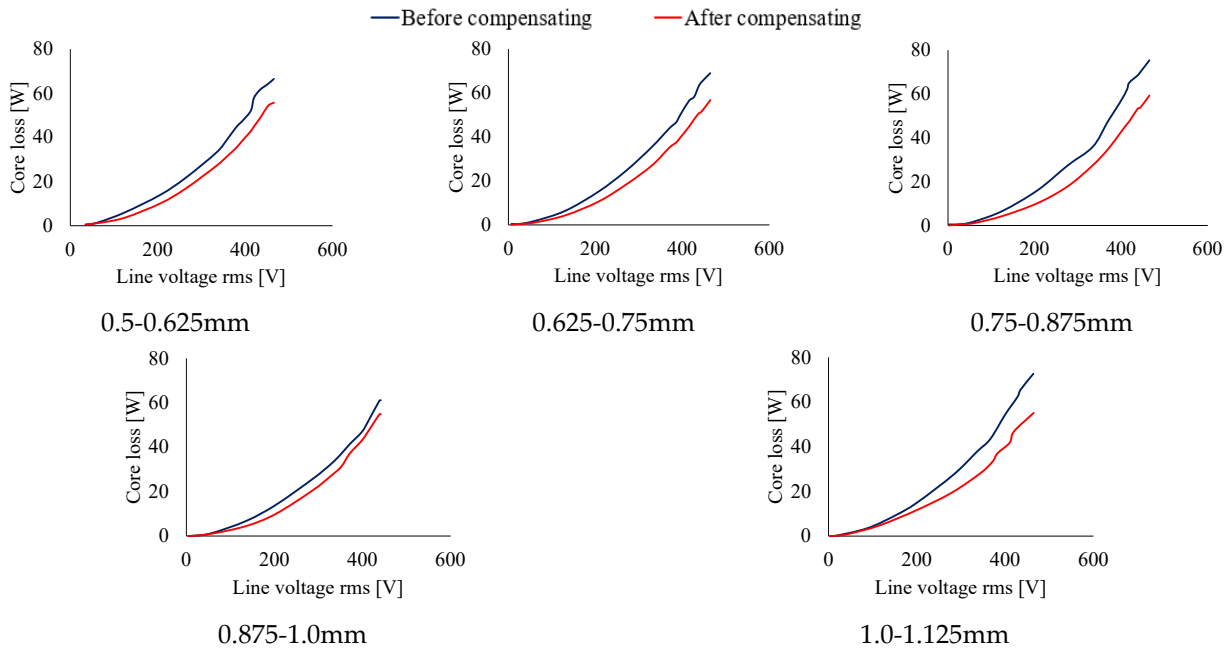
Figure 7-29 Stationary no-load core losses at different airgap lengths, comparing results before and after rotor core loss compensation.

As previously observed in Figure 7-15, the overestimated rotor core loss in the stationary condition may compromise the accuracy of the electromagnetic prediction based on stationary no-load testing. Figure 7-22 illustrates the core loss results from both experimental measurements and the 3-D FEA simulations. The FEA model shows core loss values comparable to those observed in the lab, validating the consistency between the FEA model and the prototype motor. To mitigate the effect of overestimated rotor core loss under the stationary no-load test, a semi-FEA method is employed. As confirmed in Figure 7-22, the core loss predicted by the FEA stationary no-load aligns well with lab stationary results under different airgap lengths. Leveraging this agreement, the core loss observed in stationary lab tests is adjusted to reflect the more realistic rotating condition. This semi-FEA approach (see Figure 7-29) compensates for the stationary overestimation by integrating the FEA-based insights into interpretation of the experimental data.

0.5-0.625mm   0.625-0.75mm   0.75-0.875mm

0.875-1.0mm   1.0-1.125mm
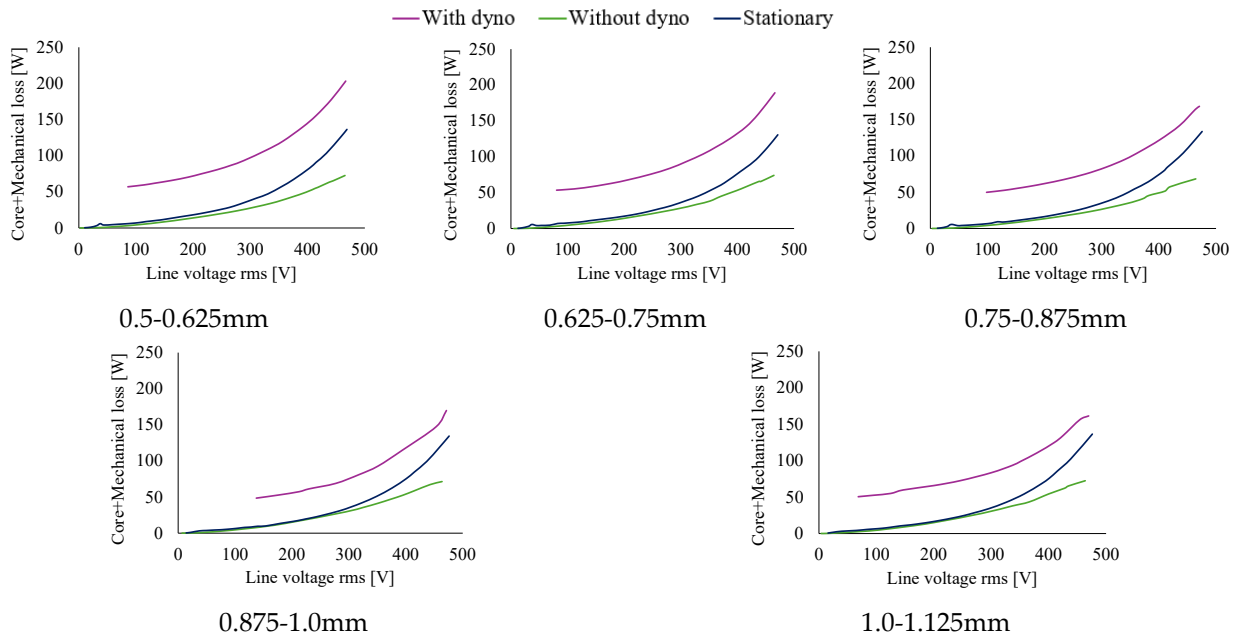
Figure 7-30 Sum of mechanical losses and core losses for stationary, with dynamometer, and without dynamometer no-load tests.

Figure 7-30 illustrates the sum of the mechanical losses and core losses obtained for stationary, with dynamometer, and without dynamometer no-load tests under various airgap lengths. Notably, for AFIMs, accurately separating the mechanical losses in conventional rotating no-load tests is challenging due to the axial force increasing quadratically with voltage. This makes the stationary no-load method a valuable approach for evaluating purely electromagnetic losses without interference from voltage-dependent mechanical effects (see Figure 7-10). The blue curve, corresponding to the without dynamometer no-load test, effectively captures the sum of mechanical losses and core losses, making it possible to estimate the total mechanical loss. By subtracting the stationary no-load results (reflecting only electromagnetic losses), the mechanical loss of the prototype motor can be separated. The purple curve represents the with dynamometer case (radial-flux machine), where the dynamometer further adds to the rotational drag, where additional rotational drag from the dynamometer leads to higher combined losses, measured to be approximately 50W. The separated mechanical loss versus voltage at different airgaps are given in Figure 7-31.
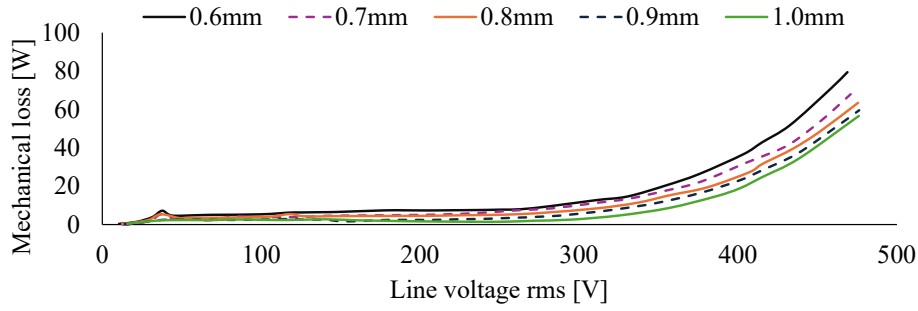
Figure 7-31 Separated mechanical loss as a function of terminal line voltage for 0.6mm to 1.0mm airgap lengths of the AFIM.
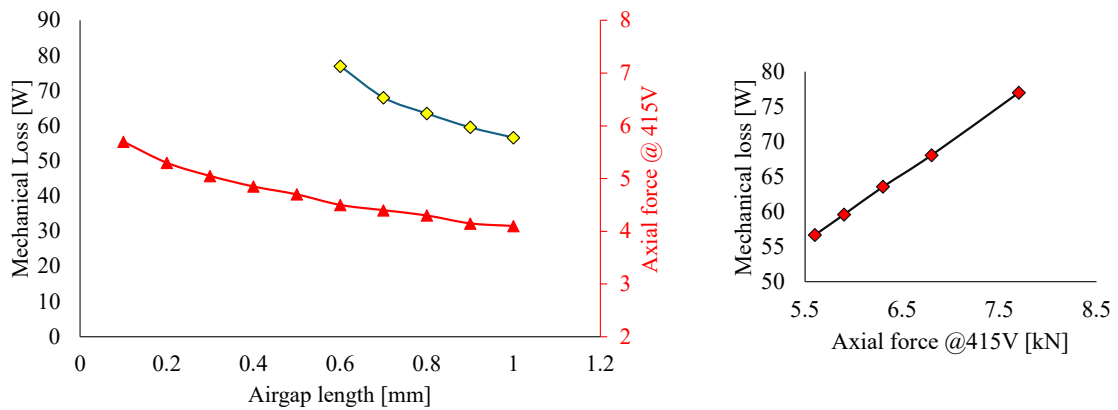
Figure 7-32 Effects of airgap length and axial force and mechanical loss for AFIM.

Figure 7-32 illustrates the relationship between the airgap length, axial force, and mechanical losses in the prototype AFIM. The axial force data are extracted from 3-D FEA, as validated in **CHAPTER 5**. In the left plot, two curves are shown: the red curve represents the axial force variation as the airgap length changes from 0.1mm to 1.0mm, while the black curve presents the corresponding mechanical losses experimentally measured under the rated voltage of 415V. It is evident that as the airgap decreases, the axial force increases significantly, and results in a corresponding increase in mechanical losses. Specifically, within the practical test range of 0.6mm to 1.0mm, the mechanical loss rises approximately 10W per around 0.1mm reduction in airgap, indicating the growing impact of rotor-stator forces and bearing friction.

The right plot shows this correlation by presenting mechanical losses directly as a function of axial force at 415V, demonstrating a near-linear relationship. This supports the theoretical prediction in Figure 7-11. Moreover, this relationship can serve as a useful reference when applying the same bearing to other axial-flux motor designs. By accurately modelling the axial force through FEA in the new design, the corresponding mechanical

loss can be approximately estimated using the established correlation. This enables more precise efficiency predictions during the early design stage, particularly when direct mechanical loss measurements are impractical.
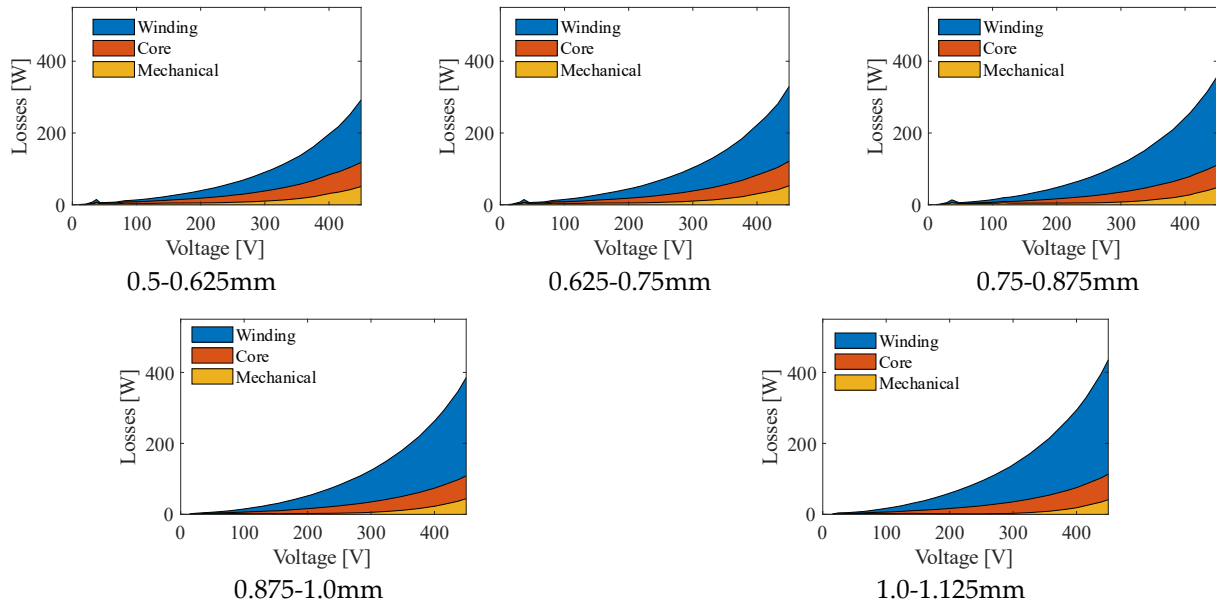
Figure 7-33 Comparison of the loss breakdown variations of the AFIM with different airgap lengths.

The loss breakdown variations of the AFIM with different airgap lengths are given in Figure 7-33. Each subplot presents the distribution of winding loss, core loss, and mechanical loss as a function of input voltage for a specific airgap interval ranging from 0.5mm to 1.125mm. As the airgap increases the mechanical loss component generally decreases due to the reduction in axial force, which drops from approximately 80W to 56W. In contrast, the winding losses increase significantly, from about 205W to 389W, primarily because the larger airgap weakens the magnetic coupling and requires higher magnetizing current, which increases in response to the increased airgap reluctance while maintaining constant flux ($E = 4.44 \cdot f \cdot N \cdot \varphi$). Meanwhile, since the average flux density is maintained, the core loss, which depends on the flux magnitude and frequency, does not change significantly (see Figure 7-22).

7.5.2 Rotating Loading Tests for AFIM with Different Airgaps

7.5.2.1 Dynamometer components for Loading Measurement of AFIM
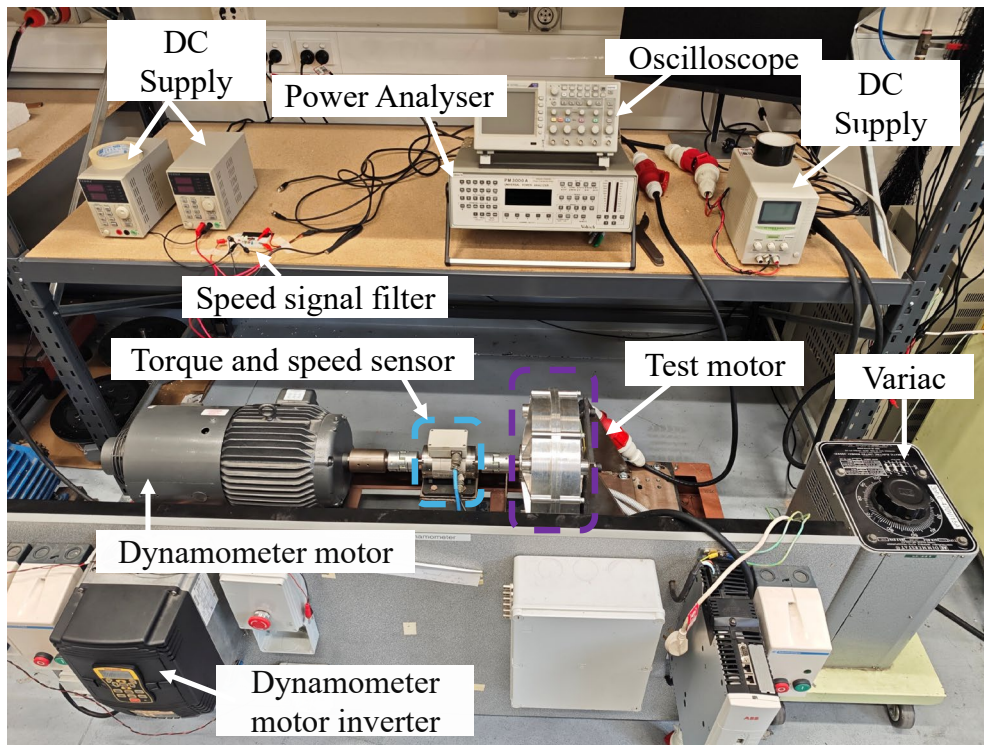
Figure 7-34 Dynamometer test rig and its components.
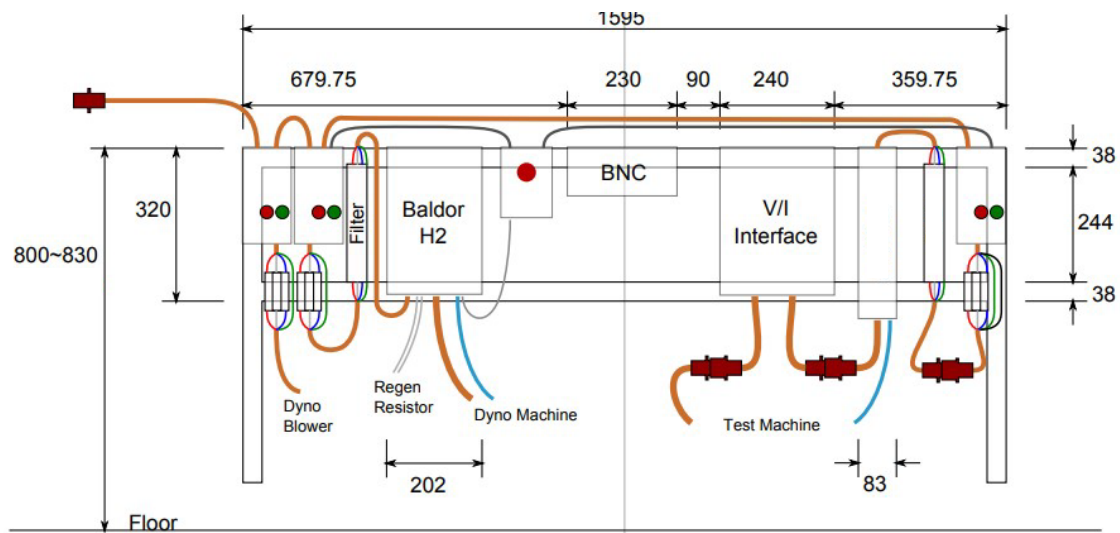
Figure 7-35 Dynamometer test frame wiring guide, provided by the University of Adelaide Laboratory.
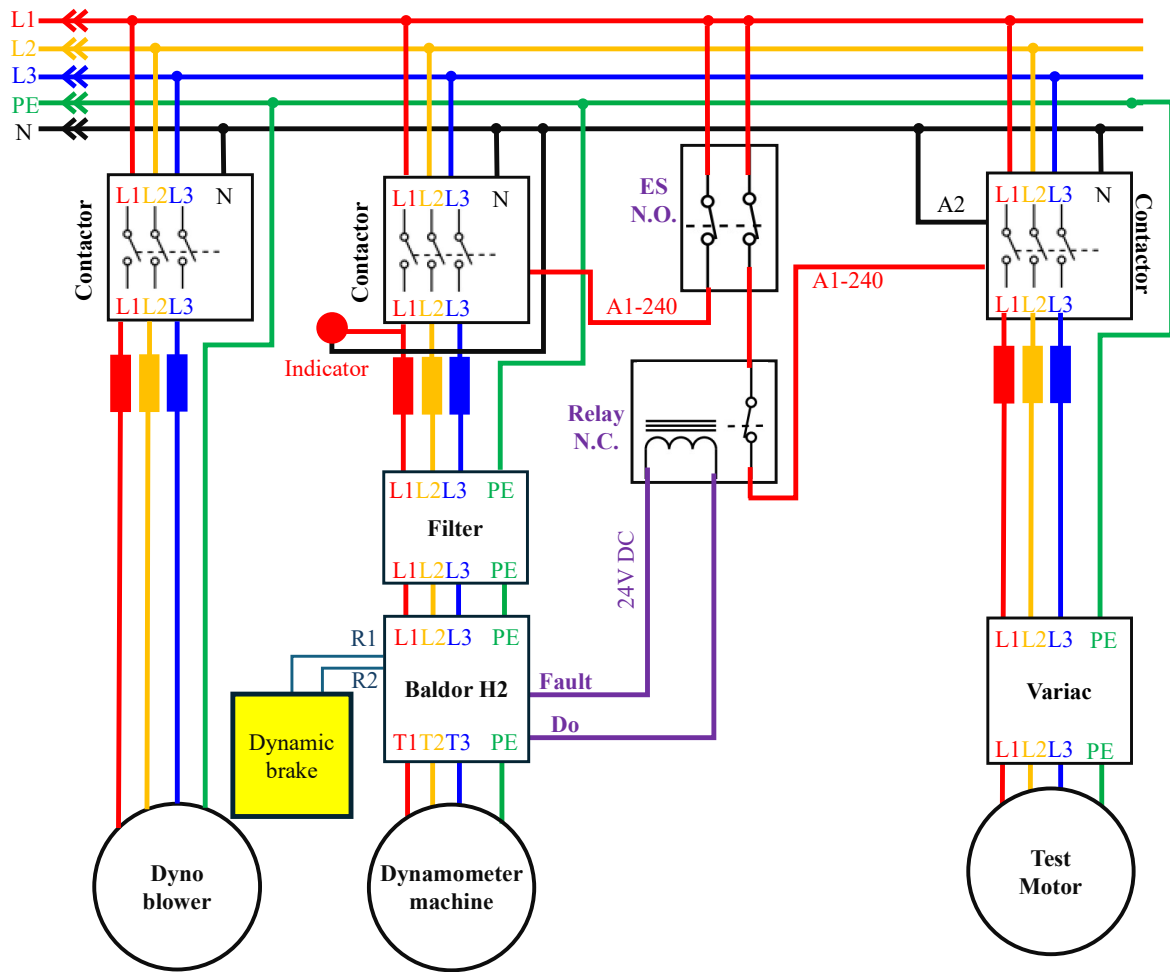
Figure 7-36 Wiring schematic of the AFIM test rig.

Figure 7-34 presents the experimental setup used for the performance evaluation of the AFIM under the load condition. The key components of the test bench are clearly labelled. The test motor (marked in the purple dashed block) is mechanically coupled to a torque and speed sensor, which is further connected to a dynamometer motor (left side). Two small DC supplies (left) power the speed sensor circuits and torque sensor, respectively. The right - hand side DC supply is used for the DC winding resistance measurement. The Variac (right bottom) controls the magnitude of the 3ph AC input voltage to the test motor. On the load side, the dynamometer motor (left) is operated through a commercial inverter (bottom-left), which controls the rotational speed of the dynamometer and hence imposes a mechanical load on the AFIM under test. The dynamometer holds the test motor at the prescribed speed, allowing torque to be measured as a function of speed, the electrical input quantities are monitored in real time using the power analyser, the oscilloscope (top) is used to check the speed pulse signal, while the mechanical data is collected through the torque and speed sensors and also fed to the power analyser.

The layout and physical dimensions of the test bench are given in Figure 7-35, detailing the placement of the terminals and measurement channels. The corresponding three-phase wiring schematic is provided in Figure 7-36, where the AFIM is supplied via the Variac (3ph 0-470V, 15A), and the dynamometer machine and dynamometer cooling fan are protected by contactors and braking circuit. The dynamometer motor is a 415V, 5.5kW (7.5hp), 14.4A, 50Hz, 37Nm induction machine. The Voltech PM3000A 3ph power analyser is used to collect key testing data, including raw efficiency (uncompensated by offset), torque, speed, voltage, current, input power, output power and power factor.

Speed measurement is performed using a sinusoidal encoder with a resolution of 60 pulses per revolution. The encoder outputs an analog voltage with a frequency proportional to the rotational speed, with a peak-to-peak amplitude of about 3V at 5000rpm.

The torque is measured using a Himmelstein strain-gauge torque transducer (Model 79002V) capable of operating over two ranges. The torque sensor provides a 5V full-scale analog output: for the low-torque range (11.3Nm), the sensitivity is 2.26Nm/V, and for the high-torque range (56.5Nm), the scale is 11.3Nm/V. The high torque range was used in this test.

7.5.2.2 Test Process for Electromagnetic Performance of the AFIM Prototype

The prototype AFIM was designed with an industrial standard operating voltage of 415V. The entire design and optimisation processes were conducted in **CHAPTER 4** are under this nominal voltage. No specific optimisation or recalibration was performed for alternative supply voltages such as 380V or 400V. Consequently, the electromagnetic performance under these voltages may not reflect an optimally tuned condition, particularly in terms of efficiency. Nevertheless, experimental tests were also conducted at 380V and 400V to evaluate the electromagnetic performance. These voltages are commonly found in other international grids (400V in Europe and 380V in parts of Asia) [103], and their inclusion enables a more comprehensive assessment of the adaptability of the prototype AFIM. To evaluate the motor under various loading conditions, a series of controlled tests are performed using the dynamometer system mechanically coupled to the shaft (Figure 7-32).

The AFIM is powered by a three-phase AC supply through a variac, allowing for gradual voltage ramp-up to the rated 415V. During the start-up, the dynamometer operates in speed control mode, maintaining a controlled rotational speed slightly below the motor's synchronous speed (750rpm for 8-pole 50Hz AFIM). By varying the dynamometer speed

setpoint, the corresponding torque developed by the motor can be measured across a range of operating slips.

At each load condition, the power analyser is used to monitor the key electrical and mechanical quantities. To ensure that only steady-state values are captured, the analyser is configured to average over 60 data points before recording the result. Moreover, any torque offset on the torque transducer or readout is first calibrated by rotating the dynamometer at in a forward and the reverse directions at the same speed.
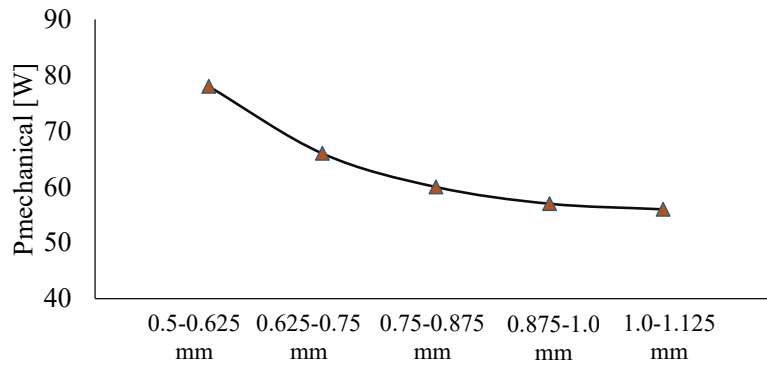
Figure 7-37 Mechanical loss @415V at different airgaps.

Figure 7-37 illustrates the measured mechanical loss across various airgap ranges at 415V. To isolate the mechanical loss component at this voltage, the AFIM is tested a different voltages while mechanically decoupled from the dynamometer. In this condition, the measured input power includes factors from stator winding loss, core loss, and voltage-dependent mechanical losses. The previously discussed stationary no-load test, along with the compensated core loss profile (see Figure 7-29). is used as a baseline to subtract the electromagnetic components. The resulting difference between the two power–voltage curves represent the estimated mechanical losses.

(a)　　　　　　　　　　　　　　　　(b)
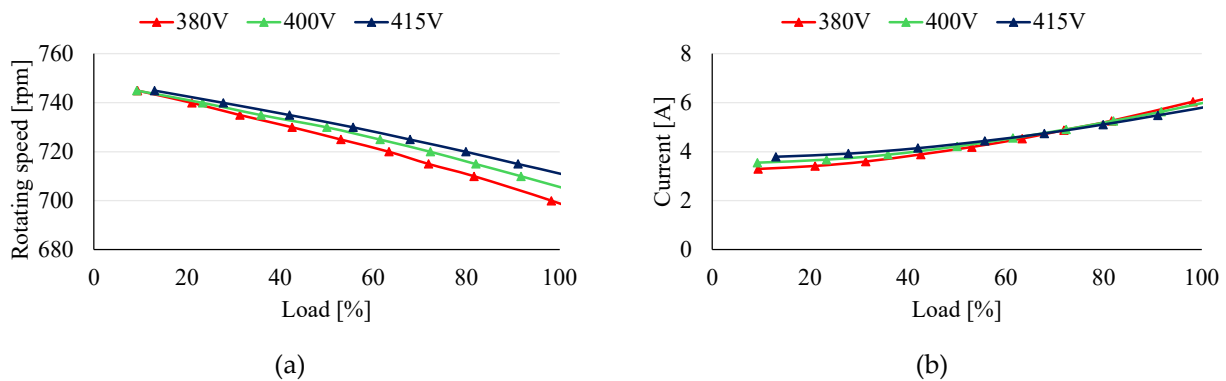
Figure 7-38 Loading performance of 0.5-0.625mm AFIM (a) rotating speed versus loading, (b) phase current versus loading.

Figure 7-38 shows the variation of rotating speed and phase current with load under three supply voltages: 380V, 400V, and 415V. These tests are conducted specifically at the 0.5-0.625mm airgap setting. This range is selected because, for larger airgaps, the test AFIM is unable to deliver the full-load torque at 380V and 400V without exceeding the rated current limit. Therefore, only the smallest allowable airgap is used for this set of tests. At lower supply voltages (380V and 400V), the speed drop is more when approaching full-load torque (30Nm) (see Figure 7-38(a)). This is because the reduced voltage leads to a lower airgap flux density, which in turn weakens the torque capability at a given slip. To compensate, the motor slip is increased to increase the rotor current and maintain the torque under weakened flux conditions. This trend is clearly reflected in Figure 7-38(b), where the phase current increases more steeply at lower voltages as the motor approaches full load.
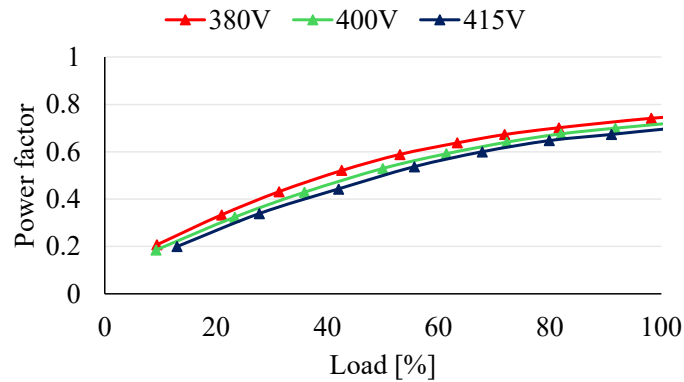
Figure 7-39 Power factor versus load under different supply voltages (380V, 400V, 415V).

Figure 7-39 shows that, at the same load level, lower supply voltages give higher power factors. This is due to the reduced magnetizing current requirement at lower voltages, which results in a smaller reactive component in the stator current. In contrast, higher voltages increase the magnetizing current and reactive power, thereby lowering the overall power factor but also increase the torque capability. It is also observed that in the low to medium load range (20%–60%), the voltage-dependent difference in the power factor is relatively small. As the load approaches full load, the gap between power factor values at different voltages narrows.
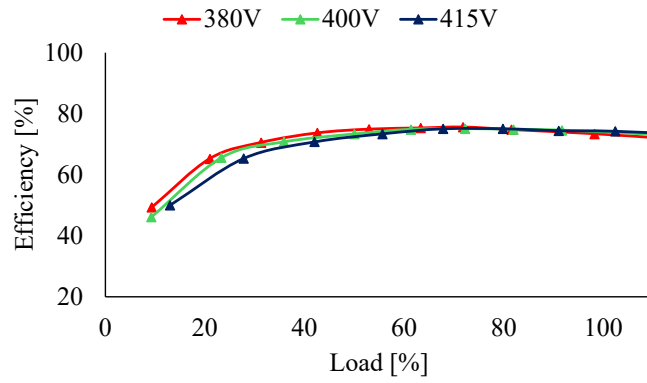
Figure 7-40 Efficiency versus load under different supply voltages (380V, 400V, 415V).

Figure 7-40 presents the measured efficiency of the AFIM across varying loadings under three supply voltages. All three voltages show similar trends, reaching peak efficiency around 60%-80% of load. At approximately 40% load, the 380V supply exhibits the highest efficiency of 75.5%, compared to 74.8% for 400V and 75.2% for 415V. At light load, the 380V case exhibits the lowest current (see Figure 7-38), resulting in reduced copper loss, and hence higher efficiency. At around 80% of load, the 415V supply delivers the highest efficiency which is measured at 75.2%. It is important to note that the reported efficiencies in Figure 7-40 excludes offset present in the torque sensor readings. To improve the measurement accuracy, an offset calibration test of the torque sensor is conducted in the following figures.

| (a) 380V | (b) 400V | (c) 415V |
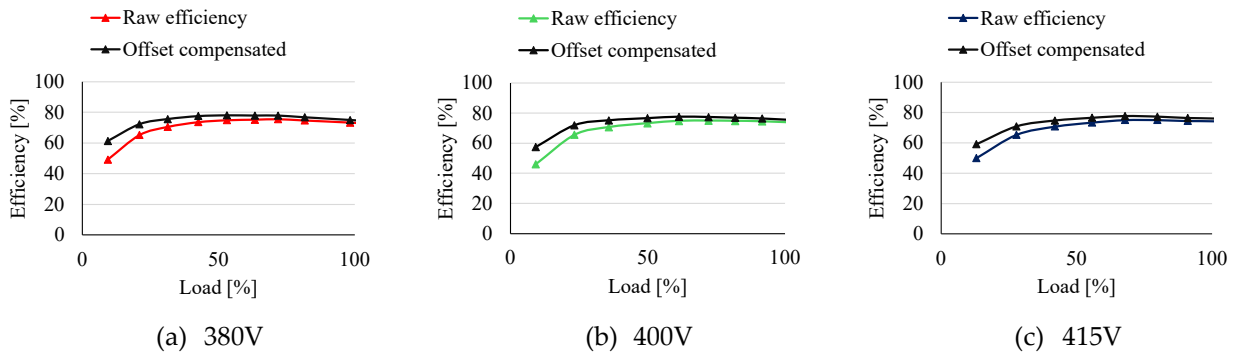
Figure 7-41 Efficiency versus load under different supply voltages (380 V, 400 V, and 415 V), comparing raw and offset compensated efficiency.

In the experimental setup, the dynamometer is capable of rotating in both forward and reverse directions, controlled via an inverter. The test AFIM is powered such that its rotational direction is reverse (REV) relative to the dyno's default direction. As a result, when measuring the output torque, the sensor reports negative values. The torque sensor offset is a non-zero reading when the transducer is unloaded. The observed torque sensor offset of 0.5Nm in the reverse direction. Therefore, the value of 0.5Nm was taken as the torque offset. Figure 7-41 compares the AFIM efficiency before and after accounting for the

torque sensor offset. However, they do not show large differences at full load at different supply voltages.
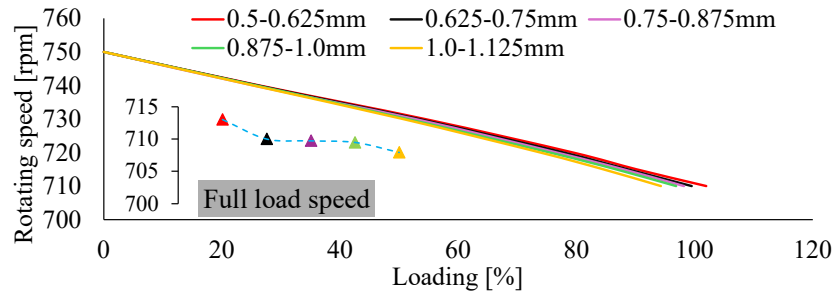
Figure 7-42 Rotating speed versus load for different airgap ranges. The rated full-load speed is indicated in the bottom-left corner.

Figure 7-42 presents the relationship between rotating speed and loading for the AFIM under varying airgap lengths. Larger airgap lengths exhibit higher slip and thus lower speeds under the same loading conditions compared to operation with smaller airgaps ($\approx 0.5 - 0.625mm$). The inset graph highlights that the full load speed for the smallest airgap is measured at 713rpm. The original design specification assumed a nominal airgap of 0.5mm, targeting a full load speed of about 720rpm. Such differences can be primarily attributed to a larger actual airgap caused by mechanical deformation, machining tolerances, or assembly misalignment.
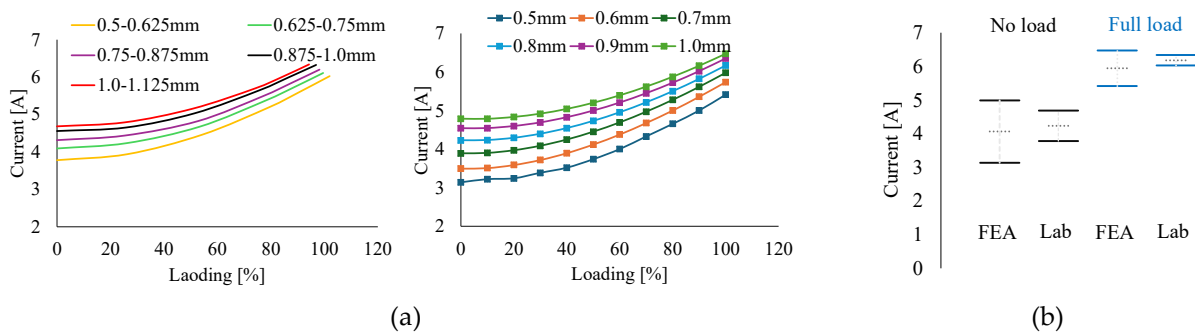
Figure 7-43 (a) Experimental (left) and 3-D FEA (middle) measured current versus load for different airgap lengths (b) Comparison of no-load and full-load current margins between the FEA predictions and laboratory measurements.

Figure 7-43 shows the experimentally measured stator current versus load for various airgap ranges. In Figure 7-43(a), both the FEA and lab results exhibit similar trends but differ in values. It is also observed that the difference in current across various airgaps is higher under no-load conditions but becomes less significant as the load increases. This is because, at no load, the stator current is dominated by the magnetizing current I_m, which is highly

sensitive to airgap length. However, under load, the load current I_{load}, an active component proportional to torque demand, becomes the dominant portion of the total stator current.

Figure 7-43(b) compares the current magnitudes obtained from FEA and lab measurements across different airgap lengths under no-load and full load conditions. For each case, the vertical bars represent the current range due to varying airgaps, while the horizontal dashed bars indicate the average value. It is observed that the lab-measured average current is slightly higher than the FEA results across various airgaps, by 4.1% at no load and 3.9% at full load.

(a)   (b)
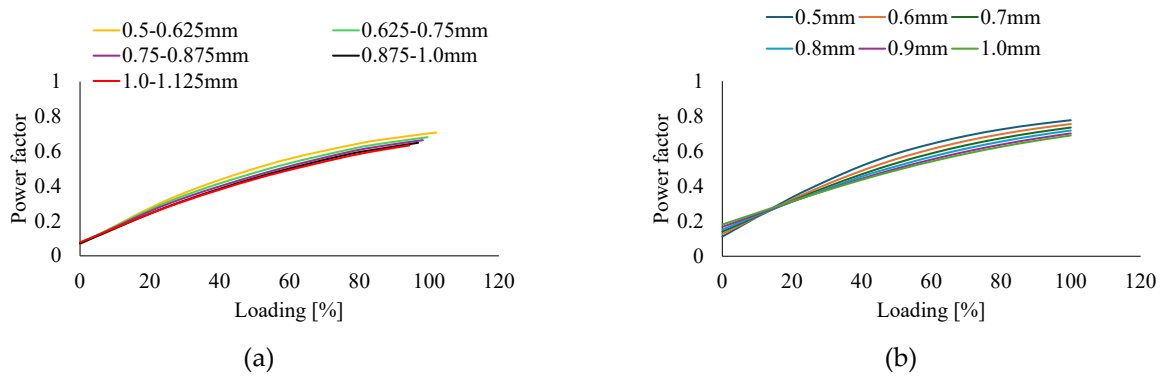
Figure 7-44 Power factor variation under different airgap lengths across loadings, (a) experimental results (b) FEA results.

Figure 7-44 presents the variation of power factor under different airgap lengths across a range of loading levels. Figure 7-44(a) presents experimental results, while Figure 7-44(b) shows FEA results. At light loads, both the lab and FEA results with larger airgaps show slightly higher power factor than at smaller gaps. This is noticeable in the FEA results below at around 20% of loading, and in the lab under even lower loads. In addition, the lab curve for the smallest airgap group (0.5-0.625mm) closely aligns with the FEA result for 0.8mm, suggesting that the actual assembled airgap is larger than that estimated by the airgap adjustor. This discrepancy may be attributed to mechanical misalignment, deformation, or fixture compliance, resulting in a larger effective average airgap than the nominal setting.

In Figure 7-45, each subplot presents the efficiency versus loading, showing both the lab and the FEA predicted results at different airgaps. For the lab results, two versions are shown: one including mechanical loss and one without (see Figure 7-45). It is observed that single-sided AFIMs are particularly sensitive to mechanical losses. In the 0.5-0.625mm airgap test, the experimental efficiency reaches around 78% efficiency at 80% loading, which is approximately 3% lower than the FEA-predicted efficiency of the 0.5mm model under the same conditions. Notably, the FEA model does not account for mechanical losses. After

applying mechanical loss compensation, the experimental efficiency improves to around 81.0%, approaching but still slightly below the FEA-predicted value of 81.6%.
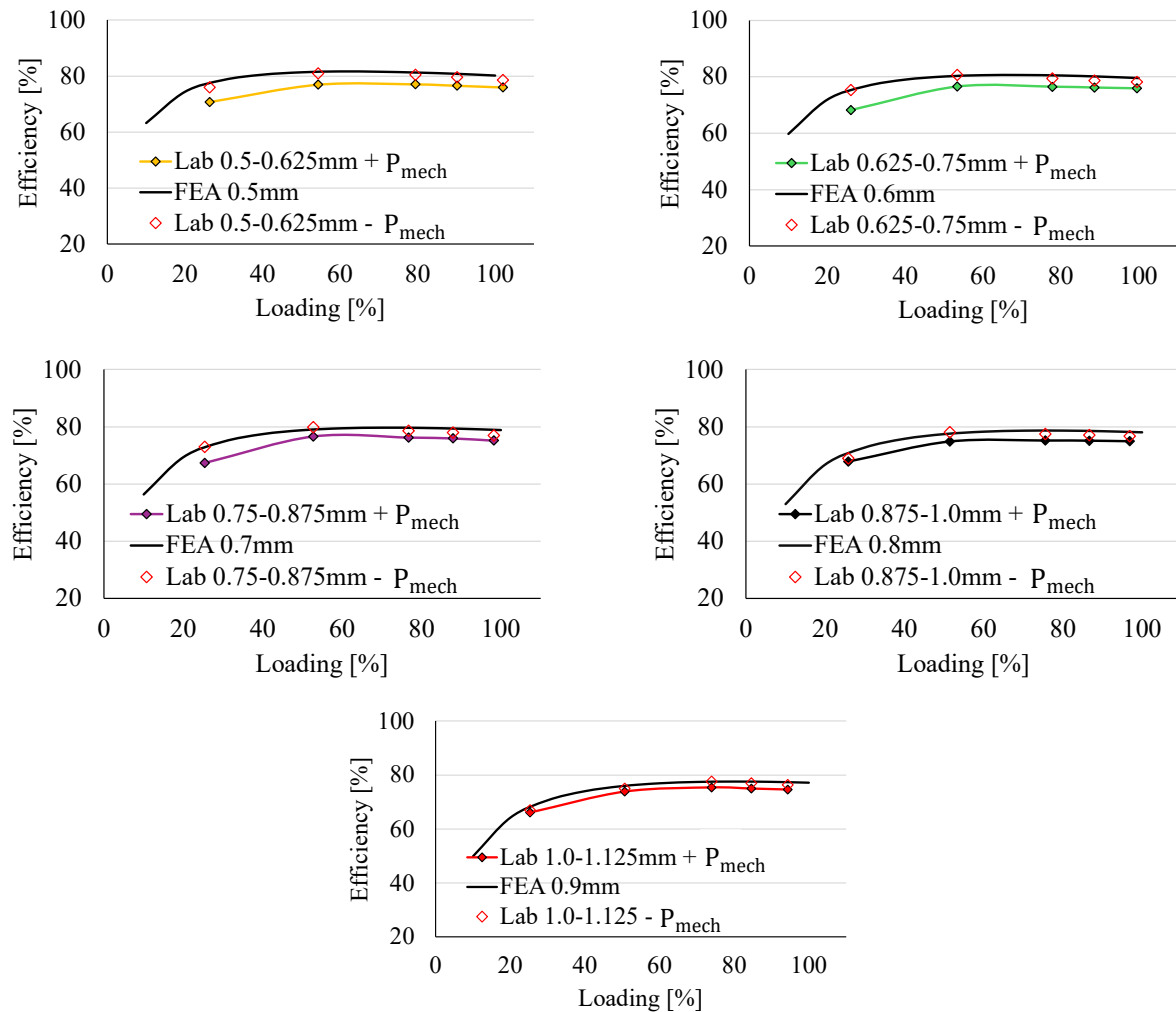
Figure 7-45 Comparison of the test AFIM efficiency between lab and the FEA results across different airgap lengths under varying loadings.
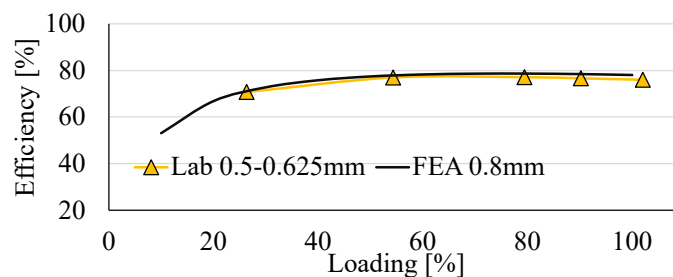
Figure 7-46 Comparison between the lab measured efficiency for the 0.5–0.625 mm airgap and the FEA-predicted efficiency at 0.8 mm.

Table 7-8 Full-load efficiency comparisons between FEA and experimental tests.

FEA airgaps	FEA loading (%)	Lab Loading (%)	Errors
0.5mm	81.6	77.4	4.2
0.6mm	80.9	77.1	3.8
0.7mm	80.2	76.1	4.1
0.8mm	78.8	75.6	3.2
0.9mm	77.6	75.2	2.4

In addition, the 0.5-0.625mm airgap lab measured efficiency including mechanical loss aligns more closely with the FEA curve for a larger airgap, such as 0.8mm, consistent with the earlier observation from the power factor analysis. Table 7-8 further shows this observation by comparing full-load efficiencies predicted from FEA and the experimental tests across a range of expected airgaps.

Table 7-9 Full-load efficiency comparisons between experimental tests and brochure.

	FEA η_r (%)	Tested η_r (%)	Brochure η_r (%)
2.2kW 8 pole RFIM	81.7	-	81.0
2.2kW 8 pole AFIM	82.6	77.5	-

Table 7-9 shows a comparison of full-load efficiency based on experimental results for the AFIM, FEA simulations for both AFIM and RFIM, and manufacturer-provided specifications for the RFIM. Due to mounting limitations on the available test bench, a full-load test for the commercial 2.2 kW 8-pole RFIM could not be performed at this stage. The prototype AFIM demonstrated a measured full-load efficiency of 77%, which is lower than both the 81% efficiency reported for the RFIM in the manufacturer's specifications and the FEA-predicted efficiency for the AFIM. However, the FEA results, conducted under idealised conditions without accounting for mechanical losses, suggest that the AFIM should outperform the RFIM in terms of electromagnetic efficiency. Given that the RFIM was not tested under the same experimental setup, a direct and reliable comparison remains inconclusive at this point.

Table 7-10 Comparison of key material weights and cost between the commercial 2.2kW 8-pole RFIM and the equivalent prototype AFIM.

	RFIM	AFIM	Differences (%)
Rotor core weight (kg)	10.5	6.5	38
Stator core weight (kg)	11.2	9.9	12
Rotor bar weight (kg)	1.8	1.4	22
Stator copper weight (kg)	3.5	2.5	29
Total weight (kg)	27	20	25
Material cost (USD)	62	45	37

Table 7-10 shows a comparison between the commercial 2.2kW eight pole RFIM and the prototype equivalent AFIM in terms of material usage and torque density. The AFIM demonstrates notable reductions in material consumption. Specifically, the rotor core, stator core, rotor bar and stator copper weights are reduced by 38%, 12%, and 29%, respectively. The total motor weight is reduced by 25%, contributing a significant increase in torque density, which improved from 1.1Nm/kg in the RFIM to 1.5Nm/kg in the AFIM, showing a 36% improvement over the RFIM. This outcome aligns with one of the key expectations of the project, enhancing the power-to-weight ratio of the motor. The weight reduction combined with comparable performance confirms that the AFIM design meets its design objectives.

7.6   Conclusion

In this chapter, comprehensive experimental investigations into the electromagnetic and mechanical performance was performed for the newly designed 2.2kW AFIM. A series of experimental tests were done, including stationary and rotating no-load, locked rotor, and loading tests. The test results were compared with FEA simulations.

A significant contribution of this chapter is to introduce and validate the proposed novel stationary no-load testing method for AFIMs. This enables no-load testing with varying airgap lengths without a fully-assembled motor. This capability not only simplifies the experimental process but also reduces costs and saves time. The stationary no-load test results were validated with FEA simulations and the conventional rotating no-load test, demonstrating the reliability of these methods in early assessment of key electromagnetic properties, such as the current versus voltage curves and core losses. In addition, the airgap offset values were found by comparing the experimental current versus voltage curves with FEA simulations. By applying this correction, unexpected effects of surface irregularities caused by manufacturing were significantly reduced.

Another important aspect introduced in this chapter is to accurately separate the loss components. The presence of axial force, which varies significantly with the applied voltage and airgap length, leads to a challenge in separating losses of the AFIM. Coupled with FEA simulation results, the non-linear mechanical loss was accurately separated from the other loss components. This method suggests that the AFIM efficiency can be further improved through the combination of both mechanical and electromagnetic design. This section also concludes that the single-sided AFIM is more sensitive to the precise airgap adjustment and requires more careful mechanical structural design compared to the conventional RFIM.

Moreover, future research directions for AFIM should focus on the following aspects. Advanced loss modelling in FEA should be developed to accurately predict the performance of the axial flux motor; this can be done by understanding better the bearing friction under different airgap lengths and terminal voltages. Enhancement of the airgap length control is also critical, given the AFIM's sensitivity to airgap variations, future research could explore the possibility of an airgap monitoring and adjustment system, perhaps enabling the automatic airgap adjustment, hence enhancing the operational stability and efficiency of the motor.

CHAPTER 8

<div style="text-align: right">

CONCLUSIONS
AND FUTURE WORKS

</div>

8.1 Conclusion

This thesis investigates the potential of AFIM as viable alternatives to conventional RFIMs for line-start applications, with particular emphasis on the unique design and operational challenges inherent to AFIMs. To achieve this aim, the research had three main objectives, (a) developing a comprehensive AFIM design methodology to convert existing RFIMs to AFIMs; (b) investigating and mitigating axial force impacts through newly designed experimental and simulation-based analysis; (c) introducing a fast and low-cost testing method, the stationary no-load test, to evaluate the AFIM electromagnetic characteristics.

CHAPTER 1 highlighted the importance of electric motors, particularly induction motors, and established the motivation for exploring AFIMs as alternatives to RFIMs, which, despite their robustness and simplicity, are limited in terms of efficiency and power density. **CHAPTER 2** provided a comprehensive review of AFIM research and identified key gaps. **CHAPTER 3** summarised the significance of AFIM electromagnetic characteristics, described an analytical approach for estimating magnetic fields at different radii, and explained the key factors influencing electric and magnetic loading.

The significance of the of AFIM electromagnetic characteristics in the design of AFIMs were summarised in the third chapter. The procedure for analytical estimation of the magnetic fields at different radii was described. The important factors which play determinative roles in the electric and magnetic loading at different motor diameters were also explained. **CHAPTER 4** introduced a new design method for the axial-flux induction motors. This approach introduced a preliminary sizing method, coupled with a developed design Pareto front curve, which incorporates newly defined electric and magnetic loading parameters. This developed method was then applied to convert existing four, six, eight pole 2.2kW RFIM designs to AFIMs.

A comprehensive comparative study was performed on the proposed axial-flux and commercial benchmark radial-flux induction motors. To further understand the differences between axial-flux and radial-flux induction motors, the effects of geometrical factors, such as the shape of the stator and rotor slots and the number of rotor slots, were also studied, and it was shown that the axial-flux induction motor design is sensitive to these parameters. The steady-state electromagnetic performance, such as efficiency, was also studied to evaluate the electric motor as it is a key parameter for both designers and customers. Given the structure and arrangement of the rotor and stator in axial-flux induction motors, the dynamic response was also investigated. The dynamic responses showed that the AFIM has longer settling time (due to its higher rotor inertia) but higher torque capability than the RFIM. More importantly, the electromagnetic performance and material cost comparisons show that at higher pole numbers, AFIMs may provide higher power density and higher efficiency. In particular for the eight-pole AFIM design considered showed a 14% material cost decrease with comparable efficiency.

The distinctive structure of single-sided AFIMs offers the potential for better electromagnetic performance but also presents a significant challenge in the form of large unbalanced axial attractive forces. The design procedure used for the difficulties of AFIM construction were described. **CHAPTER 5** focused on investigating the forces in both the newly designed 2.2kW and an existing 300W AFIM, with the goal of proposing experimental and numerical measurement methods. Based on the calculated axial force results at different airgaps, the bearing selection reference was provided. To validate the 3-D FEA results, a locked-rotor test was conducted at different airgaps. Comparative studies on double-sided axial-flux and single-sided axial-flux induction motors are performed, and it showed that only the NS-DSSR-AFIM topology can effectively cancel the axial force and reduce the negative stiffness.

CHAPTER 6 described the construction of the eight pole 2.2kW axial-flux induction motor prototype. The procedure described. Given the airgap is a key influence on the electromagnetic performance and the special structure that axial-flux motor has a specialised airgap adjustment mechanism was developed to facilitate experimental testing at various airgap lengths.

Experiments on the prototype axial-flux motor were conducted. Using the structural benefits of the disc-shape AFIM, stationary no-load tests were performed by placing the back of the rotor and stator. To the best of the author's knowledge this is the first time a stationary no-load test has been proposed for the AFIM. The stationary no-load test was conducted and used to extract the equivalent circuit parameters. The stationary no-load test

results demonstrated a strong capability in predicting the electromagnetic performance, showing reasonable accuracy in calculating the current and torque as a function of speed. Further loading tests were conducted to evaluate the AFIM steady-state performance under various load conditions. These loading results were then compared to the 3D FEA simulation results, showing that the overall performance trends across varying airgaps were in good agreement. However, when individual cases were examined in detail, it was observed that the experimental results for the AFIM with an expected airgap of 0.5mm were more closely aligned with the simulation results obtained at a larger airgap, 0.8mm. Such a deviation highlights the sensitivity of single-sided AFIM prototypes to mechanical tolerances, especially under high axial forces. Moreover, the single-sided AFIM prototype achieves a significantly higher power to electromagnetic material weight ratio of 81W/kg, compared to 110W/kg of the commercial RFIM. This power density highlights the lightweight potential of the AFIM, especially for applications where volume and mass constraints are critical.

8.2   Recommendation for Future Works/Studies

There are many avenues for further investigation. Given the direct relationship between AFIM diameter and power output, future studies could explore structural adaptions that avoid deformation in large-diameter AFIMs. In addition, addressing challenges related to imbalanced airgaps and reduced bearing lifespan in larger AFIMs could enable the use of these motors in higher-power applications while maintaining reliability and efficiency.

CHAPTER 4 described double-sided machine as a solution to reduce the axial force issues and reduce associated risks. However, it introduces a trade-off by increasing the axial length of the motor. A printed circuit board (PCB) stator for double-sided AFIMs could be a potential way to further improve the power density with reduced axial length [68-71]. Most of the existing literature focuses on the axil-flux permanent magnet motor and so the use of PCB stators in an axial-flux induction motor remains as a relatively unexplored field. Additionally, PCB stators introduce new challenges regarding thermal performance. Integrating semiconductor cooling devices into the PCB could serve as a potential research area for PCB motor.

Axial attractive forces remain a critical design challenge in single-sided AFIMs. While this thesis has proposed preliminary solutions, future work could focus on refining axial force management techniques, potentially integrating advanced materials or magnetic

solutions to minimise the axial force impact. These efforts would support the development of more stable and efficient axial-flux machines.

In current work, the AFIM has been designed for line-start applications in this research. Given the axial-flux configuration, characterised by its wheel-like shape, the integration of wheel-shaped AFIMs in electric vehicle wheel hubs could be a highly topical of research. This is driven by the need for higher power density, more efficient propulsion systems.

REFERENCE

[1]   V. S. Ramsden *et al.*, "High-performance electric machines for renewable energy generation and efficient drives," *Renewable Energy,* vol. 22, no. 1, pp. 159-167, 2001/01/01/ 2001, doi: https://doi.org/10.1016/S0960-1481(00)00054-9.

[2]   D. S. Yadav and M. Manisha, "Electric Propulsion Motors: A Comparative Review for Electric and Hybrid Electric Vehicles," in *2022 IEEE International Conference on Distributed Computing and Electrical Circuits and Electronics (ICDCECE),* 23-24 April 2022 2022, pp. 1-6, doi: 10.1109/ICDCECE53908.2022.9793099.

[3]   R. Saidur, "A review on electrical motors energy use and energy savings," *Renewable and Sustainable Energy Reviews,* vol. 14, no. 3, pp. 877-898, 2010/04/01/ 2010, doi: https://doi.org/10.1016/j.rser.2009.10.018.

[4]   Z. Cao, A. Mahmoudi, S. Kahourzade, and W. L. Soong, "An Overview of Electric Motors for Electric Vehicles," in *2021 31st Australasian Universities Power Engineering Conference (AUPEC)*, 26-30 Sept. 2021 2021, pp. 1-6, doi: 10.1109/AUPEC52110.2021.9597739.

[5]   F. C. Mushid and D. G. Dorrell, "Review of axial flux induction motor for automotive applications," in *2017 IEEE Workshop on Electrical Machines Design, Control and Diagnosis (WEMDCD)*, 20-21 April 2017 2017, pp. 146-151, doi: 10.1109/WEMDCD.2017.7947738.

[6]   R. McElveen, M. Melfi, and R. Daugherty, "Line start permanent magnet motors - Starting, standards and application guidelines," in *2014 IEEE Petroleum and Chemical Industry Technical Conference (PCIC)*, 8-10 Sept. 2014 2014, pp. 129-139, doi: 10.1109/PCICon.2014.6961876.

[7]   H. Kim *et al.*, "Study on Analysis and Design of Line-Start Synchronous Reluctance Motor Considering Rotor Slot Opening and Bridges," *IEEE Transactions on Magnetics,* vol. 58, no. 2, pp. 1-6, 2022, doi: 10.1109/TMAG.2021.3081107.

[8]   P. Kumar, H. K. Channi, and H. Singh, "A Comprehensive Review of Electrical Motors for Electric Mobility," in *2024 IEEE International Conference for Women in Innovation, Technology & Entrepreneurship (ICWITE)*, 16-17 Feb. 2024 2024, pp. 130-135, doi: 10.1109/ICWITE59797.2024.10503530.

[9]   J. W. A. Wilson, "Inverter Motor Drive Ride-Through Schemes for Continuous Process Applications," *IEEE Transactions on Industry Applications,* vol. IA-14, no. 4, pp. 330-335, 1978, doi: 10.1109/TIA.1978.4503546.

[10]   R. Tianhu, P. Haipeng, and X. Yongming, "Design and analysis of two different line-start PM synchronous motors," in *2011 2nd International Conference on Artificial Intelligence, Management Science and Electronic Commerce (AIMSEC)*, 8-10 Aug. 2011 2011, pp. 3843-3847, doi: 10.1109/AIMSEC.2011.6009932.

[11]   P. W. Huang and M. C. Tsai, "Investigation of V-Shaped Line Start Permanent Magnet Motors Based on Reactance Effect," *IEEE Transactions on Magnetics,* vol. 49, no. 5, pp. 2311-2314, 2013, doi: 10.1109/TMAG.2013.2239279.

[12]   A. H. Isfahani and S. Vaez-Zadeh, "Line start permanent magnet synchronous motors: Challenges and opportunities," *Energy,* vol. 34, no. 11, pp. 1755-1763, 2009.

[13]   B. H. Lee, J. P. Hong, and J. H. Lee, "Optimum design criteria for maximum torque and efficiency of a line-start permanent-magnet motor using response surface methodology

and finite element method," *IEEE Transactions on Magnetics,* vol. 48, no. 2, pp. 863-866, Feb 2012.

[14]   Z. Nasiri-Gheidari and H. Lesani, "A Survey on Axial Flux Induction Motors," in *PRZEGLĄD ELEKTROTECHNICZNY*, Jan 2012, pp. 300-305.

[15]   S. Saha, G. D. Choi, and Y. H. Cho, "Optimal Rotor Shape Design of LSPM With Efficiency and Power Factor Improvement Using Response Surface Methodology," *IEEE Transactions on Magnetics,* vol. 51, no. 11, pp. 1-4, 2015, doi: 10.1109/TMAG.2015.2448754.

[16]   A. D. Aliabad and F. Ghoroghchian, "Design and Analysis of a Two-Speed Line Start Synchronous Motor: Scheme One," *IEEE Transactions on Energy Conversion,* vol. 31, no. 1, pp. 366-372, 2016, doi: 10.1109/TEC.2015.2481929.

[17]   M. Popescu, L. D. Leonardo, G. Fabri, G. Volpe, N. Riviere, and M. Villani, "Design of Induction Motors With Flat Wires and Copper Rotor for E-Vehicles Traction System," *IEEE Transactions on Industry Applications,* vol. 59, no. 3, pp. 3889-3900, 2023, doi: 10.1109/TIA.2023.3256391.

[18]   J. Appelbaum, E. F. Fuchs, and J. C. White, "Optimization of Three-Phase Induction Motor Design Part I: Formulation of the Optimization Technique," *IEEE Transactions on Energy Conversion,* vol. EC-2, no. 3, pp. 407-414, 1987, doi: 10.1109/TEC.1987.4765866.

[19]   S. Kahourzade, A. Mahmoudi, E. Roshandel, and Z. Cao, "Optimal design of Axial-Flux Induction Motors based on an improved analytical model," *Energy,* vol. 237, p. 121552, 2021/12/15/ 2021, doi: https://doi.org/10.1016/j.energy.2021.121552.

[20]   J. Mei, Y. Zuo, C. H. T. Lee, and J. L. Kirtley, "Modeling and Optimizing Method for Axial Flux Induction Motor of Electric Vehicles," *IEEE Transactions on Vehicular Technology,* vol. 69, no. 11, pp. 12822-12831, 2020, doi: 10.1109/TVT.2020.3030280.

[21]   Z. Nasiri-Gheidari and H. Lesani, "Investigation of characteristics of a single-phase axial flux induction motor using three-dimensional finite element method and d–q model," *IET Electric Power Applications,* vol. 7, no. 1, pp. 47-57, 2013/01/01 2013, doi: https://doi.org/10.1049/iet-epa.2012.0131.

[22]   J. Mei, C. H. T. Lee, and J. L. Kirtley, "Design of Axial Flux Induction Motor With Reduced Back Iron for Electric Vehicles," *IEEE Transactions on Vehicular Technology,* vol. 69, no. 1, pp. 293-301, 2020, doi: 10.1109/TVT.2019.2954084.

[23]   M. Mirzaei, M. Mirsalim, and S. E. Abdollahi, "Analytical Modeling of Axial Air Gap Solid Rotor Induction Machines Using a Quasi-Three-Dimensional Method," *IEEE Transactions on Magnetics,* vol. 43, no. 7, pp. 3237-3242, 2007, doi: 10.1109/TMAG.2007.894215.

[24]   YASA. "YASA – Axial-flux electric motors and controllers." https://yasa.com/ (accessed.

[25]   Z. Cao, A. Mahmoudi, S. Kahourzade, and W. L. Soong, "An Overview of Axial-Flux Induction Machine," in *2021 31st Australasian Universities Power Engineering Conference (AUPEC)*, 26-30 Sept. 2021 2021, pp. 1-6, doi: 10.1109/AUPEC52110.2021.9597784.

[26]   F. Keskin Arabul, I. Senol, and Y. Oner, "Performance Analysis of Axial-Flux Induction Motor with Skewed Rotor," *Energies*, vol. 13, no. 19, doi: 10.3390/en13194991.

[27]   D. L. Gerling, P., "Induction motor," United States, 1997.

[28]   B. H. Smith and D. Platt, "Compound, series, axial flux induction machines: single phase analogy," *IEE Proceedings B (Electric Power Applications),* vol. 137, no. 4, pp. 265-272, 1990/07/01 1990, doi: 10.1049/ip-b.1990.0032.

[29]   A. T. d. Almeida, F. J. T. E. Ferreira, and G. Baoming, "Beyond Induction Motors—Technology Trends to Move Up Efficiency," *IEEE Transactions on Industry Applications,* vol. 50, no. 3, pp. 2103-2114, 2014, doi: 10.1109/TIA.2013.2288425.

[30]   I. Boldea, & Tutelea, L.N., *Electric Machines*

Steady State, Transients, and Design with MATLAB (1st edition). CRC Press, 2009.

[31]   T. Fan, J. Luo, X. Wen, and X. Liao, "A new sizing equation and it's application in electrical machine design," in *2011 International Conference on Electric Information and Control Engineering*, 15-17 April 2011 2011, pp. 3890-3893, doi: 10.1109/ICEICE.2011.5778044.

[32]   H. J. Lee, S. H. Im, D. Y. Um, and G. S. Park, "A Design of Rotor Bar for Improving Starting Torque by Analyzing Rotor Resistance and Reactance in Squirrel Cage Induction Motor," *IEEE Transactions on Magnetics,* vol. 54, no. 3, pp. 1-4, 2018, doi: 10.1109/TMAG.2017.2764525.

[33]   C. Heo, H. Kim, and G. Park, "A design of rotor bar inclination in squirrel cage induction motor," in *2017 IEEE International Magnetics Conference (INTERMAG)*, 24-28 April 2017 2017, pp. 1-1, doi: 10.1109/INTMAG.2017.8007748.

[34]   A. Boglietti, A. Cavagnino, M. Lazzari, and S. Vaschetto, "Preliminary induction motor electromagnetic sizing based on a geometrical approach," *IET Electric Power Applications,* vol. 6, no. 9, pp. 583-592, 2012/11/08 2012, doi: 10.1049/iet-epa.2012.0037.

[35]   K. Bitsi, M. E. Beniakar, O. Wallmark, and S. G. Bosga, "Preliminary Electromagnetic Sizing of Axial-Flux Induction Machines," in *2020 International Conference on Electrical Machines (ICEM)*, 23-26 Aug. 2020 2020, vol. 1, pp. 284-290, doi: 10.1109/ICEM49940.2020.9270719.

[36]   B. Dianati, S. Kahourzade, and A. Mahmoudi, "Optimization of Axial-Flux Induction Motors for the Application of Electric Vehicles Considering Driving Cycles," *IEEE Transactions on Energy Conversion,* vol. 35, no. 3, pp. 1522-1533, 2020, doi: 10.1109/TEC.2020.2976625.

[37]   B. Dianati, S. Kahourzade, and A. Mahmoudi, "Axial-Flux Induction Motors for Electric Vehicles," in *2019 IEEE Vehicle Power and Propulsion Conference (VPPC)*, 14-17 Oct. 2019 2019, pp. 1-6, doi: 10.1109/VPPC46532.2019.8952278.

[38]   B. Dianati, S. Kahourzade, and A. Mahmoudi, "Analytical Design of Axial-Flux Induction Motors," in *2019 IEEE Vehicle Power and Propulsion Conference (VPPC)*, 14-17 Oct. 2019 2019, pp. 1-6, doi: 10.1109/VPPC46532.2019.8952172.

[39]   S. Kahourzade, A. Mahmoudi, R. Ravji, and W. L. Soong, "Line-Start Axial-Flux PM Motors: Introduction of a New Machine Topology," in *2019 IEEE Energy Conversion Congress and Exposition (ECCE)*, 29 Sept.-3 Oct. 2019 2019, pp. 7027-7034, doi: 10.1109/ECCE.2019.8912992.

[40]   B. Guo, Y. Du, F. Peng, and Y. Huang, "Magnetic Field Calculation in Axial Flux Permanent Magnet Motor With Rotor Eccentricity," *IEEE Transactions on Magnetics,* vol. 58, no. 9, pp. 1-4, 2022, doi: 10.1109/TMAG.2022.3185708.

[41]   J. Li, R. Qu, and Y. H. Cho, "Effect of unbalanced and inclined air-gap in double-stator inner-rotor axial flux permanent magnet machine," in *2014 International Conference on*

Electrical Machines (ICEM), 2-5 Sept. 2014 2014, pp. 502-508, doi: 10.1109/ICELMACH.2014.6960227.

[42]   S. M. Mirimani, A. Vahedi, and F. Marignetti, "Effect of Inclined Static Eccentricity Fault in Single Stator-Single Rotor Axial Flux Permanent Magnet Machines," *IEEE Transactions on Magnetics,* vol. 48, no. 1, pp. 143-149, 2012, doi: 10.1109/TMAG.2011.2161876.

[43]   X. Zhang and B. Zhang, "Analysis of Magnetic Forces in Axial-Flux Permanent-Magnet Motors with Rotor Eccentricity," *Mathematical Problems in Engineering,* vol. 2021, no. 1, p. 7683715, 2021/01/01 2021, doi: https://doi.org/10.1155/2021/7683715.

[44]   Q. Wang, F. Zhao, and K. Yang, "Analysis and Optimization of the Axial Electromagnetic Force for an Axial-Flux Permanent Magnet Vernier Machine," *IEEE Transactions on Magnetics,* vol. 57, no. 2, pp. 1-5, 2021, doi: 10.1109/TMAG.2020.3005216.

[45]   W. L. Soong, E. Roshandel, Z. Cao, A. Mahmoudi, and S. Kahourzade, "Axial Force Negative Stiffness in Axial-Flux Electric Machines," in *2023 IEEE International Magnetic Conference - Short Papers (INTERMAG Short Papers)*, 15-19 May 2023 2023, pp. 1-2, doi: 10.1109/INTERMAGShortPapers58606.2023.10228209.

[46]   A. Benoudjit and N. N. Said, "New dual-airgap axial and radial-flux induction motor for on wheel drive electric propulsion systems," in *POWERCON '98. 1998 International Conference on Power System Technology. Proceedings (Cat. No.98EX151)*, 18-21 Aug. 1998 1998, vol. 1, pp. 615-619 vol.1, doi: 10.1109/ICPST.1998.729038.

[47]   K. BITSI, "On Electrical Machine Topologies for Electric Vehicle Applications," Degree of Doctor of Philosophy KTH Royal Institute of Technology, KTH Royal Institute of Technology, 2022.

[48]   W. S. Leung and J. C. C. Chan, "A New Design Approach for Axial-Field Electrical Machines," *IEEE Transactions on Power Apparatus and Systems,* vol. PAS-99, no. 4, pp. 1679-1685, 1980, doi: 10.1109/TPAS.1980.319594.

[49]   C. Hong, Q. Sun, Y. Li, and Y. Du, "Control Strategy for Self-bearing Dual Stator Solid Rotor Axial Flux Induction Motor," in *2022 IEEE Transportation Electrification Conference and Expo, Asia-Pacific (ITEC Asia-Pacific)*, 28-31 Oct. 2022 2022, pp. 1-6, doi: 10.1109/ITECAsia-Pacific56316.2022.9941913.

[50]   M. Subramanian, N. Devarajan, S. Deivasahayam, and Gopalakrishnan, "Review on efficiency improvement in squirrel cage induction motor by using dcr technology," *Journal of Electrical Engineering,* vol. 60, pp. 227-236, 08/01 2009.

[51]   G. A. Leonov, E. P. Solovyeva, and A. M. Zaretskiy, "Speed regulation of induction motors with wound rotor," *IFAC Proceedings Volumes,* vol. 46, no. 12, pp. 90-94, 2013/01/01/ 2013, doi: https://doi.org/10.3182/20130703-3-FR-4039.00031.

[52]   J. H. Choi *et al.*, "Design of High Power Permanent Magnet Motor With Segment Rectangular Copper Wire and Closed Slot Opening on Electric Vehicles*," *IEEE Transactions on Magnetics,* vol. 46, no. 9, pp. 3701-3704, 2010, doi: 10.1109/TMAG.2010.2060385.

[53]   C. Rossi, D. Casadei, A. Pilati, and M. Marano, "Wound Rotor Salient Pole Synchronous Machine Drive for Electric Traction," in *Conference Record of the 2006 IEEE Industry Applications Conference Forty-First IAS Annual Meeting*, 8-12 Oct. 2006 2006, vol. 3, pp. 1235-1241, doi: 10.1109/IAS.2006.256689.

[54]   F. Graffeo, S. Vaschetto, M. Cossale, M. Kerschbaumer, E. C. Bortoni, and A. Cavagnino, "Cylindrical Wound-Rotor Synchronous Machines for Traction Applications,"

in *2020 International Conference on Electrical Machines (ICEM)*, 23-26 Aug. 2020 2020, vol. 1, pp. 1736-1742, doi: 10.1109/ICEM49940.2020.9270992.

[55] A. Hassanpour Isfahani and S. Vaez-Zadeh, "Line start permanent magnet synchronous motors: Challenges and opportunities," *Energy,* vol. 34, no. 11, pp. 1755-1763, 2009/11/01/ 2009, doi: https://doi.org/10.1016/j.energy.2009.04.022.

[56] M. Intelligence. "Permanent Magnet Motor Market - Growth, Trends, COVID-19 Impact, and Forecasts (2023 - 2028)." https://www.mordorintelligence.com/industry-reports/permanent-magnet-motor-market (accessed.

[57] D. G. Dorrell, A. M. Knight, M. Popescu, L. Evans, and D. A. Staton, "Comparison of different motor design drives for hybrid electric vehicles," in *2010 IEEE Energy Conversion Congress and Exposition*, 12-16 Sept. 2010 2010, pp. 3352-3359, doi: 10.1109/ECCE.2010.5618318.

[58] B. Ban, "Synchronous reluctance machine optimization based on reduced set of geometric parameters with improved convergence and robust geometric feasibility verification," 2022.

[59] E. Trading, "Neodymium Rare Earth Price - Chart - Historical Data," *Trading Economics,* 2025-05-14 2025. [Online]. Available: https://tradingeconomics.com/commodity/neodymium.

[60] *Rotating Electrical Machines – Part 1: Rating and Performance*, I. E. Commission, 2010.

[61] *Rotating Electrical Machines – Part 2-1: Standard Methods for Determining Losses and Efficiency from Tests (Excluding Machines for Traction Vehicles)*, I. E. Commission, 2014.

[62] R. Mistry, W. R. Finley, and T. Gaerke, "Comparison of IEC and NEMA Requirements to Ensure Proper Specification and Design of Induction Motors & Generators for Global use-part 2: Copyright Material IEEE, Paper No. PCIC-2017-04," in *2018 IEEE Petroleum and Chemical Industry Technical Conference (PCIC)*, 24-26 Sept. 2018 2018, pp. 29-38, doi: 10.1109/PCIC31437.2018.9080456.

[63] A. De Almeida, J. Fong, C. U. Brunner, R. Werle, and M. Van Werkhoven, "New technology trends and policy needs in energy efficient motor systems - A major opportunity for energy and carbon savings," *Renewable and Sustainable Energy Reviews,* vol. 115, p. 109384, 2019/11/01/ 2019, doi: https://doi.org/10.1016/j.rser.2019.109384.

[64] W. L. Soong, Z. Cao, E. Roshandel, A. Mahmoudi, and S. Kahourzade, "Unbalanced Axial Forces in Axial-Flux Machines," in *2022 32nd Australasian Universities Power Engineering Conference (AUPEC)*, 26-28 Sept. 2022 2022, pp. 1-6, doi: 10.1109/AUPEC58309.2022.10215613.

[65] Z. Cao, A. Mahmoudi, S. Kahourzade, and W. L. Soong, "A Study on Dual and Single Stator Axial-Flux Induction Machines," in *2022 32nd Australasian Universities Power Engineering Conference (AUPEC)*, 26-28 Sept. 2022 2022, pp. 1-6, doi: 10.1109/AUPEC58309.2022.10216007.

[66] S. Kubzdela and B. Weglinski, "Magnetodielectrics in induction motors with disk rotor," *IEEE Transactions on Magnetics,* vol. 24, no. 1, pp. 635-638, 1988, doi: 10.1109/20.43996.

[67] A. Havel, M. Sobek, L. Stepanec, and J. Strossa, "Optimization of Permanent Magnet Parameters in Axial Flux Rotary Converter for HEV Drive," *Energies*, vol. 15, no. 3, doi: 10.3390/en15030724.

[68]   S. Kumar, T. A. Lipo, and B. I. Kwon, "A 32 000 r/min Axial Flux Permanent Magnet Machine for Energy Storage With Mechanical Stress Analysis," *IEEE Transactions on Magnetics,* vol. 52, no. 7, pp. 1-4, 2016, doi: 10.1109/TMAG.2015.2512939.

[69]   H. Ouldhamrane, J.-F. Charpentier, F. Khoucha, A. Zaoui, Y. Achour, and M. Benbouzid, "Optimal Design of Axial Flux Permanent Magnet Motors for Ship RIM-Driven Thruster," *Machines*, vol. 10, no. 10, doi: 10.3390/machines10100932.

[70]   A. Credo, M. Tursini, M. Villani, C. Di Lodovico, M. Orlando, and F. Frattari, "Axial Flux PM In-Wheel Motor for Electric Vehicles: 3D Multiphysics Analysis," *Energies*, vol. 14, no. 8, doi: 10.3390/en14082107.

[71]   F. Caricchi, F. Crescimbini, and E. Santini, "Basic principle and design criteria of axial-flux PM machines having counterrotating rotors," *IEEE Transactions on Industry Applications,* vol. 31, no. 5, pp. 1062-1068, 1995, doi: 10.1109/28.464520.

[72]   M. Valtonen, "Performance Characteristics of an Axial-Flux Solid-Rotor-Core Induction Motor," Doctor of Science, Lappeenranta University of Technology, 2007.

[73]   F. B. Morinigo, "Induction machine using ferromagnetic conducting material in rotor," 1996.

[74]   D. Gerling and P. Lürkens, "Axial-flow induction motor," 1996. [Online]. Available: https://patents.google.com/patent/EP0773619B1/en

[75]   H. Surong, L. Jian, F. Leonardi, and T. A. Lipo, "A comparison of power density for axial flux machines based on general purpose sizing equations," *IEEE Transactions on Energy Conversion,* vol. 14, no. 2, pp. 185-192, 1999, doi: 10.1109/60.766982.

[76]   A. Mahmoudi, S. Kahourzade, N. A. Rahim, and W. P. Hew, "Design, Analysis, and Prototyping of an Axial-Flux Permanent Magnet Motor Based on Genetic Algorithm and Finite-Element Analysis," *IEEE Transactions on Magnetics,* vol. 49, no. 4, pp. 1479-1492, 2013, doi: 10.1109/TMAG.2012.2228213.

[77]   D. Staton, A. Boglietti, and A. Cavagnino, "Solving the more difficult aspects of electric motor thermal analysis in small and medium size industrial induction motors," *IEEE Transactions on Energy Conversion,* vol. 20, no. 3, pp. 620-628, 2005, doi: 10.1109/TEC.2005.847979.

[78]   M. A. Tapia, W. Jara, R. Wallace, and J. A. Tapia, "Parameters Identification of an Axial Flux Induction Machine Using Field Equations," in *2018 XIII International Conference on Electrical Machines (ICEM)*, 3-6 Sept. 2018 2018, pp. 351-357, doi: 10.1109/ICELMACH.2018.8506891.

[79]   G. Baranov, A. Zolotarev, V. Ostrovskii, T. Karimov, and A. Voznesensky, "Analytical Model for the Design of Axial Flux Induction Motors with Maximum Torque Density," *World Electric Vehicle Journal*, vol. 12, no. 1, doi: 10.3390/wevj12010024.

[80]   S. Kahourzade, A. Mahmoudi, H. W. Ping, and M. N. Uddin, "A Comprehensive Review of Axial-Flux Permanent-Magnet Machines," *Canadian Journal of Electrical and Computer Engineering,* vol. 37, no. 1, pp. 19-33, 2014, doi: 10.1109/CJECE.2014.2309322.

[81]   A. Nobahari, A. Darabi, and A. Hassannia, "Various skewing arrangements and relative position of dual rotor of an axial flux induction motor, modelling and performance evaluation," *IET Electric Power Applications*, vol. 12, no. 4, pp. 575-580, 2018/04/01 2018, doi: 10.1049/iet-epa.2017.0716.

[82]   M. Valtonen, A. Parviainen, and J. Pyrhonen, "The Effects of the Number of Rotor Slots on the Performance Characteristics of Axial-Flux Aluminium-Cage Solid-Rotor Core Induction Motor," in *2007 IEEE International Electric Machines & Drives Conference*, 3-5 May 2007 2007, vol. 1, pp. 668-672, doi: 10.1109/IEMDC.2007.382747.

[83]   M. Valtonen, A. Parviainen, and J. Pyrhonen, "Influence of the air-gap length to the performance of an axial-flux induction motor," in *2008 18th International Conference on Electrical Machines*, 6-9 Sept. 2008 2008, pp. 1-5, doi: 10.1109/ICELMACH.2008.4800002.

[84]   G. Haines, N. Ertugrul, and W. L. Soong, "Autonomously Obtaining System Efficiency Maps from Motor Drive Systems," in *2019 IEEE International Conference on Industrial Technology (ICIT)*, 13-15 Feb. 2019 2019, pp. 231-236, doi: 10.1109/ICIT.2019.8755199.

[85]   M. Oka and M. Enokizono, "Evaluation of hysteresis loss and eddy-current loss in induction motor stator cores using the excitation inner core method," in *2016 XXII International Conference on Electrical Machines (ICEM)*, 4-7 Sept. 2016 2016, pp. 1686-1691, doi: 10.1109/ICELMACH.2016.7732751.

[86]   J. Zhang, J. Liu, and H. Wu, "Research on a Novel High-Torque-Density Axial–Radial-Flux Permanent-Magnet Motor with Annular Winding for an Elevator-Traction Machine," *Electronics*, vol. 12, no. 13, doi: 10.3390/electronics12132867.

[87]   A. P. Ferreira and A. F. Costa, "Efficient pole-arc coefficients for maximum no load flux linkage in axial flux permanent magnet machines," in *8th IEEE Symposium on Diagnostics for Electrical Machines, Power Electronics & Drives*, 5-8 Sept. 2011 2011, pp. 246-250, doi: 10.1109/DEMPED.2011.6063631.

[88]   J. F. Gieras, R.-J. Wang, and M. J. Kamper, *Axial Flux Permanent Magnet Brushless Machines*, 1 ed. Dordrecht: Springer Netherlands, 2006.

[89]   E. Yeşilbağ, Y. Ertuğrul, and L. Ergene, "Axial flux PM BLDC motor design methodology and comparison with a radial flux PM BLDC motor," *Turkish Journal of Electrical Engineering and Computer Sciences*, vol. 25, no. 4, pp. 3455-3467, 2017.

[90]   S. Kahourzade, A. Mahmoudi, N. A. Rahim, and H. W. Ping, "Sizing equation and Finite Element Analysis optimum design of axial-flux permanent-magnet motor for electric vehicle direct drive," in *2012 IEEE International Power Engineering and Optimization Conference Melaka, Malaysia*, 6-7 June 2012 2012, pp. 1-6, doi: 10.1109/PEOCO.2012.6230826.

[91]   H. Surong, M. Aydin, and T. A. Lipo, "TORUS concept machines: pre-prototyping design assessment for two major topologies," in *Conference Record of the 2001 IEEE Industry Applications Conference. 36th IAS Annual Meeting (Cat. No.01CH37248)*, 30 Sept.-4 Oct. 2001 2001, vol. 3, pp. 1619-1625 vol.3, doi: 10.1109/IAS.2001.955751.

[92]   N. Taran and M. Ardebili, "Efficiency optimization of an Axial Flux Permanent Magnet Synchronous Generator for low speed wind power applications," in *2014 22nd Iranian Conference on Electrical Engineering (ICEE)*, 20-22 May 2014 2014, pp. 539-544, doi: 10.1109/IranianCEE.2014.6999602.

[93]   A. E. Fitzgerald and C. Kingsley, *Electric machinery : the dynamics and statics of electromechanical energy conversion*, 2d ed. (McGraw-Hill electrical and electronic engineering series). New York: McGraw-Hill, 1961.

[94]   W. Yan *et al.*, "Performance Analysis of a Novel Axial Radial Flux Segmental Rotor Switched Reluctance Motor," *IEEE Transactions on Transportation Electrification,* vol. 10, no. 1, pp. 1031-1042, 2024, doi: 10.1109/TTE.2023.3272402.

[95]   Z. Hao, Y. Ma, P. Wang, G. Luo, and Y. Chen, "A Review of Axial-Flux Permanent-Magnet Motors: Topological Structures, Design, Optimization and Control Techniques," *Machines,* vol. 10, no. 12, doi: 10.3390/machines10121178.

[96]   K. H. Kim and D. K. Woo, "Novel Quasi-Three-Dimensional Modeling of Axial Flux In-Wheel Motor With Permanent Magnet Skew," *IEEE Access,* vol. 10, pp. 98842-98854, 2022, doi: 10.1109/ACCESS.2022.3206774.

[97]   Y. Zhang, Y. Wang, and S. Gao, "3-D magnetic equivalent circuit model for a coreless axial flux permanent-magnet synchronous generator," *IET Electric Power Applications,* vol. 15, no. 10, pp. 1261-1273, 2021/10/01 2021, doi: https://doi.org/10.1049/elp2.12092.

[98]   A. Egea, G. Almandoz, J. Poza, and A. Gonzalez, "Axial flux machines modelling with the combination of 2D FEM and analytic tools," in *The XIX International Conference on Electrical Machines - ICEM 2010,* 6-8 Sept. 2010 2010, pp. 1-6, doi: 10.1109/ICELMACH.2010.5608115.

[99]   J. F. Gieras, R.-J. Wang, and M. J. Kamper, *Axial flux permanent magnet brushless machines*, 2nd ed. Dordrecht?: Springer, 2008.

[100]   S. K. F. Group, "7305 BECBP - Angular contact ball bearings | SKF," 2025. [Online]. Available: https://www.skf.com/my/products/rolling-bearings/ball-bearings/angular-contact-ball-bearings/single-row-angular-contact-ball-bearings/productid-7305%20BECBP.

[101]   L. A. Pereira, M. Perin, L. F. A. Pereira, J. R. Ruthes, F. L. M. de Sousa, and E. C. P. de Oliveira, "Performance estimation of three-phase induction motors from no-load startup test without speed acquisition," *ISA Transactions,* vol. 96, pp. 376-389, 2020/01/01/ 2020, doi: https://doi.org/10.1016/j.isatra.2019.05.028.

[102]   S. Kahourzade, N. Ertugrul, and W. L. Soong, "Investigation of emerging magnetic materials for application in axial-flux PM machines," in *2016 IEEE Energy Conversion Congress and Exposition (ECCE),* 18-22 Sept. 2016 2016, pp. 1-8, doi: 10.1109/ECCE.2016.7855218.

[103]   C. International Electrotechnical, "IEC 60038: IEC Standard Voltages," Standard 2009.